

A Thesis Submitted for the Degree of PhD at the University of Warwick

Permanent WRAP URL:

<http://wrap.warwick.ac.uk/152672>

Copyright and reuse:

This thesis is made available online and is protected by original copyright.

Please scroll down to view the document itself.

Please refer to the repository record for this item for information to help you to cite it.

Our policy information is available from the repository home page.

For more information, please contact the WRAP Team at: wrap@warwick.ac.uk

**Electroactive Self-healing Elastomers and
Nanocomposites for Actuation and Energy
Harvesting**

by

Christopher David Ellingford

A thesis submitted in partial fulfilment of the requirements for the
degree of

Doctor of Philosophy in Engineering

University of Warwick

Warwick Manufacturing Group

International Institute for Nanocomposites Manufacturing

Dec 2020

Table of Contents

Table of Contents	i
List of Figures	viii
List of Tables	xx
List of Equations	xxi
Acknowledgements	xxiii
Declaration of Authorship	xxiv
Summary	xxv
Abbreviations and Terminology	xxvii
Chapter 1	1
1.1 The need for dielectric elastomers in actuators and energy harvesters in the automotive industry.....	2
1.2 Dielectric Elastomers	3
1.3 The key electrical and mechanical properties	6
1.3.1 Relative permittivity and dielectric loss ($\tan \delta$).....	6
1.3.2 Electrical breakdown strength.....	8
1.3.3 Energy storage in polymers.....	9
1.4 Polymer (nano)composites.....	10
1.5 Working mechanisms of dielectric elastomer actuator and generator	12
1.6 Research objectives and thesis structure	14
1.7 References	16
Chapter 2	20
2.1 Introduction	21
2.2 Extrinsic modification of dielectric elastomers.....	21

2.2.1 The addition of conducting fillers	21
2.2.2 The addition of ceramic fillers	29
2.3 Intrinsic modification of dielectric elastomers.....	31
2.3.1 Intrinsic modification of dielectric elastomers with polar groups	32
Silicone based elastomers	34
Styrenic based unsaturated elastomers.....	39
2.3.2 Liquid crystal elastomers (LCEs) for actuators	41
2.3.3 Conducting group grafting of dielectric elastomers.....	43
2.4 Conclusions	44
2.5 References	45
Chapter 3	50
3.1 Materials.....	50
3.2 Synthesis procedures	51
3.2.1 UV light procedure.....	51
3.2.2 Synthesis of methyl thioglycolate modified SBS (MG-SBS).....	51
3.2.3 Synthesis of methyl-3-mercaptopropionate modified SBS (M3M-SBS) ...	52
3.2.4 Synthesis of methyl thioglycolate/thioglycolic acid modified SBS (MG/TG-SBS).....	53
3.2.5 Fabrication of SBS/PVDF/EVA blends and composites	53
3.2.6 Fabrication of SBS/PVDF and MG-SBS/PVDF blends and composites .	54
3.2.7 Synthesis of methyl thioglycolate modified styrene-butadiene rubber (MG-SBR).....	54
3.2.8 Synthesis of methyl thioglycolate/thioglycolic acid modified styrene-butadiene rubber (MG/TG-SBR)	54
3.2.9 Synthesis of methyl thioglycolate modified polybutadiene (MG-PB).....	55
3.2.10 Synthesis of methyl thioglycolate/thioglycolic acid modified polybutadiene (MG/TG-PB)	55

3.2.11 Synthesis of tetraaniline (TANI).....	56
3.2.12 Synthesis of epoxidised styrene-butadiene-styrene (E-SBS).....	56
3.2.13 Synthesis of tetraaniline modified styrene-butadiene-styrene (TANI-SBS)	57
3.2.14 Synthesis of epoxidised polybutadiene (E-PB).....	57
3.2.15 Synthesis of tetraaniline modified polybutadiene (TANI-PB)	57
3.3 Characterisation.....	58
3.3.1 Nuclear magnetic resonance (NMR) spectroscopy.....	58
3.3.2 Variable temperature NMR spectroscopy	58
3.3.3 Fourier transform infrared spectroscopy (FTIR).....	58
3.3.4 Gel permeation chromatography (GPC)	58
3.3.5 Compression moulding	59
3.3.6 Density measurements	59
3.3.7 Impedance spectroscopy	59
3.3.8 Mechanical testing	59
3.3.9 UV-Vis spectroscopy	60
3.3.10 Raman spectroscopy.....	60
3.3.11 Dynamic mechanical thermal analysis (DMTA)	60
3.3.12 Differential scanning calorimetry (DSC).....	60
3.3.13 Oscillatory rheometry.....	60
3.3.14 Contact angle measurements.....	60
3.3.15 Scanning electron microscopy (SEM)	60
3.3.16 Atomic force microscopy (AFM)	61
3.3.17 Small angle X-ray scattering (SAXS).....	61
3.3.18 Self-healing investigation	61
3.3.19 Polarisation-electric field (P-E) loops testing	61
3.3.20 Electrical properties under strain	62

3.3.21 Actuation testing	62
3.3.22 Energy harvesting testing.....	63
3.4 References	63
Chapter 4	64
4.1 Introduction	65
4.2 Results and Discussion.....	68
4.2.1 Grafting of methyl thioglycolate to styrene-butadiene-styrene (MG-SBS)	68
4.2.2 Electrical and mechanical properties of MG-SBS	73
4.2.3 Mechanical self-healing abilities of MG-SBS	75
4.2.4 Electrical self-healing under low electrical field	83
4.2.5 Effect of self-healing on the mechanical behaviour of MG-SBS	85
4.2.6 Investigating the actuation abilities of MG-SBS using dielectric elastomer actuators (DEA)	87
4.2.7 Finite element modelling of MG-SBS electrical breakdown recovery ...	100
4.3 Conclusion	102
4.4 References	104
Chapter 5	106
5.1 Introduction	107
5.2 Results and Discussion.....	109
5.2.1 Intrinsic modification of SBS with methyl-3-mercaptopropionate.....	109
5.2.2 Mechanical and electrical characterisation of M3M-SBS	112
5.2.3 Self-healing ability and structural rationalisation of M3M-SBS	116
5.2.4 Actuation performance of M3M-SBS.....	120
5.2.5 Energy harvesting abilities of MG-SBS and M3M-SBS	121

5.3 Conclusion	129
5.4 References	131
Chapter 6	133
6.1 Introduction	134
6.2 Results and Discussion.....	137
6.2.1 Intrinsic modification of SBS with methyl thioglycolate and thioglycolic acid	137
6.2.2 Synergistic effects of methyl thioglycolate and thioglycolic acid on elastomer morphology and electromechanical properties	138
6.2.3 Temperature dependency of self-healing and electric properties	145
6.2.4 Actuation testing of MG/TG-SBS.....	152
6.3 Conclusion	153
6.4 References	155
Chapter 7	156
7.1 Introduction	157
7.2 Results and discussion for extrinsic modification of SBS through compositing to produce thermoplastic elastomer nanocomposites with an electrical dual percolation threshold.....	160
7.2.1 Structural characterisation of SBS/PVDF thermoplastic elastomers	160
7.2.2 Selective localisation of MWCNTs in SBS/PVDF thermoplastic elastomers	163
7.2.3 Rheological dual percolation of SBS/PVDF/EVA/MWCNT nanocomposites	169
7.2.4 Electrical dual-percolation in SBS/PVDF/EVA TPE composites	170
7.2.5 Electrical dual-percolation behaviour of SBS/PVDF/EVA TPEs under mechanical stretching.....	173

7.3 Results and discussion for extrinsic modification of intrinsically modified SBS composites with PVDF and MWCNTs.....	177
7.3.1 Electrical properties of SBS/PVDF and MG-SBS/PVDF blends	177
7.3.2 Mechanical properties of SBS/PVDF blends	178
7.3.3 Formation of SBS/PVDF and MG-SBS/PVDF composites with MWCNTs	181
7.4 Conclusion	185
7.5 References	187
Chapter 8	189
8.1 Introduction	190
8.2 The grafting of polar groups to styrene-butadiene-rubber (SBR).....	194
8.2.1 Grafting of methyl thioglycolate and thioglycolic acid to styrene-butadiene rubber.	194
8.2.2 Structural characterisation of MG-SBR and 80/20 MG/TG-SBR	198
8.2.3 Electromechanical properties of SBR elastomers	199
8.3 The grafting of polar groups to polybutadiene (PB)	202
8.3.1 Grafting of methyl thioglycolate and thioglycolic acid to polybutadiene	202
8.3.2 Structural characterisation of MG-PB and 80/20 MG/TG-PB.....	205
8.3.3 Electromechanical properties of PB elastomers.....	206
8.4 Intrinsic modification of SBS and PB with conducting groups	209
8.4.1 The synthesis of emeraldine base tetraaniline.....	209
8.4.2 Grafting of TANI to unsaturated backbones	211
8.4.3 Electromechanical properties of TANI modified elastomers.....	217
8.5 Conclusions	221
8.6 References	222

Chapter 9	224
9.1 Conclusions	225
9.2 Future perspectives.....	228
Appendix.....	230
Journal Papers and Conference Presentations.....	251
List of Journal Papers Published and Conference Presentations.....	251
Paper: Intrinsically Tuning the Electromechanical Properties of Elastomer Dielectrics: A Chemistry Perspective.....	254
Book Chapter: Chemical Modification of Dielectric Elastomers.....	285
Paper: Intrinsic Tuning of Poly(styrene-butadiene-styrene)-Based Self-Healing Dielectric Elastomer Actuators with Enhanced Electromechanical Properties.....	289
Paper: Electrical and Mechanical Self-Healing in High-Performance Dielectric Elastomer Actuator Materials.....	333
Paper: Self-Healing Dielectric Elastomers for Damage-Tolerant Actuation and Energy Harvesting.....	346
Paper: Understanding the Enhancement and Temperature-Dependency of the Self-Healing and Electromechanical Properties of Dielectric Elastomers Containing Mixed Pendant Polar Groups.....	356
Paper: Electrical Dual-percolation in MWCNTs/SBS/PVDF Based Thermoplastic Elastomer (TPE) Composites and the Effect of Mechanical Stretching.....	367
Paper: Mechanical and Dielectric Properties of MWCNT Filled Chemically Modified SBS/PVDF Blends.....	378
Paper: Structure and dielectric properties of electroactive tetraaniline grafted non-polar elastomers.....	385

List of Figures

Figure 1.1 An example of the range of sensors and driving aids present in a smart, modern vehicle. Reproduced from INSIGHTS. ⁹	2
Figure 1.2 Structures of different dielectric elastomers and semicrystalline polymers.	5
Figure 1.3 The effect of frequency on the types of polarisation present in a polymer and the relaxation peaks observed in the loss. Adapted from Bibi <i>et al.</i> ⁴²	8
Figure 1.4 Schematic graph for the behaviour of the relative permittivity as the filler content increased. Reproduced from Yuan <i>et al.</i> ⁶²	11
Figure 1.5 The different routes to create high permittivity nanocomposites <i>via</i> the addition of extrinsic fillers. Reproduced from Ellingford <i>et al.</i> ¹⁹	12
Figure 1.6 Schematic diagram for the energy harvesting cycle of a dielectric elastomer generator. The difference between the voltage in step (2) and (3) is the harvested energy in step (4). Adapted from Ellingford <i>et al.</i> ¹⁹	13
Figure 1.7 Research pathway for high performance dielectric elastomers.	16
Figure 2.1 Modification of MWCNTs with a RAFT agent and a subsequent grafting from reaction to produce polyacrylonitrile and polydiurethane monoacrylate modified MWCNTs. Reproduced from Galantini <i>et al.</i> ⁶	22
Figure 2.2 Nanosilica decorated carboxylated MWCNTs. Reproduced from George <i>et al.</i> ¹⁰	24
Figure 2.3 Electret dielectric elastomer generator set-up using nanospring containing carbon nanotubes in a PDMS composite. Reproduced from Lee <i>et al.</i> ¹²	25
Figure 2.4 Synthesis of core-shell TiO ₂ with polycatcheol/polyamine shells modified with silane. Adapted from Yang <i>et al.</i> ²³	28
Figure 2.5 Synthetic pathway for a silane and dopamine core-shell BaTiO ₃ . Reproduced from Yang <i>et al.</i> ²⁸	30
Figure 2.6 Schematic diagram of the slide ring structure. Adapted from Noda <i>et al.</i> ³⁶	31
Figure 2.7 (a) Relative permittivity vs electrical breakdown strength and (b) Young's modulus vs dielectric permittivity. Adapted from Ellingford <i>et al.</i> ⁴⁵	33
Figure 2.8 General reaction scheme for hydrosilylation of silicone dielectric elastomers. Reproduced from Ellingford <i>et al.</i> ⁴⁵	34

Figure 2.9 Pictorial representation of polar CNATS-993 (short chained allyl cyanide modified PHMS) in a non-polar PDMS matrix. Reproduced from Risse <i>et al.</i> ⁶⁰	36
Figure 2.10 SEM imaging of (a) SBS, (b) 40 mol% methyl thioglycolate modified SBS and (c) 81 mol% methyl thioglycolate modified SBS. Reproduced from Sun <i>et al.</i> ⁸⁰	40
Figure 2.11 Mesogen arrangements in a LCE. The method of inclusion of the mesogen into the polymer backbone affects the crystal arrangement formed. Adapted from Ula <i>et al.</i> ⁸²	41
Figure 2.12 Summary of different reaction types to synthesise LCEs. Reproduced from Ula <i>et al.</i> ⁸²	42
Figure 3.1 Electrode configurations for (a) DEA in strain after pre-strain and setup for actuation strain measurement; (b) dielectric elastomer actuation in force mode to pre-strain and setup for actuation force measurement; (c) a voltage input sequence of voltage enhancements for increasing the actuation response. Reproduced from Ellingford <i>et al.</i> ²	62
Figure 4.1 (a) Type I photoinitiator photo decomposition and subsequent reaction pathway and (b) Type II photoinitiator photo decomposition and subsequent reaction pathway	66
Figure 4.2 Possible products formed during thiol-ene reaction on an example of styrene-block-butadiene, showing vinyl group coupling to thiol group, intrachain cyclisation and interchain crosslinking	67
Figure 4.3 ¹ H NMR spectrum at 400 MHz in CDCl ₃ of SBS	69
Figure 4.4 (a) ¹ H NMR spectra at 400 MHz in CDCl ₃ of MG-SBS synthesised using different methyl thioglycolate excesses and (b) ¹ H NMR spectra at 400 MHz in CDCl ₃ of SBS and MG-SBS synthesised with different UV light exposure times	71
Figure 4.5 (a) FTIR spectra of SBS and MG-SBS with key peaks labelled, (b) GPC trace of SBS and MG-SBS in THF (c) GPC trace of MG-SBS in THF with the UV light detector at 254 nm and Refractive Index detector against retention time	73
Figure 4.6 Impedance spectroscopy of SBS and MG-SBS with (a) relative permittivity, (b) $\tan \delta$ loss, (c) phase angle and (d) AC conductivity	74

Figure 4.7 (a) Stress-strain curves of SBS and MG-SBS from mechanical testing and (b) Images of the self-healing process of MG-SBS	75
Figure 4.8 Self-healing of MG-SBS at room temperature results up to three days with (a) strain at break recovery and (b) tensile strength recovery	76
Figure 4.9 DMTA $\tan \delta$ results of SBS and MG-SBS for the T_g transitions of the elastomers.....	77
Figure 4.10 (a) 1D and 2D SAXS measurements of SBS and MG-SBS and (b) height distribution and indentation imagery from AFM	78
Figure 4.11 (a) Solution state UV-Vis spectra of SBS and MG-SBS in DCM, (b) solid state UV-Vis spectra of SBS and MG-SBS, (c) FTIR spectra of SBS and MG-SBS with key peak shifts and (d) Raman spectra of SBS and MG-SBS with key peak shifts	79
Figure 4.12 Diagram for the suggested electrostatic self-healing interaction present in MG-SBS.....	80
Figure 4.13 (a) Self-healing of MG-SBS (65.1%) at room temperature for strain at break recovery and (b) tensile strength recovery. (c) Self-healing for MG-SBS at 37 °C for strain at break recovery and (d) tensile strength recovery. (e) Retesting self-healing for MG-SBS at room temperature for strain at break recovery and (f) tensile strength recovery	82
Figure 4.14 Electrical self-healing testing at low electrical fields (2.5×10^{-3} MV m ⁻²) using impedance spectroscopy to obtain (a) AC conductivity, (b) capacitance and (c) phase angle vs Frequency. (d) SEM image of the pinhole defect formed in MG-SBS upon breakdown of the elastomer	84
Figure 4.15 Cyclic strain softening of SBS, MG-SBS, MG-SBS (65.1%) and MG-SBS (52.1%) at (a) 100%, (b) 300% and (c) 500% strain. In these graphs, the darker colour is the first strain cycle and the lighter colour is the fifth strain cycle for the respective materials. (d) Summary of the hysteresis loss of the elastomers between the first cycle and fifth cycle. (e) Normalised stress relaxation testing of over varying time periods until 30 mins. Samples tested until deemed to be in equilibrium.	86
Figure 4.16 (a) Radial actuation strain and (b) areal actuation strain of MG-SBS under different electric fields. (c) Actuation force of SBS, MG-SBS and VHB 4910 under increasing electric field	90
Figure 4.17 Polarisation-electric field loops for (a) pristine MG-SBS up to 4 kV and (b) healed MG-SBS up to 1 kV	92

Figure 4.18 Diagram of mechanical damage to MG-SBS for self-healing actuation test. Adapted from Zhang et al. ³⁴ SEM imaging of self-healed MG-SBS after mechanical damage with (b) image of the microscopic damage present, the scar and the bulk healed polymer and (c) close image of the scar in the healing site of MG-SBS and its disappearance	93
Figure 4.19 Impedance spectroscopy of pristine MG-SBS and healed MG-SBS after mechanical damage for (a) AC conductivity, (b) phase angle. Polarisation-electric field loops of (c) pristine MG-SBS and (d) healed MG-SBs after mechanical damage	94
Figure 4.20 SEM imaging of MG-SBS (a) after electrical breakdown forming a 90 μm pinhole defect, (b) after clearing debris with needle probe and (c) after application of finger pressure for self-healing of MG-SBS. (d) Cross-sectional view of MG-SBS after cleaning of pinhole failure with a needle probe and subsequently self-healed.....	95
Figure 4.21 (a) AC conductivity of MG-SBS before and after self-healing assisted using a needle probe, (b) phase angle of MG-SBS before and after self-healing assisted using a needle probe, (c) polarisation-electric field loop of pristine MG-SBS, (d) polarisation-electric field loop of MG-SBS after self-healing assisted using a hypodermic needle and (e) polarisation-electric field loop of MG-SBS after self-healing assisted using a needle probe	97
Figure 4.22 (a) MG-SBS after electrical breakdown in actuation device. Pinhole size is 1.5 mm. (b) MG-SBS after self-healing using a needle probe to remove carbonised debris, (c) mechanically damaged and healed MG-SBS and (d) mechanically damaged and healed MG-SBS after electrical breakdown and pinhole formation. Adapted from Zhang et al. ³⁴ (e) Radial actuation strain and (f) areal actuation strain under different electric fields for MG-SBS, MG-SBS after electrical breakdown, MG-SBS after damage through a mechanical slit, MG-SBS after damage through a mechanical puncture and MG-SBS after both damage from a mechanical slit and electrical breakdown.....	99
Figure 4.23 (a) Propagation of conductive phase during electrical breakdown in a material and (b) concentration of electric field across the material containing small defects at the surface after self-healing. Adapted from Zhang et al. ³⁴	101
Figure 4.24 (a) Conduction pathway formed and (b) concentration of electric field in a material with surface defects and pores/voids along the healed site of the material. Adapted from Zhang et al. ³⁴	102

Figure 5.1 Binding energy ranges for different types of noncovalent interactions. Reproduced from Wang <i>et al.</i> ²¹	108
Figure 5.2 (a) ¹ H NMR spectra at 400 MHz in CDCl ₃ of SBS and M3M-SBS with assigned peaks, (b) FTIR spectra of SBS and M3M-SBS with key peaks highlighted, (c) GPC trace of SBS and M3M-SBS in THF and (d) GPC trace of M3M-SBS in THF with the UV light detector at 254 nm and Refractive Index against retention time	111
Figure 5.3 The two most common conformers of methyl-3-mercaptopropionate ...	112
Figure 5.4 Stress strain curve of SBS and M3M-SBS	113
Figure 5.5 Cyclic stress softening curves of SBS and M3M-SBS at (a) 100%, (b) 300% and (c) 500% strain. The darker colour is the first cycle and the lighter colour is the fifth cycle for each material. (d) Hysteresis loss for SBS and M3M-SBS after five cycles. (e) Stress relaxation of SBS and M3M-SBS up to 30 minutes.	114
Figure 5.6 Impedance spectroscopy of SBS and M3M-SBS with (a) relative permittivity, (b) $\tan \delta$, (c) AC conductivity and (d) phase angle	116
Figure 5.7 (a) Recovery for the strain at break at various times compared to the strain at break for pristine M3M-SBS, (b) recovery for the tensile strength at various times compared to the tensile strength for pristine M3M-SBS and (c) stress strain curves for the self-healing of M3M-SBS at various times	117
Figure 5.8 (a) DMTA $\tan \delta$ and (b) Solution state UV-Vis spectroscopy of SBS and M3M-SBS in DCM	118
Figure 5.9 Temperature dependent FTIR for M3M-SBS between 30 °C and 150 °C for (a) 1734 cm ⁻¹ , (b) 1356 cm ⁻¹ and 1244 cm ⁻¹	119
Figure 5.10 (a) Radial actuation and (b) areal actuation of pristine M3M-SBS and healed M3M-SBS under different electric fields, the inset image shows the set-up of actuation testing of M3M-SBS	121
Figure 5.11 Schematic energy harvesting cycle of elastomers using air pressure. In state A, the elastomer is in the undeformed state with no applied voltage. In state B, the application of air pressure has deformed the elastomer to its stretched state. In state C, the voltage is applied and in state D the air pressure is removed to bring the elastomer to the undeformed state	122
Figure 5.12 (a) Electrical circuitry schematic for the dielectric elastomer generator and (b) application of voltage during the different states of the energy harvesting cycle	123

Figure 5.13 (a) Change in pressure and air volume flow rate compared to time for an energy harvesting cycle, (b) change in current and voltage compared to time for an energy harvesting cycle, (c) change in applied voltage as a function of strain and (d) change in electric field over one complete energy harvesting cycle.....	125
Figure 5.14 Measured energy harvesting cycles for M3M-SBS with the axial deformation of $\lambda_a = 3$ for (a) electrical and (b) mechanical work-conjugate plane. The enclosed to (a) the total converted electrical energy, W_e , of [13 mJ (52 mJ g ⁻¹)] and the actual harvested electrical energy, $W_{harvest}$, of [2.3 mJ (9.2 mJ g ⁻¹)] and (b) the expended mechanical energy, W_{mech} , of [178 mJ (324 mJ g ⁻¹)].	126
Figure 5.15 (a) The mechanical damage process on the elastomers (b) total converted electrical energy density, (c) generated electrical energy density and (d) Energy harvesting efficiency of M3M-SBS and MG-SBS	128
Figure 6.1 Formation of hydrogen bonding between carboxylic acid and amine groups on a polysiloxane chain as well as the ionic bonds formed when converted at 100 °C. Reproduced from Sun <i>et al.</i> ⁵	135
Figure 6.2 (a) ¹ H NMR spectra at 400 MHz in CDCl ₃ , (b) FTIR spectroscopy of SBS, 100/0 MG/TG-SBS and 80/20 MG/TG-SBS and (c) GPC trace of 90/10 MG/TG-SBS in THF with a Refractive Index detector.....	138
Figure 6.3 Stress strain curves of SBS, 100/0, 95/5, 90/10 and 80/20 MG/TG-SBS	139
Figure 6.4 (a) Cyclic stress softening of 95/5, 90/10 and 80/20 MG/TG-SBS at 100%, (b) cyclic stress softening of 95/5, 90/10 and 80/20 MG/TG-SBS at 300%, (c) a summary of hysteresis loss from cyclic stress softening for SBS, 100/0, 95/5, 90/10 and 80/20 MG/TG-SBS. Darker colour is cycle 1, lighter colour is cycle 5. (d) Stress relaxation of 95/5, 90/10 and 80/20 MG/TG-SBS.....	140
Figure 6.5 (a) AFM images of SBS, 95/5, 90/10 and 80/20 MG/TG-SBS with height distribution scales. Scale bar shown is 200 nm and (b) schematic diagram to explain to ordered microstructure phase transition upon increase in hydrogen bonding content. The increase in compatibility between styrene and butadiene results from electrostatic interactions (shown in green). Increase the hydrogen bonding network introduces a disorder-to-order phase transition of hydrogen bonding regions (shown in red). Reproduced from Ellingford <i>et. al.</i> ⁷	142

Figure 6.6 (a) DMTA $\tan \delta$ for SBS, 95/5, 90/10 and 80/20 MG/TG-SBS and (b) solution state UV-Vis spectroscopy for SBS, 100/0, 95/5, 90/10 and 80/20 MG/TG-SBS in DCM.....	143
Figure 6.7 Impedance spectroscopy for SBS, 95/5, 90/10 and 80/20 MG/TG-SBS for (a) relative permittivity, (b) $\tan \delta$, (c) phase angle and (d) AC conductivity.....	145
Figure 6.8 Temperature-dependent FTIR spectroscopy for MG/TG-SBS at 1730 cm^{-1} : (a) 100/0, (b) 95/5, (c) 90/10 and (d) 80/20.....	147
Figure 6.9 Variable temperature impedance spectroscopy showing the relative permittivity, $\tan \delta$ and phase angle of SBS (a-c), 100/0 MG/TG-SBS (d-f) and 80/20 MG/TG-SBS (g-i) in the temperature range of 30 °C to 130 °C	149
Figure 6.10 Master curves of 80/20 MG/TG-SBS at a reference temperature of 70 °C for (a) relative permittivity and (b) phase angle.....	150
Figure 6.11 Comparative self-healing recovery of 100/0 and 80/20 MG/TG-SBS at room temperature at 80/20 MG/TG-SBS at 80 °C at different time intervals	151
Figure 6.12 (a) Radial actuation strain and (b) areal actuation strain for pristine 80/20 MG/TG-SBS and healed 80/20 MG/TG-SBS.....	153
Figure 7.1 The three crystalline structures of PVDF, the α phase, β phase and γ phase. Reproduced from Wan <i>et al.</i> ²	158
Figure 7.2 Stress strain curve of SBS/PVDF, SBS/PVDF/EVA and SBS/PVDF/EVA with between 0.3 wt% and 3 wt% MWCNTs	160
Figure 7.3 (a) $\tan \delta$ graph of 50/50 SBS/PVDF, 50/50/20 SBS/PVDF/EVA and EVA with glass transition temperatures shown and (b) diagram of the compatibilisation interaction present within SBS/PVDF/EVA	162
Figure 7.4 SEM imaging of (a) 50/50 SBS/PVDF, (b) 50/50/20 SBS/PVDF/EVA, (c) 50/50/20/1 SBS/PVDF/EVA/MWCNT and (d) 50/50/20/3 SBS/PVDF/EVA/MWCNT.	163
Figure 7.5 (a) Normalised stress intensity for SBS/PVDF/EVA with 0-1 wt% MWCNTs and (b) cyclic stress softening of SBS/PVDF/EVA with 0-1 wt% MWCNTs.....	167
Figure 7.6 (a) α -phase and β -phase analysis of PVDF crystallinity from FTIR and (b) the effect of MWCNT concentration in the β/α phase ratio of PVDF from FTIR...	169

Figure 7.7 Rheological properties of SBS/PVDF/EVA blends and nanocomposites showing (a) storage modulus and (b) complex viscosity	170
Figure 7.8 Impedance spectroscopy of SBS/PVDF/EVA/MWCNTs between 0 wt% and 3 wt% for (a) relative permittivity, (b) $\tan \delta$, (c) AC conductivity and (d) phase angle	172
Figure 7.9 Polarisation – electric field loops (P-E) loops for SBS/PVDF/EVA containing 0 wt% - 1 wt% MWCNTs under different electric fields	174
Figure 7.10 Change in capacitance and phase angle respectively under various extensions for SBS/PVDF/EVA TPEs containing (a-b) 0 wt% MWCNTs, (c-d) 1 wt% MWCNTs and (e-f) 3 wt% MWCNTs.....	175
Figure 7.11 Schematic diagram of resistor/capacitor network in the unstrained and strained state for (a) SBS/PVDF/EVA/MWCNT (50/50/20/1) and (b) SBS/PVDF/EVA/MWCNT (50/50/20/3). Reproduced from Ellingford et al. ³¹	176
Figure 7.12 Impedance spectroscopy of SBS/PVDF and MG-SBS/PVDF blends for (a) relative permittivity, (b) $\tan \delta$, (c) AC conductivity and (d) phase angle.....	178
Figure 7.13 Stress strain curves for (a) SBS/PVDF (70/30) – SBS/PVDF (0/100) and (b) MG-SBS/PVDF (70/30) – MG-SBS/PVDF (30/70)	179
Figure 7.14 SEM imaging of left SBS/PVDF (50/50) with the PVDF phase removed using N,N-dimethylacetamide and right MG-SBS/PVDF (50/50) with the MG-SBS phase removed using chloroform.....	180
Figure 7.15 Normalised FTIR spectra for comparing peaks intensities in (a) SBS/PVDF 50/50 and PVDF, (b) MG-SBS/PVDF 50/50 and MG-SBS and (c) MG-SBS/PVDF 50/50 and PVDF	181
Figure 7.16 Stress-strain curves of SBS/PVDF 50/50, SBS/PVDF 70/30, MG-SBS/PVDF 50/50 and MG-SBS/PVDF 70/30 all containing 1 wt% MWCNT	182
Figure 7.17 SEM imaging of (a) the SBS of SBS/PVDF/MWCNT 50/50/1 and (b) the PVDF phase in MG-SBS/PVDF/MCNT 50/50/1	183
Figure 7.18 Impedance spectroscopy for SBS/PVDF 50/50 and 70/30 and MG-SBS/PVDF 50/50 and 70/30 all containing 1 wt% MWCNTs	185
Figure 8.1 Introduction of dynamic covalent diels-alder crosslinking into polybutadiene to increase the tensile strength and introduce a self-healing and recyclable nature. Reproduced from Bai <i>et al.</i> ⁷	191

Figure 8.2 The different oxidation states of TANI and the benzene ring to quinoid ring ratio. Reproduced from Wang <i>et al.</i> ¹⁰	192
Figure 8.3 (a) ¹ H NMR spectrum at 400 MHz in CDCl ₃ and (b) GPC trace of SBR and MG-SBR in THF using a Refractive Index detector	194
Figure 8.4 (a) Partially assigned ¹ H NMR spectra of MG-SBR and 80/20 MG/TG-SBR and (b) FTIR spectra of SBR, MG-SBR and 80/20 MG/TG-SBR.....	197
Figure 8.5 (a) DMTA <i>tan δ</i> loss of SBR, MG-SBR and 80/20 MG/TG-SBR and (b) UV-Vis spectroscopy of SBR, MG-SBR and 80/20 MG/TG-SBR in DCM with the UV active range of the polymers shown	198
Figure 8.6 Stress strain curves of SBR, MG-SBR and 80/20 MG/TG-SBR	200
Figure 8.7 Impedance spectroscopy for SBR, MG-SBR and 80/20 MG/TG-SBR showing (a) relative permittivity, (b) <i>tan δ</i> , (c) AC conductivity and (d) phase angle	202
Figure 8.8 (a) ¹ H NMR spectrum at 400 MHz in CDCl ₃ of PB with assigned peaks and (b) GPC trace of the molecular weight of PB and MG-PB in THF using a Refractive Index detector.....	203
Figure 8.9 (a) Assigned ¹ H NMR spectra of MG-PB and 80/20 MG/TG-PB and (b) FTIR spectra of PB, MG-PB and 80/20 MG/TG-PB.....	205
Figure 8.10 (a) DMTA <i>tan δ</i> graphs for MG-PB and 80/20 MG/TG-PB and (b) UV-Vis spectra of PB, MG-PB and 80/20 MG/TG-PB	206
Figure 8.11 Stress strain curve of PB, MG-PB and 80/20 MG/TG-PB	207
Figure 8.12 Impedance spectroscopy for PB, MG-PB and 80/20 MG/TG-PB with (a) relative permittivity, (b) <i>tan δ</i> loss, (c) AC conductivity and (d) phase angle.....	209
Figure 8.13 (a) GPC trace of TANI with a two hour reaction time and a 1.5 hour reaction time (b) assigned ¹ H NMR spectrum of TANI and (c) FTIR spectrum of TANI with key peaks are highlighted.....	210
Figure 8.14 Assigned ¹ H NMR spectra at 400 MHz in CDCl ₃ of E-SBS and E-PB	212
Figure 8.15 (a) Assigned ¹ H NMR for TANI-SBS and TANI-PB and (b) FTIR of TANI-SBS and TANI-PB with key peaks highlighted.....	213
Figure 8.16 SEM imaging of (a) 25 mol% TANI-SBS, (b) 35 mol% TANI-SBS, (c) 50 mol% TANI-SBS, (d) 25 mol% TANI-PB and (e) 50 mol% TANI-PB.....	214
Figure 8.17 DMTA <i>tan δ</i> for SBS, 25 mol% TANI-SBS, 35 mol% TANI-SBS and 50 mol% TANI-SBS	215

Figure 8.18 Solution state UV-Vis spectroscopy in chloroform for (a) SBS, 25 mol% TANI-SBS and 35 mol% TANI-SBS and (b) PB, 1 mol% TANI-PB and 25 mol% TANI-PB	217
Figure 8.19 Stress strain curves of (a) 25 mol% TANI-SBS and 35 mol% TANI-SBS and (b) 1 mol% TANI-PB, 25 mol% TANI-PB and 35 mol% TANI-PB.....	218
Figure 8.20 Impedance spectroscopy of SBS, 25 mol% TANI-SBS and 35 mol% TANI-SBS and the (a) relative permittivity, (c) $\tan \delta$ loss and (e) phase angle and of PB, 1 mol% TANI-PB, 25 mol% TANI-PB and 35 mol% TANI-PB and the (b) relative permittivity, (d) $\tan \delta$ loss and (f) phase angle	220
Appendix Figure 1 (a) storage modulus of SBS and MG-SBS, (b) loss modulus of SBS and MG-SBS	230
Appendix Figure 2 (a) ^1H NMR of MG-SBS (65.1%), (b) FTIR of MG-SBS (65.1%)	230
Appendix Figure 3 Stress-Strain curve of MG-SBS (65.1%).....	231
Appendix Figure 4 (a) ^1H NMR of MG-SBS (52.1%) and (b) FTIR of MG-SBS (52.1%).....	231
Appendix Figure 5 Polarisation electric field loops of pristine MG-SBS and healed MG-SBS under an electric field with a maxima of 5.9 MV m^{-1}	232
Appendix Figure 6 Optical images of (a) thin needle on a Needle Probe and (b) a hypodermic needle used to clear the pinhole defect site of MG-SBS after electrical breakdown.....	232
Appendix Figure 7 Comparison of electric field-polarisation loops under 10 MV m^{-1} electrical field for pristine MG-SBS, healed MG-SBS using a hypodermic needle to clear the pinhole site and healed MG-SBS using a needle probe to clear the pinhole site	233
Appendix Figure 8 (a) Strain at break after self-healing for various times and (b) tensile strength after self-healing for various times for M3M-SBS.....	233
Appendix Figure 9 (a) Storage modulus and (b) loss modulus of M3M-SBS.....	234
Appendix Figure 10 Temperature dependent FTIR for SBS between $30 \text{ }^\circ\text{C}$ and $150 \text{ }^\circ\text{C}$ for (a) 1730 cm^{-1} , (b) 1356 cm^{-1} and 1243 cm^{-1}	234

Appendix Figure 11 (a) Pressure and (b) air flow of MG-SBS energy harvesting cycles at different axial deformations. (c) Pressure and (d) air flow of M3M-SBS energy harvesting cycles at different axial deformations.....	235
Appendix Figure 12 (a) Voltage, (b) charging current and (c) Harvesting current of MG-SBS energy harvesting cycles at different axial deformations. (d) Voltage, (e) charging current and (f) Harvesting current of M3M-SBS energy harvesting cycles at different axial deformations.	236
Appendix Figure 13 (a) Pressure and (b) air flow of healed MG-SBS energy harvesting cycles at different axial deformations. (c) Pressure and (d) air flow of healed M3M-SBS energy harvesting cycles at different axial deformations.....	237
Appendix Figure 14 (a) Voltage, (b) charging current and (c) Harvesting current of healed MG-SBS energy harvesting cycles at different axial deformations. (d) Voltage, (e) charging current and (f) harvesting current of healed M3M-SBS energy harvesting cycles at different axial deformations.	238
Appendix Figure 15 ¹ H NMR Spectroscopy of 95/5, 90/10 and 80/20 MG/TG-SBS	239
Appendix Figure 16 FTIR spectroscopy of 95/5, 90/10 and 80/20 MG/TG-SBS ...	239
Appendix Figure 17 Temperature dependant FTIR for 100/0, 95/5, 90/10 and 80/20 MG/TG-SBS at 3320 cm ⁻¹ upon heating.....	240
Appendix Figure 18 Variable temperature ¹ H NMR spectra of 80/20 MG/TG-SBS at 25 °C, 50 °C and 70 °C	240
Appendix Figure 19 (a) Healed strain at break and (b) strain at break recovery for 95/5, 90/10 and 80/20 MG/TG-SBS at room temperature and at 80 °after testing immediately, after 15 minutes, after 3 hours and after 3 days	241
Appendix Figure 20 (a) Healed tensile strength and (b) tensile strength recovery for 95/5, 90/10 and 80/20 MG/TG-SBS at room temperature and at 80 °after testing immediately, after 15 minutes, after 3 hours and after 3 days	241
Appendix Figure 21 (a) Storage modulus and (b) loss modulus of 50/50 SBS/PVDF, 50/50/20 SBS/PVDF/EVA and EVA.....	242
Appendix Figure 22 SEM imaging of SBS/PVDF/EVA (50/50/20) containing (a) 0 wt% MWCNTs, (b) 0.3 wt% MWCNTs, (c) 0.5 wt% MWCNTs, (d) 1 wt% MWCNTs, (e) 2 wt% MWCNTs and (f) 3 wt% MWCNTs	243
Appendix Figure 23 Relative permittivity of PVDF.....	244

Appendix Figure 24 (a) Storage modulus and (b) loss modulus of SBR, MG-SBR and 80/20 MG/TG-SBR.....	245
Appendix Figure 25 $\tan \delta$ graph from impedance spectroscopy of SBR, MG-SBR and 80/20 MG/TG-SBR with the $\tan \delta$ in \log_{10} form to highlight the atomic relaxation peaks.....	245
Appendix Figure 26 (a) Storage modulus and (b) loss modulus of MG-PB and 80/20 MG/TG-PB between -120 °C and 60 °C.....	246
Appendix Figure 27 SEM image of emeraldine salt form TANI acidified using trifluoroacetic acid	246
Appendix Figure 28 ^{13}C NMR spectrum of E-SBS	247
Appendix Figure 29 HSQC spectrum of E-SBS	247
Appendix Figure 30 ^{13}C NMR spectrum of TANI-SBS	248
Appendix Figure 31 HSQC spectrum of TANI-SBS.....	248
Appendix Figure 32 HMBC spectrum of TANI-SBS.....	249
Appendix Figure 33 DMTA $\tan \delta$ spectrum of 50 mol% TANI-PB.....	249
Appendix Figure 34 Solution state UV-Vis spectroscopy of TANI in emeraldine salt state	250
Appendix Figure 35 Impedance spectroscopy AC conductivity graphs for (a) SBS, 25 mol% TANI-SBS and 35 mol% TANI-SBS and (b) PB, 1 mol% TANI-PB, 25 mol% TANI-PB and 35 mol% TANI-PB.....	250

List of Tables

Table 1.1 Summary of key electrical and mechanical properties for dielectric elastomers.....	5
Table 4.1 Table of experimentally determined properties of SBS and MG-SBS and the theoretically determined $FoM_{Actuation}$	88
Table 5.1 Table of experimentally determined properties of M3M-SBS and the theoretically determined $FoM_{Actuation}$	120
Table 6.1 Summary of mechanical properties for SBS and MG/TG-SBS elastomers with grafting ratios between 100/0 and 80/20 respectively.....	139
Table 7.1 Surface energy data for H_2O and CH_2I_2 for the total surface energy, the dispersive part of surface energy and polar part of surface energy. ^{30, 31}	164
Table 7.2 Experimental contact angles of H_2O and CH_2I_2 for SBS, PVDF and EVA	165
Table 7.3 Calculated wetting coefficient, ω_a , between polymer phases and the preferential locality of MWCNTs.	165
Table 7.4 Percentage crystallinity of PVDF and EVA in SBS/PVDF TPE blends and composites.....	167
Appendix Table 1 α/β phase crystallinity ratios in PVDF and SBS/PVDF/EVA TPEs and the change with increasing MWCNT concentration	242
Appendix Table 2 Normalised transmission intensity ratios for SBS/PVDF 50/50 and MG-SBS/PVDF 50/50 compared to SBS, PVDF and MG-SBS peaks	243
Appendix Table 3 DSC crystallinity ($X_c(\%)$), Crystallisation temperature (T_c) and melting temperature (T_m) for SBS/PVDF and MG-SBS/PVDF 50/50 and 70/30 blends and composites containing 1 wt% MWCNTs.....	244
Appendix Table 4 GPC containing M_n , M_w and \bar{D} for TANI synthesised with a two hour reaction time and a 90 minute reaction time.....	246

List of Equations

Equation 1.1 Polarisation of a material formula.....	6
Equation 1.2 Polarisation induced under an electric field formula.....	6
Equation 1.3 Formula of susceptibility.....	6
Equation 1.4 Polarisation in terms of susceptibility and electric field formula.....	6
Equation 1.5 Polarisability of a material formula.....	6
Equation 1.6 Clausius-Mossotti equation for polymers.....	6
Equation 1.7 Total polarisation formula.....	7
Equation 1.8 Complex form of relative permittivity formula.....	8
Equation 1.9 $\tan \delta$ loss formula.....	8
Equation 1.10 Joule heating formula.....	9
Equation 1.11 Capacitance of a polymer formula.....	9
Equation 1.12 Theoretical energy density formula.....	9
Equation 1.13 The formula for the energy stored in a polymer capacitor during an energy harvesting cycle.....	10
Equation 1.14 The formula for charge stored in an elastomer.....	13
Equation 1.15 Maxwell pressure for actuated strain in a given direction.....	14
Equation 4.1 Calculation for percentage of styrene in SBS from NMR spectra.....	69
Equation 4.2 Calculation for percentage of butadiene from NMR spectra.....	69
Equation 4.3 Calculation of mass formula.....	69
Equation 4.4 Calculation of weight fraction.....	70
Equation 4.5 Calculation for percentage of thiol group grafting from NMR spectra...	70
Equation 4.6 Calculation of reacted alkene groups from NMR spectra.....	70
Equation 4.7 Figure of merit for actuation formula.....	87
Equation 4.8 Formula for true electrical field.....	88

Equation 4.9 Actuation stress in a planar direction formula.....	89
Equation 4.10 Actuation strain in a radial direction formula.....	89
Equation 4.11 Change in area due to actuation formula.....	89
Equation 4.12 Nominal electrical field formula.....	91
Equation 5.1 Figure of merit for energy harvesting formula.....	121
Equation 5.2 Volumetric change of an elastomer during an energy harvesting cycle.....	123
Equation 5.3 The charging current in an energy harvesting cycle.....	124
Equation 5.4 The charge in an elastomer during an energy harvesting cycle.....	124
Equation 5.5 The harvested charge from an energy harvesting cycle.....	124
Equation 5.6 The leakage charge from an energy harvesting cycle.....	125
Equation 5.7 Total converted electrical energy formula.....	126
Equation 5.8 Total generated electrical energy formula.....	126
Equation 5.9 Total mechanical work input formula.....	126
Equation 5.10 Efficiency of energy conversion formula.....	126
Equation 6.1 The time-frequency superposition principal formula.....	148
Equation 7.1 Wetting coefficient formula.....	163
Equation 7.2 Geometric mean interfacial tension formula.....	164
Equation 7.3 Geometric mean interfacial liquid-vapour formula.....	164
Equation 7.4 Interfacial surface-vapour formula.....	164
Equation 7.5 Formula for the calculation of phase angle.....	173

Acknowledgements

First of all, I would like to thank my parents, Elizabeth and Dave, and brother, Andrew MEng, for their support and love over the years. I would like to thank my parents for providing the environment which has nurtured us to both pursue our dreams and achieve our goals, and to never give up. I also thank Andrew for being a great little brother; he is full of kindness and determination and I know that he will be incredibly successful in life – and I am the proud big brother who will get to see this.

I would like to thank Isabel for being an amazing partner, for loving and supporting me throughout the PhD, for introducing me to new things and new ways of seeing and being, and for being hilarious (even when she isn't trying to be). I know that you too will complete your PhD soon, and you will carry on achieving things that were never meant to be possible. Thank you for the light you bring into my life.

I would like to thank Mr Simon Woolley, Mr Darren Magor and Mr Ross Percy-Jones for being excellent friends, for providing witty banter and comedy and for their support over the many years that I have known them. May we all meet again in the pub soon. I would like to congratulate Ross and his wife, Emma, on their new-born son, Jasper. I know that they are excellent parents and will build a loving family together.

I would like to thank my supervisor, Dr Chaoying Wan, for her support and patience over the past four years. Her determination, dedication and guidance have been instrumental in the success of this research project and for my development as an independent researcher. I also would like to thank Professor Tony McNally and Dr Łukasz Figiel for their assistance and support during the PhD, as well as Mr Martin Worrall for all his help and technical assistance during the project. Finally, I would like to thank the IINM, WMG and the University of Warwick for providing me the world-class facilities to carry out my research in.

Finally, and most importantly, I would like to dedicate this thesis to my grandma and grandad, June Rose Ellingford and Michael Ellingford. I am eternally grateful to the love, kindness and doting that they provided to Andrew and I. I am certain that they would be proud of us both, for everything that we have achieved. They are sorely missed.

Declaration of Authorship

This thesis is submitted to the University of Warwick in support of my application for the degree of Doctor of Philosophy in Engineering. It has been composed by myself and has not been submitted in any previous application for any degree to any other university or higher education institution or as any part of any other submission to the University of Warwick. It describes the work carried out from October 2016 to October 2020.

The work presented in this thesis (including data generated and data analysis) was carried out by the author except in the case outlined below:

Collaboration with Professor Chris Bowen for measurement of actuation and energy harvesting performance of synthesised dielectric elastomers.

Parts of this thesis have been published and submitted to journals and books during the PhD period by the author as detailed at the beginning of each chapter and summarised in a list of publications at the end of this thesis.

Summary

Dielectric elastomers are of great interest for actuation and energy harvesting devices due to their ability to transduce mechanical energy input to electrical energy and vice versa. The dielectric elastomer generators can be designed for harvesting waste mechanical and vibration energy from automotive vehicles and converting to electrical energy to power the wireless sensors. This is to reduce the use of copper cabling and batteries, therefore to achieve smart and sustainable operation systems.

The electroactive properties of dielectric elastomers are related to the relative permittivity, electrical breakdown strength and Young's modulus, although secondary factors such as dielectric loss ($\tan \delta$), strain at break and cycle lifetime can influence the performance of the materials and devices. Whilst dielectric elastomers have intrinsically high breakdown strength and good deformability as compared to dielectric ceramics, typically their relative permittivity is low (2~3), impacting the charge that can be stored within the elastomer during an energy harvesting cycle. To enhance the relative permittivity, both intrinsic and extrinsic modification approaches are investigated in a number of commodity elastomers in this work.

Firstly, an unsaturated styrenic block copolymer of styrene-butadiene-styrene (SBS) was selected, which is a type of thermoplastic elastomer that are widely applied in industry. A number of polar groups were chemically grafted to the polymer backbone via a one-step thiol-ene 'click' reaction under UV light at ambient conditions. The grafting of polar groups enhanced the electromechanical properties of the elastomers, as well as enabled autonomous self-healing behaviour at room temperature. The mechanisms were investigated from the aspects of polar group types, grafting ratios, intra- and inter-molecular interactions.

Three types of polar groups: methyl thioglycolate (MG), methyl-3-mercaptopropionate (M3M) and thioglycolic acid (TG) were selected for grafting modification of SBS. The M3M grafted SBS elastomers demonstrated higher self-healing, strain at break, deformability and breakdown strength as compared to MG-SBS, due to the longer carbon chain of M3M. The grafting of TG introduced hydrogen bonding through carboxyl functionality into the modified SBS elastomers, which also introduced a temperature-dependent self-healing behaviour, giving rise to the potential

of using the elastomer for actuation or energy harvesting in higher temperature environments.

MG-SBS showed enhanced relative permittivity and low $\tan \delta$ loss, whereby the relative permittivity increased to 11.4, and was able to autonomously self-heal under room temperature conditions. Both M3M-SBS and MG-SBS exhibited excellent energy harvesting performances, whilst showing that they could be readily actuated and recover their actuation ability up to 85% after failure. Finite Element Modelling was used to demonstrate that defects in the elastomers acted as sites for initiation of breakdown, preventing the elastomers from recovering their electrical properties fully.

Furthermore, styrene-butadiene rubber and polybutadiene were investigated and modified with both methyl thioglycolate and thioglycolic acid to enhance both the electrical properties and mechanical strength through hydrogen bonding. In addition, the grafting of a conducting polar group, TANI, to the backbone of SBS enhanced the relative permittivity of the elastomers while maintaining a flexible and stretchable nature. This was achieved due to the compatibility between the styrene block of SBS and tetraaniline via π - π stacking.

Extrinsic modification of SBS and MG-SBS was investigated *via* melt compounding with polyvinylidene fluoride (PVDF) and multi-walled carbon nanotubes (MWCNTs). A third polymer, ethylene vinyl acetate (EVA), was introduced to improve the compatibility between SBS and PVDF. Significant enhancements in the relative permittivity of the PVDF/SBS/MWCNT composites were observed, whilst $\tan \delta$ loss was suppressed after the first percolation threshold due to a dual-percolation behaviour at 1 wt% and 3 wt%. This was in addition to a rheological dual percolation behaviour at the same MWCNT weight fractions.

Overall, this thesis presents a series of intrinsic and extrinsic modification pathways for dielectric elastomers and nanocomposites. The demonstrated facile and scalable approaches and self-healing dielectric elastomer actuators and energy generators will make contribution to smart and high performance soft devices applications.

Abbreviations and Terminology

In order of appearance in thesis:

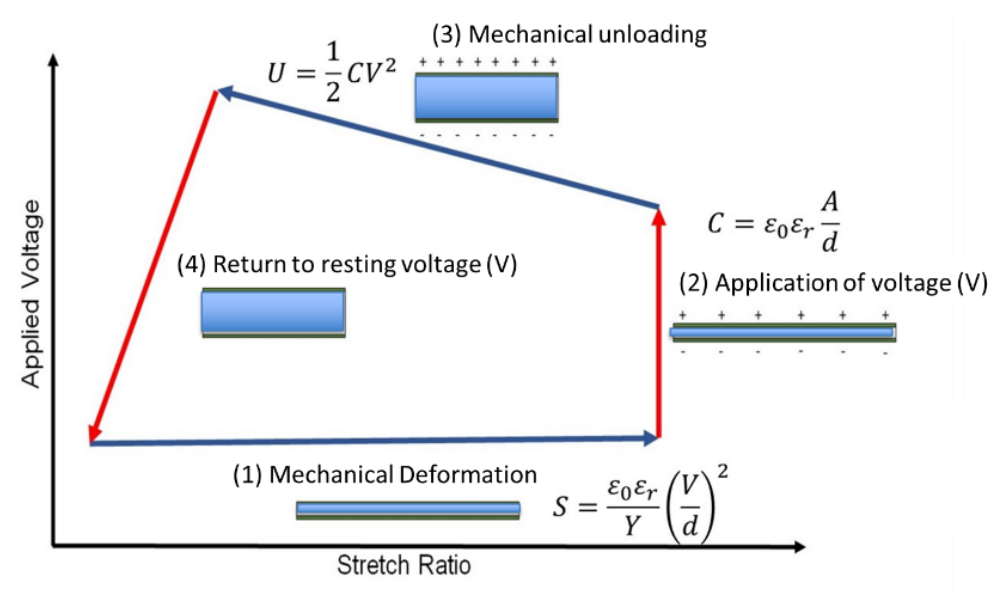
DEG	Dielectric elastomer generator
DEA	Dielectric elastomer actuator
PDMS	Polydimethylsiloxane
EPDM	Ethylene-propylene-diene monomer rubber
PVDF	Polyvinylidene fluoride
SBS	Styrene-butadiene-styrene
SEBS	Styrene-ethylene-butadiene-styrene
SBR	Styrene-butadiene rubber
PVDF-co-HFP	Polyvinylidene fluoride-co-hexafluoropropylene
PVDF-TrFE-CFE	Polyvinylidene fluoride-trifluoroethylene-chlorofluoroethylene
TiO ₂	Titanium dioxide
BaTiO ₃	Barium titanate
PZT	Lead zirconium titanate
ZrO ₂	Zirconium dioxide
EVA	Ethylene-vinyl-acetate
MG-SBS	Methyl thioglycolate modified styrene-butadiene-styrene
M3M-SBS	Methyl-3-mercaptopropionate modified styrene-butadiene-styrene
MG/TG-SBS	Methyl thioglycolate/thioglycolic acid modified styrene-butadiene-styrene
MG-SBR	Methyl thioglycolate modified styrene-butadiene rubber

MG/TG-SBR	Methyl thioglycolate/thioglycolic acid modified styrene-butadiene rubber
PB	Polybutadiene
MG-PB	Methyl thioglycolate modified polybutadiene
MG/TG-PB	Methyl thioglycolate modified polybutadiene
TANI	Tetraaniline
TANI-SBS	Tetraaniline modified styrene-butadiene-styrene
TANI-PB	Tetraaniline modified polybutadiene
MWCNTs	Multi-walled carbon nanotubes
GNPs	Graphene nanoplatelets
GO	Graphene oxide
rGO	Reduced graphene oxide
CCTO	Copper calcium titanate
PHMS	Polymethylhydridesiloxane
PVMS	Polyvinylmethylsiloxane
LCE	Liquid crystal elastomer
PANI	Polyaniline
DMPA	2,2-dimethoxy-2-phenylacetophenone
NMR	Nuclear magnetic resonance spectroscopy
FTIR	Fourier transform infrared spectroscopy
E-SBS	Epoxidised styrene-butadiene-styrene
E-PB	Epoxidised polybutadiene
GPC	Gel permeation chromatography
UV-Vis	Ultra-violet visible spectroscopy
DMTA	Dynamic mechanical thermal analysis

DSC	Differential scanning calorimetry
SEM	Scanning electron microscopy
AFM	Atomic force microscopy
SAXS	Small angle X-ray scattering
P-E loops	Polarisation-electric field loops
\mathcal{D}	Dispersity
M_n	Number average molecular weight
M_w	Weight average molecular weight
$FoM_{\text{Actuation}}$	Figure of merit for actuation
$FoM_{\text{Harvesting}}$	Figure of merit for energy harvesting
TPE	Thermoplastic elastomer
HSQC	Hetereonuclear single quantum coherence spectroscopy
HMBC	Hetereonuclear multiple bond correlation spectroscopy

Chapter 1

Introduction



Publications:

C. Ellingford, C. Bowen, T. McNally and C. Wan*, Intrinsicly tuning the electromechanical properties of elastomer dielectrics: a chemistry perspective, *Macromol. Rapid Commun.*, 2018, **39**, 18, 1800340.

1.1 The need for dielectric elastomers in actuators and energy harvesters in the automotive industry

The efficiency and reduction of wasted energy during a vehicle lifecycle is actively pursued by automotive manufacturers to increase their desirability to consumers and to achieve the stricter emissions and efficiency regulations imposed onto them, particularly within Europe¹ but also in Brazil, China and the USA.²⁻⁴ To achieve this, automotive manufacturers utilise a number of approaches including developing more efficient internal combustion engines or developing methods to reduce the weight of the vehicle, such as light weighting materials to replace current components.⁵

However, each new generation of automotive vehicles uses more technology and sensors to develop driver aids, semi-autonomous functionality and fully autonomous vehicles,⁶⁻⁸ see Figure 1.1. Overall, this improves the smartness, driving comfort and convenience of the vehicle whilst reducing manufacturing costs, vehicle usage costs and improving their safety.⁶

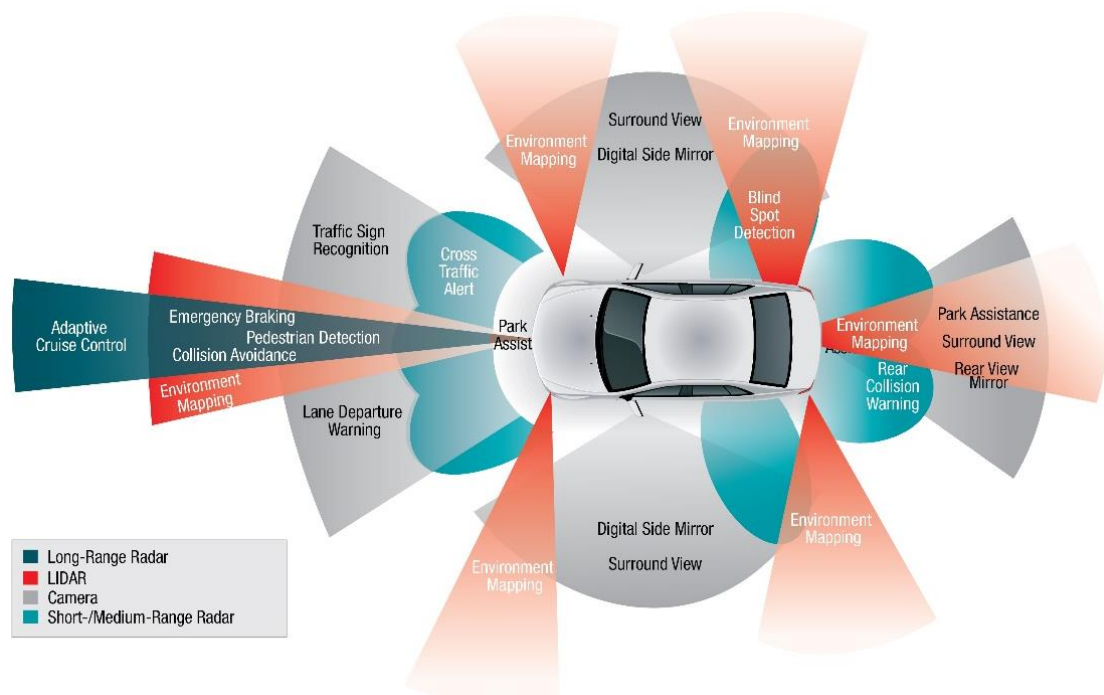


Figure 1.1 An example of the range of sensors and driving aids present in a smart, modern vehicle. Reproduced from INSIGHTS.⁹

To power the smart features of an automotive vehicle, such as sensors, cameras and lighting, cabling is required from the battery. A wiring harness within a vehicle can

weight up to 70 kg, be over a mile long and be one of the heaviest components of a car.¹⁰ The addition of more technology, sensors and lighting only adds to the weight of the wiring harness.

Therefore, to reduce weight, increase efficiency and reduce cost, energy can be harvested from dielectric elastomer generators (DEG) within a vehicle. These can harvest waste mechanical and vibrational energy from the suspension, body panels and tyres, amongst other places.¹¹ Dielectric elastomers are soft, high strain polymers and therefore have an increased suitability for this application compared to other types of energy harvesting devices such as piezoelectric energy harvesters. The energy harvested from a DEG could be stored in a battery and used to power localised sensors and lighting, and reduce the length of cabling, and therefore copper, required throughout the car. This saves weight, reduces the manufacturing cost and improves the efficiency of the vehicle.

In addition, the elastomer used within the generator could be used inversely in a dielectric elastomer actuator (DEA). Energy applied to the material can induce a movement or change in shape, removing the need for heavy mechanical parts and motors in automated movement components such as wing mirrors or can be used for tactile displays within a vehicle.¹²

However, before dielectric elastomers can be utilised in DEAs or DEGs, improvements in their electroactive abilities need to be realised first. Currently for energy harvesting, dielectric elastomers have a low energy harvesting efficiency, 15-16%, whereas for both energy harvesting and actuation, operating voltages of 5 kV are commonly reported.^{13, 14} In addition to this, the low capacitance of dielectric elastomers, due to their typically low relative permittivity (2~3), means that DEGs are required to work in tandem with complementary technologies, such as batteries, for energy storage as dielectric elastomers cannot store enough energy themselves.

1.2 Dielectric Elastomers

Electroactive polymers such as dielectric elastomers are able to exhibit a mechanical response to an applied electric field,^{15, 16} or transduce mechanical energy into electrical energy upon mechanical deformation.^{17, 18} The chemical structures of polymers

determine the electromechanical properties, and large elastic deformations are required to ensure a repeatable, deformable and flexible behaviour.

Common, commercially available dielectric elastomers include crosslinked silicone based polymers such as polydimethylsiloxane (PDMS) or ethylene-propylene-diene monomer rubber (EPDM) elastomers and uncrosslinked styrenic based elastomers, shown in Figure 1.2. For dielectric elastomers to be utilised successfully, key mechanical and electrical properties need to be optimised. Mechanically, a dielectric elastomer requires a high strain at break ($> 200\%$), high tensile strength (> 2 MPa) but a low Young's modulus (≈ 1 MPa) for easy deformability. Electrically, a high relative permittivity (> 10), low $\tan \delta$ loss (< 0.05) and high electrical breakdown strength (50 MV m⁻¹) is required to ensure a large, efficient electric output or actuation response.¹⁶
¹⁹ The typical properties of some dielectric elastomers are shown in Table 1.1.

As can be seen from Table 1.1, all elastomers are below the desirable relative permittivity of greater than 10. Commercially available acrylic based VHB 4905 has the highest relative permittivity for an elastomer of 4.6. Therefore, dielectric elastomers in their current state are not suitable to harvest enough energy in a dielectric elastomer, or actuate sufficiently without further modification.

Other high permittivity polymers are available, most commonly utilised are polyvinylidene fluoride (PVDF) based, Figure 1.2. Their high polarity from fluorine groups on the polymer backbone give rise to a semicrystalline nature, through regions of crystallinity. A relative permittivity of 12 is commonly observed, although the composition of crystallinity affects this greatly.²⁰ However, PVDF based polymers typically have a very low strain at break and are suitable for vibration based or low strain applications.²¹⁻²³

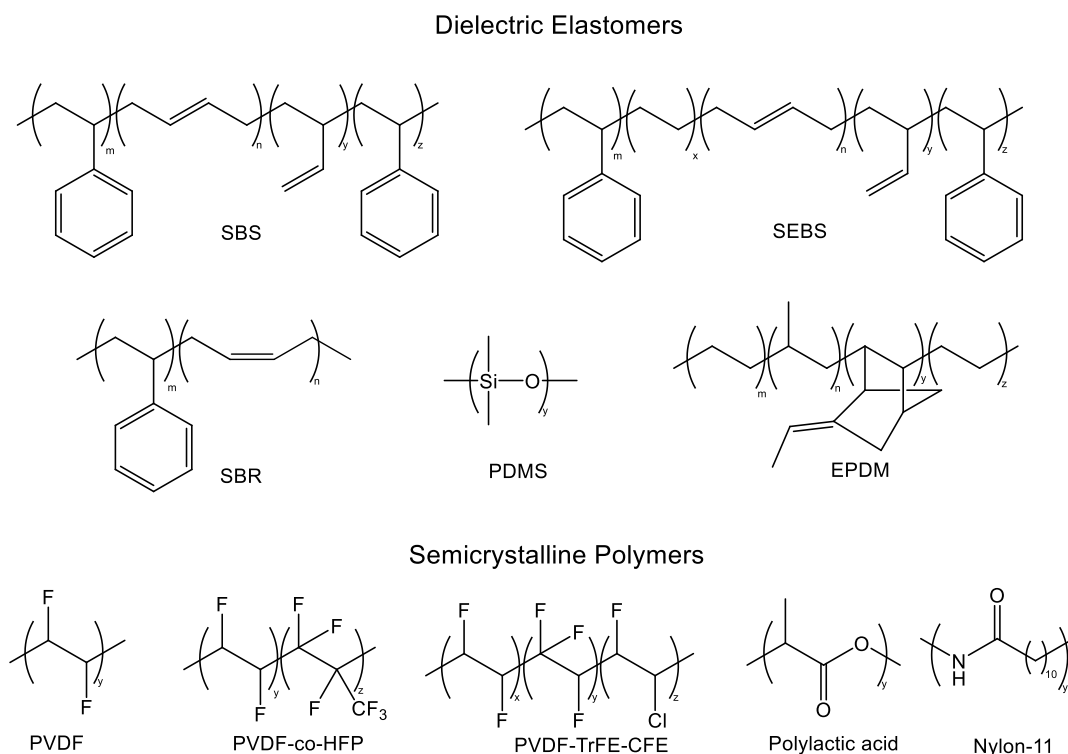


Figure 1.2 Structures of different dielectric elastomers and semicrystalline polymers.

Table 1.1 Summary of key electrical and mechanical properties for dielectric elastomers

Material	Relative permittivity (ϵ_r)	Dielectric loss ($\tan \delta$)	Electrical breakdown strength (MV m^{-1})	Tensile strength (MPa)	Young's modulus (MPa)	Strain at break (%)
SBS ²⁴	3.9	3.0×10^{-4}	65	16.4	0.5	1350
SEBS ^{25, 26}	2.5	5.0×10^{-4}	25	27.1	25.4	518
PDMS ^{27, 28}	2.5	2.0×10^{-4}	80	1.1	0.9	200
EDPM ²⁹	3.0	1.0×10^{-3}	20	1.0	0.09	600
VHB 4905 ^{24, 30-34}	4.6	1.0×10^{-2}	218	0.8	0.4	500

1.3 The key electrical and mechanical properties

1.3.1 Relative permittivity and dielectric loss ($\tan \delta$)

The relative permittivity (ϵ_r) of a polymer is related to the polarisation induced upon application of an applied field. Polarisation in a material is defined as the dipole moment per unit volume,³⁵ as shown in equation 1.1:

$$P = \frac{\sum d}{V} \quad (1.1)$$

where P is the polarisation, d is the dipole moment and V is the volume. The two concepts are linked through equation 1.2.³⁶

$$P = \epsilon_0(\epsilon_r - 1)E \quad (1.2)$$

where ϵ_0 is the permittivity of free space, ϵ_r is the relative permittivity which is the factor by which the permittivity of the material is different compared to the permittivity of free space and E is the electric field. The degree under which polarisation affects the relative permittivity is governed by the susceptibility, χ , defined in equation 1.3:

$$\chi = \epsilon_0(\epsilon_r - 1) \quad (1.3)$$

and thus equation 1.2 can be rewritten as:

$$P = \chi E \quad (1.4)$$

In a polymer, both structural factors and the polarisability of the polymer contribute to the relative permittivity of it. The polarisability of a material is defined in equation 1.5:

$$d = \rho E \quad (1.5)$$

where ρ is the polarisability of a material. The Clausius-Mossotti equation can be utilised for polymers to link relative permittivity, polarisability and structural components, as shown in equation 1.6.³⁷

$$\rho_m = \frac{\epsilon_r - 1}{\epsilon_r + 2} \times \frac{M}{D} = \frac{N_A \rho}{3\epsilon_0} \quad (1.6)$$

where ρ_m is the molar polarisability, M is the molecular weight of the repeating polymer unit, D is the density of the polymer and N_A is Avogadro's constant.

The overall polarisation, P_T , present in a polymer is a combination of three types of polarisation, as shown in equation 1.7:

$$P_T = P_E + P_A + P_O \quad (1.7)$$

where P_E is the contribution from electronic polarisation, P_A is the contribution from atomic polarisation and P_O is the contribution from orientation polarisation.

All types of polarisation are affected at different frequencies of electric field. Orientation polarisation, also known as dipolar polarisation, is the alignment of permanent dipoles under an electric field to induce a net polarisation in a given direction. Prior to the application of an electric field, the dipoles are orientated in a random direction with an overall net zero as they continually change orientation due to thermal energy. Orientation polarisation is typically present up to the frequency range of $10^9 - 10^{12}$ Hz, although this can be lower for polymers. Furthermore, orientation polarisation is frequency dependent, see Figure 1.3. The contribution of orientation polarisation to overall polarisation is typically low, and thus under an electric field of 10^5 V mm^{-1} , only 0.01% of the induced polarisation is from aligned dipoles.³⁸

Atomic polarisation arises from the distortion of the atomic nuclei arrangement, such as bond bending or twisting. Overall, atomic polarisation is 10% the strength of electronic polarisation and is typically present in electric fields below 10^{13} Hz.

Electronic polarisation arises from the displacement of the electronic cloud from atoms in the polymer. It forms almost instantaneously, is temperature independent and is present until an applied field of 10^{18} Hz.³⁹

Finally, interfacial polarisation, also known as Maxwell-Wagner-Sillars polarisation, is present in low frequencies only. It can be present up to frequencies of 10^6 Hz, but in polymer composites it can relax in the region of $10^0 - 10^3$ Hz.⁴⁰ Interfacial polarisation arises due to trapped charges from impurities, inhomogeneity, voids and poor contact between the polymer and electrode.⁴¹

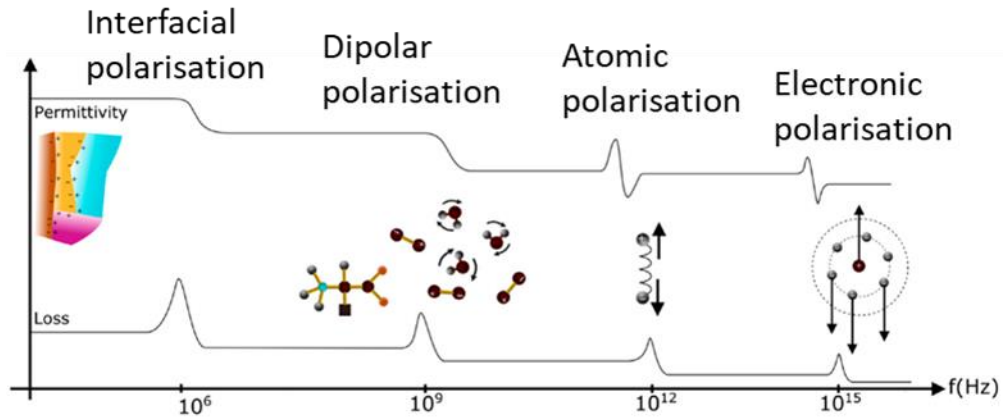


Figure 1.3 The effect of frequency on the types of polarisation present in a polymer and the relaxation peaks observed in the loss. Adapted from Bibi et al.⁴²

The complex form of relative permittivity can be expressed to also express the imaginary part, the dielectric loss, in equation 1.8:

$$\varepsilon^* = \varepsilon_r - j\varepsilon'' \quad (1.8)$$

where ε^* is the complex permittivity, ε'' is the dielectric loss and j is a constant. Relative permittivity and dielectric loss can be combined to calculate the loss tangent, $\tan \delta$, in equation 1.9:

$$\tan \delta = \frac{\varepsilon''}{\varepsilon_r} \quad (1.9)$$

The dielectric loss is a combination of two processes in a real world dielectric. Firstly, the frequency dependent process arises from the inability of the polarisation to be completed fully in response to the electric field. When the relaxation time is faster than the change in the electric field, the contribution of this process to the dielectric loss is low. However, once the relaxation is slower than the change in the electric field, energy is absorbed and dissipated in the form of heat.³⁷

The second process is frequency independent and arises from losses attributed to a leakage current, and the long range movement of charge.⁴³

1.3.2 Electrical breakdown strength

The mechanism of electrical breakdown in polymers is due to three different mechanisms: avalanche, thermal and electromechanical. These all occur fast, between $10^{-9} - 10^{-3}$ s. Thermal breakdown occurs when the heat dissipated by the polymer

under an electric field is lower than the heat generated and the polymer is unable to achieve an internal thermal equilibrium. This is known as joule heating and is calculated using equation 1.10:³⁹

$$Q_J = I^2 R \quad (1.10)$$

where Q_J is Joule heating, I is current and R is resistivity. The increase of joule heating increases the rate of electron propagation, further increasing the heating of the polymer until a mechanical failure is observed. Electrical breakdown is more likely to occur when the polymer sample is thick, has high temperature, is placed under an electric field for a prolonged time period and has a high dielectric loss.³⁷

Avalanche breakdown typically happens at low temperatures, where electrons under the influence of an electric field accelerate and ionise the polymer *via* collisions, generating more electrons to propagate the electron avalanche.^{44, 45}

At high temperatures, electromechanical breakdown is the typical breakdown mechanism. This is because the polymer softens and exhibits reduced mechanical strength. Under an applied electric field, Maxwell's pressure decreases the thickness of the polymer due to the electrostatic force between the electrodes. This increases the internal electric field in the polymer, increasing the Maxwell's pressure and propagates until mechanical failure of the polymer.^{44, 45}

Typically, electrical breakdown in polymers is the result of a combination of breakdown mechanisms and not exclusively one pathway.

1.3.3 Energy storage in polymers

The capacitance, C , of a polymer is related to the relative permittivity and as well as its physical state, given by equation 1.11:

$$C = \epsilon_r \epsilon_0 \frac{A}{t} \quad (1.11)$$

where A is the area and t is the thickness of the polymer. In a linear dielectric material, the theoretical energy density, U_d , can be described using equation 1.12:

$$U_d = \frac{1}{2} \epsilon_0 \epsilon_r E_b^2 \quad (1.12)$$

where E_b is the electrical breakdown strength of the material. However, DEG devices are not operated under the voltage of the electrical breakdown strength, nor do they retain the same size or thickness throughout. Therefore, to calculate the energy stored in a polymer capacitor during an energy harvesting cycle, W , equation 1.13 is used:

$$W = 0.5CV^2 = 0.5\epsilon_r\epsilon_0AtE^2 \quad (1.13)$$

where V is the applied voltage. As seen from equation 1.13, the applied electric field is a squared value in the equation, whereas relative permittivity is linear. Reducing the applied electric field due to a decreased breakdown strength of the polymer has a large effect on the harvested energy. Therefore, it is important to maintain a high breakdown strength alongside increasing the relative permittivity of a polymer for energy harvesting.

1.4 Polymer (nano)composites

Compositing of a polymer matrix to enhance the relative permittivity has been investigated with a wide variety of nanofillers. The fillers used can be separated into two categories: electrically conducting nanoparticles and high-permittivity nanoparticles.¹⁹ Fillers typically act to reinforce the mechanical properties, increasing the tensile strength and Young's modulus whilst decreasing the strain at break.⁴⁶

Electrically conducting nanoparticles include carbon nanotubes,⁴⁷⁻⁴⁹ graphene⁵⁰⁻⁵³ and metallic particles such as titanium dioxide (TiO₂).⁵⁴⁻⁵⁶ In a polymer matrix, electrically conducting nanoparticles behave as microcapacitors when at low filler loadings to store charge and enhance the relative permittivity of the polymer matrix. As the filler loading is increased, the number of microcapacitors increases further enhancing the relative permittivity.⁵⁷ As the percolation threshold approaches, the relative permittivity increase is more pronounced, Figure 1.4. For carbon nanotubes, the lowest reported percolation threshold was 0.07 wt% solution mixed into an EPDM based polymer.⁵⁸

However, as the percolation threshold is approached for the nanocomposite, the distance between the electrically conducting nanoparticles decreases and localised conduction pathways form as well as an increase in interfacial defects.⁵⁹ This leads to an increased leakage current and dissipates the stored energy in the form of heat, leading to an increased dielectric loss.⁶⁰ This also reduces the electrical breakdown strength of

the polymer nanocomposite due to their high permittivity creating an inhomogeneous field within the composite.^{16, 60, 61}

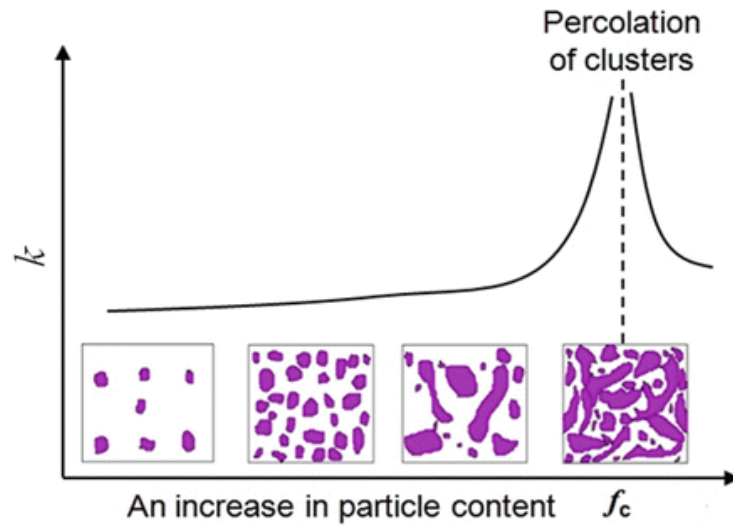


Figure 1.4 Schematic graph for the behaviour of the relative permittivity as the filler content increased. Reproduced from Yuan *et al.*⁶²

However, due to poor interfacial compatibility between electrically conducting fillers and the polymer matrix, issues with agglomeration and dispersion are prevalent, especially in melt mixing approaches compared to solution mixing approaches. This is because it is less preferable for the filler to interact with the polymer matrix, thus the fillers tend to agglomerate and remain together *via* electrostatic forces. This means that more electrically conducting filler is added to the composite to enhance the electrical properties to desired level for the application. However, adding more electrically conducting filler can be detrimental to the mechanical and electrical properties⁶³ and increases the cost of production for the composite.

Alternatively, high permittivity ceramic nanoparticles can be added into a polymer matrix. These include particles such as barium titanate (BaTiO_3),^{64, 65} lead zirconium titanate (PZT)⁶⁶ and zirconium dioxide (ZrO_2).^{67, 68} BaTiO_3 has a relative permittivity of over 1000⁶⁹ and the insulating nature of ceramic nanoparticles arises from a high band gap for electron promotion. However, a high filler content is required in order to increase the permittivity, in some examples up to 80 wt%. This significantly affects the flexibility and strain at break of the nanocomposite. Furthermore, the high permittivity particles also disrupt the homogeneity of the electric field within a polymer nanocomposite and induce electrical breakdown at a lower applied field.¹⁹

Therefore, the introduction of extrinsic nanoparticles into polymers to form nanocomposites is accompanied by numerous challenges and difficulties, summarised in Figure 1.5.

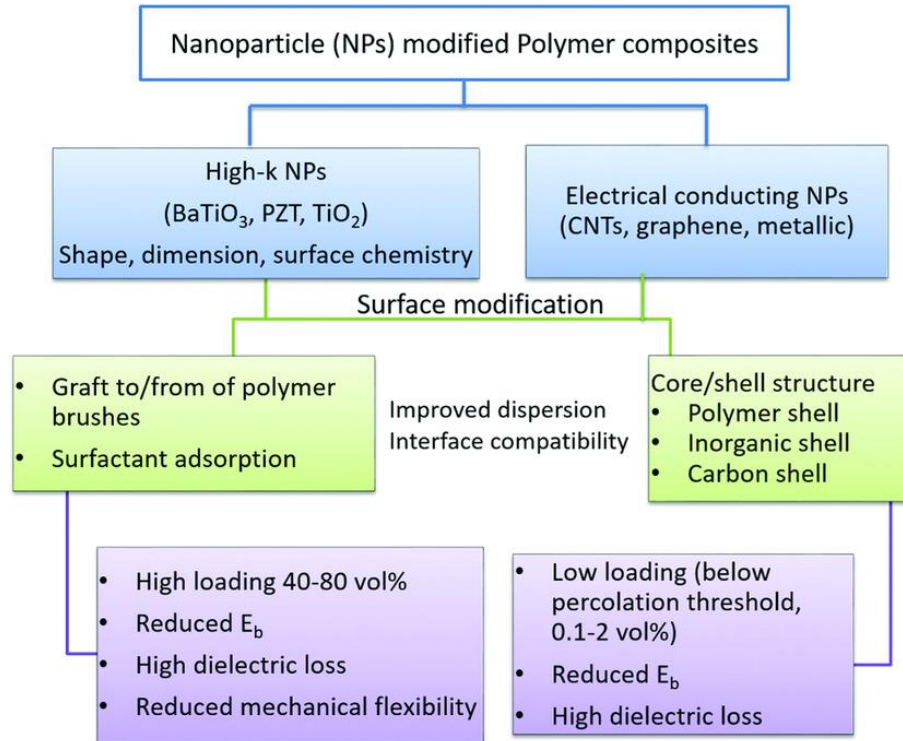


Figure 1.5 The different routes to create high permittivity nanocomposites *via* the addition of extrinsic fillers. Reproduced from Ellingford *et al.*¹⁹

1.5 Working mechanisms of dielectric elastomer actuator and generator

For DEGs, a four step energy harvesting cycle exists as the working mechanism to convert mechanical energy into electrical energy. In the first step, the dielectric elastomer is in the resting, unstrained state and a low resting voltage is applied. Next the dielectric elastomer is stretched under a mechanical deformation, increasing the capacitance due to an increased area and reduced thickness, see equation 1.11, and increasing the stored elastic energy within the elastomer.

After this, the applied voltage to the DEG is increased from its resting voltage to its harvesting voltage, which is below the electrical breakdown strength of the dielectric elastomer. This induces charges at the surface of the dielectric elastomer at the interface between it and the compliant electrodes. The mechanical deformation applied to the DEG is removed, allowing the dielectric elastomer to return to its

unstrained state. This decreases the capacitance of the dielectric elastomer as the thickness increases and area decreases, increasing the voltage at the surface of the elastomer, as seen by equation 1.14:

$$Q = CV \quad (1.14)$$

where Q is the charge in the elastomer. From equation 1.13, the increase in the voltage increases the electrical energy present in the dielectric elastomer, which can be harvested through discharging the device. A summary of the harvesting cycle is shown in Figure 1.6.

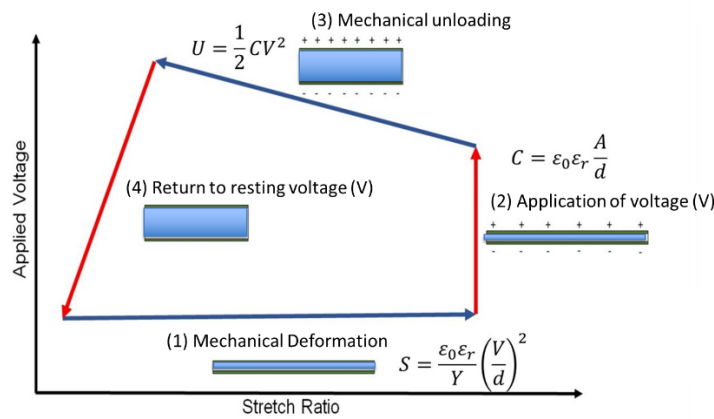


Figure 1.6 Schematic diagram for the energy harvesting cycle of a dielectric elastomer generator. The difference between the voltage in step (2) and (3) is the harvested energy in step (4). Adapted from Ellingford et al.¹⁹

Therefore, the dielectric elastomer used for a DEG device is required to simultaneously have a high relative permittivity and high electrical breakdown strength to boost the charge storage within the polymer for a given harvesting voltage, and to enhance both the maximum operating voltage of the DEG and the lifecycle time of the dielectric elastomer. Furthermore, the $\tan \delta$ loss of the dielectric elastomer needs to be as low as possible to prevent losses by heat and ensure effective conversion of mechanical energy into electrical energy. Finally, an easily deformable, high elasticity material is required to be able to undergo repeated deformations and recover its dimensions and capacitance reliably.^{19, 70, 71}

For actuation in a DEA, a dielectric elastomer is placed between two compliant electrodes, with pre-strain applied to force the elastomer to actuate with a preferred directionality. Under an applied electric field, Maxwell pressure arises as a purely

electrostatic force from the positive and negative charges formed between the electrode and the elastomer surface. This reduces the thickness of the elastomer due to compression and increases the area of the elastomer in the in-plane direction.³² Maxwell pressure is proportional to relative permittivity of an elastomer, and thus a larger relative permittivity increases the actuation performance of the DEA, see equation 1.15:

$$\sigma_{xx} = \frac{1}{2} \epsilon_0 \epsilon_r E^2 \quad (1.15)$$

where σ_{xx} is the Maxwell's pressure in a given direction. Furthermore, the strength of the applied electric field, and the Young's modulus of the material also dictate the actuation response of the dielectric elastomer.

1.6 Research objectives and thesis structure

The aim of this thesis is to develop high permittivity dielectric elastomers which retain a high strain at break, low Young's modulus, low $\tan \delta$ loss; maintain or increase their electrical breakdown strength for actuation and energy harvesting applications. The relative permittivity of dielectric elastomers can be enhanced through both intrinsic and extrinsic polymer modification approaches. Chapter 1 explains the need for dielectric elastomer actuators and generators and key parameters associated with dielectric elastomers, such as relative permittivity, electrical breakdown strength and energy storage, to make them successful for the application.

Chapter 2 investigates both intrinsic and extrinsic modification approaches to enhance the relative permittivity of dielectric elastomers and the effect that this had on their performance. Extrinsic modification investigates compositing through the introduction of conducting fillers or ceramic fillers whilst intrinsic modification investigates the modification of dielectric elastomers through polar groups, mesogenic groups and conducting groups.

Chapter 3 summarises the experimental procedures for synthesis and characterisation of the dielectric elastomers presented in this thesis. In addition, the set up and procedure for investigating the actuation and energy harvesting properties of some of the dielectric elastomers is presented.

In this thesis, intrinsic modification of polymer backbones *via* grafting of polar groups and extrinsic modification approaches *via* the introduction of carbon nanotubes to a polymer matrix, and the combination of both intrinsic and extrinsic modification approaches, were investigated.

Therefore, the routes undertaken to produce dielectric elastomers with high permittivity, high breakdown strength, high mechanical strain and low loss are discussed in Chapter 4-8, as shown in Figure 1.7.

1. Chemical grafting methyl thioglycolate to an unsaturated styrenic block copolymer (SBS) to enhance its relative permittivity (Chapter 4).
2. Introducing methyl-3-mercaptopropionate as an alternative polar group to SBS to adjust the electrical, mechanical and self-healing properties (Chapter 5).
3. Introducing hydrogen bonding by grafting both methyl thioglycolate and thioglycolic acid to SBS for a high permittivity and self-healing dielectric elastomers (Chapter 6).
4. Blending modified SBS with PVDF and carbon nanotubes flexible, stretchable high permittivity composites (Chapter 7).
5. Modification of styrene butadiene rubber (SBR) and polybutadiene (PB) with methyl thioglycolate and thioglycolic acid to enhance the electrical properties and tailor the mechanical properties of the polymers (Chapter 8).
6. Grafting electrically conducting tetraaniline to elastomers to enhance the relative permittivity (Chapter 8).

Chapter 9 summarises the work presented in this thesis and provides a future perspective for developing high permittivity dielectric elastomers for actuators and generator devices.

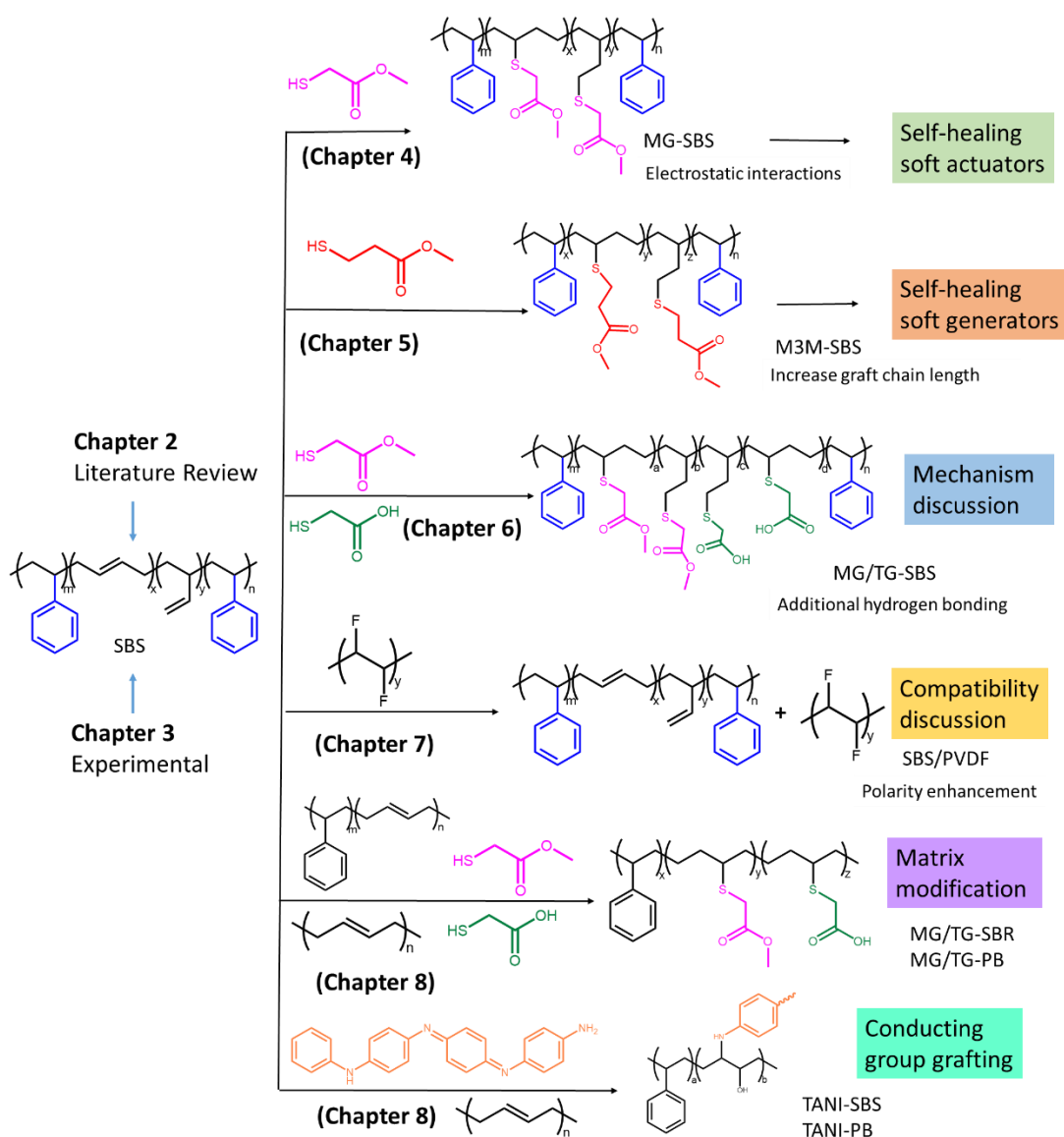


Figure 1.7 Research pathway for high performance dielectric elastomers.

1.7 References

1. C. Thiel, W. Nijs, S. Simoes, J. Schmidt, A. van Zyl and E. Schmid, *Energy Policy*, 2016, **96**, 153-166.
2. C. Bastin, A. Szklo and L. P. Rosa, *Energy Policy*, 2010, **38**, 3586-3597.
3. Y. Liu and A. Kokko, *Energy Policy*, 2013, **57**, 21-29.
4. C. Berggren and T. Magnusson, *Energy Policy*, 2012, **41**, 636-643.
5. C. R. Vaz, T. R. S. Rauen and Á. G. R. Lezana, *Sustainability*, 2017, **9**, 880.
6. A. L. Kun, S. Boll and A. Schmidt, *IEEE Pervasive Computing*, 2016, **15**, 32-38.
7. E. Uhlemann, *IEEE Vehicular Technology Magazine*, 2015, **10**, 20-23.

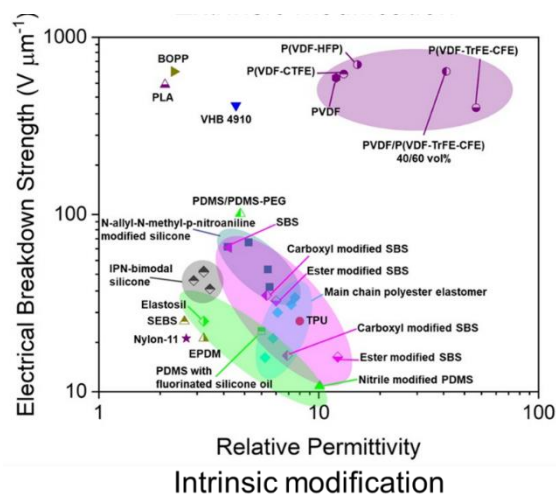
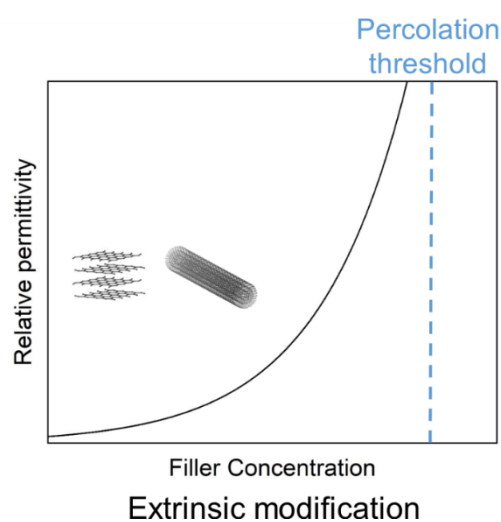
8. S. A. Birrell, M. Fowkes and P. A. Jennings, *IEEE Transactions on Intelligent Transportation Systems*, 2014, **15**, 1801-1810.
9. INSIGHTS, Insights into Issues: Autonomous Vehicle Technology, <https://www.insightsonindia.com/2016/11/30/insights-issues-autonomous-vehicle-technology/>, (accessed April 2020).
10. S. Rambo, Shedding Pounds In Automotive Electronics, <https://semiengineering.com/shedding-pounds-in-automotive-electronics/>, (accessed April 2020).
11. F. Carpi, D. De Rossi, R. Kornbluh, R. E. Pelrine and P. Sommer-Larsen, *Dielectric Elastomers as Electromechanical Transducers: Fundamentals, Materials, Devices, Models and Applications of an Emerging Electroactive Polymer Technology*, Elsevier Science, 2011.
12. H. Phung, C. T. Nguyen, H. Jung, T. D. Nguyen and H. R. Choi, *Smart Mater. Struct.*, 2020, **29**, 035007.
13. S. Chiba and M. Waki, *Sustainable Chem. Pharm.*, 2020, **15**, 100205.
14. H. T. Cheng, Z. Q. Song, S. Zhu and K. Ohyama, *Key Eng. Mater.*, 2019, **804**, 63-67.
15. R. Pelrine and R. Kornbluh, in *Dielectric Elastomers as Electromechanical Transducers*, Elsevier, Amsterdam, 2008, ch. 1, pp. 3-12.
16. F. B. Madsen, A. E. Daugaard, S. Hvilsted and A. L. Skov, *Macromol. Rapid Commun.*, 2016, **37**, 378-413.
17. J. Zhou, L. Jiang and R. E. Khayat, *Soft Matter*, 2015, **11**, 2983-2992.
18. C. Racles, M. Ignat, A. Bele, M. Dascalu, D. Lipcinski and M. Cazacu, *Smart Mater. Struct.*, 2016, **25**, 085024.
19. C. Ellingford, C. Bowen, T. McNally and C. Wan, *Macromol. Rapid Commun.*, 2018, **39**, 1800340.
20. C. Wan and C. R. Bowen, *J. Mater. Chem. A*, 2017, **5**, 3091-3128.
21. S. Park, Y. Kim, H. Jung, J.-Y. Park, N. Lee and Y. Seo, *Sci. Rep.*, 2017, **7**, 17290.
22. N. Meng, X. Zhu, R. Mao, M. J. Reece and E. Bilotti, *J. Mater. Chem. C*, 2017, **5**, 3296-3305.
23. J. Song, G. Zhao, B. Li and J. Wang, *Heliyon*, 2017, **3**, e00377.
24. H. Sun, C. Jiang, N. Ning, L. Zhang, M. Tian and S. Yuan, *Polym. Chem.*, 2016, **7**, 4072-4080.
25. R. M. Grigorescu, F. Ciuprina, P. Ghioca, M. Ghiurea, L. Iancu, B. Spurcaci and D. M. Panaitescu, *J. Phys. Chem. Solids*, 2016, **89**, 97-106.
26. AzoMaterials, <http://www.azom.com/article.aspx?ArticleID=873>, (accessed December 2016).
27. S. S. Banerjee, I. Ramakrishnan and B. K. Satapathy, *Polym. Eng. Sci.*, 2016, **56**, 491-499.
28. S. Risse, B. Kussmaul, H. Krüger and G. Kofod, *Adv. Funct. Mater.*, 2012, **22**, 3958-3962.
29. Advanced Rubber Coatings, <http://www.advancedrubbercoatings.com/site/1584080/page/765223>, (accessed December 2016).
30. T. G. McKay, E. Calius and I. A. Anderson, presented in part at the Electroactive Polymer Actuators and Devices (EAPAD), San Diego, Mar 08, 2009.
31. V. L. Tagarielli, R. Hildick-Smith and J. E. Huber, *Int. J. Solids Struct.*, 2012, **49**, 3409-3415.

32. G. Kofod, P. Sommer-Larsen, R. Kornbluh and R. Pelrine, *J. Intell. Mater. Syst. Struct.*, 2003, **14**, 787-793.
33. B. Chen, M. Kolloosche, M. Stewart, J. Busfield and F. Carpi, *Int. J. Smart Nano Mater.*, 2015, **6**, 290-303.
34. T. Vu-Cong, C. Jean-Mistral and A. Sylvestre, *Smart Mater. Struct.*, 2012, **21**, 105036.
35. V. I. Belyavskii and A. A. Gorbatshevich, *JETP Lett.*, 2017, **105**, 464-472.
36. L. Dissado, in *Springer Handbook of Electronic and Photonic Materials*, eds. S. Kasap and P. Capper, Springer International Publishing, Cham, 2017, pp. 219-243.
37. A. Zulkifli, in *Dielectric Materials*, eds. M. A. Silaghi, IntechOpen, London, 2012, pp. 1-24.
38. C. J. F. Böttcher, in *Theory of Electric Polarization (Second Edition)*, ed. C. J. F. Böttcher, Elsevier, Amsterdam, 1973, pp. 91-127.
39. K. C. Kao, in *Dielectric Phenomena in Solids*, ed. K. C. Kao, Academic Press, San Diego, 2004, pp. 41-114.
40. M. Samet, V. Levchenko, G. Boiteux, G. Seytre, A. Kallel and A. Serghei, *J. Chem. Phys.*, 2015, **142**, 194703.
41. H. Luo, X. Zhou, C. Ellingford, Y. Zhang, S. Chen, K. Zhou, D. Zhang, C. R. Bowen and C. Wan, *Chem. Soc. Rev.*, 2019, **48**, 4424-4465.
42. F. Bibi, M. Villain, C. Guillaume, B. Sorli and N. Gontard, *Sensors*, 2016, **16**, 1232.
43. D. D. L. Chung, in *Composite Materials: Functional Materials for Modern Technologies*, ed. D. D. L. Chung, Springer London, London, 2003, pp. 125-166.
44. M. Ieda, M. Nagao and M. Hikita, *IEEE Trans. Dielectr. Electr. Insul.*, 1994, **1**, 934-945.
45. S. Li, G. Yin, G. Chen, J. Li, S. Bai, L. Zhong, Y. Zhang and Q. Lei, *IEEE Trans. Dielectr. Electr. Insul.*, 2010, **17**, 1523-1535.
46. H. Zhao, Y.-J. Xia, Z.-M. Dang, J.-W. Zha and G.-H. Hu, *J. Appl. Polym. Sci.*, 2013, **127**, 4440-4445.
47. S. Zhao, J. Li, D. Cao, Y. Gao, W. Huang, G. Zhang, R. Sun and C.-P. Wong, *J. Mater. Chem. C*, 2016, **4**, 6666-6674.
48. S. Zhao, G. Zhang, Y. Gao, L. Deng, J. Li, R. Sun and C.-P. Wong, *ACS Appl. Mater. Interfaces*, 2014, **6**, 22823-22829.
49. W. Wu, T. Liu, D. Zhang, Q. Sun, K. Cao, J. Zha, Y. Lu, B. Wang, X. Cao, Y. Feng, V. A. L. Roy and R. K. Y. Li, *Composites, Part A*, 2019, **127**, 105650.
50. D. Wang, Y. Bao, J.-W. Zha, J. Zhao, Z.-M. Dang and G.-H. Hu, *ACS Appl. Mater. Interfaces*, 2012, **4**, 6273-6279.
51. T. Chen, J. Qiu, K. Zhu, X. He, X. Kang and E. I. Dong, *Mater. Lett.*, 2014, **128**, 19-22.
52. W. Tong, Y. Zhang, Q. Zhang, X. Luan, F. Lv, L. Liu and Q. An, *Adv. Funct. Mater.*, 2015, **25**, 7029-7037.
53. M. Panahi-Sarmad and M. Razzaghi-Kashani, *Smart Mater. Struct.*, 2018, **27**, 085021.
54. S. Zakaria, A. F. A. Osman, S. N. H. Mustapha and L. K. Yiew, *AIP Conf. Proc.*, 2018, **2030**, 020183.
55. N. González, M. d. À. Custal, D. Rodríguez, J.-R. Riba and E. Armelin, *Mat. Res.*, 2017, **20**, 1082-1091.
56. L. Liu, W. Zhang, N. Ning and L. Zhang, *Chem. Eng. J.*, 2019, **375**, 121993.

57. Q. Guo, Q. Xue, J. Sun, M. Dong, F. Xia and Z. Zhang, *Nanoscale*, 2015, **7**.
58. K. Shehzad, A. A. Hakro, Y. Zeng, S.-H. Yao, Y. Xiao-Hong, M. Mumtaz, K. Nadeem, N. S. Khisro and Z.-M. Dang, *Appl. Nanosci.*, 2015, **5**, 969-974.
59. S. Nayak, T. K. Chaki and D. Khastgir, *Ind. Eng. Chem. Res.*, 2014, **53**, 14982-14992.
60. H. Stoyanov, D. Mc Carthy, M. Kolloosche and G. Kofod, *Appl. Phys. Lett.*, 2009, **94**, 232905.
61. J. Wang, F. Guan, L. Cui, J. Pan, Q. Wang and L. Zhu, *J. Polym. Sci., Part B: Polym. Phys.*, 2014, **52**, 1669-1680.
62. J. Yuan, S. Yao and P. Poulin, in *Polymer Nanocomposites: Electrical and Thermal Properties*, eds. X. Huang and C. Zhi, Springer International Publishing, Cham, 2016, pp. 3-28.
63. C. G. Hardy, M. S. Islam, D. Gonzalez-Delozier, J. E. Morgan, B. Cash, B. C. Benicewicz, H. J. Ploehn and C. Tang, *Chem. Mater.*, 2013, **25**, 799-807.
64. D. Yang, M. Ruan, S. Huang, Y. Wu, S. Li, H. Wang, X. Ao, Y. Liang, W. Guo and L. Zhang, *RSC Adv.*, 2016, **6**, 90172-90183.
65. D. Yang, F. Ge, M. Tian, N. Ning, L. Zhang, C. Zhao, K. Ito, T. Nishi, H. Wang and Y. Luan, *J. Mater. Chem. A*, 2015, **3**, 9468-9479.
66. S. Nayak and D. Khastgir, *J. Appl. Polym. Sci.*, 2019, **136**, 47307.
67. X.-Z. Chen, X. Li, X.-S. Qian, M. Lin, S. Wu, Q.-D. Shen and Q. M. Zhang, *Polymer*, 2013, **54**, 5299-5302.
68. J. Hou, Y. Feng, J. Liao, W. Ding, L. Shui, H. Li, Y. Wang, B. Tang, A. Umar and G. Zhou, *Polymers*, 2018, **10**, 1119.
69. A. C. Dent, C. R. Bowen, R. Stevens, M. G. Cain and M. Stewart, *J. Eur. Ceram. Soc.*, 2007, **27**, 3739-3743.
70. X. Zhang, Y. Shen, Q. Zhang, L. Gu, Y. Hu, J. Du, Y. Lin and C.-W. Nan, *Adv. Mater.*, 2015, **27**, 819-824.
71. E. Baer and L. Zhu, *Macromolecules*, 2017, **50**, 2239-2256.

Chapter 2

Literature Review



Publications:

C. Ellingford, C. Bowen, T. McNally and C. Wan*, Intrinsically tuning the electromechanical properties of elastomer dielectrics: a chemistry perspective, *Macromol. Rapid Commun.*, 2018, **39**, 18, 1800340.

C. Ellingford, C. Wan*, Ł. Figiel and T. McNally, Chemical modification of dielectric elastomers in *Modern Physical Chemistry: Engineering Models, Materials, and Methods with Applications*, eds. R. K. Haghi, E. Besalu, M. Jaroszewski, S. Thomas and K. M. Praveen, CRC Press, New York, 2018, pp. 59-94

2.1 Introduction

This chapter overviews the modification approaches of dielectric elastomers for energy actuation and generation applications. This chapter includes two sections. The first section investigates the extrinsic modification approaches to enhance the relative permittivity of dielectric elastomers by incorporation of conducting filler, ceramic fillers or blending with other polar polymers. The second section investigates the intrinsic modification of dielectric elastomers by chemical grafting of polar groups or electrical conducting groups to the elastomer main chains, and grafting of mesogens to produce liquid crystal elastomers. The introduction of polar organic groups or inorganic fillers enhances the polarity and relative permittivity of the polymers. In addition, the mechanical properties such as the Young's modulus or strain at break and the electrical properties such as the electrical breakdown strength and dielectric loss also need to be considered in order to design high performance dielectric elastomers for actuation and energy harvesting applications.

2.2 Extrinsic modification of dielectric elastomers

Extrinsic modification of dielectric elastomers is classified into two different approaches. The first approach is the blending of different polymers to utilise advantageous properties for the polymer blend. The second approach is the addition of conducting or high permittivity ceramic nanoparticles into a polymer matrix to enhance its electrical properties. In addition to this, the configuration design of the composite can be considered to introduce multi-layered devices.¹ A multi-layered structure can consist of stacked polymer layers between insulating/conducting or semicrystalline polymer/elastomer.² Within this, the thickness and interface are key factors for the electromechanical properties of the device.^{3,4} For the purposes of this literature review on extrinsic modification, the incorporation of conducting and ceramic fillers is discussed. For more information on multi-layered devices, please see the following review by Luo *et al.*³

2.2.1 The addition of conducting fillers

The addition of conducting fillers such as carbon nanotubes, graphene or metal nanoparticles into a dielectric elastomer matrix has the sole purpose of enhancing the relative permittivity. However, as mentioned in section 1.4, the direct addition of

nanofillers results in issues of agglomeration and dispersion due to poor interfacial compatibility between the filler and the polymer matrix.⁵ Furthermore, the $\tan \delta$ loss typically increases, the electrical breakdown strength decreases and mechanical flexibility is reduced. The poorer electrical breakdown strength arises from an inhomogeneous electric field experience by the composite from the difference in the permittivity of the filler compared to the polymer.

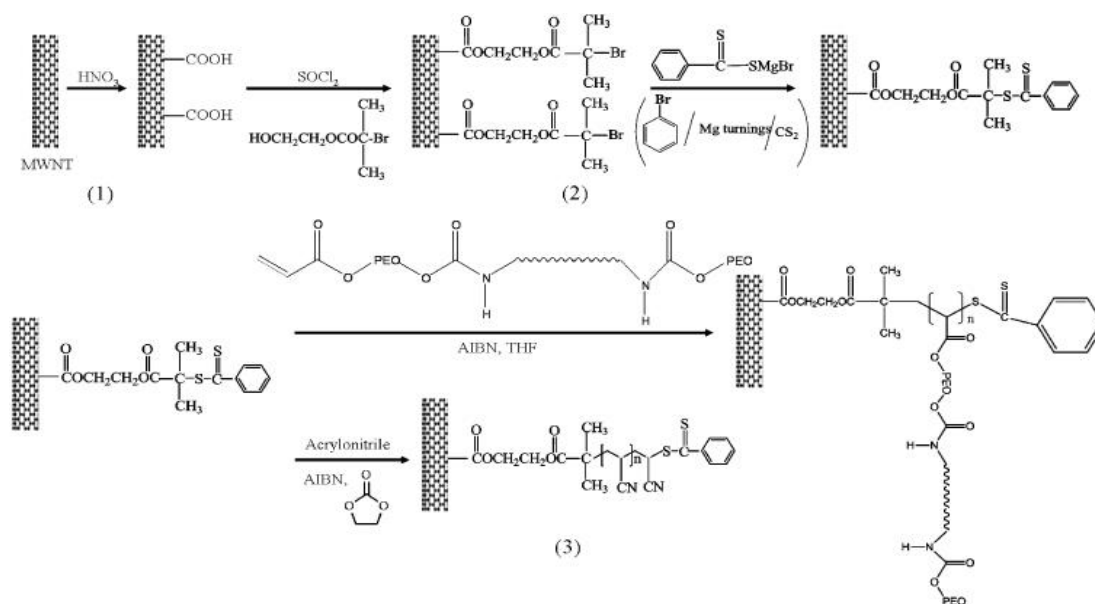


Figure 2.1 Modification of MWCNTs with a RAFT agent and a subsequent grafting from reaction to produce polyacrylonitrile and polydiurethane monoacrylate modified MWCNTs. Reproduced from Galantini et al.⁶

To overcome this, different approaches are used within the literature to homogenise the electric field experienced by the composite and also reduce the dielectric loss from the addition of the fillers. One recent approach is to surface modify the nanofillers to introduce functional groups to interact more favourably with the polymer matrix. Galantini *et al.* surface functionalised multi-walled carbon nanotubes (MWCNTs) with a RAFT agent and grew polyacrylonitrile and polydiurethane monoacrylate on the MWCNTs in a grafting from polymerisation, shown in Figure 2.1. The functionalised MWCNTs were mixed into a polyurethane matrix and 1 wt% polydiurethane monoacrylate functionalised MWCNTs increased the relative permittivity to 7 whilst 5 wt% of polyacrylonitrile functionalised MWCNTs enhanced the relative permittivity to 9 and both retained a low dielectric loss. Therefore, the surface modification of these MWCNTs suppressed percolation, as unmodified

MWCNTs percolated at 1 wt%. Furthermore, a 1.1% transverse actuation strain was observed under a $5.5 \text{ V } \mu\text{m}^{-1}$ electric field for 0.5 wt% of poly(diurethane monoacrylate) functionalised MWCNTs, whilst the pure polyurethane actuated 1.2% under an electric field of $7.5 \text{ V } \mu\text{m}^{-1}$, showing that the electrical breakdown strength reduced after addition of MWCNTs but the electromechanical sensitivity of the composite increased.⁶ Quinsa *et al.* demonstrated the advantages of encapsulating silver nanoparticles in insulating silica shells of differing thicknesses for enhancing the relative permittivity whilst simultaneously suppressing the $\tan \delta$ loss.⁷ Balancing the thickness of the shell was important as shells that are too thick prevent the filler from enhancing the relative permittivity of the polymer matrix, whereas too thin causes an insulator-to-metal transition for the filler and increases the electrical losses of the system.⁸

An alternative to this is to surface functionalise the MWCNTs with small functional groups such as silane or nitric acid. Up to 2 wt% of these modified MWCNTs were also added into a polyurethane matrix. This had the effect of strengthening and stiffening the mechanical properties, whilst also increasing the strain at break, however no explanation was given for this. Both types of functionalised MWCNTs increased the relative permittivity up to 9.5 at 10^3 Hz , and they suppressed the $\tan \delta$ loss below 0.05 at 2 wt% addition. A $\tan \delta$ loss of greater than 0.05 was observed for pristine MWCNTs.⁹ Silane modified MWCNTs were also mixed into a silicone elastomer using a solution mixing approach. An increase in relative permittivity from 2.5 to 3.2 at 10^2 Hz was observed at 4 phr of silane modified MWCNTs addition, whilst the $\tan \delta$ remained low.¹⁰

A core-shell approach was utilised by Kohlmeyer *et al.* to modify the MWCNTs with an insulating shell. The simplest MWCNTs core-shell is based on hydroxyl groups and was used to develop a polydimethylsiloxane core-shell around MWCNTs. This reduced the $\tan \delta$ loss whilst increasing the relative permittivity of a PDMS elastomer. It also delayed percolation of the carbon nanotubes from 2 wt% for pristine MWCNTs to 4 wt% for MWCNTs with a core shell of OH groups, and thus suppressed the $\tan \delta$ loss in the region of 2 wt% – 4 wt% MWCNTs whilst an increase in the relative permittivity was observed.¹¹

Nanosilica was used to form an insulating layer over carboxylated MWCNTs dispersed in natural rubber, Figure 2.2, through hydrogen bonding between the two. With 3 phr nanosilica decorated MWCNTs in natural rubber, the tensile strength increased from 21 MPa to 35 MPa and the strain at break remained high at 1306%. Percolation was observed at 2 phr of nanosilica decorated MWCNTs. Prior to percolation, the relative permittivity of the composite was 10.¹²

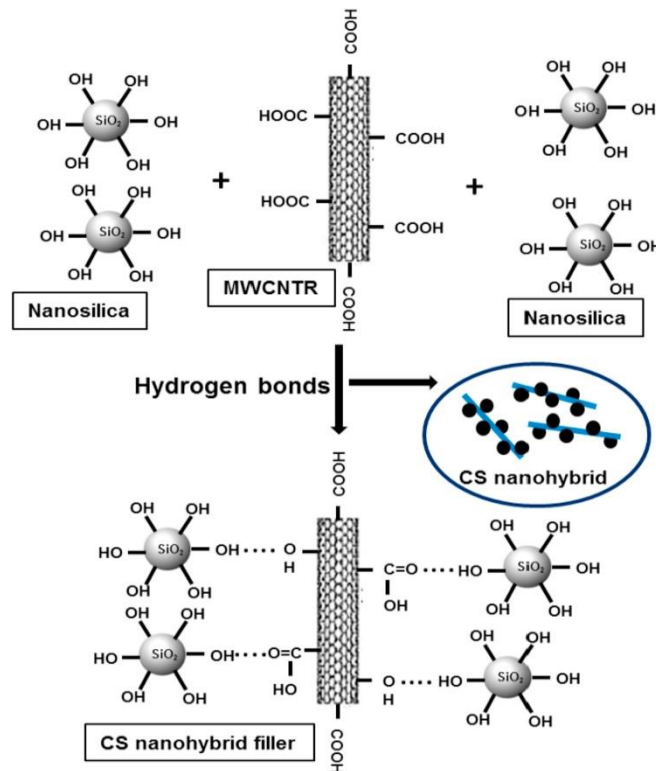


Figure 2.2 Nanosilica decorated carboxylated MWCNTs. Reproduced from George *et al.*¹²

An alternative approach is to utilise branched carbon nanotubes to modify a polymer matrix instead of linear nanotubes. The addition of 0.5 vol% branched carbon nanotubes resulted in a decreased tensile strength and strain at break from 27.5 MPa to 20 MPa and 1360% to 810% respectively. However, the relative permittivity of the elastomer increased from 7 to 13 at 10³ Hz and a low loss was observed.¹³

For a DEG device, a silicone elastomer composite crosslinked with a polar crosslinker and nanospring carbon nanotubes was devised. With 10 wt% addition of nanospring carbon nanotubes, the relative permittivity of the composite increased to 4.6 and had a low $\tan \delta$ loss of 0.03. The composite was able to strain up to 270% and had a higher tensile strength than neat PDMS by 0.5 MPa. Furthermore, the electrical breakdown

strength of the composite remained high, failing under an electric field of $41 \text{ V } \mu\text{m}^{-1}$. This was lower than for pure PDMS. The set-up of the DEG, where an electret was used to induce charge, is shown in Figure 2.3. As the DEG was stretched, the pleated electret sheet was forced to contact the PDMS composite film, inducing a charge. The elastomer composite was able to harvest 14.5 V under a 66% strain and had a theoretical maximum energy harvesting of $1.2 \times 10^{-4} \text{ J}$.¹⁴

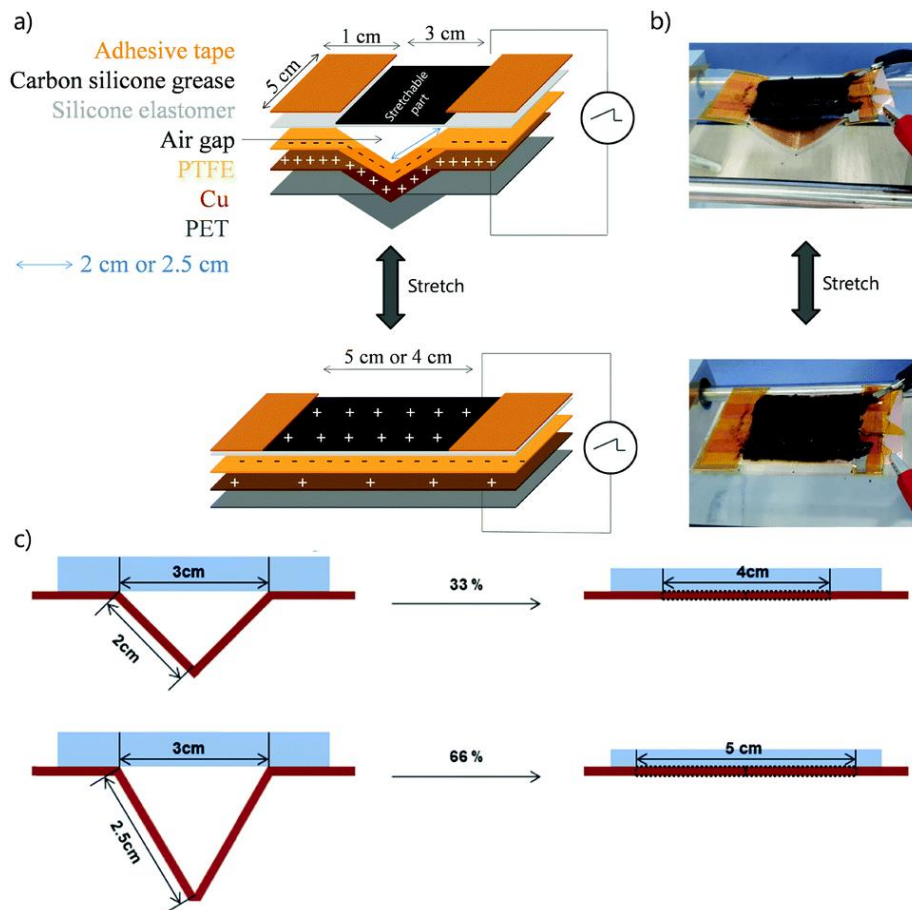


Figure 2.3 Electret dielectric elastomer generator set-up using nanospring containing carbon nanotubes in a PDMS composite. Reproduced from Lee *et al.*¹⁴

For graphene based nanofillers, there are a broad array of different types that can be utilised to enhance the relative permittivity of a polymer.¹⁵ Pristine graphene is an ideal material of single layer graphene which possesses a high conductivity from both a high charge carrier mobility and high charge carrier concentration.¹⁵ This means a single graphene sheet has a conductivity of up to $6 \times 10^5 \text{ S m}^{-1}$.¹⁶ However due to difficulty in its synthesis, this form of graphene is rarely used. Instead, graphene nanoplatelets (GNPs), graphene oxide (GO) or reduced graphene oxide (rGO) are

commonly utilised. Graphene nanoplatelets are an agglomerated form of graphene¹⁵ but possess high conductivities if less than 50 nm thick.¹⁶

GO is synthesised from the graphite to introduce a large array of oxygenation to the sheets in the form of hydroxyl groups, epoxides, alcohols, ketones and carboxylic acids,¹⁷ and has a significantly lower conductivity.¹⁸ Due to the high level of functionalisation, the graphene sheets are highly exfoliated and agglomeration is low. However, to enhance the conductivity of GO, it can be thermally or chemically reduced to form rGO. At low levels of reduction, the increase in conductivity arises from tunnelling and hopping between pristine graphene regions on the rGO sheet.¹⁵ High levels of reduction form a percolated network between the graphene regions on the sheet to enhance conduction further.^{15, 19}

Recently, the use of GNPs in silicone rubber enhanced the relative permittivity up to 8.4 and maintained a low dielectric loss of 1.35×10^{-2} . Whilst no mechanical properties are reported in this study, the silicone elastomer was able to actuate 4.1 mm under an applied voltage of 2.5 kV.²⁰

The use of GO showed more promise in carboxylated nitrile rubber whereby either GO or dopamine coated GO were introduced into the polymer matrix. The mixing of 0.5 vol% GO caused percolation within the rubber and increased the permittivity up to 171 whilst the dielectric loss increased to 1.33. Thus the rubber could only actuate 1.7% under a 1 kV mm^{-1} electric field. However, by coating the GO in insulating polydopamine, the permittivity decreased and the dielectric loss was suppressed upon a thicker dopamine shell. This also enhanced the electrical breakdown strength of the composite up to 4.4 kV mm^{-1} , and enabled it to actuate 4.4% before failure.²¹

However, 3 wt% rGO increased the relative permittivity of a polyurethane matrix to 101.9 whilst maintaining a low dielectric loss of 0.03. A high breakdown strength was maintained of $33 \text{ V } \mu\text{m}^{-1}$ and the device was able to actuate in the direction of the thickness by 40%. In addition to this, this study also investigated the TiO₂ decorated rGO to the polyurethane matrix. The hybrid filler approach resulted in weaker and more brittle mechanical properties, but was able to actuate up to 70% in the thickness up to a breakdown field of $37.5 \text{ V } \mu\text{m}^{-1}$. The superiority of the hybrid filler approach was attributed to the strong interfacial interaction between the TiO₂ and the polymer, forcing the rGO to be more homogeneously dispersed.²²

Based on this approach, silica has also been utilised to decorate rGO to improve the dielectric and actuation response of PDMS. By coating rGO in SiO₂, the relative permittivity of the composite was suppressed for 3 wt%, down to 6 at 10³ Hz from 20. A denser SiO₂ shell around rGO suppressed the relative permittivity further to 4 at 10³ Hz. The dielectric loss of the composite was dependent on the thickness of the SiO₂ shell and the dielectric loss was three orders of magnitude lower for 3 wt% rGO with the densest SiO₂ shell compared to no SiO₂ shell. Furthermore, the actuation performance of the densest silica decorated rGO was the highest across all samples and peaked at a 1 wt% inclusion, which had an in-plane actuation of 13% and failed under an electric field of 25 kV mm⁻¹.²³ This was despite 1 wt% silica-shelled rGO having low permittivity, and demonstrates the importance of a high breakdown strength, low dielectric loss and high deformability of the sample in addition to permittivity.

An alternative core shell structure was developed based on lower conductivity GNPs. A polydopamine core-shell was produced around the GNPs, followed by silver nanoparticles embedded into the shell, named as Gns@PDA-Ag. The hybrid filler was then dispersed into a polyurethane matrix. Upon the addition of up to 4 wt% Gns@PDA-Ag, the tensile strength of the composite increased and the Young's modulus decreased relative to the unmodified polyurethane. At 10³ Hz, the relative permittivity of 4 wt% Gns@PDA-Ag in polyurethane was 8, whilst at lower frequency there was a large increase in the relative permittivity due to Maxwell-Wagner-Silars polarisation. At 2 wt% addition of Gns@PDA-AG, the electrical breakdown strength decreased by 5 kV mm⁻¹ compared to the pure polyurethane, down to 21 kV mm⁻¹. Comparatively, at the same filler fraction unmodified GNPs had a lower breakdown strength of 16 kV mm⁻¹ due to a poorer interfacial bonding with the polymer matrix.²⁴

The incorporation of metal nanoparticles has been investigated as a cost effective and efficient method to enhance the electromechanical properties of polymers. Recently, Yang *et al.* used TiO₂ and created a core-shell from polycatechol/polyamine to enhance the performance of natural rubber, see Figure 2.4. The mechanical properties of natural rubber increased upon increasing concentrations of modified TiO₂ nanoparticles. No degradation was observed in the strain at break compared to pristine natural rubber up to 50 phr of modified TiO₂ nanoparticles, but the tensile strength of the composite increased from 4 MPa to 16 MPa. As the metal nanoparticles are not

conducting due to their smaller size, the fraction of filler added to the matrix is higher compared to carbon nanotubes and graphene. The relative permittivity increased at 50 phr of modified TiO_2 compared to pure natural rubber from 2.55 to 3.48, whilst the $\tan \delta$ loss decreased from 9×10^{-3} to 3×10^{-3} . Furthermore, the electrical breakdown strength at this filler concentration was 25 kV mm^{-1} , greater than natural rubber, and the composite broke down under an electric field of 90 kV mm^{-1} .

However, when 10 phr of modified TiO_2 was incorporated into natural rubber superior actuation was observed and the composite could actuate up to 12% under an electric field of 70 kV mm^{-1} . This was due to the decrease in the Young's modulus of the composite, as well as a small increase in the relative permittivity.²⁵

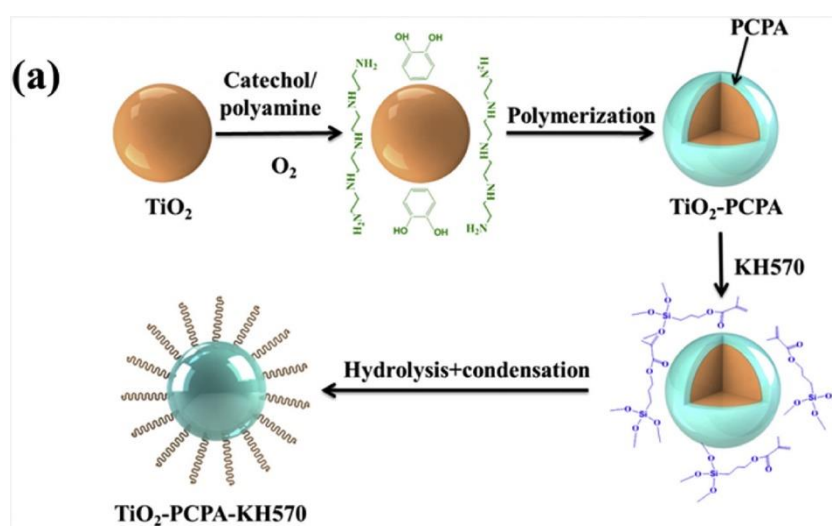


Figure 2.4 Synthesis of core-shell TiO_2 with polycatcheol/polyamine shells modified with silane. Adapted from Yang *et al.*²⁵

An example of a self-healing dielectric elastomer through hydrogen bonding was synthesised from sebacic acid and citric acid which was composited through the addition of TiO_2 with a urea core-shell. After three days, the core-shell TiO_2 containing composite was able to recover 100% of its stress by leaving the polymer at room temperature. The introduction of the TiO_2 nanoparticles increased the strain at break of the elastomer and reduced the tensile strength and Young's modulus significantly. With 5 wt% addition, the relative permittivity increased to a maximum of 37.5 at 10^3 Hz, and had a $\tan \delta$ loss of 1.15. However, increasing the filler content further to 9 wt% led to a decrease in relative permittivity to 15.0 and a reduced $\tan \delta$ loss of 0.74.²⁶ This was attributed to an increased presence of air voids in the composite from

additional filler, reducing the relative permittivity.²⁷ The inclusion of 1 wt% core-shell TiO₂ into the dielectric elastomer demonstrated the greatest actuation performance. Under an 8.5 V μm^{-1} electric field, it was able to actuate 7.5%. After 24 hours self-healing, the elastomer was able to recover more than 100% of its actuation performance and actuated 7.8%. Additionally, it recovered almost 100% of its breakdown strength.²⁶

Overall, rGO based and TiO₂ based composites have exhibited superior actuation performance. This typically arises from composites which do not have the highest relative permittivity, but experience a reduction in Young's modulus, a reduction in $\tan \delta$ loss or an increase in the breakdown strength of the material. Additionally, very few examples are present for energy harvesting from dielectric elastomers and most present actuation results only. This is attributed to two factors, firstly the research focus of the author and secondly a DEA is more simple in its fabrication and configuration compared to a DEG and thus contributes to the lack of reported DEG devices.

2.2.2 The addition of ceramic fillers

The addition of high permittivity ceramic fillers into a polymer matrix is used as an alternative route to conducting fillers to enhance the relative permittivity of a dielectric elastomer. However, typically high weight fractions of ceramic fillers are required to achieve this, increasing the brittleness and reducing the flexibility of the composite and reducing the electrical breakdown strength.

In a PZT/PDMS composite by Nayak *et al.*, up to 41.2 wt% PZT was incorporated into the dielectric elastomer to enhance its dielectric properties. As the filler loading increased to 41.2 wt%, the tensile strength of the PDMS composite decreased from 5.6 MPa to 4.1 MPa whilst the strain at break decreased from 550% to 320%. The large filler fraction enhanced the relative permittivity from 3.5 at 10³ Hz to 8.5 but the $\tan \delta$ loss increased from 0.1 to 0.3 at 10³ Hz.²⁸

BaTiO₃ was used to composite a hydrogenated nitrile rubber/PVDF blend for a flexible, bendable actuator. Up to 15 wt% BaTiO₃ was introduced, however a 5 wt% inclusion of BaTiO₃ demonstrated the superior actuation properties and was able to exhibit 8% strain under a 112 kV mm^{-1} electric field, whilst 10 wt% BaTiO₃ could

actuate further to 10% strain, but failed under a lower electric field of 105 kV mm^{-1} . Actuation could not be observed below 85 kV mm^{-1} for both of these composites due to their high Young's modulus.²⁹

To improve the electromechanical properties of ceramic filled composites, a core-shell approach can also be utilised to increase the homogeneity of the internal electric field when under an applied voltage. Silane and dopamine was used to develop a core shell around BaTiO_3 for compositing silicone rubber, see Figure 2.5. The core-shell approach helped reduce agglomerations of the BaTiO_3 nanofillers. The addition of 10 phr dopamine and silane core-shell BaTiO_3 to silicone rubber had the highest actuation performance, actuating 8.2% under a 73 kV mm^{-1} electric field. This was because the addition of only 10 phr BaTiO_3 reduced the Young's modulus of the elastomer whilst simultaneously enhancing the relative permittivity and maintaining the electrical breakdown strength.³⁰ Individual studies on both dopamine and silane modified BaTiO_3 have also been investigated.^{31, 32}

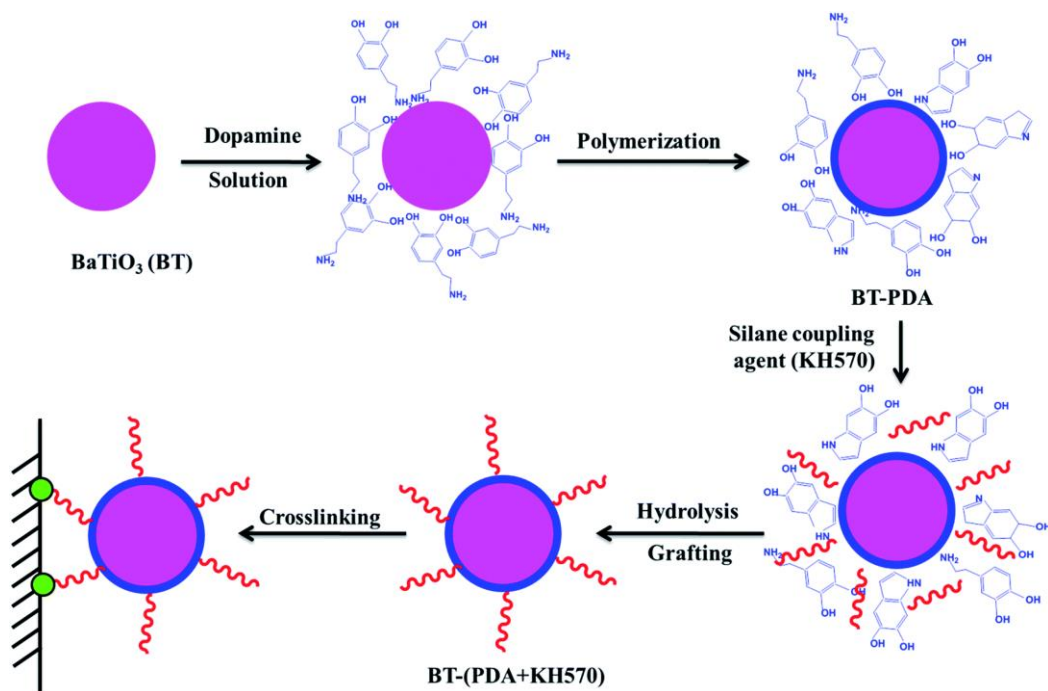


Figure 2.5 Synthetic pathway for a silane and dopamine core-shell BaTiO_3 . Reproduced from Yang *et al.*³⁰

A recent example by Zhang *et al.* used dopamine modified copper calcium titanate (CCTO) to composite silicone rubber for a dielectric elastomer generator. 26 wt% of dopamine modified CCTO in silicone rubber exhibited an energy harvesting density

of 0.7 mJ cm^{-3} under a 1.5 kV operating voltage, with an energy conversion efficiency of 3.4%.³² Comparatively, the energy harvesting density of BaTiO₃ dielectric elastomer generators from literature reports was higher, but their energy conversion efficiency was lower than using CCTO as a filler.³³⁻³⁵

A unique approach by Yang *et al.* developed a slide ring type polymer network with an interlocked structure consisting of polyrotaxanes,³⁶ see Figure 2.6. The slide rings are able to move along the polymer structure and simulate a pulley system, allowing the polymer chains to autonomously equilibrate mechanical stress, thus experience the internal force homogeneously.^{36, 37} This can assist with high actuation strain without failure of the polymer. To enhance the actuation properties of this, silane modified BaTiO₃ was added into the polymer matrix. The addition of 10 wt% silane modified BaTiO₃ enabled the composite to actuate 26% under a 12 kV mm^{-1} electric field. This was partly due to the high permittivity of the elastomer, 10.5 at 10^3 Hz , and partly due to the gel like nature of the material which had a Young's modulus of $5.6 \times 10^{-2} \text{ MPa}$.

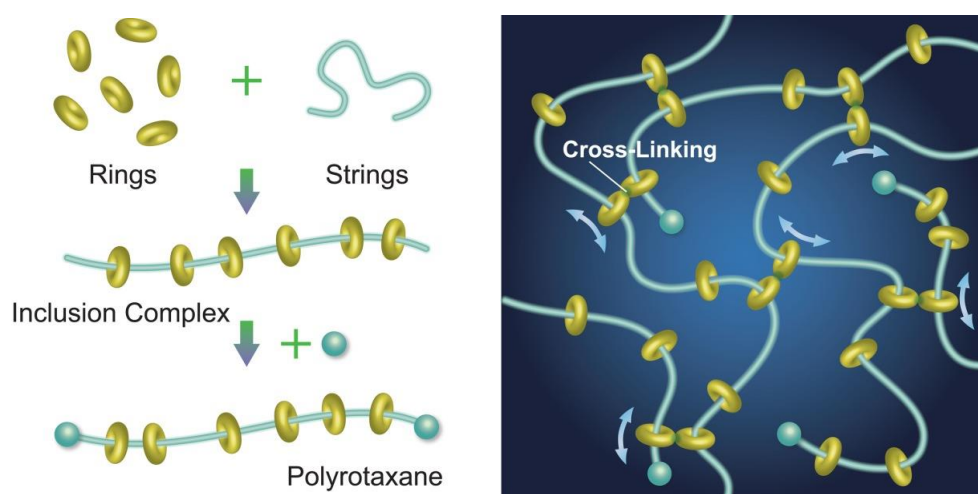


Figure 2.6 Schematic diagram of the slide ring structure. Adapted from Noda *et al.*³⁸

Overall, for ceramic nanofillers whilst high filler weight fractions enhances greater the relative permittivity, the best performing actuators balance the mechanical properties and electric properties, so that the composite was still easily deformable.

2.3 Intrinsic modification of dielectric elastomers

The intrinsic modification of dielectric elastomers involves the attachment of a polar or conducting group to the polymer backbone to enhance the electromechanical properties. Typically the relative permittivity of a non-polar polymer is 2~3, primarily

due to the low electronic polarisation exhibited. Only a small shift in the position of the electronic cloud is observed relative to the atomic nuclei, because the intra-atomic field is stronger and reduces the distortion of the electronic cloud.³⁹

By covalently introducing polar groups into the polymer backbone, the polymer structure can be permanently changed and its electromechanical properties enhanced. The polar groups increase the atomic polarisation present in the dielectric elastomer, because the charge difference across the polymer backbone increases, and thus the relative permittivity increases. This also affects the dipole moment of the polymer.⁴⁰⁻⁴² Furthermore, depending on the introduced polar group, orientation polarisation can be incorporated into the polarisation of the polymer. Orientation polarisation will only occur when the permanent dipoles are introduced to the polymer backbone which can align under an applied electric field. For further information about the contribution of polarisation within a polymer, see section 1.3.1.

However, the grafted polar group size should also be considered. A larger side group increases the free volume of the polymer, providing the polar group with more space to orientate with the electric field. Furthermore, larger grafted groups decrease polymer chain entanglement, reducing the Young's modulus. The reduction in the Young's modulus is advantageous for actuation,⁴³ see section 1.5, however crosslinking in some dielectric elastomers, such as silicone based elastomers, can also decrease the elasticity.⁴⁴ Additionally, the grafting of polar groups affect the physical properties of the dielectric elastomer by increasing the water sensitivity of the polymer and shifting the glass transition temperature to higher temperatures.^{45, 46}

This literature review into intrinsic modification of dielectric elastomers is split into three major sections: polar groups, mesogenic groups and conducting groups. The intrinsic modification of dielectric elastomers with polar groups is further split into two categories: silicone based elastomer and styrenic based elastomers.

2.3.1 Intrinsic modification of dielectric elastomers with polar groups

A summary of different polymers and intrinsic modifications from the literature is shown in Figure 2.7. These graphs show that typically as the relative permittivity of a dielectric elastomer is increased, a decrease is observed for the electrical breakdown strength. However, semi-crystalline PVDF based polymers do not show this and thus

have highly desirable electrical behaviour. Figure 2.7b shows how the Young's modulus for different polymer types changes with respect to permittivity. For dielectric elastomers, the Young's modulus is low, and rarely exceeds 3 MPa, irrespective of the relative permittivity. Therefore dielectric elastomers exhibit excellent mechanical properties for DEA and DEG applications. However, despite their desirable electrical properties, semi-crystalline PVDF based polymers have a very high Young's modulus, approximately 1 GPa, making them too stiff and highly undesirable for use in a DEA or DEG device.

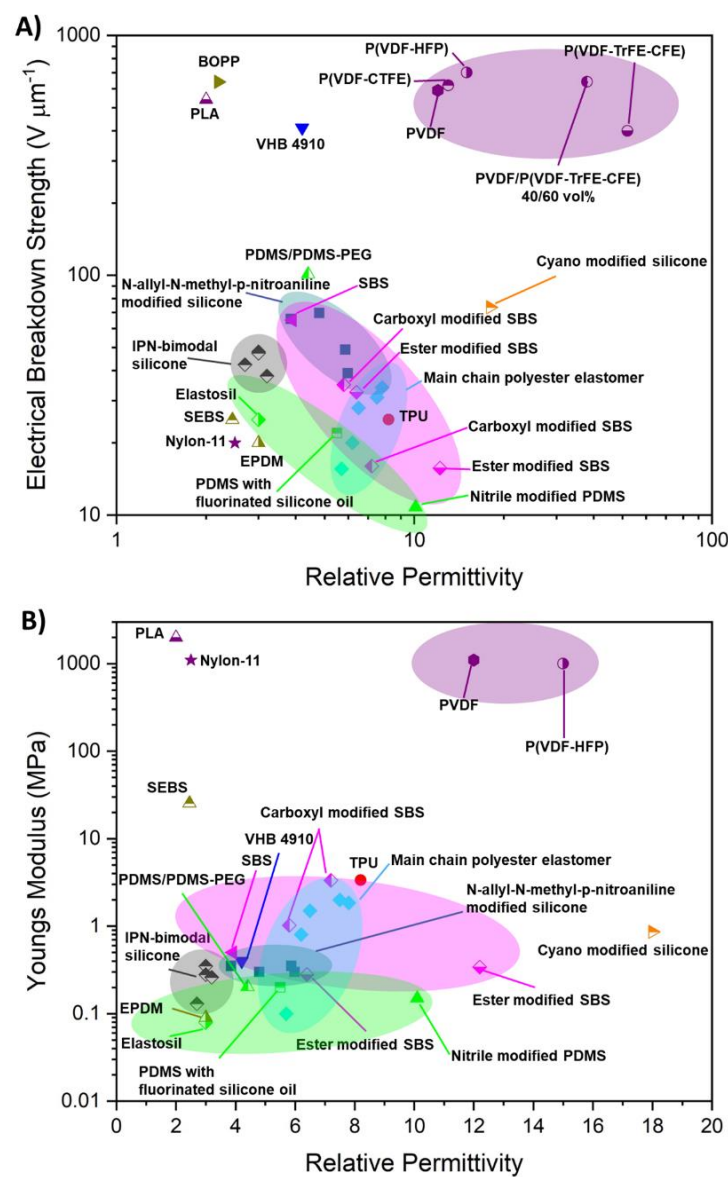


Figure 2.7 (a) Relative permittivity vs electrical breakdown strength and (b) Young's modulus vs dielectric permittivity. Adapted from Ellingford *et al.*⁴⁷

Silicone based elastomers

Silicone based elastomers are non-polar polymers which require a crosslinking curing reaction to convert them from a gel-like state to a solid polymer. Examples of silicone based elastomers include polydimethylsiloxane (PDMS) and polymethylhydridesiloxane (PHMS). Typically, the relative permittivity for silicone based elastomers is between 2 ~ 3⁴⁸ and they exhibit an electrical breakdown strength of ~ 80 MV m⁻¹.⁴⁹

Silicones have been modified extensively throughout the literature, not just for DEA or DEG applications. Modifications include the grafting of esters,⁵⁰ carboxylic acids⁵¹ and amines⁵⁰ amongst others.⁵²⁻⁵⁵ In most cases, the grafting to the silicone backbone is achieved by hydrosilylation, where a vinyl group is grafted at a Si-H bond. The reaction is normally in solution, in the presence of Karstedt's catalyst, and at an elevated temperature for a number of hours, see Figure 2.8. Typically hydrosilylation reactions occur under an inert atmosphere, in anhydrous conditions, as the reaction is water sensitive.^{49, 56} Thin films, typically 100 – 150 μm thick,^{57, 58} can be made *via* solution casting onto a film such as Teflon and crosslinked thermally in under an hour.⁴⁹ Due to sensitivity of hydrosilylation, large scale and industrial scale reactions have been difficult to realise due to the additional cost and complexity that this introduces.

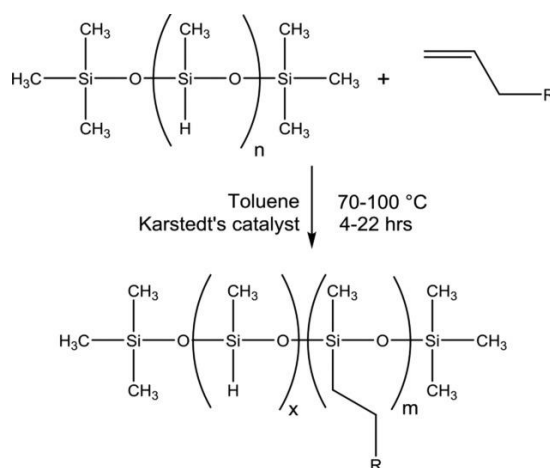


Figure 2.8 General reaction scheme for hydrosilylation of silicone dielectric elastomers. Reproduced from Ellingford *et al.*⁴⁷

The grafting of 89 mol% allyl cyanide to silicone enhanced the relative permittivity of the polymer up to 15.9 but was accompanied by a high dielectric loss of 2.5. The high

loss is attributed to conductivity losses due to the presence of charge carriers.⁵⁹ By reducing the level of grafting to 23 mol% and 8 mol%, the relative permittivity of allyl cyanide modified PHMS decreased to 6.5 and 4.2 respectively. This was accompanied by large decreases in the dielectric loss to 6.0×10^{-1} and 4.2×10^{-3} .^{58, 60}

Therefore to improve the dielectric loss, two different approaches were utilised. PHMS-co-PDMS polymer chains were grafted with 62 mol% allyl cyanide, where the PHMS/PDMS ratio was 1:2, to form regions of high polarity and regions of non-polar polymer. Additionally, a short chain version of allyl cyanide modified PHMS was incorporated as a filler into PDMS, called CNATS-993.

The modified silicone copolymer exhibited a relative permittivity of 4.5, and a low dielectric loss of 9.5×10^{-2} . Mechanically, the elastomer was easily stretchable as it had a Young's modulus of 0.8 MPa, but the elastomer was only suitable for DEA applications due to a strain at break of 170%. The electrical breakdown strength of the copolymer in an actuation device was higher than for pure PDMS, $56 \text{ V } \mu\text{m}^{-1}$ compared to $49 \text{ V } \mu\text{m}^{-1}$. Furthermore, the copolymer was able to actuate 8% before failure, 13 times greater than the unmodified PDMS. This was attributed to the softness of the material, easily allowing actuation to take place.⁶¹

For the addition of CNATS-993 into the polymer matrix, the filler acted as both a plasticiser and a permittivity enhancer, see Figure 2.9. The addition of 7.3 wt% CNATS-993 fractionally increased the relative permittivity above the permittivity level of PDMS, and also maintained a low loss. However, the Young's modulus of the elastomer composites were affected significantly by the plasticising effect of CNATS-993. 7.3 wt% addition of CNATs-993 reduced the Young's modulus for PDMS from 0.9 MPa to 0.7 MPa. Further increases in CNATS-993 content reduced the Young's modulus further as the filler reduced the crosslinking density of PDMS.⁶² This also decreased the electrical breakdown strength of the elastomer as well because of the material softening.^{63, 64} High actuation strains of 8 – 10% strain were observed for the addition of 7.3 wt% and 19.4 wt% CNATS-993 to PDMS, and had a maximum applied electric field of $48 \text{ V } \mu\text{m}^{-1}$. Therefore, both the compositing approach and the copolymer approach yielded a good actuation performance from the silicone elastomers.

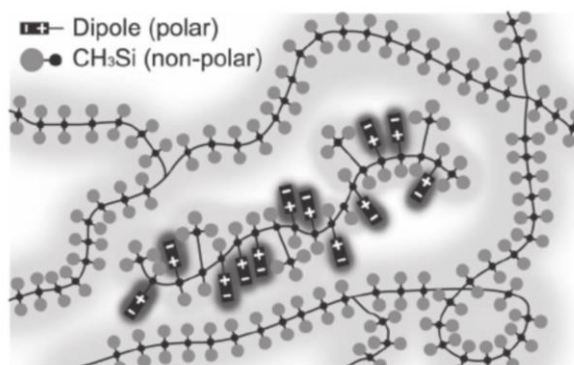


Figure 2.9 Pictorial representation of polar CNATS-993 (short chained allyl cyanide modified PHMS) in a non-polar PDMS matrix. Reproduced from Risse *et al.*⁶²

The actuation performance of grafted allyl cyanide to silicone was investigated alongside crosslinkers with different length alkyl chains attached. Crosslinkers with an attached butyl chain and the silicone polymer with 33 mol% allyl cyanide grafted resulted in the greatest actuation performance of up to 17.5% under a $31 \text{ V } \mu\text{m}^{-1}$ electric field when 7.5% prestrain is applied. It was able to actuate under a low electric field additionally due to its higher permittivity, 7, and soft nature, with a Young's modulus of 0.5 MPa.⁶⁵ Allyl cyanide modified PHMS was also used to harvest energy from small lightweight balls dropped onto a DEG and was able to harvest up to 460 nJ per impact, up from 94 nJ for an unmodified PHMS elastomer.⁶⁶

An alternative polar group grafted to silicone is allyl chloride. The polarity of allyl chloride is less than that of allyl cyanide,⁶⁷ however it has shown that it can enhance the relative permittivity and increase the breakdown strength, whilst maintaining a low $\tan \delta$ loss and a reduced Young's modulus.⁵⁷ At 20 mol% grafting, the relative permittivity was increased to 5.4 and exhibited a low Young's modulus of 0.3 MPa. With 7.5% prestrain, allyl chloride modified silicone could actuate up to 24% under a $53 \text{ V } \mu\text{m}^{-1}$ electric field. Furthermore, enhancing prestrain up to 30% enabled it to stretch up to 30% under a $45 \text{ V } \mu\text{m}^{-1}$ electric field. Allyl chloride modified silicones had a better actuation performance compared to allyl cyanide modified silicones due to their higher breakdown strength from lower polymer conductivity. Finally, allyl chloride modified silicones demonstrated long lifetimes and reliability after undergoing 50,000 actuation testing cycles under a $27 \text{ V } \mu\text{m}^{-1}$ electric field.⁶⁵

Trifluoropropyl modified silicone elastomers were synthesised and the relative permittivity increased linearly with trifluoropropyl grafting up to 9 at 100% grafting.

53 mol% grafting of trifluoropropyl exhibited the best actuation performance and actuated with 5.4% strain but failed under a low electric field of $7.8 \text{ V } \mu\text{m}^{-1}$. All elastomers containing trifluoropropyl experienced electrical breakdown below electric fields of $20 \text{ V } \mu\text{m}^{-1}$, however the cause of this was not determined. Possibly it could be due to high charge carrier mobility, similar to cyanopropyl modified silicone dielectric elastomers.

A study by Racles *et al.* into the dipole moment of the grafted polar group at low grafting levels (8 mol%) was conducted. They found that the polarity of the grafted polar group does not directly correlate with the relative permittivity observed in the overall polymer.⁵⁸ This is because other secondary factors also play a role in the relative permittivity. If the polar group increased the hydrophilicity of the polymer to atmospheric water vapour, then the permittivity will be increased due to ionic conductivity from the presence of water in the sample.^{68, 69} Such water sensitive behaviour was observed for pyridine and carboxylic acid grafted functional groups.

Bele *et al.* investigated the grafting of polar groups to the crosslinker used in silicone elastomer formation. Overall, this had a small effect on the electrical properties, whereby the relative permittivity for the overall elastomer increased with an increase in the polarity of the crosslinker used, except for the chloropropyl modified crosslinking agent, which produced a dielectric elastomer with a lower relative permittivity. This lower relative permittivity was attributed to a larger free space volume generated by this polar crosslinker due to the size of the chloro group. However, for the mechanical properties the more polar the crosslinker was, the higher the tensile strength and lower the strain at break was. This was attributed to the non-polar crosslinkers having better compatibility with the polymer matrix compared to polar crosslinkers, and thus the elastic properties were retained.⁷⁰

An alternative approach to the use of hydrosilylation to graft polar groups to silicone dielectric elastomers is to use thiol-ene chemistry between a thiol group and a vinyl group. For these reactions polyvinylmethylsiloxane (PVMS) is used for the vinyl group along the polymer backbone. The reaction can be a thermal or photoinitiated reaction, see section 4.1 for more information on the thiol-ene reaction. Typically the reaction is carried out under normal atmospheric conditions and the grafting of the

polar group to the dielectric elastomer backbone is controlled through UV exposure time.

Cyano groups were introduced *via* thiol-ene chemistry in different grafting ratios to PVMS and were able to increase the permittivity up to 18.4 in the uncrosslinked state and 17.4 in the crosslinked state.^{46,71} 100 mol% cyano group grafting to PVMS yielded the greatest actuation performance of 21% under an electric field of $12 \text{ V } \mu\text{m}^{-1}$, and failed under an electric field of $15.6 \text{ V } \mu\text{m}^{-1}$. The high actuation performance was due to the high relative permittivity and low Young's modulus that the elastomer exhibited. An increased $\tan \delta$ loss and reduced breakdown strength is attributed to the increase in ion conductivity from the polar group.⁷¹ When crosslinked with a multifunctional crosslinker, where four polymer chains could be crosslinked by 4 chains at once, the electrical breakdown strength of the polymer was enhanced to $25.5 \text{ V } \mu\text{m}^{-1}$ and could actuate 14% under an $18 \text{ V } \mu\text{m}^{-1}$ electric field. The higher breakdown strength is attributed to a higher purity of starting materials, and improved thin film processing with less defects present. Finally, the dielectric elastomer was able to actuate at low voltages of 550V and 600V for up to 10 minutes and exhibit observable strains.⁷²

Thioacetic acid, thioglycolic acid and 2-mercaptoethanol modified silicone elastomers have also been reported in the literature,⁷³⁻⁷⁵ introducing ketone and carboxylic acid functionality to the dielectric elastomers. Thioacetic acid modified silicone containing 10 wt% silica particles exhibited an enhanced relative permittivity of 4.7 and a Young's modulus of 0.2 MPa. This allowed the elastomer to actuate up to 14.5% under a $29 \text{ V } \mu\text{m}^{-1}$ electric field. The low breakdown strength of the elastomer was attributed to the lack of strain stiffening as the material elongated,⁷⁶ making it electromechanically unstable.⁷³

The modification of PVMS with 95 mol% methyl thioglycolate, thioglycolic acid and 2-mercaptoethanol was reported by Sun *et al.* They found that the higher the level of grafting, the higher the permittivity and the softer the resulting silicone elastomer was. The lower Young's modulus was attributed to a combination of two competing factors. Firstly, the interactions from the grafted groups result in a greater cohesive energy density and increased the Young's modulus. However, simultaneously the grafting introduced steric hindrance and reduced the density of the elastomer and reduced chain

entanglement.^{57, 75} The reduction in Young's modulus was accompanied by increases in the $\tan \delta$ loss from the increase in conductivity of the dielectric elastomers. 2-mercaptoethanol modified PVMS had the greatest actuation performance of the three different modifications, and actuated 12.3%, failing under a 17 kV mm^{-1} field. Methyl thioglycolate modified PVMS exhibited the second greatest actuation performance of 7.8% strain and failed under a 21 kV mm^{-1} electric field. Finally, thioglycolic acid modified PVMS had the worst actuation performance of the three dielectric elastomers. It actuated only 6.8% and failed under a 20 kV mm^{-1} electric field. This was attributed to the hydrogen bonding formed between the thioglycolic acid groups which inhibit dipole orientation and mobility. For methyl thioglycolate, the larger size was attributed to hindering the dipole orientation and mobility, and thus smaller 2-mercaptoethanol modified PVMS was able to exhibit a higher actuation performance.⁷⁵

High permittivity has been achieved in PVMS modified by 100 mol% 2-(methylsulfonyl)-ethanethiol of 22.7 at 10^3 Hz . However, the polymer was synthesised *via* a six step reaction procedure, five to synthesise the polar group and one step to attach it to PVMS, but no mechanical or actuation properties were reported.⁷⁷ Finally, it was recently reported that silicone elastomers can be crosslinked without the need for solvent in low molecular weight and low viscosity formulations, increasing their viability for use in industry.⁷⁸

Styrenic based unsaturated elastomers

The vast majority of the literature focuses on the use of silicone based dielectric elastomers for DEA and DEG applications. However, some examples of styrenic based unsaturated elastomers containing vinyl groups exist and are modified using thiol-ene chemistry. Modifications for amine,^{79, 80} carboxylic acid⁷⁹⁻⁸¹ and ester^{80, 81} functionality in addition to other groups have been demonstrated previously.^{79, 81}

Methyl thioglycolate and thioglycolic acid have been used to modify SBS using photoinitiated thiol-ene chemistry to boost its electromechanical activity. The grafting of 81 mol% methyl thioglycolate to the butadiene backbone indicated a compatibilisation interaction between the butadiene block and the styrene block to increase phase mixing, see Figure 2.10. The relative permittivity was increased up to 6.4 and 12.2 at 40 mol% and 81 mol% grafting and the Young's modulus was low for

both, approximately 0.3 MPa. 81 mol% methyl thioglycolate modified SBS was able to actuate 3.3% under an electric field of 15.7 kV mm^{-1} , whilst 40 mol% methyl thioglycolate modified SBS was able to actuate 5.4% and failed under a 32.5 kV mm^{-1} electric field. Comparatively, pristine SBS actuated 0.8% and failed under a 65 kV mm^{-1} electric field. The difference in electromechanical behaviour between the two modified SBS elastomers was due to the localised current generated by the grafted polar group to the polymer backbone, increasing the conductivity of the elastomer and producing an inhomogeneous electric field.⁸² However, for thioglycolic acid modified SBS, only 1.75% actuation strain was achieved under an electric field of 35 kV mm^{-1} due to the increased interchain interactions from hydrogen bonding increasing the Young's modulus of the elastomer.⁸³

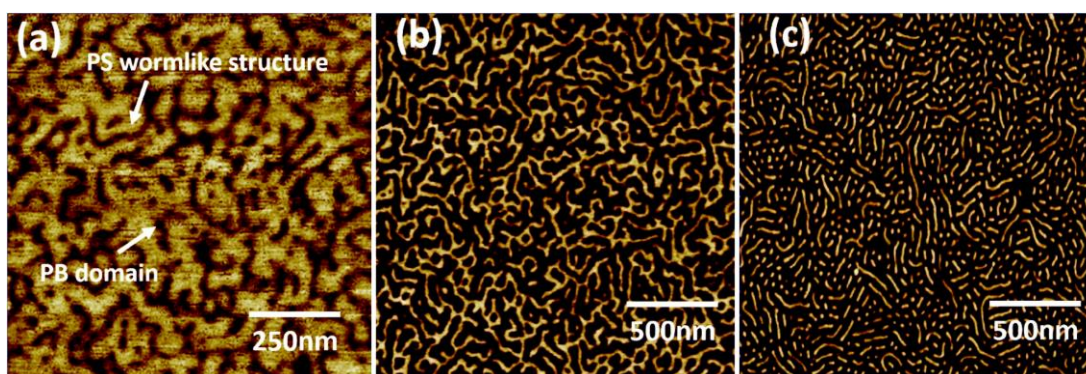


Figure 2.10 SEM imaging of (a) SBS, (b) 40 mol% methyl thioglycolate modified SBS and (c) 81 mol% methyl thioglycolate modified SBS. Reproduced from Sun *et al.*⁸²

An alternative block copolymer of styrene-(2-ethylhexyl acrylate)-styrene was used for the grafting of different sized alkyl groups. The purpose of this study was not to enhance the permittivity of the dielectric elastomer, but to decrease the Young's modulus through the grafting of different alkyl chain lengths to increase the actuation performance. In this example, the length and the branching of the large side chain increased the free volume in the polymer matrix and reduced polymer chain entanglement. Thus the Young's modulus decreased to 0.12 MPa for the largest alkyl groups, 10 times lower than for smaller side chains used. This enabled the polymer to actuate up to 25.2% and fail under an electric field of 35 kV mm^{-1} despite only having a relative permittivity of 3.7.⁴³

2.3.2 Liquid crystal elastomers (LCEs) for actuators

The inclusion of liquid crystals (mesogens) into an elastomer is an alternative method to develop an actuation device. By attaching the mesogen groups to a polymer backbone, they are able to behave as a soft elastomer and undergo actuation under an applied electric field.⁸⁴ Until recently, the synthesis of LCEs required complicated synthetic chemistry^{85, 86} however recent advances in the use of click chemistry reactions and 3D printing have simplified and allowed the facile scale up of LCE synthesis.⁸⁴ In this section, a brief overview of what makes LCEs exciting for actuation and energy harvesting applications will be discussed, and recent examples in the literature presented.

The alignment of mesogens are commonly in two classes of order, the Smectic phase and the Nematic phase, and their alignment is also affected by how they are incorporated into a polymer chain, see Figure 2.11.

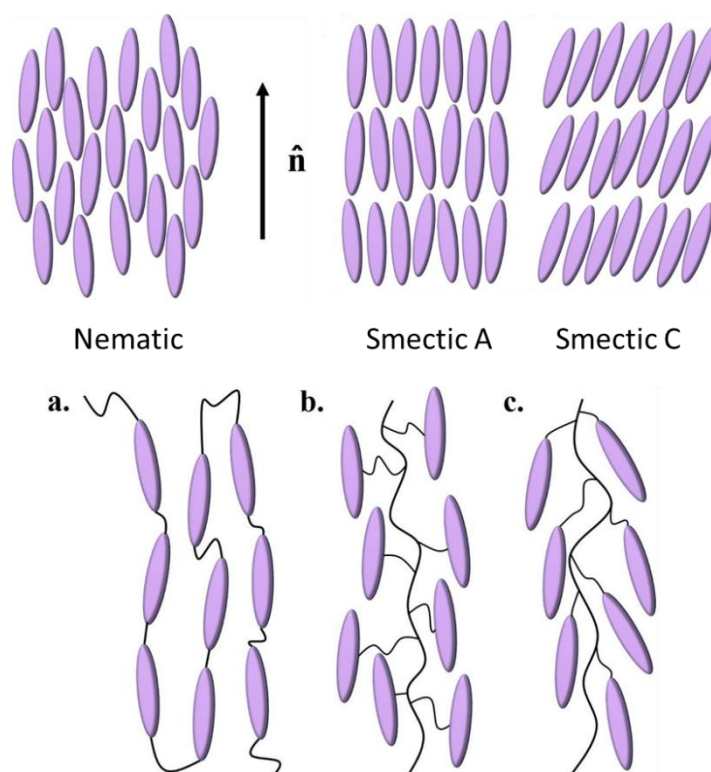


Figure 2.11 Mesogen arrangements in a LCE. The method of inclusion of the mesogen into the polymer backbone affects the crystal arrangement formed. Adapted from Ula *et al.*⁸⁴

The nematic phase is caused by long range orientational order of the mesogens, but short range positional order.^{87, 88} In comparison, the smectic phase is arranged into layers and have a rough long range orientational order. However, the layers have no positional order and thus the mesogens can change position within the layers easily.^{88, 89} A disordered isotropic phase and a high ordered phase also can exist for mesogens, however, these do not contribute to the actuation performance of an LCE.⁸⁹ Under the application of a stimulus such as thermal or electrical, the polar domains from the crystal groups rotate and align with the electric field. This rotation, such as from side chain groups, reorders the polymer chains and introduces an actuation strain. Removal of the electric field allows the crystal groups to randomise and the actuation strain disappears.^{47, 90} Various different synthetic routes for the synthesis of LCE exist,⁹¹⁻⁹⁵ and a summary of this is shown in Figure 2.12.

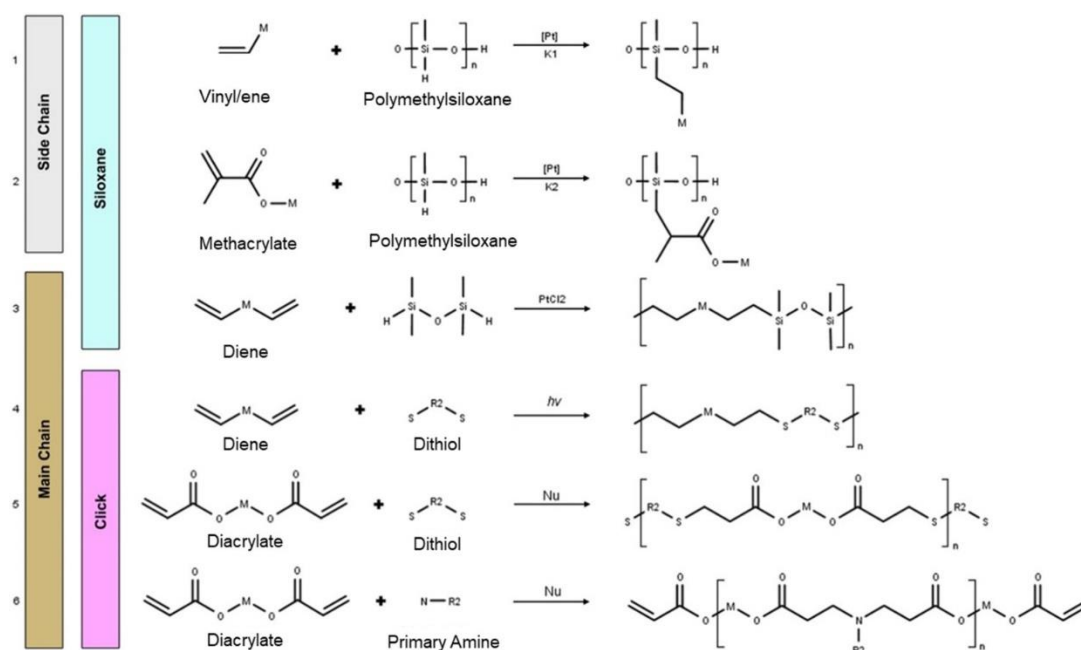


Figure 2.12 Summary of different reaction types to synthesise LCEs. Reproduced from Ula *et al.*⁸⁴

Multiple recent examples of LCE actuators are based on a thermoresponsive nature of the polymer.⁹⁶⁻¹⁰⁰ However, an example of a LCE based on a 1,5-pentanedithiol and 1,4-bis-[4-(6-acryloyloxy-hexyloxy)benzoyloxy]-2-methylbenzene was synthesised using a thiol-acrylate reaction and its mechanical response under an electric field was investigated. The elastomer was able to strain 5% under a 3 kV applied voltage, whilst

under a 0.27 N load. This load was 790 times greater than the weight of the LCE film in the device and overall the actuator actuated with a 20% efficiency.¹⁰¹

Alternatively, a PDMS elastomer was modified with side chain mesogen groups of disperse red 19 to act as a ‘push-pull’ azobenzene.¹⁰² Disperse red 19 is an azobenzene chromophore synthesised from N,N-diethanolaniline and the diazonium salt of 4-nitroaniline. It is a highly polar molecule with a dipole moment of 9 D.¹⁰³ The grafting of 7.1 wt% disperse red 19 to silicone allowed it to actuate up to 17% strain and it failed under an electric field of $70 \text{ V } \mu\text{m}^{-1}$. Comparatively, pristine silicone failed under an electric field of $65.7 \text{ V } \mu\text{m}^{-1}$ and actuated just 4%. The grafting of disperse red 19 increased the breakdown strength of the elastomer because the polar group increased the cohesive energy density of the silicone rubber. However, above a 7.1 wt% grafting, the electrical breakdown strength decreased again because the higher grafting level increased the probability of electron avalanche because of their highly polar nature.^{102, 104} Furthermore, the grafting of disperse red 19 enhanced the relative permittivity from 2.5 to 4.5 at 10^3 Hz , whilst maintaining the same Young’s modulus as the pristine silicone. At higher grafting levels of disperse red 19, the Young’s modulus also increased, inhibiting its actuation performance.

No examples currently exist in the literature for the use of LCEs in DEG devices.

2.3.3 Conducting group grafting of dielectric elastomers

The grafting of conducting groups to a polymer backbone introduces the opportunity to graft microcapacitors to boost the permittivity of a polymer matrix whilst maintaining a homogenous dispersion and a high processability. Primarily in the literature, the grafting of conducting groups involves either oligomeric or polymeric aniline – polyaniline. More information about oligomeric and polymeric aniline can be found in section 8.1.

Several examples have been reported in the literature for DEA and DEG applications. Oligomeric aniline doped with camphorsulfonic acid was grafted as endcaps onto polystyrene to enhance the relative permittivity. 10.9 wt% grafting as endcaps increased the relative permittivity of the elastomer up to 24 at 10^3 Hz , and maintained a low $\tan \delta$ loss. Furthermore, it was found that the polymer could store 12 times as much energy as could be stored in pristine polystyrene, attributed to its highly

polarisable nature.¹⁰⁵ This indicates its possible use in a DEG device, however, no further details were reported.

Polyaniline was grafted to maleic anhydride grafted SEBS through a ring opening reaction. It was found that 2.1 vol% of conductive PANI (where PANI was in the emeraldine salt oxidation state) was the percolation threshold for the dielectric elastomer and the elastomer became conducting. However, the actuation abilities of the modified elastomer were low, and only 2.8% actuation strain was observed under a $90 \text{ V } \mu\text{m}^{-1}$ electric field, although the electrical breakdown strength of the elastomer was higher at $120 \text{ V } \mu\text{m}^{-1}$.¹⁰⁶ Whilst no mechanical properties are reported, it is possible that the material has a high Young's modulus which inhibits its actuation abilities.

A final example for the grafting of conductive groups is based on 14.4 vol% conductive polyaniline grafted to a polyurethane *via* 23 vol% copper phthalocyanine rings. The copper phthalocyanine ring contains four copper ions in addition to carboxylic acid groups to covalently attach to the polyaniline chains and to the polyurethane matrix. Due to the rigidity of the copper phthalocyanine ring and polyaniline, the Young's modulus increased to 80 MPa, but the relative permittivity increased to over 200 at 10^3 Hz , and maintained a low dielectric loss of 0.3. Therefore, it was able to actuate over 6% under a $23 \text{ V } \mu\text{m}^{-1}$ electric field, and failed at $24 \text{ V } \mu\text{m}^{-1}$.¹⁰⁷ The actuation response of this modified polyurethane is unexpected and represents an example where the relative permittivity was increased sufficiently to overcome the large increase in Young's modulus, and not experience an ultra-low breakdown strength.

2.4 Conclusions

Overall, both extrinsic and intrinsic modification approaches have been explored to enhance the performance of dielectric elastomers in a DEA or DEG device. For extrinsic approaches, the addition of conducting and ceramic fillers have been explored extensively, but due to issues regarding their interfacial compatibility with the polymer matrix, and introduction of inhomogeneous internal electric fields, modification approaches such as the core-shell approach are utilised to prevent the elastomer from prematurely failing. An example of an electret DEG using a CNT filled PDMS was able to harvest up to 14.5V and $1.2 \times 10^{-4} \text{ J}$ per cycle under a 66% strain.

The intrinsic approach to the modification of dielectric elastomers has predominantly focussed on silicone-based elastomers, using PHMS and PVMS for hydrosilylation and thiol-ene reactions. This is partly due to the ease of commercial availability of silicone elastomer, and the tunability from tailoring the crosslinking degree of the elastomer. The grafting of polar groups enhances the dipole moment of the polymer chains to enhance the relative permittivity. However, it is important that the Young's modulus remains low and the electrical breakdown strength remains high to achieve a maximum actuation and energy harvesting performance. Only several examples thus far have focussed on styrenic-based elastomers or commodity rubbers.

Furthermore, liquid crystal groups have shown promise DEA and DEG applications through the formation of LCE, or by grafting mesogens as side chain groups. The liquid crystals reorganise upon application of an electric field and thus induces a strain. Until recently, the complicated synthesis of LCEs has held back their development, however by utilising click chemistry more examples are reported, albeit most examples reported focus on thermoresponsive actuation.

Finally, the grafting of conducting groups has been demonstrated, primarily through aniline based polymers. The grafting of a conducting group to the polymer backbone introduces microcapacitors, which can be charged to enhance the permittivity. Typically, conductive polymers introduce difficulties such as poor processability and this is attributed to why there are only a few works in this field.

2.5 References

1. C. Wan and C. R. Bowen, *J. Mater. Chem. A*, 2017, **5**, 3091-3128.
2. E. Baer and L. Zhu, *Macromolecules*, 2017, **50**, 2239-2256.
3. H. Luo, X. Zhou, C. Ellingford, Y. Zhang, S. Chen, K. Zhou, D. Zhang, C. R. Bowen and C. Wan, *Chem. Soc. Rev.*, 2019, **48**, 4424-4465.
4. Y. Huang, C. Ellingford, C. Bowen, T. McNally, D. Wu and C. Wan, *Int. Mater. Rev.*, 2019, 1-35.
5. Y. Li, F. Qin, D. Estevez, H. Wang and H.-X. Peng, *Sci. Rep.*, 2018, **8**, 14547.
6. F. Galantini, S. Bianchi, V. Castelvetro and G. Gallone, *Smart Mater. Struct.*, 2013, **22**, 055025.
7. J. E. Q. Quinsaat, M. Aledandru, F. A. Nüesch, H. Hofmann, A. Borgschulte and D. M. Opris, *J. Mater. Chem. A*, 2015, **3**, 14675-14685.
8. J. E. Q. Quinsaat, F. A. Nüesch, H. Hofmann and D. M. Opris, *RSC Adv.*, 2013, **3**, 6964-6971.

9. U. Tayfun, Y. Kanbur, U. Abacı, H. Y. Güney and E. Bayramlı, *J. Compos. Mater.*, 2017, **51**, 1987-1996.
10. H. Li, H. Liu, J. Li, D. Wei, Y. Wang and B. Song, *Sci. Eng. Compos. Mater.*, 2015, **22**, 215.
11. R. R. Kohlmeyer, A. Javadi, B. Pradhan, S. Pilla, K. Setyowati, J. Chen and S. Gong, *J. Phys. Chem. C*, 2009, **113**, 17626-17629.
12. N. George, B. Venugopal, H. John, A. Mathiazhagan and R. Joseph, *Polymer*, 2019, **161**, 170-180.
13. K. Ke, M. McMaster, W. Christopherson, K. D. Singer and I. Manas-Zloczower, *Composites, Part B*, 2019, **166**, 673-680.
14. Y. J. Lee, P. Caspari, D. M. Opris, F. A. Nüesch, S. Ham, J.-H. Kim, S.-R. Kim, B.-K. Ju and W. K. Choi, *J. Mater. Chem. C*, 2019, **7**, 3535-3542.
15. A. J. Marsden, D. G. Papageorgiou, C. Vallés, A. Liscio, V. Palermo, M. A. Bissett, R. J. Young and I. A. Kinloch, *2D Mater.*, 2018, **5**, 032003.
16. X. Du, I. Skachko, A. Barker and E. Y. Andrei, *Nat. Nanotechnol.*, 2008, **3**, 491-495.
17. V. B. Mohan, R. Brown, K. Jayaraman and D. Bhattacharyya, *Mater. Sci. Eng., B*, 2015, **193**, 49-60.
18. S. Stankovich, D. A. Dikin, R. D. Piner, K. A. Kohlhaas, A. Kleinhammes, Y. Jia, Y. Wu, S. T. Nguyen and R. S. Ruoff, *Carbon*, 2007, **45**, 1558-1565.
19. C. Mattevi, G. Eda, S. Agnoli, S. Miller, K. A. Mkhoyan, O. Celik, D. Mastrogiovanni, G. Granozzi, E. Garfunkel and M. Chhowalla, *Adv. Funct. Mater.*, 2009, **19**, 2577-2583.
20. T. Chen and B. Liu, *Mater. Lett.*, 2018, **211**, 69-73.
21. N. Ning, Q. Ma, S. Liu, M. Tian, L. Zhang and T. Nishi, *ACS Appl. Mater. Interfaces*, 2015, **7**, 10755-10762.
22. T. Chen, J. Qiu, K. Zhu and J. Li, *Mater. Des.*, 2016, **90**, 1069-1076.
23. M. Sadroddini and M. Razzaghi-Kashani, *Smart Mater. Struct.*, 2019, **29**, 015028.
24. P. Zhu, L. Weng, X. Zhang, X. Wang, L. Guan and L. Liu, *J. Mater. Sci.*, 2020, **55**, 7665-7679.
25. D. Yang, Y. Ni, X. Kong, H. Xue, W. Guo and L. Zhang, *Appl. Surf. Sci.*, 2019, **495**, 143638.
26. L. Liu, W. Zhang, N. Ning and L. Zhang, *Chem. Eng. J.*, 2019, **375**, 121993.
27. P. Kim, N. M. Doss, J. P. Tillotson, P. J. Hotchkiss, M.-J. Pan, S. R. Marder, J. Li, J. P. Calame and J. W. Perry, *ACS Nano*, 2009, **3**, 2581-2592.
28. S. Nayak and D. Khastgir, *J. Appl. Polym. Sci.*, 2019, **136**, 47307.
29. S. Saha, A. K. Bhowmick, A. Kumar, K. Patra, P.-J. Cottinet and K. Thetraphi, *Ind. Eng. Chem. Res.*, 2020, **59**, 3413-3424.
30. D. Yang, M. Ruan, S. Huang, Y. Wu, S. Li, H. Wang, X. Ao, Y. Liang, W. Guo and L. Zhang, *RSC Adv.*, 2016, **6**, 90172-90183.
31. C. Guo and M. Fuji, *Adv. Powder Technol.*, 2016, **27**, 1162-1172.
32. L. Zhang, F. Song, X. Lin and D. Wang, *Mater. Chem. Phys.*, 2020, **241**, 122373.
33. G. Yin, Y. Yang, F. Song, C. Renard, Z.-M. Dang, C.-Y. Shi and D. Wang, *ACS Appl. Mater. Interfaces*, 2017, **9**, 5237-5243.
34. D. Yang, Y. Xu, M. Ruan, Z. Xiao, W. Guo, H. Wang and L. Zhang, *AIP Adv.*, 2019, **9**, 025035.
35. Y. Yang, Z.-S. Gao, M. Yang, M.-S. Zheng, D.-R. Wang, J.-W. Zha, Y.-Q. Wen and Z.-M. Dang, *Nano Energy*, 2019, **59**, 363-371.

36. D. Yang, F. Ge, M. Tian, N. Ning, L. Zhang, C. Zhao, K. Ito, T. Nishi, H. Wang and Y. Luan, *J. Mater. Chem. A*, 2015, **3**, 9468-9479.
37. K. Ito, *Curr. Opin. Solid State Mater. Sci.*, 2010, **14**, 28-34.
38. Y. Noda, Y. Hayashi and K. Ito, *J. Appl. Polym. Sci.*, 2014, **131**.
39. C. C. Ku and R. Liepins, *Electrical Properties of Polymers: Chemical Principles*, Hanser, 1987.
40. S. Wu, M. Shao, Q. Burlingame, X. Chen, M. Lin, K. Xiao and Q. M. Zhang, *Appl. Phys. Lett.*, 2013, **102**, 013301.
41. V. K. Thakur, E. J. Tan, M.-F. Lin and P. S. Lee, *Polym. Chem.*, 2011, **2**, 2000-2009.
42. N. M. Putintsev and D. N. Putintsev, *Russ. J. Phys. Chem.*, 2006, **80**, 1949-1952.
43. J. Mao, T. Li and Y. Luo, *J. Mater. Chem. C*, 2017, **5**, 6834-6841.
44. D. M. Opris, *Adv. Mater.*, 2018, **30**, 1703678.
45. J. Biggs, K. Danielmeier, J. Hitzbleck, J. Krause, T. Kridl, S. Nowak, E. Orselli, X. Quan, D. Schapeler, W. Sutherland and J. Wagner, *Angew. Chem. Int. Ed.*, 2013, **52**, 9409-9421.
46. S. J. Dunki, M. Tress, F. Kremer, S. Y. Ko, F. A. Nuesch, C.-D. Varganici, C. Racles and D. M. Opris, *RSC Adv.*, 2015, **5**, 50054-50062.
47. C. Ellingford, C. Bowen, T. McNally and C. Wan, *Macromol. Rapid Commun.*, 2018, **39**, 1800340.
48. J. E. Mark, *Polymer Data Handbook (2nd Edition)*, Oxford University Press, 2009.
49. S. Risse, B. Kussmaul, H. Kruger and G. Kofod, *RSC Adv.*, 2012, **2**, 9029-9035.
50. B. Marciniak, J. Guliński, L. Kopylova, H. Maciejewski, M. Grundwald-Wyspiańska and M. Lewandowski, *Appl. Organomet. Chem.*, 1997, **11**, 843-849.
51. Z. Zhu, A. G. Einset, C.-Y. Yang, W.-X. Chen and G. E. Wnek, *Macromolecules*, 1994, **27**, 4076-4079.
52. J. G. Matisons and A. Provasas, *Macromolecules*, 1994, **27**, 3397-3405.
53. X. Coqueret, A. Lablache-Comber and C. Loucheux, *Eur. Polym. J.*, 1988, **24**, 1137-1143.
54. X. Coqueret and G. Wegner, *Organometallics*, 1991, **10**, 3139-3145.
55. L. C. Chien and L. G. Cada, *Macromolecules*, 1994, **27**, 3721-3726.
56. M. Dascalu, S. J. Dunki, J.-E. Q. Quinsaat, Y. S. Ko and D. M. Opris, *RSC Adv.*, 2015, **5**, 104516-104523.
57. F. B. Madsen, L. Yu, A. E. Daugaard, S. Hvilsted and A. L. Skov, *RSC Adv.*, 2015, **5**, 10254-10259.
58. C. Racles, V. Cozan, A. Bele and M. Dascalu, *Des. Monomers Polym.*, 2016, **19**, 496-507.
59. C. Racles, M. Alexandru, A. Bele, V. E. Musteata, M. Cazacu and D. M. Opris, *RSC Adv.*, 2014, **4**, 37620-37628.
60. C. Racles, C. Maria, F. Beatrice and M. O. Dorina, *Smart Mater. Struct.*, 2013, **22**, 104004.
61. C. Racles, A. Bele, M. Dascalu, V. E. Musteata, C. D. Varganici, D. Ionita, S. Vlad, M. Cazacu, S. J. Dunki and D. M. Opris, *RSC Adv.*, 2015, **5**, 58428-58438.
62. S. Risse, B. Kussmaul, H. Krüger and G. Kofod, *Adv. Funct. Mater.*, 2012, **22**, 3958-3962.

63. M. Kolloosche and G. Kofod, *Appl. Phys. Lett.*, 2010, **96**, 071904.
64. K. H. Stark and C. G. Garton, *Nature*, 1955, **176**, 1225-1226.
65. P. Caspari, S. J. Düнки, F. A. Nüesch and D. M. Opris, *J. Mater. Chem. C*, 2018, **6**, 2043-2053.
66. C. Racles, M. Ignat, A. Bele, M. Dascalu, D. Lipcinski and M. Cazacu, *Smart Mater. Struct.*, 2016, **25**, 085024.
67. P. J. Collings and M. Hird, *Introduction to Liquid Crystals: Chemistry and Physics*, CRC Press, 1997.
68. F. B. Madsen, A. E. Daugaard, S. Hvilsted and A. L. Skov, *Macromol. Rapid Commun.*, 2016, **37**, 378-413.
69. L. R. Grace, *Compos. Struct.*, 2015, **128**, 305-312.
70. A. Bele, M. Cazacu, C. Racles, G. Stiubianu, D. Ovezza and M. Ignat, *Adv. Eng. Mater.*, 2015, **17**, 1302-1312.
71. S. J. Dunki, F. A. Nüesch and D. M. Opris, *J. Mater. Chem. C*, 2016, **4**, 10545-10553.
72. Y. Sheima, P. Caspari and D. M. Opris, *Macromol. Rapid Commun.*, 2019, **40**, 1900205.
73. E. Perju, Y. S. Ko, S. J. Düнки and D. M. Opris, *Mater. Des.*, 2020, **186**, 108319.
74. G.-O. Turcan-Trofin, M. Asandulesa, M. Balan-Porcarasu, C.-D. Varganici, V. Tiron, C. Racles and M. Cazacu, *J. Mol. Liq.*, 2019, **282**, 187-196.
75. H. Sun, X. Liu, H. Yan, Z. Feng, B. Yu, N. Ning, M. Tian and L. Zhang, *Polymer*, 2019, **165**, 1-10.
76. J. Huang, T. Li, C. C. Foo, J. Zhu, D. R. Clarke and Z. Suo, *Appl. Phys. Lett.*, 2012, **100**, 041911.
77. S. J. Dunki, E. Cuervo-Reyes and D. M. Opris, *Polym. Chem.*, 2017, **8**, 715-724.
78. P. Caspari, F. A. Nüesch and D. M. Opris, *J. Mater. Chem. C*, 2019, **7**, 12139-12150.
79. Z. Hordyjewicz-Baran, L. You, B. Smarsly, R. Sigel and H. Schlaad, *Macromolecules*, 2007, **40**, 3901-3903.
80. J. Justynska, Z. Hordyjewicz and H. Schlaad, *Polymer*, 2005, **46**, 12057-12064.
81. N. ten Brummelhuis, C. Diehl and H. Schlaad, *Macromolecules*, 2008, **41**, 9946-9947.
82. H. Sun, C. Jiang, N. Ning, L. Zhang, M. Tian and S. Yuan, *Polym. Chem.*, 2016, **7**, 4072-4080.
83. M. Tian, H. Yan, H. Sun, L. Zhang and N. Ning, *RSC Adv.*, 2016, **6**, 96190-96195.
84. S. W. Ula, N. A. Traugutt, R. H. Volpe, R. R. Patel, K. Yu and C. M. Yakacki, *Liq. Cryst. Rev.*, 2018, **6**, 78-107.
85. C. Zhang, D. Wang, J. He, M. Liu, G.-H. Hu and Z.-M. Dang, *Polym. Chem.*, 2014, **5**, 2513-2520.
86. C. Zhang, D. Wang, J. He, T. Liang, G.-H. Hu and Z.-M. Dang, *Polym. Adv. Technol.*, 2014, **25**, 920-926.
87. P. G. de Gennes and J. Prost, *The Physics of Liquid Crystals*, Clarendon Press, 1995.
88. F. Brömmel, D. Kramer and H. Finkelmann, in *Liquid Crystal Elastomers: Materials and Applications*, ed. W. H. de Jeu, Springer Berlin Heidelberg, Berlin, Heidelberg, 2012, vol. 250, pp. 1-48.

89. A. M. Menzel, *Phys. Rep.*, 2015, **554**, 1-45.
90. J. Su, J. S. Harrison and T. S. Clair, IEEE International Symposium on Applications of Ferroelectrics, 2000, **2**, 811-814.
91. C. Ohm, M. Brehmer and R. Zentel, *Adv. Mater.*, 2010, **22**, 3366-3387.
92. H. Finkelmann and G. Rehage, *Makromol. Chem., Rapid Commun*, 1980, **1**, 733-740.
93. H. Jiang, C. Li and X. Huang, *Nanoscale*, 2013, **5**, 5225-5240.
94. P. Beyer, L. Braun and R. Zentel, *Macromol. Chem. Phys.*, 2007, **208**, 2439-2448.
95. J. Lub, D. J. Broer and N. van den Broek, *Liebigs Ann.*, 1997, 2281-2288.
96. M. O. Saed, R. H. Volpe, N. A. Traugutt, R. Visvanathan, N. A. Clark and C. M. Yakacki, *Soft Matter*, 2017, **13**, 7537-7547.
97. L. Yu, R. Peng, G. Rivers, C. Zhang, P. Si and B. Zhao, *J. Mater. Chem. A*, 2020, **8**, 3390-3396.
98. M. O. Saed, C. P. Ambulo, H. Kim, R. De, V. Raval, K. Searles, D. A. Siddiqui, J. M. O. Cue, M. C. Stefan, M. R. Shankar and T. H. Ware, *Adv. Funct. Mater.*, 2019, **29**, 1806412.
99. T. Guin, M. J. Settle, B. A. Kowalski, A. D. Auguste, R. V. Beblo, G. W. Reich and T. J. White, *Nat. Commun.*, 2018, **9**, 2531.
100. Q. He, Z. Wang, Y. Wang, A. Minori, M. T. Tolley and S. Cai, *Sci. Adv.*, 2019, **5**, eaax5746.
101. Z. S. Davidson, H. Shahsavan, A. Aghakhani, Y. Guo, L. Hines, Y. Xia, S. Yang and M. Sitti, *Sci. Adv.*, 2019, **5**, eaay0855.
102. L. Zhang, D. Wang, P. Hu, J.-W. Zha, F. You, S.-T. Li and Z.-M. Dang, *J. Mater. Chem. C*, 2015, **3**, 4883-4889.
103. J. M. Simmons, I. In, V. E. Campbell, T. J. Mark, F. Léonard, P. Gopalan and M. A. Eriksson, *Phys. Rev. Lett.*, 2007, **98**, 086802.
104. S. Li, G. Yin, G. Chen, J. Li, S. Bai, L. Zhong, Y. Zhang and Q. Lei, *IEEE Trans. Dielectr. Electr. Insul.*, 2010, **17**, 1523-1535.
105. C. G. Hardy, M. S. Islam, D. Gonzalez-Delozier, J. E. Morgan, B. Cash, B. C. Benicewicz, H. J. Ploehn and C. Tang, *Chem. Mater.*, 2013, **25**, 799-807.
106. H. Stoyanov, M. Kolloosche, D. N. McCarthy and G. Kofod, *J. Mater. Chem.*, 2010, **20**, 7558-7564.
107. C. Huang and Q. M. Zhang, *Adv. Mater.*, 2005, **17**, 1153-1158.

Chapter 3

Materials and Methods

3.1 Materials

Styrene-butadiene-styrene (SBS), Vector 8508A, a linear triblock copolymer was purchased from Dexco in pellet form. It has a 29 wt% styrenic content, determined experimentally, a diblock content of less than 1 wt%, density $0.41 \text{ g}\cdot\text{cm}^{-3}$ (ASTM D1895), a melt flow rate of $12 \text{ g}\cdot 10 \text{ min}^{-1}$ (ASTM D1238) and processing temperature $180 \text{ }^{\circ}\text{C} - 225 \text{ }^{\circ}\text{C}$.

Polyvinylidene fluoride (PVDF), Kynar 740, was purchased from Arkema in pellet form. It had a melt flow rate of $1.5 - 3.0 \text{ g}\cdot 10 \text{ min}^{-1}$ (ASTM D1238), a density of $0.96 \text{ g}\cdot\text{cm}^{-3}$ and processing temperature of $200 \text{ }^{\circ}\text{C} - 240 \text{ }^{\circ}\text{C}$.

Ethylene vinyl acetate (EVA), ELVAX 3190, was purchased from DuPont in pellet form and had a 25 wt% vinyl acetate content. It had a density of $0.95 \text{ g}\cdot\text{cm}^{-3}$ (ASTM D792), melt flow rate of $2 \text{ g}\cdot 10 \text{ min}^{-1}$ (ASTM D1238), a melting point of $77 \text{ }^{\circ}\text{C}$ (ASTM D3418).

Non functionalised multi-walled carbon nanotubes (MWCNTs), NC7000, produced by catalytic carbon vapour deposition were purchased from Nanocyl S.A. The MWCNTs had a purity of $> 90\%$, a length of $1.5 \text{ }\mu\text{m}$ and a density of $1.85 \text{ g}\cdot\text{cm}^{-3}$. The MWCNTs were used as received.

Styrene-butadiene rubber (SBR), Buna SBR 2300, was purchased from Arlanxeo. It had a 27.1 wt% styrene content and a density of $0.95 \text{ g}\cdot\text{cm}^{-3}$.

Polybutadiene (PB), Buna CB 24, was purchased from Arlanxeo. It had a 96% cis 1,4 butadiene content and a density of $0.91 \text{ g}\cdot\text{cm}^{-3}$.

General reagents methyl thioglycolate (MG, 95%), 2,2-dimethoxy-2-phenylacetophenone (DMPA, 99%), thioglycolic acid (TG, 99%), methyl-3-mercaptopropionate (M3M, 98%), *N*-phenyl-*p*-phenylenediamine (98%), ammonium persulfate (APS, 98%), formic acid (95%), hydrogen peroxide (30% w/w) and trifluoroacetic acid (99%) were purchased from Sigma-Aldrich. Ammonium

hydroxide (30%), was purchased from Acros Organics. Hydrochloric acid (37%) was purchased from Fisher Scientific. Conducting carbon grease was purchased from MG Chemicals for a complaint electrode in the DEA and DEG devices. All chemicals were used as received.

Solvents hexane (HPLC grade, > 95%), dichloromethane (DCM, HPLC grade, 99.8%) diiodomethane (99%), Toluene-d8 (99.5%) and d-chloroform (99.8%) were purchased from Sigma-Aldrich. Tetrahydrofuran (THF, GPR Rectapur, > 99%) was purchased from VWR. Methanol (Analytical grade, 99%) and acetone (Extra Pure, 99%) were purchased from Fisher Scientific. Distilled H₂O was produced using in-house distillation equipment. All solvents were used as received.

3.2 Synthesis procedures

3.2.1 UV light procedure

An OmniCure Series 2000 200 W UV lamp with a 365 nm wavelength light filter was used as a UV light source. The light source was supplied into a walled container and placed approximately 15 cm above the reaction solution. The intensity of UV light used was 20% (40 W output) for small scale (typically 1 g starting polymer unless otherwise stated) reactions and 25% (50 W output) for large scale (typically 10 g starting polymer unless otherwise stated) reactions, unless the UV light intensity was otherwise stated.

3.2.2 Synthesis of methyl thioglycolate modified SBS (MG-SBS)

Following a typical large scale reaction, 10 g SBS was dissolved in 90 g THF. Once fully dissolved, 0.2 g DMPA and 46.9 ml (4× molar excess of thiol compared to the butadiene block of SBS) was mixed into the solution and the solution irradiated with UV light for 20 minutes. Afterwards, the solution was concentrated and precipitated in hexane. The precipitated polymer was redissolved in THF and the process was repeated a further two times. After the third precipitation, wet MG-SBS was dried in a vacuum oven for three days at 40 °C. The mass of the resulting polymer was 21.3 g and had a grafting ratio of 97.2 mol%. ¹H NMR (400 MHz, CDCl₃): δ = 7.06 (br, 3 H, H_{benzene}), 6.52 (br, 2 H, H_{benzene}), 5.40 (br, 4 H, -HC=CH- and HC=CH₂), 3.73 (s, 3 H, COOCH₃), 3.23 (s, 2 H, OOC-CH₂-S), 2.75 (br, 1 H, (CH₂)₂CHS), 2.64 (br, 2 H, H₂CCH₂S), 1.74 (br, 2 H, H₂C-CH₂-CH), 1.55 (br, 6 H, (-H₂C)₂CH₂), 1.43 (br, 2 H, -

HCCH₂CH₂), 1.26 (br, 1 H, (H₂C)₃CH) ppm. FTIR (cm⁻¹): 2927, 1729, 1435, 1272, 1128, 1007, 757.

For the small scale optimisation reactions for the synthesis of MG-SBS in section 4.2, the thiol content was varied between 2× (2.35 ml), 3× (3.52 ml), 4× (4.69 ml) and 5× (5.68 ml) excess methyl thioglycolate. The UV exposure time was ranged from 5 to 30 minutes whilst the thiol excess was maintained at 3×.

For synthesis of MG-SBS (65.1%) and MG-SBS (52.1%) the reaction followed the same procedure as for MG-SBS, but the UV exposure time was decreased to 10 minutes and 5 minutes respectively.

MG-SBS (65.1%): 16.8 g final mass. ¹H NMR (400 MHz, CDCl₃): δ = 7.06 (br, 3 H, H_{benzene}), 6.52 (br, 2 H, H_{benzene}), 5.40 (br, 4 H, -HC=CH- and HC=CH₂), 3.73 (S, 3 H, COOCH₃), 3.22 (S, 2 H, OOC-CH₂-S), 2.74 (br, 1 H, (CH₂)₂CHS), 2.63 (br, 2 H, H₂CCH₂S), 2.11 (br, 1 H, (-H₂C)₂CHCH-), 2.03 and 1.99 (br, 3 H, (-H₂C)₂CHCH_{benzene} and (-CH₂)₂CH₂CH-), 1.73 (br, 2 H, H₂C-CH₂-CH), 1.55 (br, 6 H, (-H₂C)₂CH₂), 1.43 (br, 2 H, -HCCH₂CH₂), 1.26 (br, 1 H, (H₂C)₃CH) ppm. FTIR (cm⁻¹): 2924, 1730, 1434, 1270, 1129, 1006, 757.

MG-SBS (52.1%): 13.0 g final mass. ¹H NMR (400 MHz, CDCl₃): δ = 7.06 (br, 3 H, H_{benzene}), 6.53 (br, 2 H, H_{benzene}), 5.41 (br, 4 H, -HC=CH- and HC=CH₂), 3.73 (S, 3 H, COOCH₃), 3.21 (S, 2 H, OOC-CH₂-S), 2.74 (br, 1 H, (CH₂)₂CHS), 2.63 (br, 2 H, H₂CCH₂S), 2.10 (br, 1 H, (-H₂C)₂CHCH-), 2.03 (br, 3 H, (-H₂C)₂CHCH_{benzene} or (-CH₂)₂CH₂CH-), 1.99 (br, 3 H, (-H₂C)₂CHCH_{benzene} or (-CH₂)₂CH₂CH-), 1.73 (br, 2 H, H₂C-CH₂-CH), 1.55 (br, 9 H, (-H₂C)₂CH₂ and -HCCH₂CH₂ and (H₂C)₃CH) ppm. FTIR (cm⁻¹): 2923, 1730, 1434, 1271, 1129, 1006, 967, 757.

3.2.3 Synthesis of methyl-3-mercaptopropionate modified SBS (M3M-SBS)

Following a typical large scale reaction, 10 g SBS was dissolved in 90 g THF. Once fully dissolved, 0.2 g DMPA and 145.3 ml (10× molar excess of thiol relative to the butadiene block of SBS) of methyl-3-mercaptopropionate was mixed into the solution. The solution was irradiated with UV light for 20 minutes. Afterwards, the solution was concentrated and precipitated in hexane. The precipitated polymer was redissolved in THF and the process was repeated a further two times. After the third precipitation, wet M3M-SBS was dried in a vacuum oven for three days at 40 °C. The mass of the resulting polymer was 23.7 g and had a grafting ratio of 95.2 mol%. ¹H

NMR (400 MHz, CDCl₃): δ = 7.08 (br, 3 H, H_{benzene}), 6.54 (br, 2 H, H_{benzene}), 3.72 (s, 3 H, COOCH₃), 2.78 (t, 2 H, SCH₂CH₂, J = 7 Hz), 2.61 (t, 2 H, CH₂CH₂COO, J = 7 Hz) and (br, 1 H, (CH₂)₂CHS) and (br, 2 H, H₂CCH₂S), 1.75 (br, 2 H, H₂C-CH₂-CH), 1.57 (br, 6 H, (-H₂C)₂CH₂), 1.45 (br, 2 H, -HCCH₂CH₂), 1.28 (br, 1 H, (H₂C)₃CH) ppm. FTIR (cm⁻¹): 2928, 1733, 1435, 1243, 1169, 1018, 979, 758.

3.2.4 Synthesis of methyl thioglycolate/thioglycolic acid modified SBS (MG/TG-SBS)

Following a typical large scale reaction, 10 g SBS was dissolved in 90 g THF. Once fully dissolved, 0.2 g DMPA and the thiol ratio between methyl thioglycolate/thioglycolic acid was adjusted depending on the final product ratio. For the ratio of 95/5, 90/10 and 80/20 the thiol added to the reaction was 44.6 ml/1.8 ml, 42.3 ml/3.7 ml and 37.5 ml/7.3 ml, respectively. This represented overall a 4× molar excess of thiol with respect to the butadiene block of SBS. The solution was irradiated with UV light for 20 minutes. Afterwards, the solution was concentrated and precipitated in hexane. The precipitated polymer was redissolved in THF and the process was repeated a further two times. After the third precipitation, wet MG/TG-SBS was dried in a vacuum oven for three days at 40 °C. The mass of the resulting polymer was 20.4 g, 21.5 g and 22.0 g for 95/5, 90/10 and 80/20 methyl thioglycolate/thioglycolic acid ratios respectively. Overall, a total grafting ratio of 97.5%, 97.8% and 93.4% was observed for 95/5, 90/10 and 80/20 methyl thioglycolate/thioglycolic acid grafting. This was then split into 95.3%/4.7%, 92.1%/7.9% and 84.1%/15.9% between the two different thiol groups respectively. ¹H NMR (400 MHz, CDCl₃): δ = 7.09 (br, 3 H, H_{benzene}), 6.55 (br, 2 H, H_{benzene}), 3.76 (s, 3 H, COOCH₃), 3.25 (s, 2 H, OOC-CH₂-S), 2.77 (br, 1 H, (CH₂)₂CHS), 2.66 (br, 2 H, H₂CCH₂S), 1.76 (br, 2 H, H₂C-CH₂-CH), 1.57 (br, 6 H, (-H₂C)₂CH₂), 1.45 (br, 2 H, -HCCH₂CH₂), 1.28 (br, 1 H, (H₂C)₃CH) ppm. FT-IR (cm⁻¹): 2929, 1728, 1435, 1273, 1129, 1007, 757.

3.2.5 Fabrication of SBS/PVDF/EVA blends and composites

SBS/PVDF and SBS/PVDF/EVA in a 50/50 wt% ratio and a 50/50/20 wt% ratio respectively, were melt compounded in a HAAKE Rheomix OS Lab Mixer under the conditions of 190 °C at 60 rpm for 10 minutes. The weight fraction of MWCNTs, between 0.3 – 3 wt%, was added to the composite based on the overall total weight of SBS/PVDF/EVA 50/50/20. These composites were denoted as

SBS/PVDF/EVA/MWCNT 50/50/20/X where X was the weight fraction of MWCNTs. All samples were compression moulded using a Rondol manual hot press at 190 °C under 10 kN.

3.2.6 Fabrication of SBS/PVDF and MG-SBS/PVDF blends and composites

SBS/PVDF and MG-SBS/PVDF polymer blends were fabricated in ratios of 30/70 wt% to 70/30 wt% by melt compounding using a HAAKE Minilab II twin screw extruder at 225 °C and 50 rpm screw speed. MWCNTs were incorporated into the 50/50 and 70/30 wt% blends at a 1 wt% loading. All blends and composites were injection moulded into a HAAKE Minijet Pro injection moulder with a cylinder temperature of 225 °C and mould temperature of 70 °C. Injection pressure used was 400 bar for 10 seconds and a post pressure of 300 bar was used for 15 seconds.

3.2.7 Synthesis of methyl thioglycolate modified styrene-butadiene rubber (MG-SBR)

Following a typical large scale reaction, 10 g SBR was dissolved in 90 g THF. Once fully dissolved, 1 g DMPA and 61.6 ml (5× molar excess of thiol compared to the butadiene region of SBR) was mixed into the solution. The solution was irradiated with UV light for 3 hrs. Afterwards, the solution was concentrated and precipitated in hexane. The precipitated polymer was redissolved in THF and the process was repeated a further two times. After the third precipitation, wet MG-SBR was dried in a vacuum oven for three days at 40 °C. The mass of the resulting polymer was 22.7 g and had a grafting ratio of 98.1 mol%. ¹H NMR (400 MHz, CDCl₃): δ = 7.28 (br, 2 H, H_{benzene}), 7.13 (br, 3 H, H_{benzene}), 3.74 (s, 3 H, COOCH₃), 3.23 (s, 2 H, OOC-CH₂-S), 2.71 – 1.29 (polymer backbone) ppm. FTIR (cm⁻¹): 2928, 1729, 1452, 1272, 1129, 1008, 765.

3.2.8 Synthesis of methyl thioglycolate/thioglycolic acid modified styrene-butadiene rubber (MG/TG-SBR)

Following a typical large scale reaction, 10 g SBR was dissolved in 90 g THF. Once fully dissolved, 1 g DMPA, 49.3 ml methyl thioglycolate and 9.6 ml thioglycolic acid (total thiol content was 5× molar excess of thiol compared to the butadiene region of SBR) was mixed into the solution. The solution was irradiated with UV light for 3 hrs. Afterwards, the solution was concentrated and precipitated in hexane. The precipitated polymer was redissolved in THF and the process was repeated a further two times. After the third precipitation, wet MG/TG-SBR was dried in a vacuum oven for three

days at 40 °C. The mass of the resulting polymer was 23.4 g and had a grafting ratio of 97.1 mol%. Grafted methyl thioglycolate/thioglycolic acid was 90.5% methyl thioglycolate, 9.5% thioglycolic acid. ^1H NMR (400 MHz, CDCl_3): $\delta = 7.96$ (s, 1 H, COOH), 7.20 (br, 2 H, $\text{H}_{\text{benzene}}$), 7.07 (br, 3 H, $\text{H}_{\text{benzene}}$), 3.67 (s, 3 H, COOCH_3), 3.16 (s, 2 H, $\text{OOC-CH}_2\text{-S}$), 2.90 – 1.29 (polymer backbone) ppm. FTIR (cm^{-1}): 2928, 1729, 1452, 1275, 1131, 1008, 765.

3.2.9 Synthesis of methyl thioglycolate modified polybutadiene (MG-PB)

Following a typical large scale reaction, 10 g PB was dissolved in 210 g THF. Once fully dissolved, 0.4 g DMPA, 99.2 ml methyl thioglycolate (6 \times molar excess of thiol compared to the butadiene region of PB) was mixed into the solution. The solution was irradiated with UV light for 25 minutes. Afterwards, the solution was concentrated and precipitated in hexane. The precipitated polymer was redissolved in THF and the process was repeated a further two times. After the third precipitation, wet MG-PB was dried in a vacuum oven for three days at 40 °C. The mass of the resulting polymer was 19.4 g and had a grafting ratio of 99.9 mol%. ^1H NMR (400 MHz, CDCl_3): $\delta = 3.73$ (s, 3 H, COOCH_3), 3.22 (s, 2 H, $\text{OOC-CH}_2\text{-S}$), 2.75 (br, 1 H, $(\text{CH}_2)_2\text{CHS}$), 2.08 (br, 2 H, $\text{H}_2\text{CCH}_2\text{S}$), 1.74 (br, 2 H, $\text{H}_2\text{C-CH}_2\text{-CH}$), 1.55 (br, 6 H, $(-\text{H}_2\text{C})_2\text{CH}_2$), 1.42 (br, 2 H, $-\text{HCCCH}_2\text{CH}_2$), 1.26 (br, 1 H, $(\text{H}_2\text{C})_3\text{CH}$) ppm. FTIR (cm^{-1}): 2928, 1729, 1435, 1272, 1128, 1008, 627.

3.2.10 Synthesis of methyl thioglycolate/thioglycolic acid modified polybutadiene (MG/TG-PB)

Following a typical large scale reaction, 10 g PB was dissolved in 210 g THF. Once fully dissolved, 0.4 g DMPA, 79.3 ml methyl thioglycolate and 15.4 ml thioglycolic acid (total thiol content was 6 \times molar excess of thiol compared to the butadiene region of PB) was mixed into the solution. The solution was irradiated with UV light for 25 minutes. Afterwards, the solution was concentrated and precipitated in water. The precipitated polymer was redissolved in THF and the process was repeated a further two times. After the third precipitation, wet MG/TG-PB was dried in a vacuum oven for three days at 40 °C. The mass of the resulting polymer was 20.2 g and had a grafting ratio of 99.2 mol%. Grafted methyl thioglycolate/thioglycolic acid was 88.0% methyl thioglycolate, 12.0% thioglycolic acid. ^1H NMR (400 MHz, CDCl_3): $\delta = 3.74$ (s, 3 H, COOCH_3), 3.24 (s, 2 H, $\text{OOC-CH}_2\text{-S}$), 2.76 (br, 1 H, $(\text{CH}_2)_2\text{CHS}$), 2.05 (br, 2 H, $\text{H}_2\text{CCH}_2\text{S}$), 1.74 (br, 2 H, $\text{H}_2\text{C-CH}_2\text{-CH}$), 1.56 (br, 6 H, $(-\text{H}_2\text{C})_2\text{CH}_2$), 1.44 (br, 2 H, -

HCCH₂CH₂), 1.26 (br, 1 H, (H₂C)₃CH) ppm. FTIR (cm⁻¹): 2929, 1729, 1435, 1272, 1128, 1007, 631.

3.2.11 Synthesis of tetraaniline (TANI)

The synthesis of TANI followed a previously reported literature protocol.¹ 18.5 g *N*-phenyl-*p*-phenylenediamine (0.1 mol) was dissolved into 150 ml of acetone at 0 °C followed by the subsequent addition of 100 ml of HCl (8.3 %v/v). Separately, 45.6 g (0.2 mol) of APS was dissolved into 80 ml of HCl (8.3 %v/v). Then the APS containing solution was added into the *N*-phenyl-*p*-phenylenediamine solution dropwise under a rate of 2 – 4 ml min⁻¹. The solution was stirred for 1.5 hours and then filtered. The filtrate was washed with 30 ml of HCl (8.3 %v/v) and 80 ml H₂O. The filtrate was mixed into excess ammonium hydroxide and stirred for two hours. The solution was filtered and the filtrate was washed with plenty of water until the washing solution had a pH of 7. The wet emeraldine base TANI was dried in a vacuum oven at 25 °C for 48 hours. 9.5 g emeraldine based TANI was obtained. ¹H NMR (400 MHz, CDCl₃): δ = 7.52 (br, 1 H, H_{benzene}), 7.37 (br, 2 H, H_{benzene}), 7.00 (br, 2 H, H_{benzene}), 6.94 (br, 1 H, H_{benzene}), 3.75 (br, 2 H, NH₂) ppm. FTIR (cm⁻¹): 3367, 3192, 1598, 1579, 1513, 1495, 1307, 1155, 818, 748, 694.

3.2.12 Synthesis of epoxidised styrene-butadiene-styrene (E-SBS)

3 g of SBS was dissolved in 27 g of toluene followed by the addition of formic acid and H₂O₂. The formic acid and H₂O₂ addition depended on the desired epoxidation level of the backbone of the SBS. For 25 mol% epoxidation, 0.74 ml formic acid and 2.39 ml H₂O₂ were added. For 35 mol% epoxidation 1.04 ml formic acid and 3.35 ml H₂O₂ were added. For 50 mol% epoxidation 1.49 ml formic and 4.79 ml H₂O₂ were added. The solution was stirred for 4 hours at 60 °C and the resultant E-SBS was precipitated in methanol and dried in air for 2 hours. ¹H NMR (400 MHz, CDCl₃): δ = 7.10 (br, 3 H, H_{benzene}), 6.61 (br, 2 H, H_{benzene}), 5.45 (br, 4 H, -HC=CH- and -HC=CH₂), 5.00 (br, 1 H, -HC=CH₂), 2.96 (br, 1 H, -CH-O-CH-), 2.72 (br, 1 H, -CH-O-CH-), 2.11 (br, 1 H, (-H₂C)₂CHCH-), 2.07 (br, 3 H, (-H₂C)₂CHCH_{benzene} and -CH₂CH₂CH-), 1.61 (br, 2 H, (H₂C)₂CH₂), 1.45 (br, 2 H, (CH)₂CH₂) ppm. ¹³C NMR (75 MHz, CDCl₃): δ = 129.07 (HC=CH and HC=CH₂), 125.33 (C_{benzene}), 114.80 (HC=CH₂), 58.56 (-CH-O-CH-), 56.86 (-CH-O-CH-), 32.75 ((-H₂C)₂CH- and -H₂CCH₂CH-), 27.43 ((-H₂C)₂CHCH-) ppm.

3.2.13 Synthesis of tetraaniline modified styrene-butadiene-styrene (TANI-SBS)

E-SBS was dissolved in 50 ml THF and subsequently emeraldine base TANI was added. The quantity of TANI was dependent on the epoxidation level of E-SBS. For 25 mol% E-SBS, 3.6 g TANI was added, for 35 mol% E-SBS 5.1 g TANI was added and for 50 mol% E-SBS, 7.2 g TANI was added and the solution was stirred overnight. The resultant TANI-SBS was acidified using trifluoroacetic acid, which varied depending on the TANI grafting level. For 25 mol% TANI-SBS, 9.6 ml trifluoroacetic acid was added, for 35 mol% TANI-SBS, 13.0 ml trifluoroacetic acid was added and for 50 mol% TANI-SBS, 18.0 ml trifluoroacetic acid was added and the solution was allowed to react for 5 hours. The solution was purified by filtration and then precipitated in methanol and dried in a vacuum oven at 40 °C overnight. ^1H NMR (400 MHz, CDCl_3): δ = 7.10 (br, 3 H, $\text{H}_{\text{benzene}}$), 6.62 (br, 2 H, $\text{H}_{\text{benzene}}$), 5.45 (br, 4 H, $-\text{HC}=\text{CH}-$ and $-\text{HC}=\text{CH}_2$), 5.01 (br, 1 H, $-\text{HC}=\text{CH}_2$), 4.42 (br, 1 H, $-(\text{CH}_2)(\text{CHOH})\text{CHNH}-$), 2.96 (br, 1 H, CHOH), 2.72 (br, 1 H, $-\text{CH}-\text{O}-\text{CH}-$), 2.11 (br, 1 H, $(-\text{H}_2\text{C})_2\text{CHCH}-$), 2.07 (br, 3 H, $(-\text{H}_2\text{C})_2\text{CHCH}_{\text{benzene}}$ and $-\text{CH}_2\text{CH}_2\text{CH}-$), 1.61 (br, 2 H, $(\text{H}_2\text{C})_2\text{CH}_2$), 1.45 (br, 2 H, $(\text{CH})_2\text{CH}_2$) ppm. ^{13}C NMR (75 MHz, CDCl_3): δ = 129.07 ($\text{HC}=\text{CH}$ and $\text{HC}=\text{CH}_2$), 125.33 ($\text{C}_{\text{benzene}}$), 114.80 ($\text{HC}=\text{CH}_2$), 65.54 ($-(\text{CH}_2)(\text{CHOH})\text{CHNH}-$), 58.54 ($-\text{CHOH}-$), 32.75 ($(-\text{H}_2\text{C})_2\text{CH}-$ and $-\text{H}_2\text{CCH}_2\text{CH}-$), 27.43 ($(-\text{H}_2\text{C})_2\text{CHCH}-$) ppm. FTIR (cm^{-1}): 3262, 2918, 2967, 1781, 1672, 1667, 1493, 1302.

3.2.14 Synthesis of epoxidised polybutadiene (E-PB)

3 g of PB was dissolved in 80 g of toluene followed by the addition of formic acid and H_2O_2 . The formic acid and H_2O_2 addition depended on the epoxidation level on the SBS backbone. For 1 mol% epoxidation, 0.021 ml formic acid and 0.22 ml H_2O_2 were added. For 25 mol% epoxidation, 1.03 ml formic acid and 3.32 ml H_2O_2 were added. For 35 mol% epoxidation 1.43 ml formic acid and 4.61 ml H_2O_2 were added. For 50 mol% epoxidation 2.06 ml formic and 6.64 ml H_2O_2 were added. The solution was stirred for 4 hours at 60 °C. E-SBS was precipitated in methanol and dried in air for 2 hours. ^1H NMR (400 MHz, CDCl_3): δ = 5.42 (br, 2 H, $-\text{HC}=\text{CH}-$), 2.95 (br, 1 H, br, $-\text{CH}-\text{O}-\text{CH}-$), 2.70 (br, 1 H, $-\text{CH}-\text{O}-\text{CH}-$) ppm

3.2.15 Synthesis of tetraaniline modified polybutadiene (TANI-PB)

E-PB was dissolved in 50 ml THF and subsequently emeraldine base TANI was added. The quantity of TANI was dependent on the epoxidation level of E-PB. For 1 mol%

E-PB 0.1 g TANI was added, 25 mol% E-PB, 5.0 g TANI was added, for 35 mol% E-PB 7.0 g TANI was added and for 50 mol% E-PB, 10.0 g TANI was added. The solution was stirred overnight. After this, the resultant TANI-PB was acidified using trifluoroacetic acid, which varied depending on the TANI grafting level. For 1 mol% TANI-PB, 11.99 ml was added, 25 mol% TANI-PB, 13.0 ml trifluoroacetic acid was added, for 35 mol% TANI-PB, 18.0 ml trifluoroacetic acid was added and for 50 mol% TANI-SBS, 26.0 ml trifluoroacetic acid was added and the solution was allowed to react for 5 hours. The solution was purified by filtration and precipitated in methanol and dried in a vacuum oven at 40 °C overnight. ^1H NMR (400 MHz, CDCl_3): $\delta = 5.42$ (br, 2 H, $-\text{HC}=\text{CH}-$), 4.38 (br, 1 H, $-(\text{CH}_2)(\text{CHOH})\text{CHNH}-$), 2.74 (br, 1 H, CHOH) ppm. FTIR (cm^{-1}): 3253, 3068, 3003, 2919, 1672, 1572, 1505, 1370.

3.3 Characterisation

3.3.1 Nuclear magnetic resonance (NMR) spectroscopy

All ^1H NMR, ^{13}C NMR, Heteronuclear Single Quantum Coherence (HSQC) and Heteronuclear Multiple Bond Correlation (HMBC) spectroscopy were performed on a Bruker Avance III HD 400 MHz spectrometer in CDCl_3 and all chemical shifts were internally referenced to TMS. The spectra were processed using ACD/NMR processor ACD/Labs version 12.01.

3.3.2 Variable temperature NMR spectroscopy

All variable temperature ^1H NMR spectroscopy was performed on a Bruker Avance 500 MHz instrument between 25 °C and 70 °C in d_8 -toluene. The spectra were processed using ACD/NMR processor ACD/Labs version 12.01.

3.3.3 Fourier transform infrared spectroscopy (FTIR)

FTIR spectra was collected on a Bruker TENSOR 27 with a resolution of 4 cm^{-1} and 32 sample scans and 32 background scans in transmission mode. Prior to use, the FTIR spectrometer was cleaned using isopropanol. For variable temperature measurements, an additional Specac Eurotherm 2216e heating stage was attached and used at 10 °C intervals between 30 °C – 150 °C. The samples were allowed to equilibrate their temperature for 10 minutes before analysis.

3.3.4 Gel permeation chromatography (GPC)

GPC was performed on an Agilent 390-MDS with two PLgel mixed-C columns, a refractive index detector, a UV detector at 254 nm and THF containing 2%

triethylamine and 0.01% butylated hydroxytoluene as an eluent. The results were analysed using Agilent GPC/SEC software.

3.3.5 Compression moulding

Both thick (~1 mm) and thin (~ 100 – 200 μm) films were hot pressed using a Rondol manual hot press at 190 °C for SBS and SBR based samples and 130 °C for PB based samples. All samples were pressed under an applied pressure of 5 – 10 kN.

3.3.6 Density measurements

The density of samples was recorded using a Mettler Toledo NewClassic Balance (model ME204) with a density kit fitted and deionised water used to measure the displacement.

3.3.7 Impedance spectroscopy

Impedance spectroscopy was performed using a Princeton Applied Research Parstat MC with a PMC-2000 card and a homemade two point probe set-up between 10^0 – 10^6 Hz on thin films with a sample thickness of 100 – 200 μm and a 4 cm \times 4 cm square conducting carbon grease electrode on both sides of the sample.

For variable temperature impedance spectroscopy, the samples were heated in an oil bath between 30 °C – 150 °C and allowed to equilibrate their temperature for 10 minutes before electrical analysis.

3.3.8 Mechanical testing

Tensile testing was investigated using a Shimadzu Autograph AGS-X and samples conforming to ASTM-D638-14 type V. The samples were tested at 50 mm min (under a strain rate of 10.95% s^{-1}) with a 10 kN load cell and under room temperature conditions.

For stress relaxation testing, a Shimadzu Autograph AGS-X and samples conforming to ASTM-D638-14 type V was used. Samples were elongated to 100% strain at 50 mm min^{-1} and held until an equilibrium stress was achieved or for a 30 minute time period.

For cyclic stress softening, a Shimadzu Autograph AGS-X and samples conforming to ASTM-D638-14 type V was used. The samples were elongated to either 100%, 300% or 500% for five cycles under a controlled strain rate of 50 mm min^{-1} .

3.3.9 UV-Vis spectroscopy

Solution state UV-Vis spectroscopy was performed using an Agilent Cary 60 photospectrometer between 200 nm – 800 nm. The solvent used was DCM and the samples had a concentration of $1 \times 10^{-5} \text{ mol} \cdot \text{dm}^{-3}$.

Solid state UV-Vis spectroscopy was performed using an Agilent Cary 60 photospectrometer between 190 nm – 800 nm. The sample thickness was $\sim 200 \mu\text{m}$.

3.3.10 Raman spectroscopy

Raman spectroscopy was performed using a Renishaw inVia reflex Raman microscopy with a 532 nm diode-pumped solid state laser.

3.3.11 Dynamic mechanical thermal analysis (DMTA)

DMTA was investigated by using a Triton Tritec 2000 DMA in single cantilever mode with a 50 μm amplitude and a 1 Hz frequency. The heating rate was 2 K min^{-1} from -120 $^{\circ}\text{C}$ – 135 $^{\circ}\text{C}$ unless otherwise stated. The sample sizes used were 5.0 mm \times 10 mm \times 2.3 mm.

3.3.12 Differential scanning calorimetry (DSC)

DSC was performed using a Mettler Toledo DSC1 Star^c from -40 $^{\circ}\text{C}$ to 175 $^{\circ}\text{C}$ or 225 $^{\circ}\text{C}$ for PVDF containing samples. All samples were recorded for two cycles at a heating and cooling rate of 10 K min^{-1} .

3.3.13 Oscillatory rheometry

Oscillatory rheometry was performed using a Haake MarsIII rheometer at 190 $^{\circ}\text{C}$ with a frequency range of 0.1 – 100 Hz on 25 mm parallel disc plates with 1 mm separation. A pressure of 10 Pa was used in the testing.

3.3.14 Contact angle measurements

Contact angle measurements were performed using an Attension Theta Lite utilising H_2O and CH_2I_2 as the wetting solvents. Drops of 2.5 μl were deposited on the surface on the sample and the contact angle recorded for three seconds and averaged over the time period.

3.3.15 Scanning electron microscopy (SEM)

SEM images were obtained using a Carl Zeiss sigma field SEM using the InLens detector at a working distance of 2.5 mm and an acceleration voltage of 5 kV. Before imaging, the samples were cryofractured after submersion in liquid nitrogen for 30

mins. The fractured surface was mounted onto an aluminium stub and fixed with carbon tape. The sample was sputter coated using a Cressington 108 auto for 40 seconds under a weak argon atmosphere.

3.3.16 Atomic force microscopy (AFM)

AFM was performed using a Bruker Dimension Icon microscope in PeakForce QNM mode with ScanAsyst tips in tapping mode at a scan rate of 0.2 Hz.

3.3.17 Small angle X-ray scattering (SAXS)

SAXS was performed using a Xenocs Xeuss 2.0 SAXS system equipped with a 1D and 2D detector. Thin films of 200 μm were used as samples and investigated at 25 $^{\circ}\text{C}$.

3.3.18 Self-healing investigation

The mechanical self-healing abilities of polymers were tested by cutting a dogbone with a fresh scalpel blade and reconnecting the dogbone under light finger pressure. The dogbone was left at room temperature or placed into an oven at 37 $^{\circ}\text{C}$ or 80 $^{\circ}\text{C}$ for the self-healing time required before tensile tested.

Electrical self-healing behaviour was evaluated by testing the electrical breakdown using an external DC voltage from a PPM modulus 15A24 high voltage power supply. A binocular microscope with a Leica camera (Plan APO 1.0 \times) was attached and used to visualise the breakdown area. To clear the breakdown site, a micropositioner (KRN-09S, J micro Technology, Inc) with a needle probe (ProbePoint W20, J micro Technology, Inc) was utilised. After clearing of the site, the healed site was recovered using finger pressure application for 5 minutes and electrodes reapplied to investigate the breakdown strength recovery.

3.3.19 Polarisation-electric field (P-E) loops testing

The P-E loop response of polymers was investigated using a Radiant RT66B-HVi Ferroelectric Test system with a maximum applied voltage of 4 kV under room temperature conditions. The loop test was completed over a 10 ms time period. The conductive silver electrode size was 1.3 – 1.5 cm^2 and the samples had a thickness of 1.09 – 1.21 mm.

3.3.20 Electrical properties under strain

Dogbone samples were fitted into a Hounsfield test machine and wires attached *via* a conductive epoxy resin were attached to the gauge length of the sample. This was attached to a Solatron 1260 and 1296 Dielectric interface which recorded the samples electrical behaviour upon application of up to 30% strain.

3.3.21 Actuation testing

To investigate the actuation properties of the polymers, films with a thickness of 300 μm were pre-strained by 33% within a rigid frame. Conductive carbon grease was applied as a circular electrode with a diameter of 15 mm. The applied voltage was increased incrementally from 0 kV to 10 kV and the actuation performance was recorded by a camera until electrically induced failure.

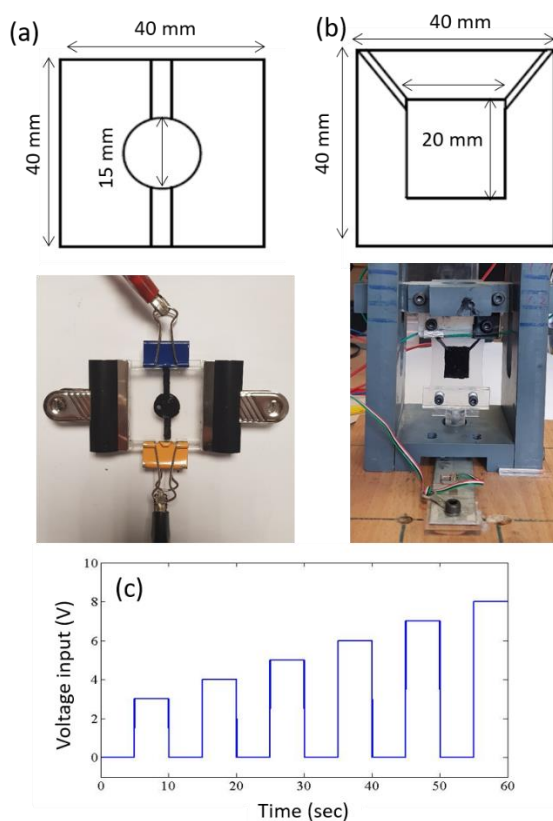


Figure 3.1 Electrode configurations for (a) DEA in strain after pre-strain and setup for actuation strain measurement; (b) dielectric elastomer actuation in force mode to pre-strain and setup for actuation force measurement; (c) a voltage input sequence of voltage enhancements for increasing the actuation response. Reproduced from Ellingford *et al.*²

The electrical self-healing was investigated by using a needle probe to mechanically damage the elastomer film and finger pressure was applied for five minutes to self-heal it. The film was stretch to 120% to investigate the damage region and to ensure self-healing had taken place. The healed elastomer was allowed to heal for three days before its actuation properties were investigated. The change in its electrical breakdown strength corresponded to its electrical self-healing and the change in its actuation performance corresponded to its healed actuation abilities.

3.3.22 Energy harvesting testing

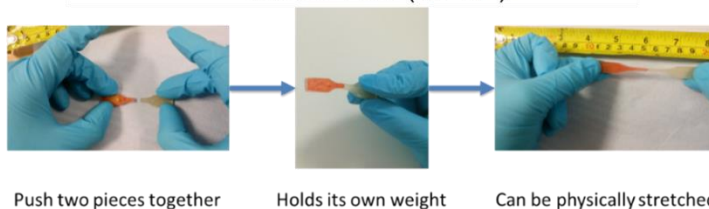
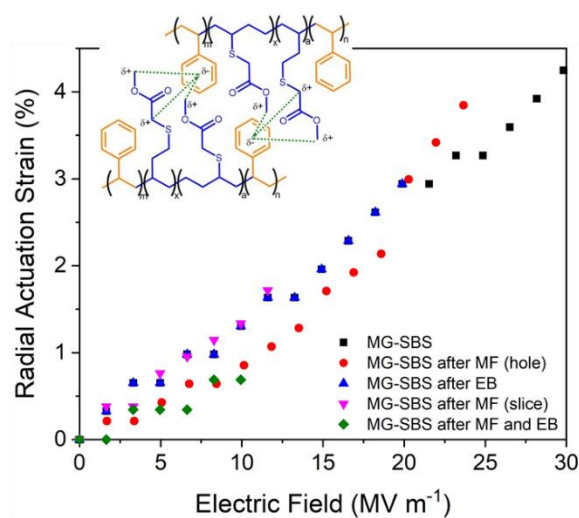
Polymer films with a thickness of 300 μm were mounted onto an air chamber with a volume of 55 cm^3 without the application of pre-strain. Circular conductive carbon grease electrodes were applied in the undeformed state with a radius of 1.5 cm and subsequently reapplied during the deformed state to ensure continuous electrode coverage. A typical energy harvesting cycle lasted for 20 seconds where under $t = 0 - 10$ s the air chamber was pressurised until the volumetric change was achieved. The air chamber was depressurised between $t = 10 - 20$ s to atmospheric pressure. The entire region of the elastomer (radius = 2.25 cm) deformed uniformly in a spherical shape in axial deformations (λ_a) of $\lambda_a = 1.3 - 3.0$. The λ_a was approximated from the volumetric change in the air chamber and was confirmed *via* recorded videos and photography. The failure voltage and electrical breakdown strength of both pristine and healed elastomers were evaluated to determine the electrical self-healing and energy harvesting recovery of the polymers in a DEG.

3.4 References

1. W. Zhao, L. Glavas, K. Odellius, U. Edlund and A.-C. Albertsson, *Polymer*, 2014, **55**, 2967-2976.
2. C. Ellingford, R. Zhang, A. M. Wemyss, C. Bowen, T. McNally, Ł. Figiel and C. Wan, *ACS Appl. Mater. Interfaces*, 2018, **10**, 38438-38448.

Chapter 4

Methyl thioglycolate grafted SBS elastomers for self-healing dielectric elastomer actuators



Publications:

C. Ellingford, R. Zhang, A. M. Wemyss, C. Bowen, T. McNally, L. Figiel and C. Wan*, Intrinsic tuning of poly(styrene-butadiene-styrene)-based self-healing dielectric elastomer actuators with enhanced electromechanical properties, *ACS Appl. Mater. Interfaces*, 2018, **10**, 44, 38438

Y. Zhang, C. Ellingford, R. Zhang, J. Roscow, M. Hopkins, P. Keogh, T. McNally, C. Bowen and C. Wan*, Electrical and mechanical self-healing in high performance dielectric elastomer actuator materials, *Adv. Funct. Mater.*, 2019, **29**, 15, 1808431

4.1 Introduction

The structure of the polar group for the intrinsic modification of a dielectric elastomer dictates how the electromechanical properties are affected. Mechanically, the dielectric elastomer requires a high tensile strength and strain at break but a low Young's modulus to be able to elastically deform without failure in an actuation or energy harvesting device.¹ Additionally, the relative permittivity needs to be high and the $\tan \delta$ loss low to maximise actuation performance and energy harvesting efficiency.² To prevent electrically induced failure, a high electrical breakdown strength allows actuation and energy harvesting devices to be operated under a higher electrical field for maximum performance.³

Utilisation of thiol-ene chemistry demonstrated an ideal reaction pathway to successfully develop elastomers with an enhanced electromechanical activity whilst simultaneously being scalable, quick and straightforward to synthesise.⁴ There are two potential routes for thiol-ene chemistry: *via* thermally induced initiation and *via* photo induced initiation. A thermally induced reaction typically requires a longer reaction time and results in a lower grafting efficiency due to its slower rate.⁵ Comparatively, a photoinitiated reaction has a faster reaction rate^{5, 6} as long as the photo initiator is miscible with the reaction system but the choice between two classes of photo initiators affects this greatly,⁵ see Figure 4.1 for radical mechanisms.

For Type I photoinitiators, the absorption of a photon from UV light causes unimolecular cleavage to form radicals⁷ which can either react directly with a vinyl group or remove a proton to initiate the thiol-ene reaction.⁶ Examples of Type I photo initiators include 2,2-dimethoxy-2-phenylacetophenone (DMPA) and diphenyl(2,4,6-trimethylbenzoyl)phosphine oxide.

For Type II photoinitiators, sulfenyl and ketyl radicals are formed *via* cleavage upon application of UV light. However, ketyl radicals are unreactive for thiol-ene chemistry due to steric hindrance and stabilisation of the radical through delocalisation.⁶ Thus, only sulfenyl radicals can react with vinyl groups on a polymer backbone. Examples of Type II photo initiators include benzophenone, thioxanthone and camphorquinone.

Therefore, due to the structural differences between Type I and Type II photoinitiators, Type I photoinitiators have a faster reaction rate and higher efficiency for grafting

compared to Type II photoinitiators.^{8,9} Type I photoinitiators form excited singlet and triplet states with short lifetimes, inhibiting quenching of the radical from the thiols.^{6,10} Thus using a Type I photoinitiator such as DMPA for a photoinitiated thiol-ene reaction is the optimum pathway.

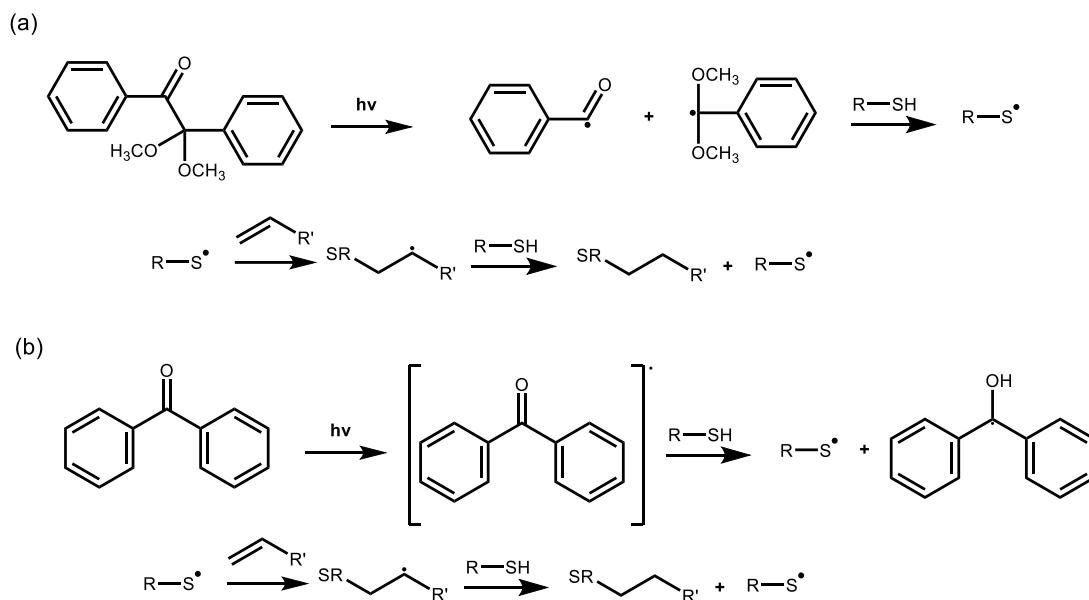


Figure 4.1 (a) Type I photoinitiator photo decomposition and subsequent reaction pathway and (b) Type II photoinitiator photo decomposition and subsequent reaction pathway

However, as noted by Silverstein *et al.*, the thiol-ene reaction is a competitive reaction between the desired coupling between thiol groups and vinyl groups and intrachain cyclisation reactions and interchain cross-linking reactions,¹¹ and the products formed are shown in Figure 4.2. Crosslinking is more prevalent in thermally initiated thiol-ene reactions compared to photoinitiated reactions due to the slow rate of reaction.¹² Therefore, low degrees of functionalisation from the thiol-ene reaction are inversely proportional to the interchain crosslinking formed.¹³ However, by controlling the excess of thiol used, the coupling reaction between the vinyl groups and thiol groups can be promoted and the rate of intrachain cyclisation and interchain crosslinking is inhibited.¹¹ Finally, the application of UV light to a polymer chain can induce polymer chain scission through photo-aging.¹⁴ This increases the dispersity of the polymer, leading to vastly different chain lengths present, possibly affecting the physical properties.

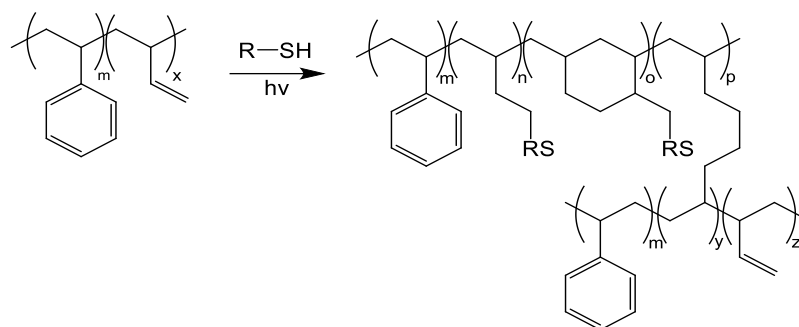


Figure 4.2 Possible products formed during thiol-ene reaction on an example of styrene-block-butadiene, showing vinyl group coupling to thiol group, intrachain cyclisation and interchain crosslinking

In this chapter, commercially available SBS was chosen as the polymer for modification *via* thiol-ene chemistry due to its mechanical properties from hard/soft blocks and ability to be modified. SBS has a low dielectric $\tan \delta$ loss and a high electrical breakdown strength, strain at break, deformability and strength.¹⁵ In addition, the commercial availability of SBS allows the easy scale up of a reaction procedure as well as industrial implementation. A unique feature of SBS arises from its block copolymer structure, whereby its mechanical properties arise only from chain entanglement and its phase separated structure, and is not dependent on any crosslinking, unlike polysiloxanes. Thus the grafting of the polar groups to SBS can be tuned to directly influence the electromechanical properties

The polar group selected for grafting to SBS *via* thiol-ene chemistry was methyl thioglycolate. Methyl thioglycolate introduces polarity to the backbone of the non-polar elastomer through its ester functionality without any expected interactions.¹⁵ Furthermore, methyl thioglycolate was easily obtained in quantities suitable for large scale syntheses to SBS, increasing the long-term viability of use for the resulting methyl thioglycolate modified SBS (MG-SBS) elastomer. Initially, the reaction conditions including the excess of methyl thioglycolate required for efficient thiol group and vinyl group coupling and minimal interchain crosslinking were investigated.

Afterwards, this chapter investigates the effect of grafting of methyl thioglycolate to the backbone of SBS on the electrical and mechanical properties. An unexpected self-healing ability of MG-SBS was discovered and its cause was investigated through structural characterisation and changes in the self-healing conditions. This was further

investigated through its ability to recover its electrical properties after both mechanical damage and electrical failure. Improvements to the recovery of the electrical properties after electrical breakdown *via* a mechanically based cleaning method of the defect site was also demonstrated.

In addition to this, the actuation abilities of pristine MG-SBS and after recovery from mechanical and electrical failures were investigated by placing thin elastomer films on a rigid frame and subjected to increasing electrical fields. Finally, to explain the nature of electrical recovery of MG-SBS finite element modelling was used to discover the effect of surface defects and voids within the failure site on the localised electric field experienced by the elastomer.

This work demonstrates that SBS elastomers can be successfully modified using thiol-ene click chemistry to enhance their electromechanical properties for use in actuation and energy harvesting devices, and electrostatic interactions can be utilised to increase the longevity of the material within a device.

4.2 Results and Discussion

4.2.1 Grafting of methyl thioglycolate to styrene-butadiene-styrene (MG-SBS)

The reaction conditions of grafting methyl thioglycolate (MG) to styrene-butadiene-styrene terpolymer (SBS) under a photo-initiated thiol-ene reaction were investigated. The molar excess of thiol relative to SBS and the UV-light exposure time were varied to determine their effects on the grafting efficiency of methyl thioglycolate modified SBS (MG-SBS). To determine the quantity of thiol required for different thiol excess ratios, the composition of SBS and, more specifically the concentration of vinyl groups within SBS, was established.

The assigned ^1H NMR spectrum of SBS is given in Figure 4.3. The peaks at 7.1 and 6.6 ppm are attributed to the aromatic ring from the styrene block, containing three protons and two protons at the combined *meta*- and *para*- positions and *ortho*-positions, respectively. The alkene peaks from the butadiene block are present at 5.4 and 5.0 ppm. The peak at 5.4 ppm contains four protons in its environment, two from the *exo* and two from the *endo* alkene of butadiene, and the peak at 5.0 ppm is from the remaining proton environment on the adjacent carbon in the *exo* alkene of butadiene and agrees well with ^1H NMR spectra of SBS observed in the literature¹⁵.

Comparison of the integration values between these two peaks confirmed that the alkenes in SBS are 19.6% *exo* and 80.4% *endo*.

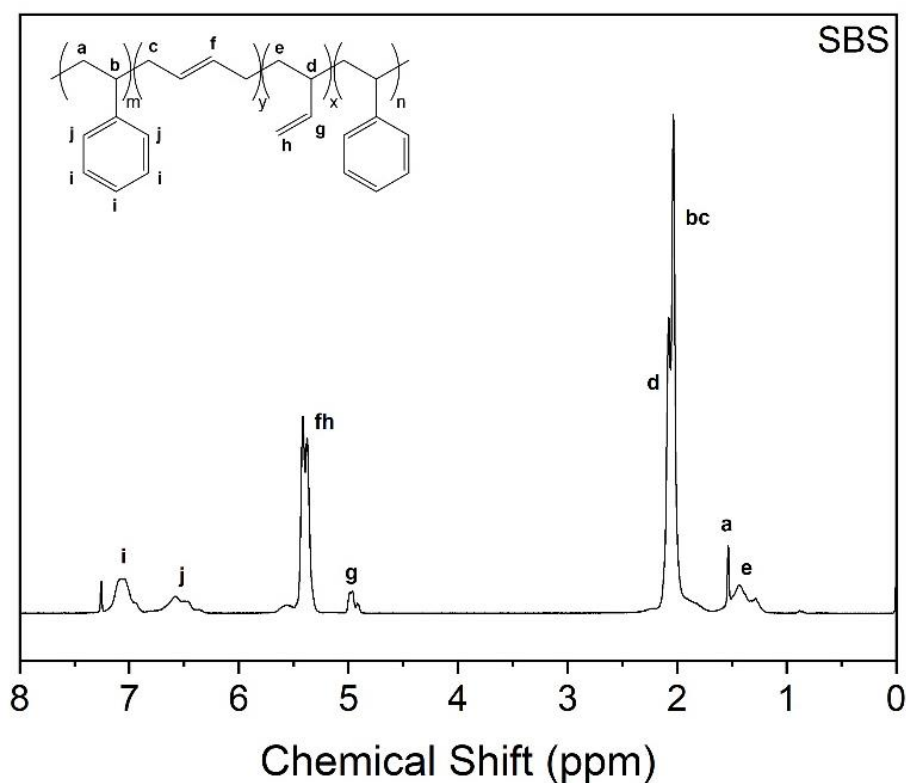


Figure 4.3 ¹H NMR spectrum at 400 MHz in CDCl₃ of SBS

Furthermore, the ratio of alkene to styrene in SBS was calculated *via* the integration values to obtain the relative concentrations of each using equations 4.1 and 4.2:

$$\frac{\int \text{styrene}}{\int \text{styrene} + \int \text{butadiene}} \times 100 = \% \text{styrene in SBS} \quad (4.1)$$

$$\frac{\int \text{butadiene}}{\int \text{styrene} + \int \text{butadiene}} \times 100 = \% \text{butadiene in SBS} \quad (4.2)$$

where $\int \text{styrene}$ and $\int \text{butadiene}$ are the proton adjusted integration values of the styrene block and the butadiene block in SBS respectively. From the alkene peak at 5.4 ppm and styrene peak at 6.6 ppm, the butadiene content of SBS was 82.1 mol% and styrene content of SBS was 17.9 mol%. From this, the weight fraction, W_f , of styrene and butadiene was calculated to be 29.6 wt% and 70.4 wt% using equation 4.3 and 4.4. In addition, it was established that on average there was 13.01 mmol of butadiene per gram of SBS which was used to calculate the excess of thiol for the reaction.

$$m = n \times M_w \quad (4.3)$$

$$W_f = \frac{m_a}{m_a + m_b} \quad (4.4)$$

where n is number of moles, M_w is the weight average molecular weight of butadiene or styrene and m , m_a and m_b are the mass of butadiene or styrene. To understand the effect of thiol excess on the grafting degree of MG-SBS and rate of interchain crosslinking side reactions during the thiol-ene click reaction, the thiol excess of methyl thioglycolate was varied between 2× – 5× excess whilst a constant UV light exposure time of 10 minutes was maintained. MG-SBS synthesised using a 2× thiol excess formed a gelled product during the reaction due to interchain crosslinking from a free radical side reaction between the SBS chains¹¹ and could not be redissolved for purification. However, MG-SBS could be successfully synthesised with a 3× thiol excess without crosslinking side reactions affecting the final product. This is despite literature recommendations that a 10× excess of thiol is required to produce an uncrosslinked product during the thiol-ene reaction.¹¹

The effect on the grafting degree is observed in the ¹H NMR spectra, given in Figure 4.4a for 3×, 4× and 5× excess methyl thioglycolate reactions. The grafting of methyl thioglycolate introduced two additional peaks at 3.7 ppm and 3.2 ppm attributed to the CH₃ and CH₂ environment of the methyl thioglycolate ester. Additionally, the alkene peak at 5.4 ppm reduced significantly in intensity relative to styrene due to the thiol-ene reaction. Two methods were used to calculate the grafting ratio. Firstly, the calculation of the grafted thiol was calculated by equation 4.5:

$$\%grafting = \frac{\int thiol}{\int styrene + \int butadiene} \quad (4.5)$$

where $\int thiol$ is the integral value for the CH₂ group at 3.2 ppm of MG-SBS and $\int styrene$ and $\int butadiene$ are the integral values from SBS before the modification reaction. From this, the thiol grafting was calculated to be 71.5%, 88.3% and 94.1% for 3×, 4× and 5× thiol excess respectively. However, the degree of side reactions from the thiol-ene reaction is not quantified. To calculate this, the reduction in the alkene peak can be used as a second measure of grafting, calculated by equation 4.6:

$$\%reacted_{alkene} = \frac{\int butadiene'}{\int styrene + \int butadiene} \quad (4.6)$$

where $\int butadiene'$ is the new integration value for the butadiene peak at 5.4 ppm after the reaction. Thus, the alkene reacted was 82.6%, 96.2% and 98.0% for 3×, 4× and 5×

thiol excess respectively, indicating that the degree of side reactions reduced upon a greater thiol excess as the free radical addition of methyl thioglycolate had a higher rate of reaction. Therefore, this shows that the quantity of thiol used in the reaction has an effect on the structure of MG-SBS formed, and can be used to minimise side reactions occurring.

The second parameter to control for the reaction was the exposure time to UV light. The UV light exposure time was varied between 5 minutes and 30 minutes whilst maintaining a constant methyl thioglycolate excess of 3 \times . The ^1H NMR spectra in Figure 4.4b show an identical MG-SBS structure to that seen in Figure 4.4a demonstrating that the increased UV light exposure time also affected the grafting efficiency of MG-SBS. Thus the grafting of methyl thioglycolate was 57.7%, 71.5%, 87.9%, 88.1% and 95.1% for 5 minutes, 10 minutes, 15 minutes, 20 minutes and 30 minutes of UV light exposure time respectively. Additionally, the gap between the reacted alkene ratio and thiol grafting closed upon increased levels of grafting (*i.e.* reacted alkene after 10 minutes UV exposure was 82.6% compared to 30 minutes exposure of 97.7%). This indicates that the amount of side reactions such as interchain crosslinking reaction was low during the reaction.

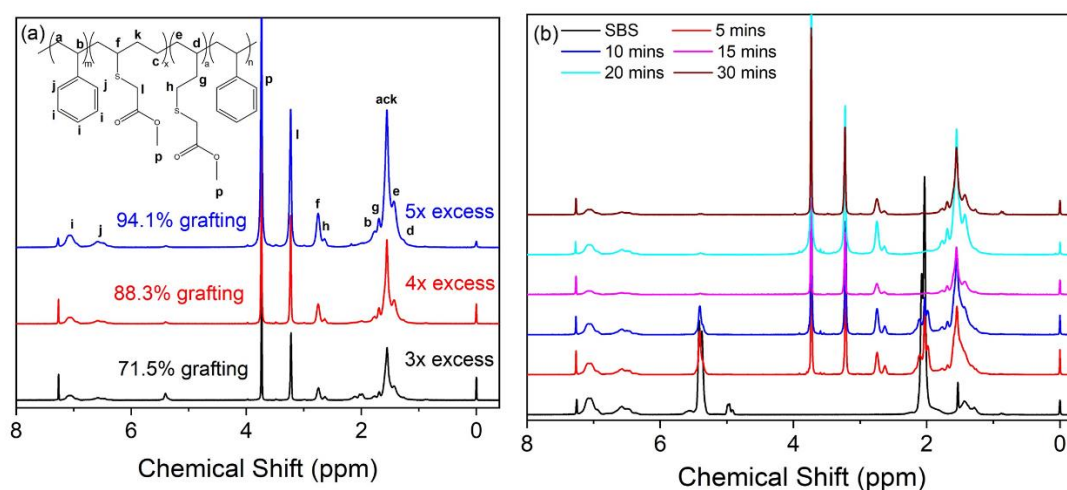


Figure 4.4 (a) ^1H NMR spectra at 400 MHz in CDCl_3 of MG-SBS synthesised using different methyl thioglycolate excesses and (b) ^1H NMR spectra at 400 MHz in CDCl_3 of SBS and MG-SBS synthesised with different UV light exposure times

Therefore, optimised conditions for the synthesis of MG-SBS were devised from these results. UV light exposure was limited to 20 minutes whilst maintaining a 4 \times methyl thioglycolate excess to obtain a maximum grafting efficiency with minimal side

reactions. ^1H NMR confirmed the successful nature of these conditions in a small, 1 g scale reaction by a thiol grafting efficiency of 96.1% and alkene reaction of 98.9% on the butadiene backbone. Subsequent scaling up of the synthesis to produce 21.3 g MG-SBS showed that there was no reduction in the thiol grafting efficiency nor increase in side products (97.2% thiol grafting efficiency, 97.9% reacted alkenes).

FTIR was used to further confirm the successful grafting of methyl thioglycolate to SBS, as shown in Figure 4.5a. Prior to the reaction, SBS exhibited a C-H alkene stretch at 3006 cm^{-1} , which disappeared after the reaction. In addition, a C=O stretch for the ester group of methyl thioglycolate appeared at 1729 cm^{-1} , and an asymmetric C-O stretch and a symmetric C-O stretch at 1272 cm^{-1} and 1020 cm^{-1} appeared respectively.

Finally, Gel Permeation Chromatography (GPC) was used as final confirmation of the successful synthesis of MG-SBS, as seen in Figure 4.5b. Prior to the reaction, SBS had a number average molecular weight (M_n) of $86,000\text{ g mol}^{-1}$, a weight average molecular weight (M_w) of $101,000\text{ g mol}^{-1}$ and a dispersity (\mathcal{D}) of 1.17. After the reaction, the M_w increased to $204,000\text{ g mol}^{-1}$ to confirm the successful grafting and formation of MG-SBS. A high molecular weight shoulder is present which indicates the presence of some soluble crosslinked polymer chains. Additionally, the M_n decreased to $79,000\text{ g mol}^{-1}$ and the \mathcal{D} increased to 2.57 indicating UV-initiated polymer chain scission had taken place. The polymer chain scission was further confirmed by the UV light detector trace at 254 nm in Figure 4.5c. Only a low concentration of UV active styrene was detected at high retention times (lower molecular weight) and thus most polymer chain scission took place in the polybutadiene block of SBS.

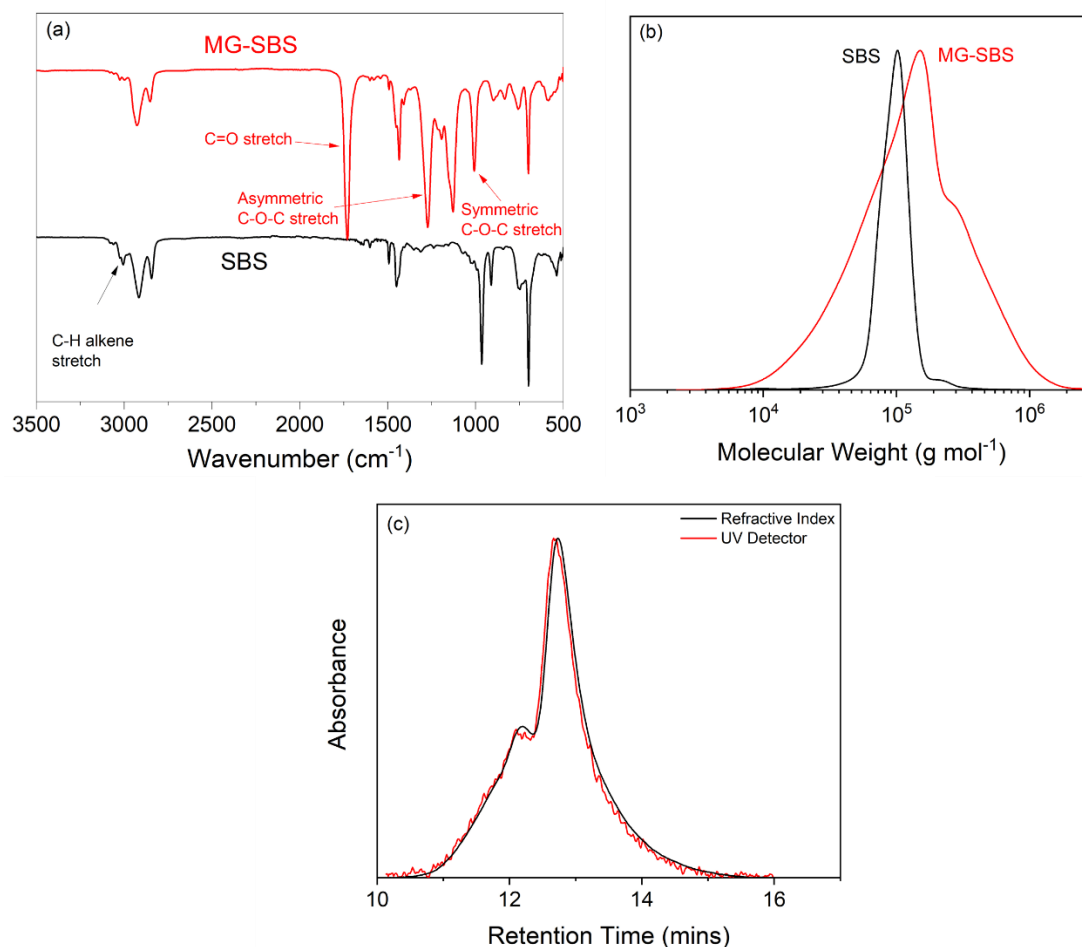


Figure 4.5 (a) FTIR spectra of SBS and MG-SBS with key peaks labelled, (b) GPC trace of SBS and MG-SBS in THF and (c) GPC trace of MG-SBS in THF with the UV light detector at 254 nm and Refractive Index detector against retention time.

4.2.2 Electrical and mechanical properties of MG-SBS

The grafting of methyl thioglycolate had a significant effect on the electrical properties of SBS, Figure 4.6. The presence of the intrinsic polar groups on the polymer backbone produced a giant permittivity elastomer which increased the relative permittivity of SBS from 2.8 at 10^3 Hz to 11.4 at 10^3 Hz in MG-SBS. In addition, the $\tan \delta$ loss of MG-SBS (where $\tan \delta = \text{dielectric loss}/\text{relative permittivity}$) was 0.01 at 10^3 Hz, very similar to that of unmodified SBS ($\tan \delta = 0.009$ at 10^3 Hz). An increase in both relative permittivity and $\tan \delta$ was observed in MG-SBS between 1 Hz and 50 Hz. This was attributed to electrode polarisation, where charge build up at the electrode/polymer interface occurred due to electrode blocking.¹⁶⁻¹⁸ The effect of the grafting on the phase angle of the elastomers is seen in Figure 4.6c, where the phase

angle remained at -90° for MG-SBS and SBS. This indicated that the elastomers are both purely capacitive in nature. However, due to electrode polarisation, MG-SBS displayed a deviation from -90° between 1 Hz and 50 Hz. The AC conductivity for both SBS and MG-SBS displayed a frequency dependent behaviour across all frequency ranges. Prior to modification, the AC conductivity of SBS was $1 \times 10^{-9} \text{ S m}^{-1}$ at 10^3 Hz, whilst for MG-SBS, the AC conductivity increased only marginally to $6 \times 10^{-9} \text{ S m}^{-1}$.

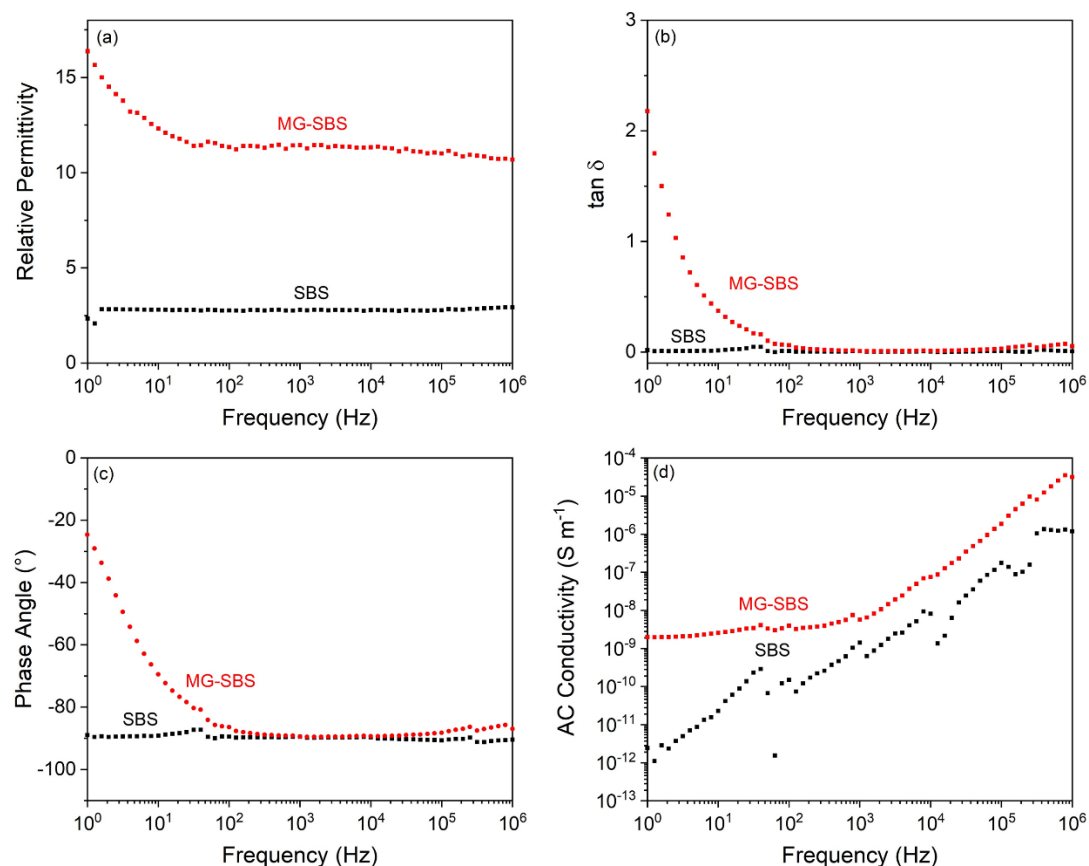


Figure 4.6 Impedance spectroscopy of SBS and MG-SBS with (a) relative permittivity, (b) $\tan \delta$ loss, (c) phase angle and (d) AC conductivity

MG-SBS also exhibits very different mechanical properties to that of unmodified SBS, Figure 4.7a. Before modification, SBS exhibited a Young's modulus of 51.7 ± 6.4 MPa, a strain at break of $857 \pm 45.8\%$ and a tensile strength of 8.92 ± 0.7 MPa. MG-SBS exhibited a significantly reduced Young's modulus of 2.87 ± 0.6 MPa, a reduced tensile strength of 3.13 ± 0.12 MPa and a reduced strain at break of $569 \pm 25.9\%$. The reduced Young's modulus of the material is advantageous for both actuation and energy harvesting as it makes the elastomer more responsive to electric fields and more

responsive to mechanical deformations.² The reduced tensile strength and strain at break are greater than the desired tensile strength and strain at break for energy transducers from Madsen *et al.*¹⁹

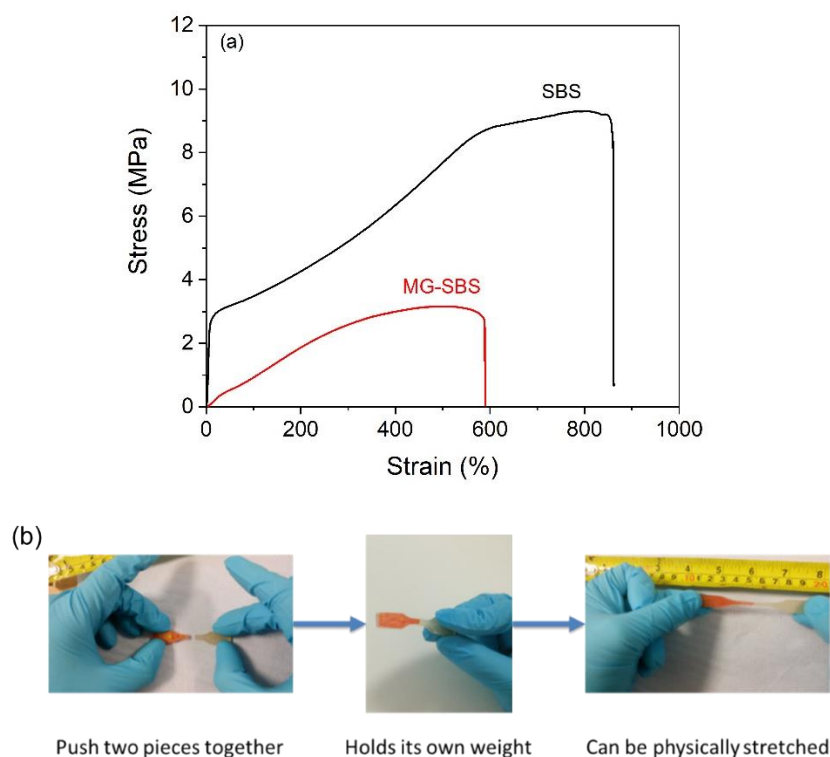


Figure 4.7 (a) Stress-strain curves of SBS and MG-SBS from mechanical testing and (b) Images of the self-healing process of MG-SBS

4.2.3 Mechanical self-healing abilities of MG-SBS

MG-SBS displayed a time dependent self-healing behaviour, requiring no external stimulus at room temperature. After adhering two dogbone pieces together by reconnecting them, the MG-SBS dogbones were allowed time for recovery, followed by tensile testing, see Figure 4.7b.

MG-SBS displayed a time dependent self-healing nature, whereby leaving it for longer time periods allowed a greater healing to be observed. From Figure 4.8, immediate tensile testing after cutting of the dogbone resulted in a strain at break recovery of 12.3% ($68.9 \pm 4.0\%$ strain at break) and a tensile strength recovery of 10.0% (0.32 ± 0.01 MPa tensile strength) due to excellent tack between the two polymer pieces. However, once left for three days, the strain at break recovery increased to 20.9% ($116.6 \pm 8.5\%$ strain at break) and the tensile strength recovery increased to 25.4%

(0.80 ± 0.03 MPa tensile strength). This time dependent behaviour was attributed to the ability of the MG-SBS polymer chains to bridge the gap between the two pieces and re-entangle the polymer chains, which was assisted by a weak electrostatic interaction between the polymer chains.²⁰

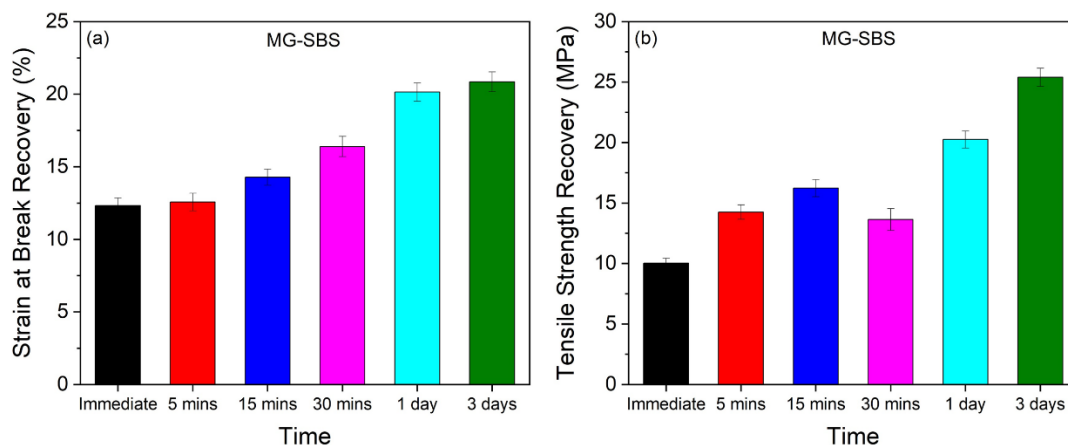


Figure 4.8 Self-healing of MG-SBS at room temperature results up to three days with (a) strain at break recovery and (b) tensile strength recovery

To fully understand the mechanism of self-healing in MG-SBS, dynamic mechanical thermal analysis (DMTA) was carried out on both SBS and MG-SBS to determine the effect of the grafting on the two polymer blocks of styrene and butadiene, see Figure 4.9. Prior to modification, SBS exhibits two glass transition temperatures (T_g), one for the butadiene block at -83 °C and one for the styrene block at 97 °C as SBS exhibits a phase separated morphology.²¹ However, after modification, MG-SBS exhibits only one T_g at -22 °C, indicating that the two phases have been compatibilised by the modification and resulted in just one polymer phase. The storage and loss modulus for SBS and MG-SBS are observed in Appendix Figure 1.

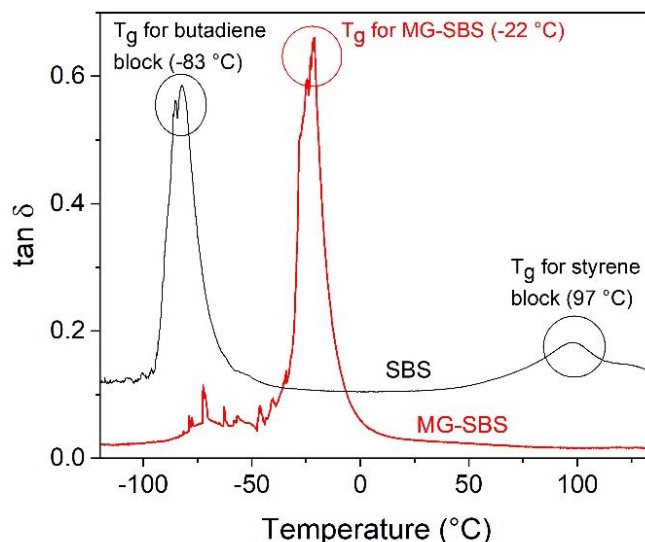


Figure 4.9 DMTA $\tan \delta$ results of SBS and MG-SBS for the T_g transitions of the elastomers

This singular polymer phase was further supported by small angle X-ray scattering (SAXS) and atomic force microscopy (AFM), in Figure 4.10. AFM visually depicts the cylindrical worm-like structure of phase separate SBS, surrounded by a butadiene matrix. The height distribution graph shows two peaks for the two phases of SBS as well. After the reaction, the cylindrical styrene phase disappeared to show one almost uniform polymer phase in MG-SBS, as increased intermolecular interactions and phase compatibility can influence the polymer morphology evolution. Additionally, the height distribution graph also shows one peak for one polymer phase. However, the existence of a disordered arrangement of several dark dots remained, which are attributed to the remainder of the uncompatibilised styrene phase. SAXS elucidates further the structures within SBS and MG-SBS. In SBS, 2D SAXS showed that SBS exhibits partial long-range order in one direction. The 1D spectra also showed strong q peaks at $\sqrt{3}$ and $\sqrt{7}$, as well as a small peak at $\sqrt{4}$. This demonstrates that SBS has hexagonally arranged cylindrical styrene microdomains in a butadiene continuous phase.^{22, 23} In contrast to SBS, the 2D image of MG-SBS showed a solid and homogenous intensity indicating a spherical morphology is present. From the 1D graph, a small secondary q -peak at $\sqrt{3}$ remains, indicating that the morphology of MG-SBS shifted to misaligned spheres rather than spheres or cylinders, as no q -peaks are present at $\sqrt{2}$, $\sqrt{4}$ or $\sqrt{7}$. The transition from a hexagonally arranged cylindrical styrene phase to a more disordered misaligned spherical morphology indicates that there is an

increase in compatibility or a higher degree of mixing between the two polymer blocks, reinforcing the observations from DMTA and AFM.

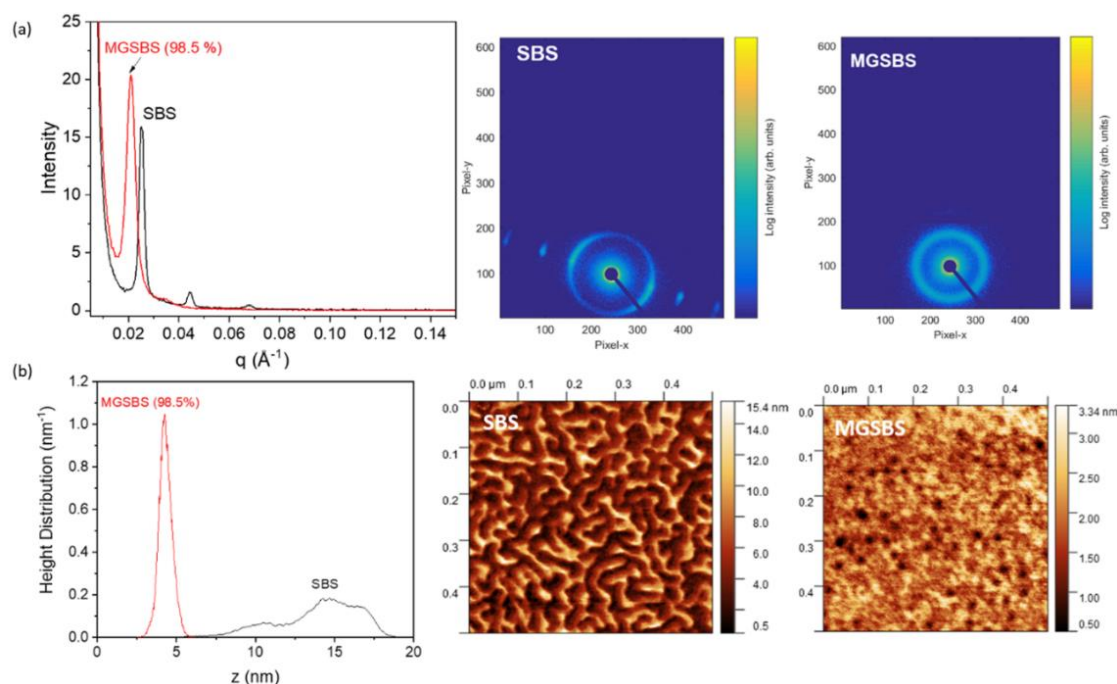


Figure 4.10 (a) 1D and 2D SAXS measurements of SBS and MG-SBS and (b) height distribution and indentation imagery from AFM

To understand the macromolecular interactions present within the polymer matrix, UV-Vis, FTIR and Raman spectroscopy were performed. Solid state and solution state UV-Vis spectroscopy were implemented to probe the effect observed on the styrene block of SBS, see Figure 4.11a-b. From the solution state UV-Vis spectroscopy, the major peak observed is at 262 nm, attributed to the π - π^* transition for free styrene. A secondary, broad peak is observed at 290 nm attributed to the π - π^* transition for π -stacking styrene groups. In contrast, the solid state UV-Vis spectrum of SBS revealed that the π - π^* transition for π -stacking styrene has a strong intensity in the solid state, indicating that this interaction is diminished in the solution state. Additionally, solid state UV-Vis showed the π - π^* transition for alkene groups on the butadiene block at 205 nm.

For MG-SBS, the absorbance peak for the π - π^* transition of free styrene blue shifts to 247 nm in the solution state, and 248 nm in the solid state, a shift of 15 nm and 16 nm respectively. Likewise, the π - π^* transition for π -stacking styrene was not visible in the solution state but was present in the solid state, albeit blue shifted to 274 nm which

was a shift of 20 nm. Finally, the π - π^* transition for alkene groups on butadiene was not visible, providing further evidence of the high grafting efficiency of MG-SBS from ^1H NMR. The blue shift observed indicates that there is an increase in the transition energy for electron promotion within the styrene groups, because of weak interactions removing delocalised aromatic electron density away from the styrene ring, and increasing the energy required to promote a remaining delocalised aromatic electron.²⁴ Thus, UV-Vis spectroscopy demonstrated that the compatibility of the two polymer phases is due to an interaction with the styrenic block.

To further understand this interaction, FTIR and Raman spectroscopy were used to indicate which bonds within the polymer were affected, see Figure 4.11c-d. Both FTIR and Raman observed a large red shift in the wavenumber of the C=O and two C-O stretches compared to unreacted methyl thioglycolate in FTIR (or MG-SBS with a very low grafting efficiency – see section 4.2.5 for more information). In addition, the C-C aromatic bond observed a 2 cm^{-1} red shift in both FTIR and Raman spectroscopy for styrene. Normally, a shift in wavenumber of less than 4 cm^{-1} is attributed to normal variance within the equipment, however as the exact same behaviour is observed in both FTIR and Raman, it is considered to be important in this case. Overall, the elongation of the C-C aromatic bonds of styrene and the ester group of methyl thioglycolate indicate that these two are the interacting groups and result in the compatibilisation and the observed self-healing. More specifically, self-healing is likely to originate from either the δ^+ CH₂ or δ^+ CH₃ group on either side of the MG ester, which accepts electron density from the δ^- aromatic ring, as shown in Figure 4.12. As the electron density within the aromatic ring decreases, the HC-CH aromatic bonds experience a weaker pull from the centre of the ring, increasing the bond length slightly. A similar interaction is observed in nature to give proteins their secondary structure.²⁵

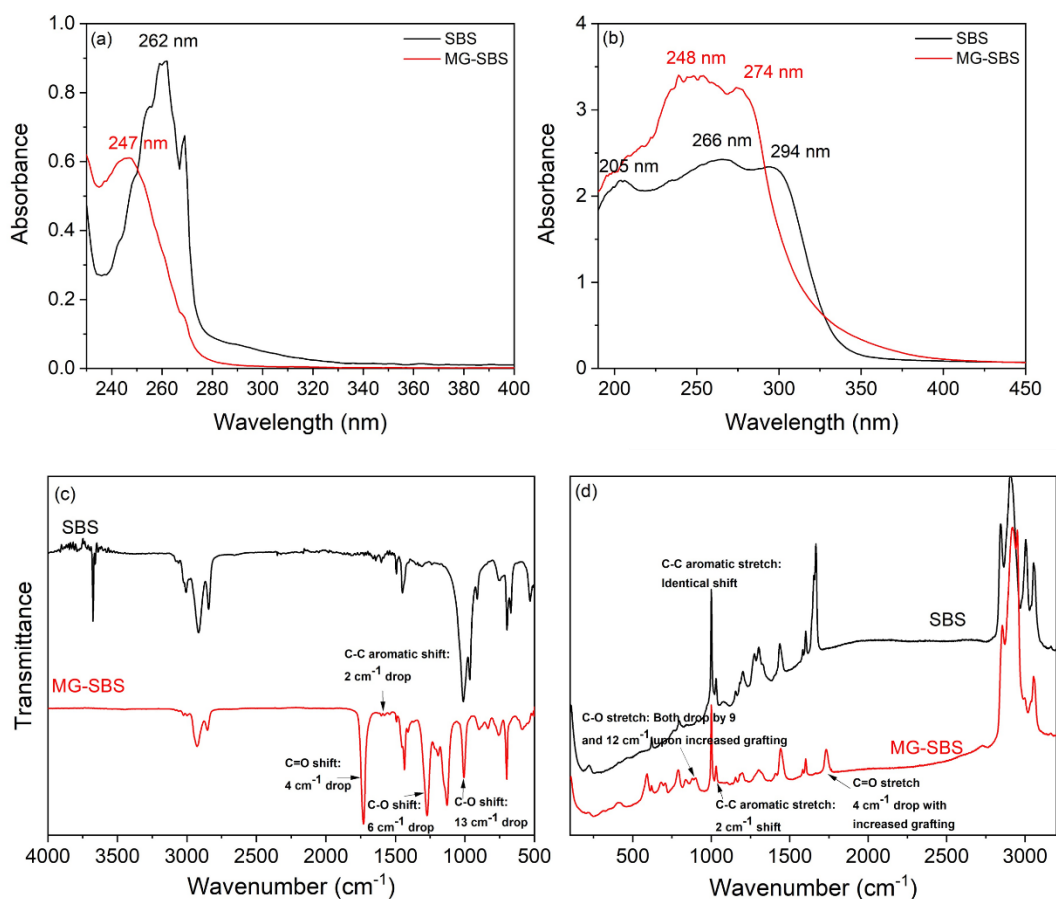


Figure 4.11 (a) Solution state UV-Vis spectra of SBS and MG-SBS in DCM, (b) solid state UV-Vis spectra of SBS and MG-SBS, (c) FTIR spectra of SBS and MG-SBS with key peak shifts and (d) Raman spectra of SBS and MG-SBS with key peak shifts

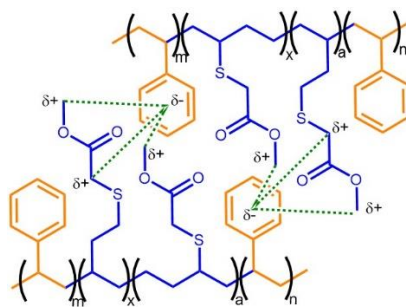


Figure 4.12 Diagram for the suggested electrostatic self-healing interaction present in MG-SBS

To understand the effect further of grafting of methyl thioglycolate on the self-healing properties of MG-SBS, an elastomer with a lower grafting degree of 65.1 mol% grafting was synthesised (MG-SBS (65.1%)). The ^1H NMR and FTIR spectra are shown in Appendix Figure 2a-b. The ^1H NMR spectrum for MG-SBS (65.1%) is

similar to MG-SBS, however the alkene peak at 5.40 ppm is increased, demonstrating the reduced level of grafting in this material. Additionally, the FTIR spectrum of MG-SBS (61.5%) showed a combination of peaks from both MG-SBS and SBS due to its lower grafting level. MG-SBS (65.1%) also had a higher tensile strength and a higher strain at break of 4.73 ± 1.2 MPa and $668 \pm 96\%$ respectively, with a stress strain curve shown in Appendix Figure 3.

Self-healing testing was performed on MG-SBS (65.1%) up to 3 days at room temperature, as seen in Figure 4.13a-b. The results show that there is an initial self-healing recovery in both the strain at break and the tensile strength immediately, similar to MG-SBS. However, this recovery is very low, only 2.2% and 4.0% for strain at break recovery and tensile strength recovery respectively. Additionally, MG-SBS (65.1%) does not show an increase in the self-healing recovery with respect to time. This is because the self-healing interaction between methyl thioglycolate and styrene is significantly weaker from the reduced methyl thioglycolate grafting level. The initial self-healing effect is therefore provided by the tackiness of the elastomer holding the two pieces together.

To further understand the limits of the self-healing ability of MG-SBS, the self-healing abilities were evaluated at an elevated temperature of 37 °C, see Figure 4.13c-d. The immediate self-healing of MG-SBS at 37 °C is similar to MG-SBS at room temperature with a strain at break recovery and a tensile strength recovery of 9.9% and 13.7% respectively. However, the self-healing recovery plateaus at approximately 13% and 16% for strain at break recovery and tensile strength recovery after five minutes respectively. This is because the increased thermal energy within the elastomer increased the rate of breaking and reforming the electrostatic interaction, and increased the mobility of the polymer chains to re-entangle across the failure point. However, the maximum self-healing recovery for both strain at break and tensile strength was lower due the increased temperature overcoming more of the electrostatic interactions at any one time in the elastomer, compared to self-healing at room temperature. Therefore, the temperature increases the rate of self-healing, but reduces the self-healing recovery overall.

The final self-healing investigation demonstrated the potential to heal MG-SBS more than once. This involved re-utilising the cut dogbones of MG-SBS for the self-healing

process once more, see Figure 4.13e-f. Compared to the first self-healing test (see Figure 4.8), the strain at break recovery and the tensile strength recovery have a broadly similar recovery rate in the first 30 minutes of the testing, reach a strain at break recovery of 14.6% and a tensile strength recovery of 14.7%. However, when left for 1 day and 3 days, the recovery is lower than the first self-healing investigation. The strain at break recovery is 19% after 3 days and the tensile strength recovery is 18%, compared to the original self-healing results of 21% and 25% respectively. The cause behind this could be due to several factors, including damage to the contact surfaces, preventing the wetting and chain entanglement processes of self-healing, by the repeated pulling apart, or by dirt and dust contaminating the contact surfaces.

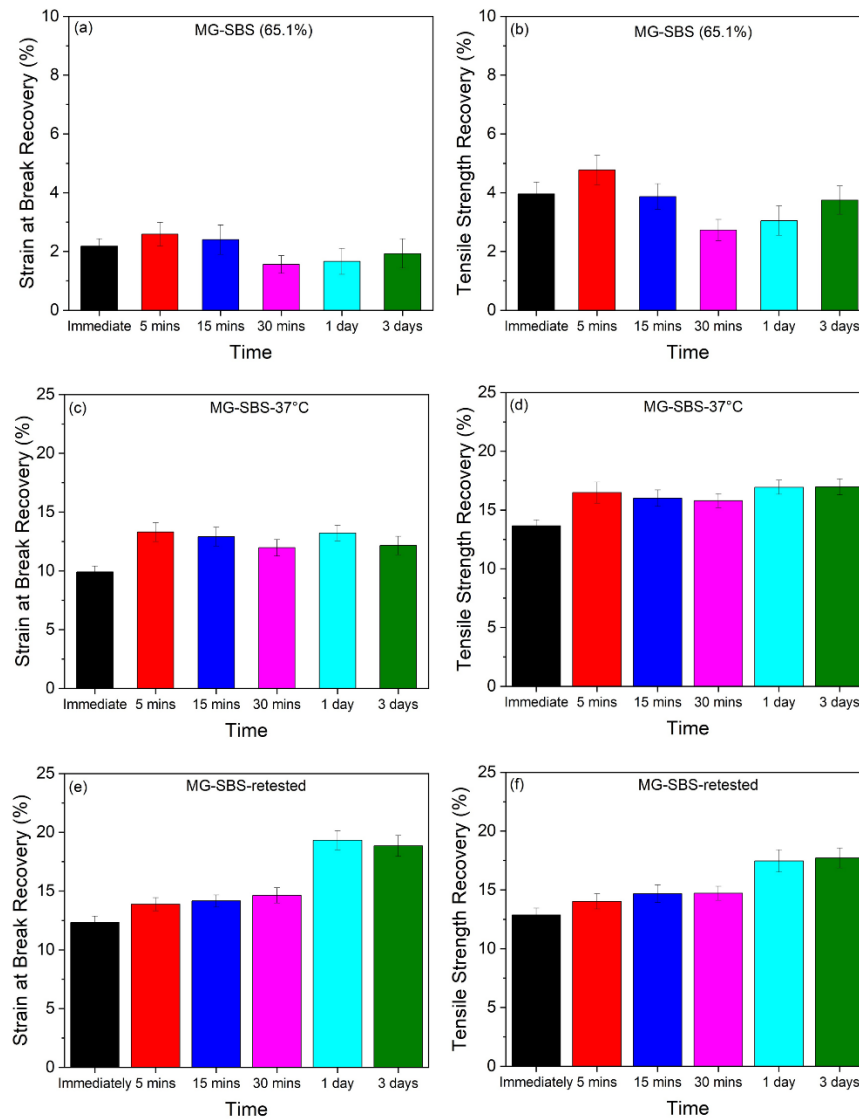


Figure 4.13 (a) Self-healing of MG-SBS (65.1%) at room temperature for strain at break recovery and (b) tensile strength recovery. (c) Self-healing for MG-SBS at 37

°C for strain at break recovery and (d) tensile strength recovery. (e) Retesting self-healing for MG-SBS at room temperature for strain at break recovery and (f) tensile strength recovery

4.2.4 Electrical self-healing under low electrical field

Thus far, the mechanical self-healing abilities of MG-SBS has been demonstrated. However, within a dielectric energy harvesting or actuation device, a significant stress is applied to the material due to high operating electrical fields. Therefore, the ability of MG-SBS to recover its electrical breakdown strength is of significant importance for a longer material lifetime and potential reusability. As seen from Figure 4.14, impedance spectroscopy was performed on MG-SBS to obtain (a) the AC conductivity, (b) the capacitance and (c) the phase angle prior to electrical breakdown, after electrical breakdown and after healing MG-SBS for 24 hours at room temperature. Prior to breakdown of MG-SBS, Figure 4.14a shows that the AC conductivity has a frequency independent response at low frequencies, where the AC conductivity is less than $1 \times 10^{-9} \text{ S m}^{-1}$. The response of the polymer becomes frequency dependent above 10^3 Hz for the AC conductivity. This behaviour is defined as the universal dielectric response and is observed in many insulating materials.²⁶ The capacitance for MG-SBS in Figure 4.14b demonstrated a frequency dependent capacitive response, also observed in the phase angle in Figure 4.14c. In a capacitive material, the ac current lags ac voltage by -90° , thus the phase angle is -90° above 10^2 Hz , but frequencies $<10^2 \text{ Hz}$, the phase angle tends towards 0° due to the small presence of conductivity within the elastomer.

To test the electrical self-healing abilities of MG-SBS, a $425 \mu\text{m}$ thick elastomer film was subjected to electrical breakdown by placing the electrode region under a 20 MV m^{-1} (8.5 kV) nominal electric field (see section 4.2.6 for more information about the electric fields used) until electrical breakdown was detected in the voltage monitoring channel of the high-voltage power supply. This resulted in a pinhole formation in the elastomer with a radius of $50 \mu\text{m}$, as seen in Figure 4.14d, caused by localised Joule heating creating thermal ‘hot-spots’ for thermal runaway. This acts as a positive feedback loop as the Joule heating increases the electrical conductivity at these hot-spots, increasing the degree of localised heating until the material breaks down.²⁷ To

prevent propagation of the material failure, the voltage supply was switched off immediately upon detection of electrical breakdown.

The result of electrical breakdown is seen clearly in the AC conductivity, capacitance and phase angle responses of MG-SBS. After breakdown, the AC conductivity increases to $1 \times 10^{-4} \text{ S m}^{-1}$ and displays a broadly frequency independent response. The phase angle is close to 0° across the entire frequency range as the voltage and current are now in-phase, typical of a pure conductor. Additionally, the capacitance increased significantly, with a larger response at lower frequencies. The now frequency dependent response of the capacitance is common in conductive materials.¹⁷

MG-SBS was then allowed to self-heal autonomously for a 24 hour period before re-testing the electrical response under a $2.5 \times 10^{-3} \text{ MV m}^{-1}$ electric field. As seen in Figure 4.14a-c, the AC conductivity, capacitance and phase angle exhibit the same response as prior to electrical breakdown, demonstrating that MG-SBS has been able to recover some of its electrical properties and its insulating nature.

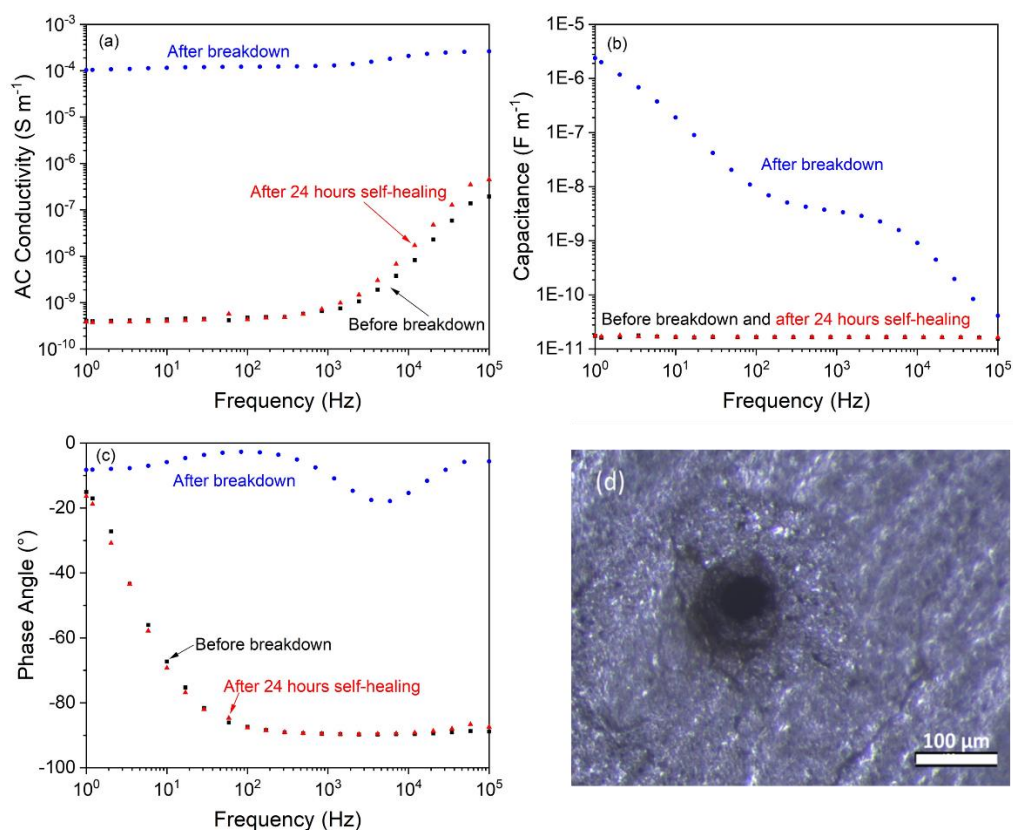


Figure 4.14 Electrical self-healing testing at low electrical fields ($2.5 \times 10^{-3} \text{ MV m}^{-2}$) using impedance spectroscopy to obtain (a) AC conductivity, (b) capacitance and (c)

phase angle vs Frequency. (d) SEM image of the pinhole defect formed in MG-SBS upon breakdown of the elastomer

4.2.5 Effect of self-healing on the mechanical behaviour of MG-SBS

The effect of self-healing on the mechanical behaviour of MG-SBS has been investigated using cyclic stress softening and stress relaxation with different degrees of grafting of methyl thioglycolate. Therefore MG-SBS and MG-SBS (65.1%) were selected due to differing strengths of self-healing, whilst a new variation of MG-SBS, MG-SBS (52.1%) was synthesised which displayed no self-healing ability whilst being influenced by the methyl thioglycolate grafting. ^1H NMR and FTIR for MG-SBS (52.1%) are available in Appendix Figure 4 and the results are consistent with previously synthesised MG-SBS versions.

Figure 4.15a-c shows the cyclic stress softening of all four elastomers for the first and fifth cycle at elongations of 100%, 300% and 500% respectively. Visually, the behaviours of SBS and the chemically modified MG-SBS based elastomers within these cycles are different. SBS has a significantly more thermoplastic response and demonstrates an increase in stress at higher strains due to polymer chain crystallisation from the polymer chains in the soft butadiene block orientating with the direction of elongation,²⁸ and large hysteresis loop. In contrast, MG-SBS displays a more linear, elastic response with a significantly smaller hysteresis loop as the side groups inhibits polymer chain crystallisation upon elongation due to steric hinderance²⁸. The hysteresis losses were calculated, Figure 4.15d. Across all three elongations, SBS and MG-SBS (52.1%) demonstrate similar hysteresis energy loss from the material, 38.6% and 40.2% at 100%, 58.0% and 48.3% at 300% and 64.8% and 56.4% at 500% respectively. The high hysteresis loss is due to large viscous losses attributed to the lack of self-healing interactions between the polymer chains and a lack of compatibilisation between the styrene and butadiene blocks of SBS. As the grafting is increased in MG-SBS (62.1%) and MG-SBS, the viscous losses decrease significantly. Both of these elastomers exhibit a degree of self-healing, arising from the electrostatic interaction between methyl thioglycolate and styrene (explained further in section 4.2.3) preventing losses in the elastomer, as well as the compatibilisation of the two blocks of SBS to form a single polymer phase.

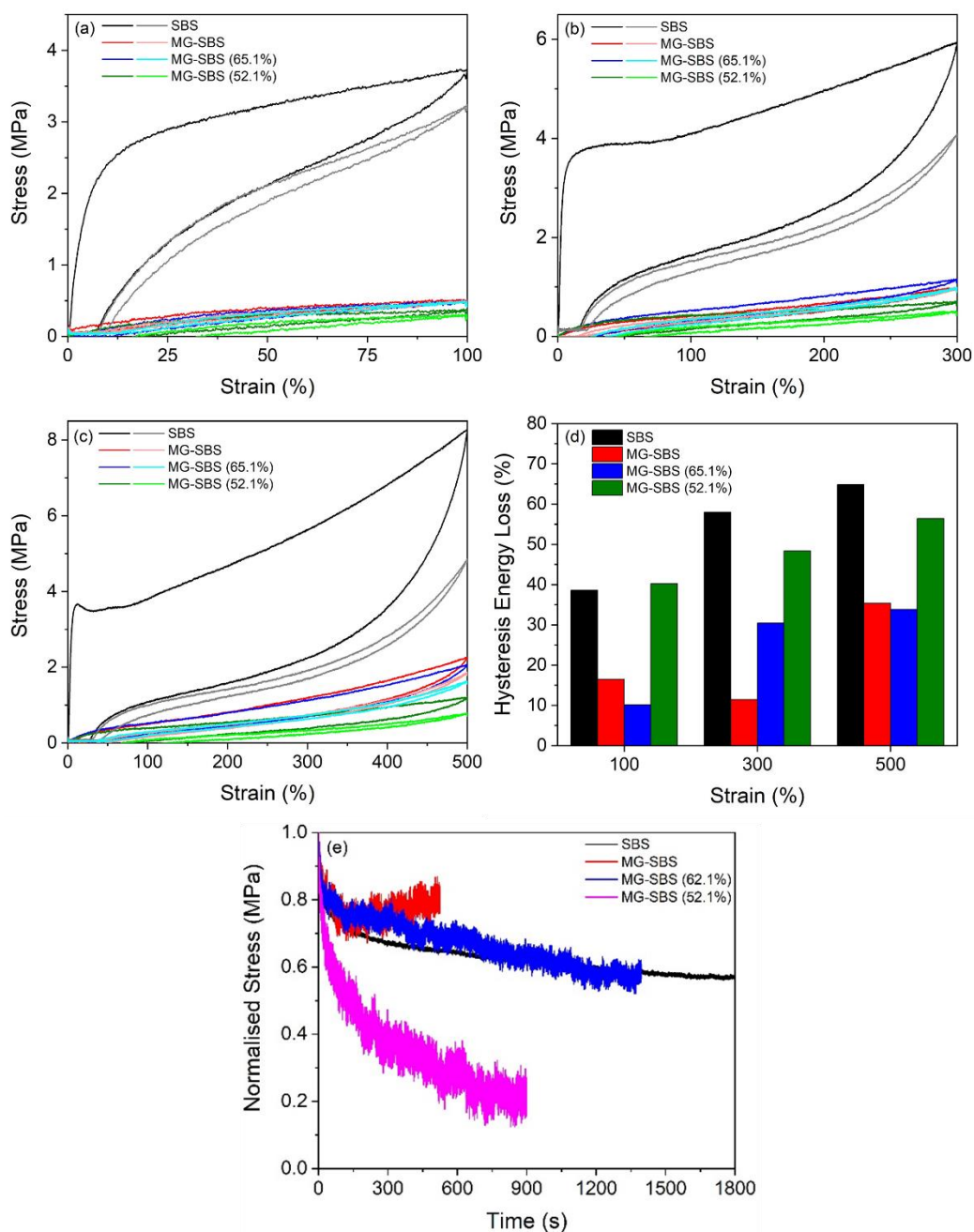


Figure 4.15 Cyclic strain softening of SBS, MG-SBS, MG-SBS (65.1%) and MG-SBS (52.1%) at (a) 100%, (b) 300% and (c) 500% strain. In these graphs, the darker colour is the first strain cycle and the lighter colour is the fifth strain cycle for the respective materials. (d) Summary of the hysteresis loss of the elastomers between the first cycle and fifth cycle. (e) Normalised stress relaxation testing of over varying time periods until 30 mins. Samples tested until deemed to be in equilibrium.

This behaviour was explored further through stress relaxation testing in Figure 4.15e. In SBS, the elastomer decreased to a normalised stress equilibrium of 0.6 MPa after a 30 minute time period. This decrease was attributed to polymer chain slippage in SBS.

Comparatively, MG-SBS (52.1%) decreased significantly more to a normalised stress equilibrium of 0.2 MPa. The difference in behaviour between MG-SBS (52.1%) and SBS was due to grafted polar groups of methyl thioglycolate reducing chain entanglement between the polymer chains and an inability for polymer chain crystallisation to take place upon elongation,²⁸ causing polymer chain slippage to occur to a much greater degree.

As the grafting degree is increased in MG-SBS (62.1%), the normalised stress equilibrium resides at a similar level to SBS between 0.55 - 0.60 MPa. The recovery in the normalised stress value of MG-SBS (62.1%) is attributed to the self-healing interaction present resulting in the interchain electrostatic interaction holding polymer chains in place and preventing them from slipping, despite the reduced polymer chain entanglement.

The behaviour of MG-SBS shows a normalised equilibrium stress at 0.8 MPa, higher than SBS. MG-SBS has the strongest interchain electrostatic behaviour present, holding the polymer chains in place. In fact, a small recovery in the normalised stress values can be observed in the elastomer. This is attributed to a small recovery of the polymer chain slippage due to self-healing.

Overall, this shows that the degree of grafting within MG-SBS has a large effect on its mechanical properties. MG-SBS exhibits the most consistent mechanical behaviour, for use in energy harvesting devices over long lifetimes compared to SBS, MG-SBS (52.1%) and MG-SBS (62.1%) and MG-SBS could recover some of its mechanical properties in-situ during stress relaxation testing.

4.2.6 Investigating the actuation abilities of MG-SBS using dielectric elastomer actuators (DEA)

As dielectric elastomers are able to behave as energy transducers, they are able to convert mechanical energy to electrical energy and *vice versa*. Therefore, the investigation into the actuation abilities of MG-SBS is key to develop highly electroactive materials able to respond to the application of an electric field. To quantify theoretically the actuation abilities of elastomers, a Figure of Merit, $FoM_{Actuation}$, from equation 4.7 was used:

$$FoM_{Actuation} = \frac{3\varepsilon_0\varepsilon_r E_b^2}{\gamma} \quad (4.7)$$

where ϵ_0 is the permittivity of free space, ϵ_r is the relative permittivity, E_b is the electrical breakdown strength of the material and Y is the Young's modulus of the material and all $FoM_{Actuation}$ values were normalised to $FoM_{Actuation}(SBS)$.^{2, 29} This allowed the theoretical actuation behaviour to be calculated for different elastomers. Table 4.1 shows the experimentally measured properties of SBS and MG-SBS below. The calculated $FoM_{Actuation}$ for MG-SBS is 161.1 indicating that the elastomer is significantly better at actuating than SBS, attributed to the lower Young's modulus, the higher ϵ_r and the higher E_b of MG-SBS.

Table 4.1 Table of experimentally determined properties of SBS and MG-SBS and the theoretically determined $FoM_{Actuation}$

	Young's modulus (MPa)	Elongation at break (%)	Elongation at break after self-healing (%)	Elongation recovery (%)	Normalised stress relaxation (MPa)	ϵ_r at 1 kHz	E_b (MV m ⁻¹)	$FoM_{Actuation}$
SBS	51.7	857	Not self-healable	-	0.55	2.8	17.7	1.0
MG-SBS	2.4	569	117% at RT for 3 days	21	0.8	11.4	29.8	161.1

Experimental actuation of SBS and MG-SBS as indicated by the $FoM_{Actuation}$ demonstrated vast differences in the actuation performance of SBS and MG-SBS. Under actuation testing, SBS with 300 μm initial thickness did not demonstrate significant actuation ability before failure under an electric field of 17.7 MV m⁻¹ when under equal bi-axial pre-strain of 33%. When pre-strain is applied, electric field is defined as the true electrical field and follows equation 4.8:

$$E = \frac{V}{H} \times \lambda^2 \quad (4.8)$$

where E is true electrical field, V is applied voltage, H is thickness of sample and λ is applied strain.

Introducing an applied pre-strain forces the material to actuate preferentially in the direction of the applied pre-strain, whilst simultaneously reducing the thickness of the material and the breakdown voltage.³⁰ In comparison, under the same conditions MG-SBS with a thickness of 510 μm demonstrated a radial actuation strain of up to 4.2% under a 29.8 MV m⁻¹ electric field before electrical breakdown took place shown in

Figure 4.16. This corresponded to an areal actuation strain of 8.7% before failure. The actuation abilities of MG-SBS demonstrate that the $FoM_{Actuation}$ value of 161.1 with respect to SBS is valid. The excellent actuation performance of MG-SBS is explained by consideration of three factors. Firstly, the lower Young's modulus of MG-SBS results in a larger material deformation under the same Maxwell pressure. Secondly, the higher relative permittivity of MG-SBS generates a larger Maxwell pressure under the same driving voltage and electric field compared to SBS. Finally, the higher breakdown strength of MG-SBS allows a higher driving voltage, and thus a higher electric field, to be applied as there can be a larger actuation stress in planar directions, $\Delta\sigma_{1,2}$, larger actuation strain in the radial direction, ΔS_r , and a larger change in area due to actuation, ΔS_a according to equations 4.9 – 11:

$$\Delta\sigma_{1,2} \propto \varepsilon E^2 \quad (4.9)$$

$$S_r \propto \varepsilon E^2, \frac{1}{Y} \quad (4.10)$$

$$S_a = S_r^2 \quad (4.11)$$

where ε is the permittivity of a dielectric elastomer ($\varepsilon = \varepsilon_r \varepsilon_0$), E is the applied electric field and Y is the Young's modulus of the elastomer.

The force generated by MG-SBS under actuation was also investigated and compared to SBS and VHB 4910. VHB 4910 is regarded as the best commercially available dielectric elastomer for actuation due to its relative permittivity of 4.5³¹ and a breakdown strength of 20 MV m⁻¹ without pre-strain³² and 55 MV m⁻¹ with 15% equibiaxial pre-strain.³⁰ In this experiment, the pre-strain of the elastomers was changed to 20% uniaxial strain, increasing the thickness of the samples and increasing the electrical breakdown strength. The actuation force is defined as the difference in the force in the unactuated and actuated state.

SBS exhibited an actuation force of 0.03 N under at 32.1 MV m⁻¹ applied electric field and showed no actuation force below 20 MV m⁻¹, Figure 4.16c. Comparatively, VHB exhibited a weak actuation response at 16.5 MV m⁻¹ however it actuated with a force of only 0.02 N under a 32.1 MV m⁻¹ electric field. Instead, MG-SBS demonstrated an actuation response of 0.015 N when investigated at 12 MV m⁻¹ which increased to 0.12 N at an electric field of 32.1 MV m⁻¹. This response is four times greater than for SBS and up to six times greater than for VHB. The actuation force of the elastomers

solely depends on the Maxwell pressure generated by the material, and is independent of Young's modulus. Therefore, from equation 4.9 as the actuation force of MG-SBS is four times greater than for SBS, it agrees well with the increase in relative permittivity observed (from 2.8 to 11.4).

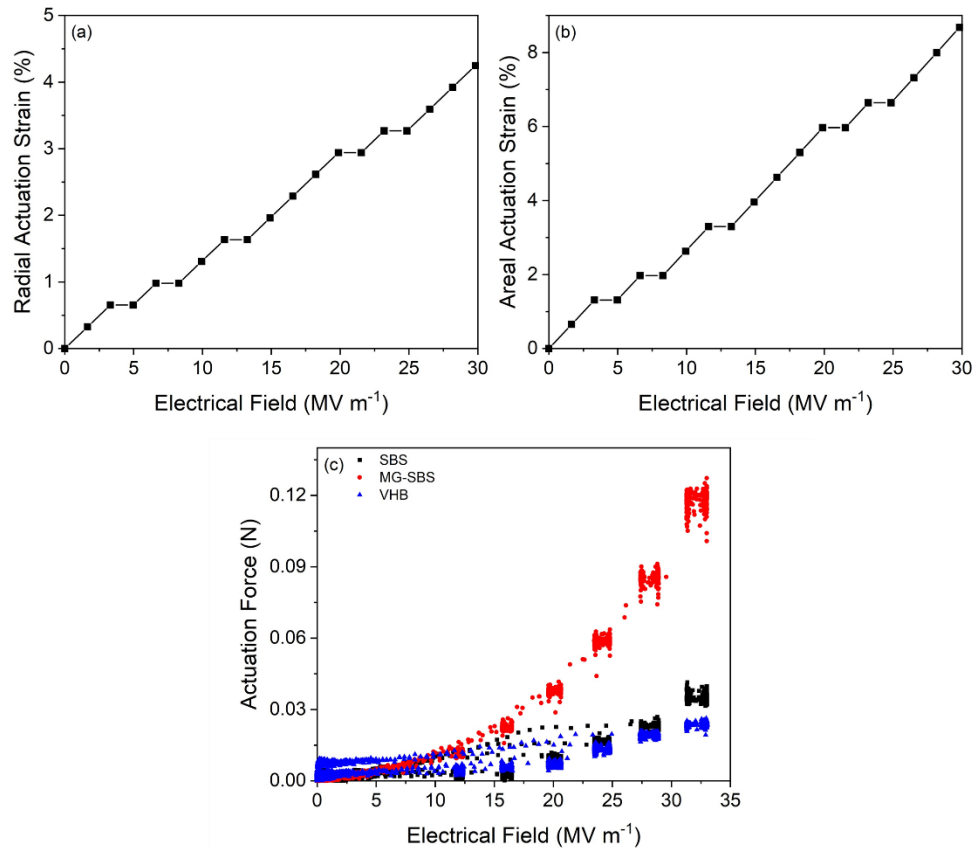


Figure 4.16 (a) Radial actuation strain and (b) areal actuation strain of MG-SBS under different electric fields. (c) Actuation force of SBS, MG-SBS and VHB 4910 under increasing electric field

However, as previously stated, MG-SBS has a mechanical self-healing and has indicated an electrical self-healing ability, from impedance testing in section 4.2.4. To quantify the electrical self-healing ability, the electrical response of MG-SBS can be retested using polarisation-electric field loops to quantify how strong an electric field can be withstood before electrical breakdown occurs. As can be seen in Figure 4.17, the polarisation-electric field loops of pristine MG-SBS up to 4 kV displayed a linear response due to its capacitive nature. As the samples in polarisation-electric field loop testing were not pre-strained, their breakdown is compared to the nominal electric field

at which MG-SBS suffered electrical breakdown at 18.1 MV m^{-1} , given by equation 4.12:

$$E = \frac{V}{H} \quad (4.12)$$

Additionally, the gradient of the response is constant as the material is insensitive to the change in electric field, due to the insulating nature of the elastomer. The polarisation-electric field loop of pristine MG-SBS could not be tested at a higher electric field due to limitations in the equipment.

In comparison, self-healed MG-SBS also demonstrated a linear response and a constant gradient as the material recovered its capacitive and insulating nature. However, the elastomer experienced electrical breakdown at a significantly lower electric field. If left for 24 hours, MG-SBS recovered its electrical breakdown strength 6.9% to an electric field strength of 1.25 MV m^{-1} (not shown). This low self-healing ability was attributed to the healed region containing electrically conductive material generated from electrical breakdown, such as carbon. The conductive material can concentrate the electric field, leading to localised Joule heating in the healed region, increasing the conductivity further and thus limiting the self-healing effect.²⁷ It was observed that the application of a small mechanical compression (by utilising a small amount of finger pressure) to the pinhole region increased the electrical breakdown strength recovery of the material up to 17.6% (at 3.1 MV m^{-1}), as observed in Figure 4.17b. This recovery agrees well with the recovery in mechanical properties observed for MG-SBS in section 4.2.3. The reason behind this can be rationalised by considering the self-healing cycle. The application of pressure increases the surface contact of the in the damage region. The contact assists surface wetting and thus leads to a greater polymer chain diffusion taking place, increasing the observed electrical breakdown strength recovery.³³

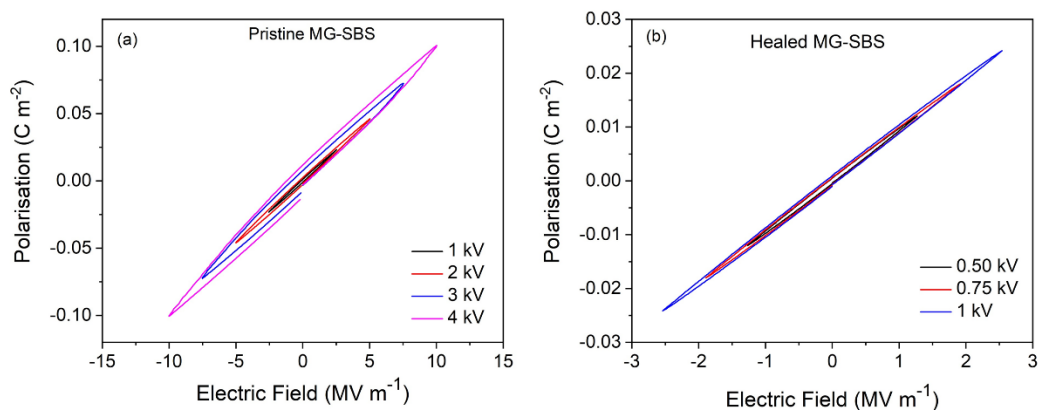


Figure 4.17 Polarisation-electric field loops for (a) pristine MG-SBS up to 4 kV and (b) healed MG-SBS up to 1 kV

Thus, this evidence of electrical breakdown strength recovery led to three important questions. Firstly, is the electrical breakdown recovery affected by the method of failure in the elastomer *i.e.* would 17.6% electrical breakdown recovery be observed if the elastomer was mechanically damaged rather than electrically damaged? Secondly, can the pinhole defect site be cleaned to remove the conductive material present and increase the observed electrical recovery? Thirdly, if MG-SBS suffers both a mechanical and an electrical failure, to what degree can the elastomer recover?

To introduce mechanical damage to MG-SBS, a sharp scalpel blade was used to cut a 25 mm slit through a 510 μm film, Figure 4.18a, and was allowed to self-heal at room temperature under the application of a 5 N load to assist with a planar surface contact between the exposed surfaces. After healing, MG-SBS is able to be stretched at the healed site, demonstrating that the mechanical damage has been macroscopically closed (see Figure 4.18a(2)).

Thus a cross-section of the healing site was imaged using Scanning Electron Microscopy (SEM) to visualise the microscopic healing of MG-SB in Figure 4.18b-c. The edge of the MG-SBS cross-section shows a gap between the two polymer surfaces of up to 50 μm , which decreases as the two polymer pieces re-join. This area is irreversibly damaged from the pressure of the scalpel blade deforming the elastomer to cut through it. Away from the edge in Figure 4.18c, a white scar line is observed immediately where the two sides of MG-SBS reconnect. This scar line was attributed to an incomplete self-healing taking place, possibly with chain diffusion occurring but not full chain randomisation, according to the self-healing theory by Kim and Wool.²⁰

However, the scar line fades and becomes unobservable in the bulk elastomer demonstrating that polymer chain entanglement took place and randomised fully, bridging the two pieces of MG-SBS.

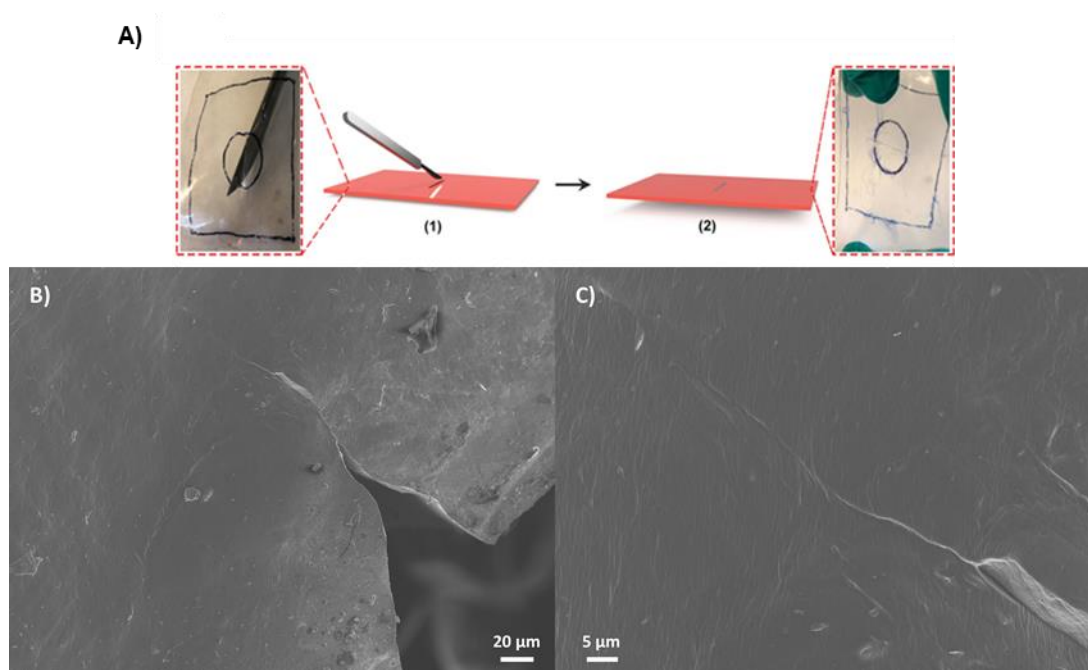


Figure 4.18 Diagram of mechanical damage to MG-SBS for self-healing actuation test. Adapted from Zhang et al.³⁴ SEM imaging of self-healed MG-SBS after mechanical damage with (b) image of the microscopic damage present, the scar and the bulk healed polymer and (c) close image of the scar in the healing site of MG-SBS and its disappearance

To assess the self-healing of MG-SBS from mechanical damage, impedance spectroscopy was initially performed to confirm an initial recovery of the electrical properties. As can be seen from Figure 4.19a-b, both the AC conductivity and phase angle recovery to similar to the original value of $5 \times 10^{-10} \text{ S m}^{-1}$ and -90° respectively. Self-healed MG-SBS does display a slightly higher AC conductivity, higher loss and a stronger phase angle response towards conducting at lower frequencies due to the residual damage at the healed site across the electrode region. In addition, Figure 4.19c-d demonstrate the polarisation-electric field loops of both MG-SBS and self-healed MG-SBS after mechanical damage. After healing, the loops remain linear and with a constant gradient demonstrating that the elastomer is still capacitive and electrically insulating.

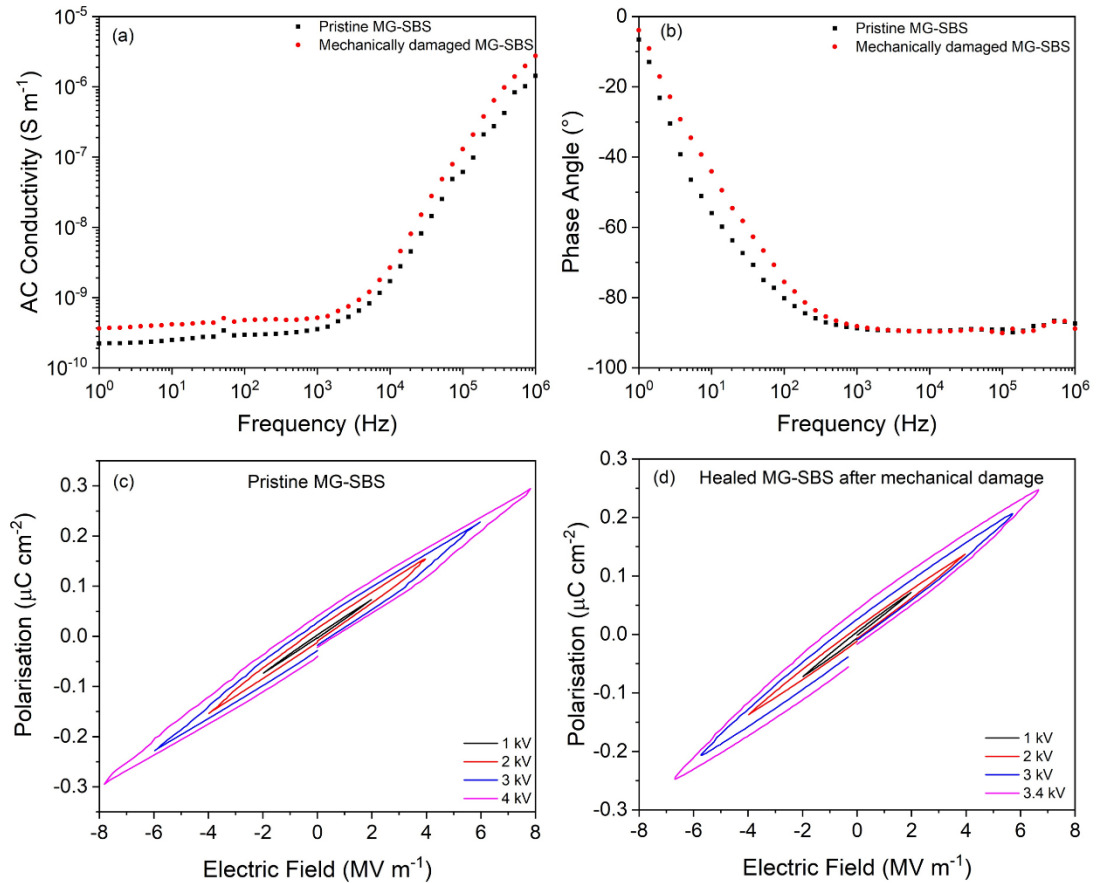


Figure 4.19 Impedance spectroscopy of pristine MG-SBS and healed MG-SBS after mechanical damage for (a) AC conductivity, (b) phase angle. Polarisation-electric field loops of (c) pristine MG-SBS and (d) healed MG-SBs after mechanical damage

Nonetheless, a comparison of the polarisation-electric field loop of MG-SBS and 500 μm thick self-healed MG-SBS under a $5.9 MV m^{-1}$ electric field in Appendix Figure 5 shows that there is a widening of the loop for the healed elastomer compared to the pristine MG-SBS. This agrees well with the observed increase in AC conductivity and phase angle of Figure 4.19a-b for healed MG-SBS.

However in terms of electrical breakdown strength recovery, whilst 500 μm thick pristine MG-SBS broke down at a nominal electrical field of $18.1 MV m^{-1}$, self-healed MG-SBS after mechanical damage broke down under an electric field of $6.7 MV m^{-1}$ corresponding to a recovery of 38% as seen from Figure 4.19d.

As recovery after mechanical damage showed an increased electrical breakdown strength compared to recovery after electrical breakdown (38% compared to 15%),

next it was investigated whether the conductive material formed during electrical breakdown could be removed to increase the electrical breakdown strength recovery.

To determine whether this is feasible, SEM imaging of the pinhole site formed during electrical breakdown of MG-SBS is shown in Figure 4.20. 300 μm thick MG-SBS was electrically broken down under a nominal electric field of 32.8 MV m^{-1} leading to a pinhole defect 90 μm in diameter. According to Zakrevskii *et al.*, electrical breakdown is the ionisation, electron avalanche and formation of a conducting channel arising from pores or low density regions within a polymer.³⁵ Conducting carbonised debris is visible around the edge of the pinhole.³⁶ The carbonised debris is formed by vaporised polymer reacting with air during electrical breakdown.³⁴

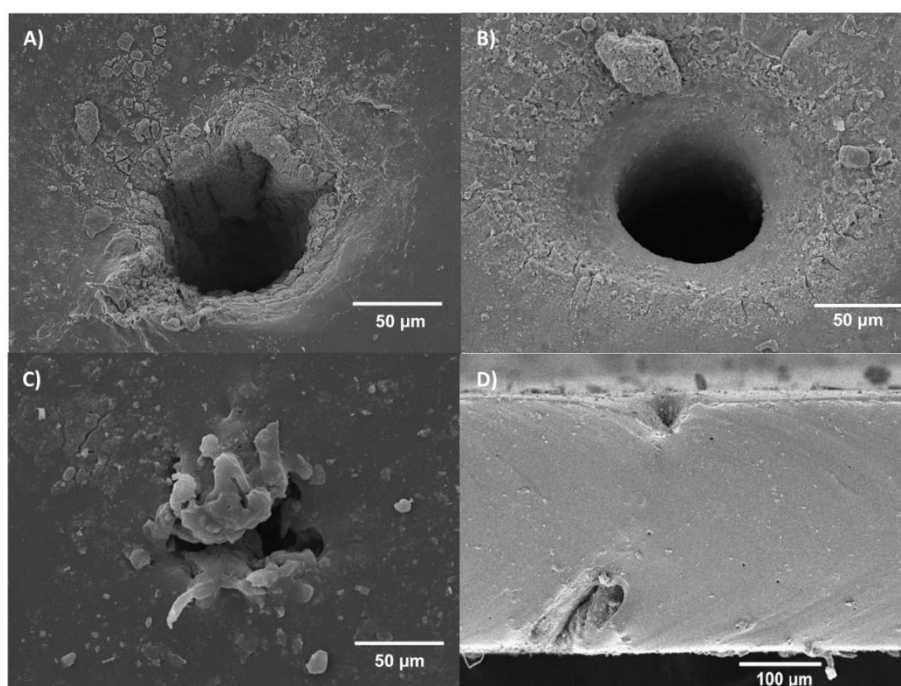


Figure 4.20 SEM imaging of MG-SBS (a) after electrical breakdown forming a 90 μm pinhole defect, (b) after clearing debris with needle probe and (c) after application of finger pressure for self-healing of MG-SBS. (d) Cross-sectional view of MG-SBS after cleaning of pinhole failure with a needle probe and subsequently self-healed

To clear the debris, one of two methods was utilised – either penetrating the pinhole region using a hollow hypodermic needle or by puncturing with a needle probe which had a thinner, solid needle, with optical images of both needles shown in Appendix Figure 6. This cleared the pinhole and produced smooth walls with less visible carbonised debris making it more suitable for self-healing, as observed in Figure

4.20b. Finally, after the application of finger pressure for self-healing, the SEM image in Figure 4.20c shows elastomer is visibly self-healed and exhibits a similar nature to other polymers which have been punctured.³⁷ As there is still some damage on the surface of the elastomer, a cross-sectional SEM image in Figure 4.20d demonstrated the extent of the healing of MG-SBS. MG-SBS indicates complete self-healing within the middle of the film, as no damage was visible. However, the edges of MG-SBS had not successfully healed. This is either due to remnant carbonised material or damage to the polymer chains in this region from electrical breakdown inhibiting self-healing. Therefore, the use of a hypodermic needle or needle probe demonstrates a simple, easy way to remove carbonised material to heal elastomers after electrical breakdown and retain self-healing at room temperature

After demonstrating the clearing of the pinhole defect improves the polymer contact sites for self-healing, the improvement in the electrical recovery was quantified. Figure 4.21a-b demonstrates the AC conductivity and phase angle of pristine MG-SBS and after MG-SBS has been healed by clearing the pinhole defect site with a needle probe. The graphs show that MG-SBS recovered to an almost identical behaviour of pristine MG-SBS of $3 \times 10^{-10} \text{ S m}^{-1}$ and -90° at 10^3 Hz respectively, certainly closer in behaviour than the recovery of MG-SBS after mechanical damage.

Figure 4.21c-e show the polarisation-electric field loops of $300 \mu\text{m}$ thick pristine MG-SBS, hypodermic needle assisted self-healed MG-SBS and needle probe assisted self-healed MG-SBS respectively. Overall, all three graphs show a linear and constant gradient polarisation response indicating the recovery of their insulating and capacitive nature. However, there is a slight different in polarisation-electric field loop behaviour for these materials when the electric field loops of 10 MV m^{-1} are compared in Appendix Figure 7. As noted from Figure 4.21c, e, both pristine MG-SBS and healed MG-SBS with needle probe withstood an electric field of 13.8 MV m^{-1} , demonstrating a minimum electrical breakdown recovery of at least 47%, whereas healed MG-SBS with a hypodermic needle failed under an electric field of 10.7 MV m^{-1} . This corresponded to an electrical breakdown recovery of 36%. The difference in the self-healing ability of the two MG-SBS elastomers is directly related to the method of cleaning the pinhole defect. The larger, hollow hypodermic needle was significantly bigger than the pinhole defect formed ($90 \mu\text{m}$ diameter) and removed the conducting carbonised material from the pinhole defect site less effectively, as noted by the wider

polarisation-electric field loop in Appendix Figure 7 indicating a higher conductivity³⁸ compared to MG-SBS and healed MG-SBS using a needle probe.

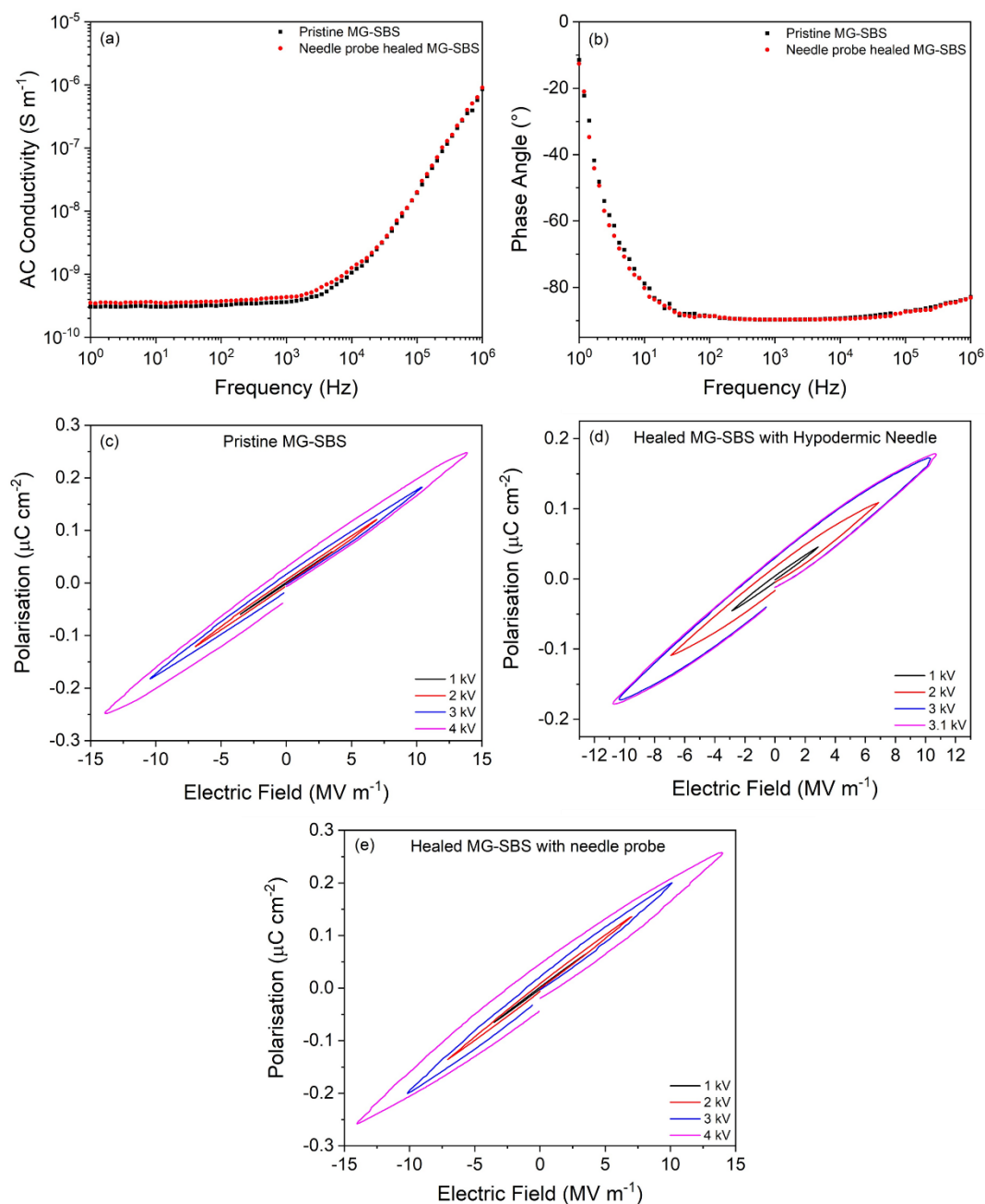


Figure 4.21 (a) AC conductivity of MG-SBS before and after self-healing assisted using a needle probe, (b) phase angle of MG-SBS before and after self-healing assisted using a needle probe, (c) polarisation-electric field loop of pristine MG-SBS, (d) polarisation-electric field loop of MG-SBS after self-healing assisted using a hypodermic needle and (e) polarisation-electric field loop of MG-SBS after self-healing assisted using a needle probe

Thus far, MG-SBS demonstrated good electrical recovery properties after both electrical failure and mechanical damage. However, this has not considered the actuation performance of the healed materials, nor has it established the true recovery of healed MG-SBS using a needle probe. Therefore, the actuation performance of MG-SBS healed after mechanical damage and MG-SBS healed using a needle probe was investigated and compared to the actuation performance of pristine MG-SBS. Additionally, the breakdown recovery of MG-SBS both mechanically damaged and electrically broken down MG-SBS was also investigated.

500 μm thick MG-SBS was actuated with 33% pre-strain applied after either electrical breakdown or mechanical damage, and actuated until electrical failure, see Figure 4.22a-d. The electrical breakdown pinhole defect formed was 1.5 mm, significantly larger than the 90 μm defect formed when no pre-strain was applied. The pre-strain caused elastic deformation at the breakdown site and can act as a site for additional mechanical damage in the elastomer film whereas a self-healing ability in elastomers can prevent this from occurring. Therefore it is equally important that the self-healing ability of an elastomer heals both the mechanical and the electrical properties of the elastomer to a high degree, otherwise the elastomer can mechanically fail under deformation.

To heal MG-SBS after electrical failure, the carbon grease electrode in Figure 4.22a was removed, before clearing debris with a needle probe followed by subsequent self-healing as seen in Figure 4.22b. The elastomer was then subjected to an applied electric field. As seen in Figure 4.22e-f, pristine MG-SBS failed at 29.8 MV m^{-1} , actuating radially 4.2% and exhibited an areal actuation of 8.7%. Comparatively, healed MG-SBS after electrical breakdown experience an electrical recovery of 66.7% to 19.9 MV m^{-1} . Before failure, the elastomer was able to actuate radially 2.9% and exhibited areal actuation of 6.0%, a 69% recovery in the actuation ability. This demonstrates that the solid needle was able to very efficiently clear away conducting carbon debris, especially compared to the efficiency of using a large hollow needle.

MG-SBS mechanically damaged by a 25 mm slit demonstrated a lower electrical recovery of 39%, failing under an electric field of 11.6 MV m^{-1} . Before failure, mechanically damaged MG-SBS actuated radially 1.7% and exhibited an areal actuation of 3.5% corresponding to a actuation recovery of 40%. The healing

efficiency from this failure mode is significantly lower than after electrical failure despite no presence of conducting debris from failure. This was attributed to the large size of the mechanical failure.

Therefore, MG-SBS was also punctured with a small hole (1.5 mm in diameter) and then healed. MG-SBS recovered 79% of its original electrical breakdown strength, failing under an electric field of 23.7 MV m^{-1} . The smaller hole allowed better contact at the failure site within MG-SBS, enabling stronger self-healing to take place. MG-SBS was also able to recovery its actuation abilities by 90%, actuating radially by 3.8% before failure and exhibiting an areal actuation of 7.8%.

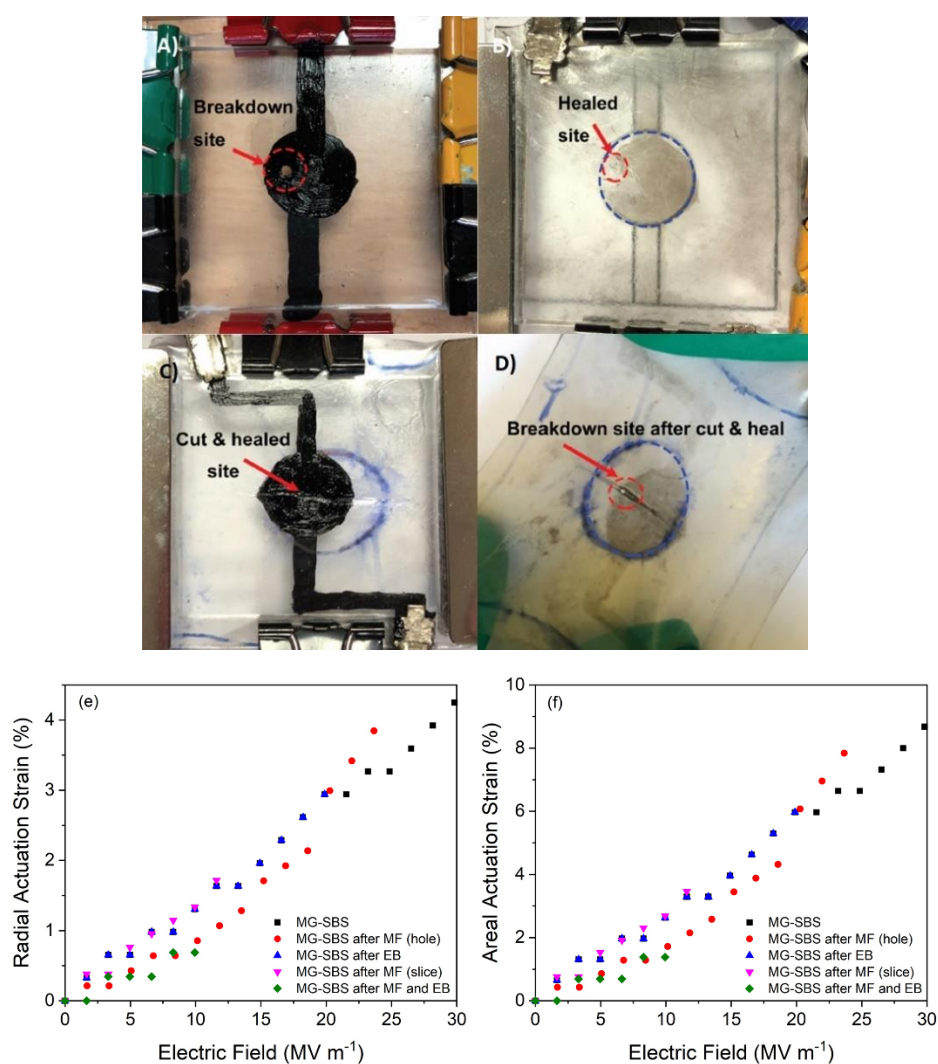


Figure 4.22 (a) MG-SBS after electrical breakdown in actuation device. Pinhole size is 1.5 mm. (b) MG-SBS after self-healing using a needle probe to remove carbonised debris, (c) mechanically damaged and healed MG-SBS and (d) mechanically damaged and healed MG-SBS after electrical breakdown and pinhole formation. Adapted from

Zhang et al.³⁴ (e) Radial actuation strain and (f) areal actuation strain under different electric fields for MG-SBS, MG-SBS after electrical breakdown, MG-SBS after damage through a mechanical slit, MG-SBS after damage through a mechanical puncture and MG-SBS after both damage from a mechanical slit and electrical breakdown

Thus far, the investigation into the electrical recovery of MG-SBS only considers one failure mode at one time. Subjecting MG-SBS to both mechanical and electrical failure enables the recovery of MG-SBS to be further demonstrated. Initially, MG-SBS recovers 39% of its electrical properties after mechanical failure from a 25 mm slice. After further electrical breakdown, MG-SBS recovered 86% and 33% of its healed breakdown strength after mechanical damage and of its total breakdown strength respectively. This corresponds to a breakdown field of 9.9 MV m^{-1} , a radial actuation of 0.7% and an areal actuation of 1.4%.

4.2.7 Finite element modelling of MG-SBS electrical breakdown recovery

The presence of voids and defects in the healed MG-SBS elastomers led to inhomogeneity in the electric field distribution under an applied electric field, leading to premature electrical breakdown of the elastomer. To model this, a finite element model was created to simulate MG-SBS under different self-healing conditions. The first model simulated the geometry of the MG-SBS elastomer, and contained surface defects at the top and bottom which are present after healing of the pinhole, see Figure 4.23. Under application of an electric field, the surface defects demonstrate an increase in the localised electric field which act as the site for initiation of electrical breakdown in the elastomer. The conductive phase grows as electrical breakdown is propagated through the material to form a channel, as the increased localised electric field remained at the edges of the defects in the sample. Once electrical breakdown has propagated far enough, the electric fields from the two defect sites begin to overlap with each other and generate an increased electric field across the remaining thickness of the sample. Once this localised electric field increased to failure point, it created a conducting pathway through the elastomer and completed electrical breakdown. As small defects remain after self-healing, despite clearing away conducting carbonised debris, MG-SBS does not recover 100% of its electrical properties.

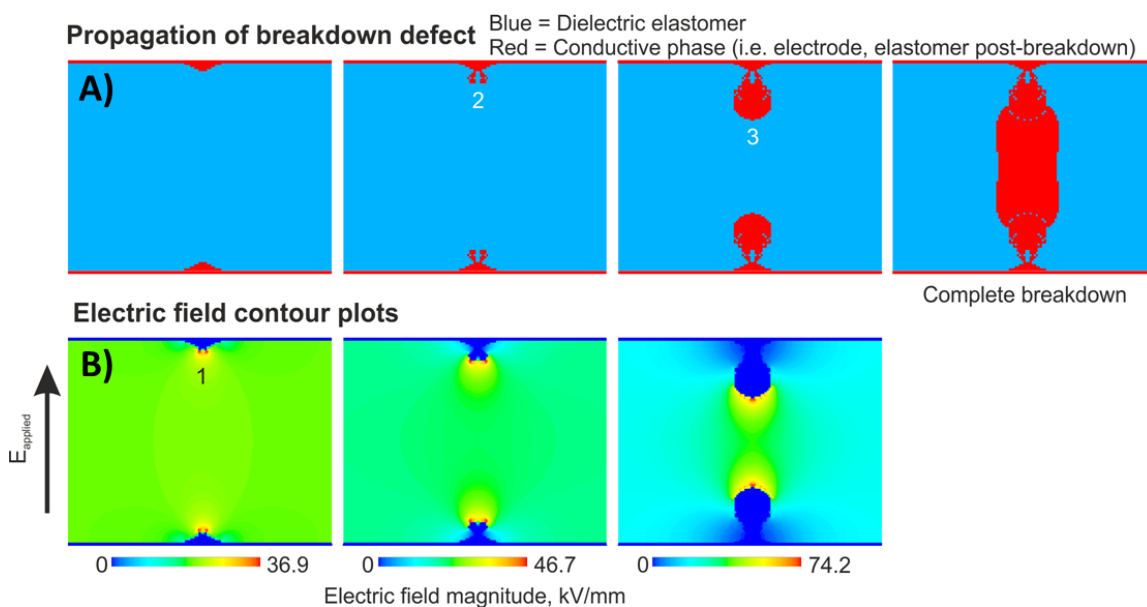


Figure 4.23 (a) Propagation of conductive phase during electrical breakdown in a material and (b) concentration of electric field across the material containing small defects at the surface after self-healing. Adapted from Zhang et al.³⁴

However, the model in its current form does not elaborate why application of finger pressure increased the electrical recovery of MG-SBS from 6.9% to 17.6%, nor why the cleaning step with a needle was necessary to enhance the recovery. Therefore, the model was adjusted to incorporate pores and voids into the self-healed point of the material, see Figure 4.24. Under the application of an electric field, the regions containing the voids also experience an increased electrical field, representing more sites of electric field inhomogeneity within the elastomer. These act as a site for electrical breakdown initiation, forming a conductive path through the material. Once electrical breakdown has been initiated, the high electric field in the next void along assists the propagation of electrical breakdown further through the material, as if hopping from void to void until an electrically conducting channel is formed. This caused electrical breakdown to be experienced by the material under a lower electric field.

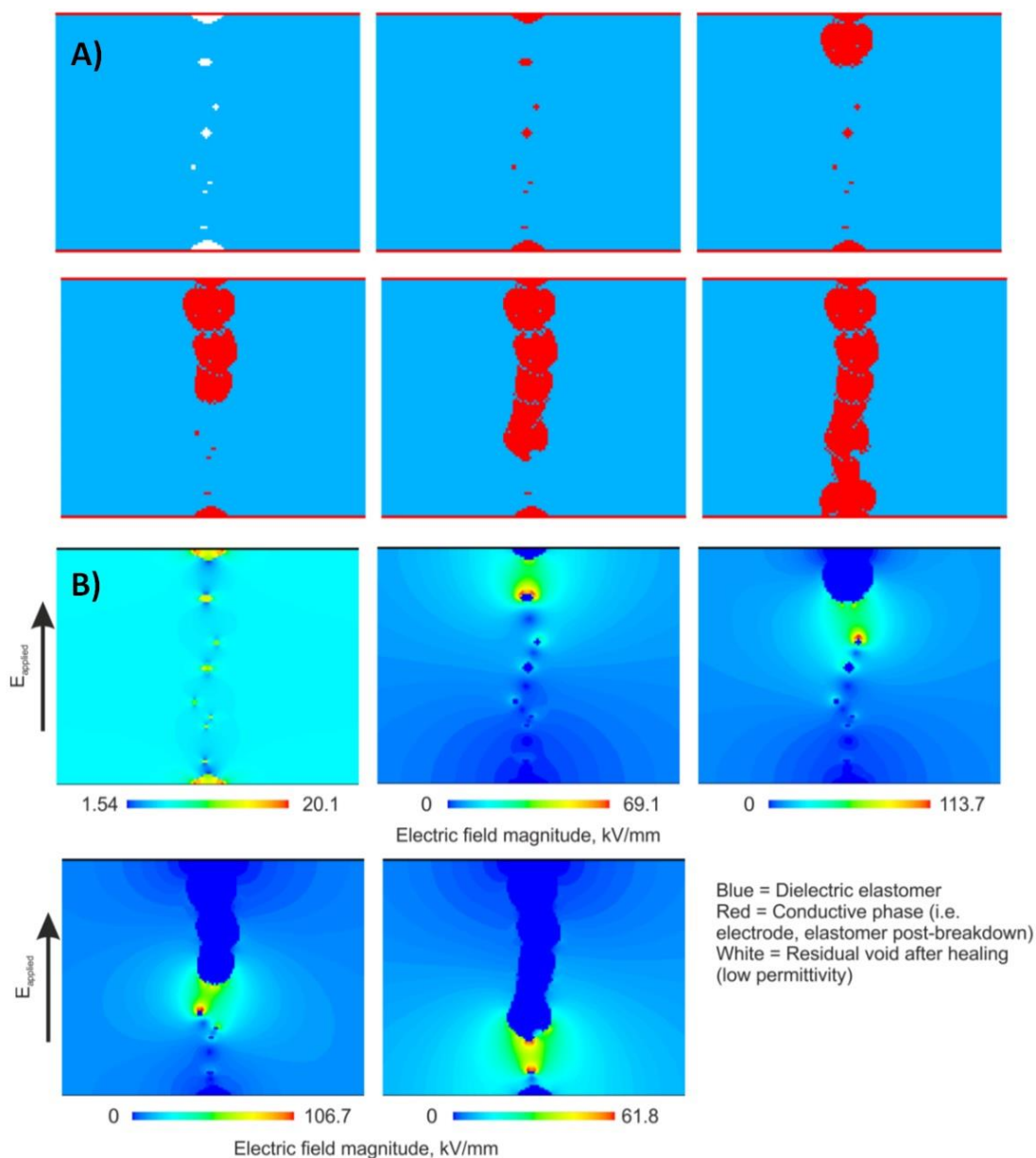


Figure 4.24 (a) Conduction pathway formed and (b) concentration of electric field in a material with surface defects and pores/voids along the healed site of the material. Adapted from Zhang et al.³⁴

4.3 Conclusion

In this chapter, the synthesis conditions for MG-SBS with a high grafting efficiency were optimised. The conditions of 9:1 THF solvent to polymer ratio, 4× excess methyl thioglycolate, 20 minute UV light exposure at 50 W, 0.6 mol% of photoinitiator DMPA at room temperature were used for scaling up reactions. The structure of the synthesised MG-SBS was confirmed *via* ¹H NMR, FTIR and GPC and the grafting

efficiency of methyl thioglycolate was 97.2%. In addition, MG-SBS with a lower grafting ratios, MG-SBS (62.1%) and MG-SBS (52.1%), were synthesised to observe the effect of different grafting ratios on the mechanical properties of the elastomer.

The electrical and mechanical properties of synthesised MG-SBS were investigated. The relative permittivity of MG-SBS was significantly enhanced from originally 2.8 to 11.4 whilst maintaining a low $\tan \delta$ loss and its insulating properties. Meanwhile MG-SBS exhibited a reduced strain at break of 569% whilst a reduction in polymer chain entanglement reduced the Young's modulus making MG-SBS easier to deform compared to SBS. Furthermore, MG-SBS exhibited a lower viscoelastic loss in cyclic stress softening and stress relaxation testing. It was deduced that an interaction kept the polymer chains from slipping and enhanced the cyclic properties of MG-SBS.

Furthermore, MG-SBS exhibited a unique self-healing behaviour whereby after three days at room temperature, the strain at break recovered by 21%. The nature of the mechanical self-healing was found to be dependent on the grafting ratio of methyl thioglycolate, testing temperature and time for self-healing. An investigation into the nature of the self-healing determined that it was caused by the δ^+ protons adjacent to the ester of methyl thioglycolate electrostatically interacting with the δ^- aromatic centre of styrene. This interaction also compatibilised the normally phase separated SBS block copolymer morphology.

Furthermore, the electrical self-healing of MG-SBS, initially under a low electric field was investigated. The electric field was subsequently increased to determine the electrical breakdown strength. Overall it was found that pristine MG-SBS broke down under a 29.8 MV m^{-1} electric field whilst actuation 4.2% radially. Under these conditions, SBS broke down before actuation. The actuation force of MG-SBS was calculated to be 0.12 N, four times higher than for pristine SBS.

Next, the electrical recovery of MG-SBS, after both mechanical damage and electrical failure was investigated. After mechanical damage with a scalpel blade MG-SBS was able to recover up to 39% to an electric field of 11.6 MV m^{-1} whilst still actuating 1.7%. However, upon reduction of the mechanical damage to a small hole from a needle, the electrical recovery increased up to 79% and failed under an electric field of 23.7 MV m^{-1} whilst actuating 3.8%. Furthermore, after electrical failure, MG-SBS was only able to recover 15% of its electrical breakdown strength. However, by

clearing the pinhole defect site of conducting carbonaceous material from electrical breakdown, the electrical breakdown strength of MG-SBS was able to be recovered to 19.9 MV m^{-1} , a 67% recovery whilst actuating 2.9%.

In addition, Finite Element Modelling provided an insight into why MG-SBS does not recover to 100% its electrical breakdown strength. The presence of voids within the healing site enhance the localised electric field and caused failure along the pinhole defect. Furthermore, surface defects from damaged polymer chains or incomplete self-healing act as regions for electrical failure. These also exhibit an enhanced localised electric field, causing localised Joule heating and failure of the elastomer at a lower electric field.

Overall, this chapter demonstrates that MG-SBS has superior electromechanical properties both theoretically and experimentally. MG-SBS exhibits a good actuation performance and is able to self-heal, unlike SBS or MG-SBS with lower grafting ratios. The self-healing enables MG-SBS to have a long lifetime within an actuation or energy harvesting device compared to SBS. MG-SBS also has potential reusability after failure within a device, something which cannot be achieved using unmodified SBS.

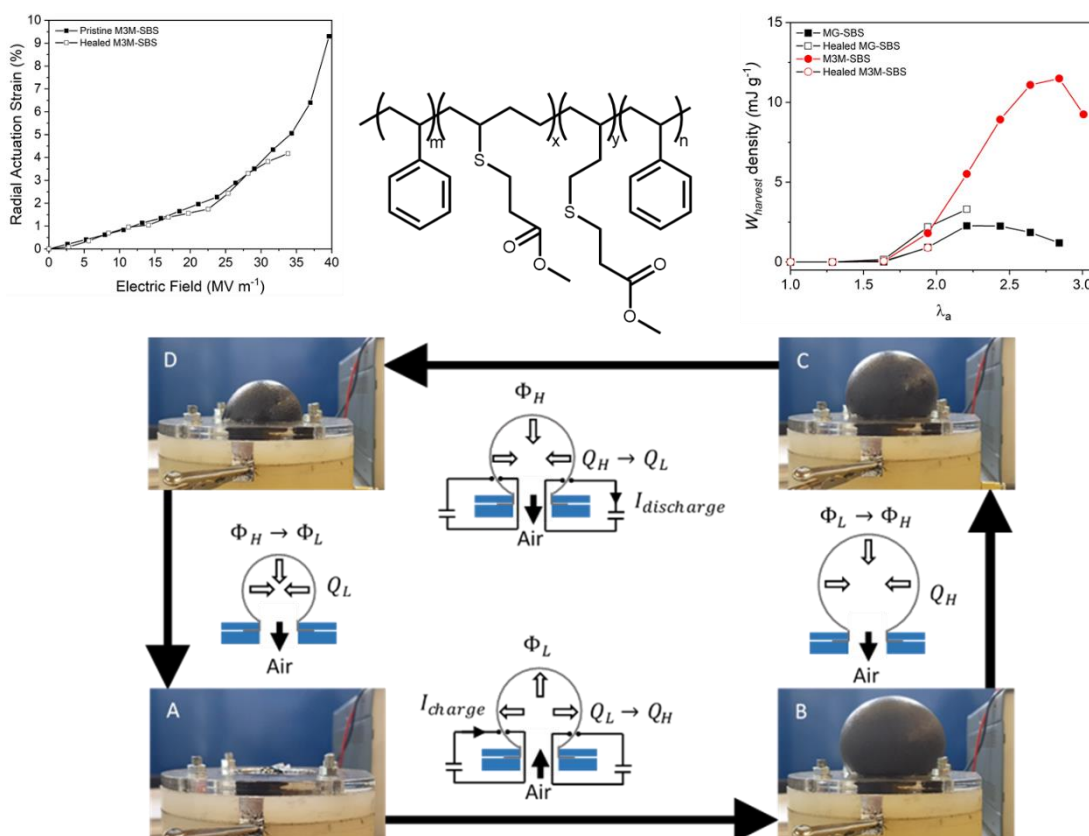
4.4 References

1. F. B. Madsen, L. Yu and A. L. Skov, *ACS Macro Letters*, 2016, **5**, 1196-1200.
2. C. Ellingford, C. Bowen, T. McNally and C. Wan, *Macromol. Rapid Commun.*, 2018, **39**, 1800340.
3. R. Kornbluh, R. Pelrine, H. Prahald, A. Wong-Foy, B. McCoy, S. Kim, J. Eckerle and T. Low, *MRS Bull.*, 2012, **37**, 246-253.
4. C. Ellingford, C. Wan, L. Figiel and T. McNally, in *Modern Physical Chemistry: Engineering Models, Materials, and Methods with Applications*, eds. R. K. Haghi, E. Besalu, M. Jaroszewski, S. Thomas and K. M. Praveen, CRC Press, New York, 2018, pp. 59-94.
5. L. M. Campos, K. L. Killops, R. Sakai, J. M. J. Paulusse, D. Dameron, E. Drockenmuller, B. W. Messmore and C. J. Hawker, *Macromolecules*, 2008, **41**, 7063-7070.
6. M. Uygun, M. A. Tasdelen and Y. Yagci, *Macromol. Chem. Phys.*, 2010, **211**, 103-110.
7. Yagci, Y. and A. Önen, *J. Macromol. Sci., Chem.*, 1991, **28**, 129-141.
8. C. E. Hoyle, T. Y. Lee and T. Roper, *J. Polym. Sci., Part A: Polym. Chem.*, 2004, **42**, 5301-5338.
9. D. Burget, C. Mallein and J. P. Fouassier, *Polymer*, 2004, **45**, 6561-6567.

10. N. B. Cramer and C. N. Bowman, *J. Polym. Sci., Part A: Polym. Chem.*, 2001, **39**, 3311-3319.
11. J. S. Silverstein, B. J. Casey, M. E. Natoli, B. J. Dair and P. Kofinas, *Macromolecules*, 2012, **45**, 3161-3167.
12. E. Passaglia and F. Donati, *Polymer*, 2007, **48**, 35-42.
13. P. J. Flory, *Principles of Polymer Chemistry*, Cornell University Press, 1953.
14. T. McNally, *Polymer Modified Bitumen: Properties and Characterisation*, Elsevier Science, 2011.
15. H. Sun, C. Jiang, N. Ning, L. Zhang, M. Tian and S. Yuan, *Polym. Chem.*, 2016, **7**, 4072-4080.
16. D. P. Almond and C. R. Bowen, *Phys. Rev. Lett.*, 2004, **92**, 157601.
17. D. P. Almond and C. R. Bowen, *J. Phys. Chem. Lett.*, 2015, **6**, 1736-1740.
18. S. Panteny, R. Stevens and C. R. Bowen, *Ferroelectrics*, 2005, **319**, 199-208.
19. F. B. Madsen, A. E. Daugaard, S. Hvilsted and A. L. Skov, *Macromol. Rapid Commun.*, 2016, **37**, 378-413.
20. Y. H. Kim and R. P. Wool, *Macromolecules*, 1983, **16**, 1115-1120.
21. G. Kim and M. Libera, *Macromolecules*, 1998, **31**, 2569-2577.
22. C. Ellingford, R. Zhang, A. M. Wemyss, C. Bowen, T. McNally, Ł. Figiel and C. Wan, *ACS Appl. Mater. Interfaces*, 2018, **10**, 38438-38448.
23. F. A. Morrison and H. H. Winter, *Macromolecules*, 1989, **22**, 3533-3540.
24. L. Sobczyk, S. J. Grabowski and T. M. Krygowski, *Chem. Rev.*, 2005, **105**, 3513-3560.
25. C. H. Suresh, M. Neetha, K. P. Vijayalakshmi, G. Renjumon and J. M. Mathew, *J. Comput. Chem.*, 2009, **30**, 1392-1404.
26. A. K. Jonscher, *Philos. Mag. B*, 1978, **38**, 587-601.
27. L. Yu, F. B. Madsen and A. L. Skov, *Int. J. Smart Nano Mater.*, 2017, DOI: 10.1080/19475411.2017.1376358, 1-16.
28. K. Kojio, M. Furukawa, Y. Nonaka and S. Nakamura, *Materials*, 2010, **3**, 5097-5110.
29. C. Ellingford, R. Zhang, A. M. Wemyss, Y. Zhang, O. B. Brown, H. Zhou, P. Keogh, C. Bowen and C. Wan, *ACS Appl. Mater. Interfaces*, 2020, **12**, 7595-7604.
30. R. Pelrine, R. Kornbluh, Q. Pei and J. Joseph, *Science*, 2000, **287**, 836-839.
31. T. G. McKay, E. Calius and I. A. Anderson, presented in part at the Electroactive Polymer Actuators and Devices (EAPAD), San Diego, Mar 08, 2009.
32. G. Kofod, R. Kornbluh, R. Pelrine and P. Sommer-Larsen, *Actuation response of polyacrylate dielectric elastomers*, SPIE, 2001.
33. D. Y. Wu, S. Meure and D. Solomon, *Prog. Polym. Sci.*, 2008, **33**, 479-522.
34. Y. Zhang, C. Ellingford, R. Zhang, J. Roscow, M. Hopkins, P. Keogh, T. McNally, C. Bowen and C. Wan, *Adv. Funct. Mater.*, 2019, **29**, 1808431.
35. V. A. Zakrevskii, N. T. Sudar, A. Zaopo and Y. A. Dubitsky, *J. Appl. Phys.*, 2003, **93**, 2135-2139.
36. M. Ghilardi, J. J. Busfield and F. Carpi, *Electrical breakdown detection system for dielectric elastomer actuators*, SPIE, 2017.
37. S. J. Kalista, T. C. Ward and Z. Oyetunji, *Mech. Adv. Mater. Struct.*, 2007, **14**, 391-397.
38. J. F. Scott, *J. Phys.: Condens. Matter*, 2007, **20**, 021001.

Chapter 5

Methyl-3-mercaptopropionate grafted SBS elastomers for self-healing dielectric elastomer generators



Publications:

C. Ellingford, R. Zhang, A. M. Wemyss, Y. Zhang, O. Brown, H. Zhou, P. Keogh, C. Bowen and C. Wan*, Self-healing dielectric elastomers for damage-tolerant actuation and energy harvesting, ACS Appl. Mater. Interfaces, 2020, 12, 6, 7595

5.1 Introduction

Prolonged usage of dielectric elastomers in actuators and energy harvesting devices can result in irreversible electrical and mechanical failure. However, the introduction of self-healing into dielectric elastomers can improve the cycle lifetimes of the elastomer by enhancing its operational stability.¹

Self-healing can be introduced into dielectric elastomers *via* noncovalent interactions or reversible covalent linkages.² Noncovalent interactions include introducing functional groups for hydrogen bonding,³⁻⁵ π -bonding,^{6, 7} ionic bonding⁸ and metal-ligand coordination.^{9, 10} Through their breaking and reforming nature, these interactions facilitating self-healing by assisting polymer chain entanglement through interchain interactions. The interaction strength between noncovalent interactions determines the rate at which self-healing takes place, with a high interaction strength reducing the rate of self-healing. In addition, stronger non-covalent interactions can increase the rigidity of the polymer and inhibit the contact and wetting stage of self-healing.¹¹ For larger scale supramolecular interactions, phase separation, crystallinity and the degree of polymer chain entanglement also affects self-healing.^{2, 12}

Additionally, reversible covalent bonds can be introduced using dynamic diels-alder bonding,¹³⁻¹⁵ disulphide linkages¹⁶⁻¹⁸ and imine bonds.^{18, 19} Upon application of a thermal stimulus, the covalent bonds break leaving the polymer chains free to interact and move. Upon cooling, new interchain covalent bonds are formed, acting as the mechanism for self-healing. Therefore, commercially available industrial polymers can be easily adapted into self-healing polymers. Self-healing can improve the sustainability of these devices and reduce the impact on the environment from their use.²⁰

As seen in the previous chapter, the grafting of methyl thioglycolate to SBS enhanced the electromechanical properties of SBS and introduced self-healing into MG-SBS through an electrostatic interaction. The grafted polar group is key to maximising actuation performance and energy harvesting efficiency by balancing the electromechanical properties. Increasing the size of the grafted polar group can reduce polymer chain entanglement due to steric constraints and thus lower the Young's modulus of the elastomer. Furthermore, the increased size of the polar group can assist self-healing as the polar group is more able to establish electrostatic interactions.

However, a large polar group can suppress the relative permittivity of the elastomer as the change in polarity across the elastomer backbone is decreased due to the increased distance involved.

An electrostatic interaction is amongst the weakest form of non-covalent interactions with a low binding energy of no more than 50 kJ mol^{-1} ,^{21, 22} as shown by Figure 5.1. Therefore, an electrostatic interaction is able to freely break and reform, assisting self-healing under room temperature conditions. However, the application of thermal energy easily overcomes the low binding energy of the weak noncovalent interaction.

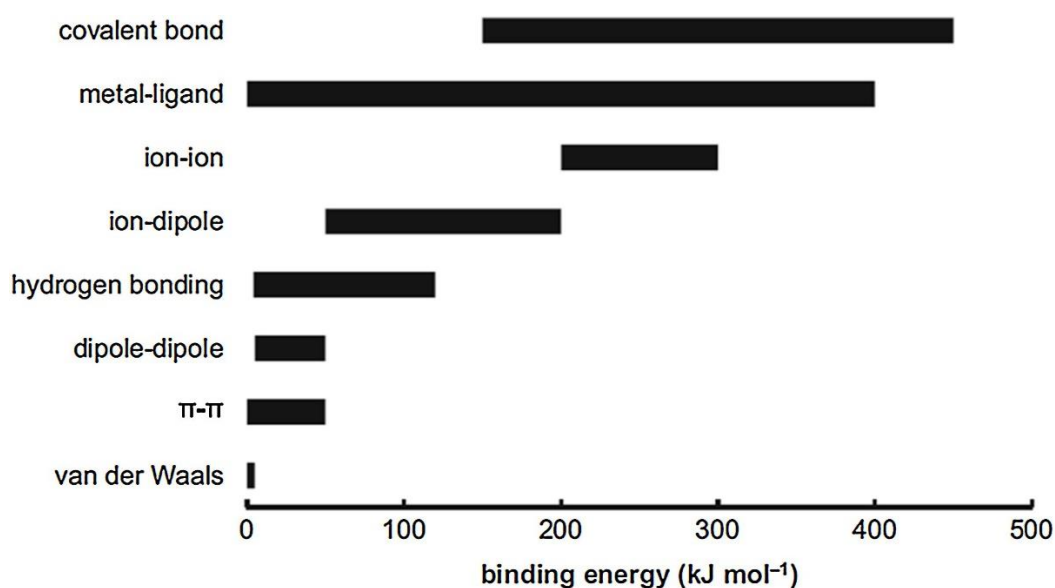


Figure 5.1 Binding energy ranges for different types of noncovalent interactions. Reproduced from Wang *et al.*²¹

In this chapter an analogous polar group to methyl thioglycolate, methyl-3-mercaptopropionate (M3M), was grafted to SBS which had a two carbon chain between the thiol group and the ester functionality instead of one. This allowed the effect of the size and flexibility of the grafted polar group on the mechanical, electrical and self-healing properties of SBS to be determined and attempt to maximise their actuation and energy harvesting performance. Furthermore, cyclic mechanical behaviour and stress relaxation were investigated to determine the potential for high longevity of M3M-SBS within a device. Due to the ability for M3M to electrostatically interact with styrene, the ability of M3M-SBS to self-heal was observed. By extending the length of the polar group, the freedom of the group to break and reform was expected to facilitate chain entanglement to a greater degree compared to MG-SBS.

The actuation performance of M3M-SBS before and after mechanical failure was tested and compared to MG-SBS. Finally, the energy harvesting ability of both M3M-SBS and MG-SBS was explored within an energy harvesting device, which utilised air pressure to simulate a mechanical deformation. The harvested energy, the harvesting efficiency and the axial deformation required for optimum energy harvesting was calculated for each material. Furthermore, energy harvesting after damage was also tested for both MG-SBS and M3M-SBS to determine the potential feasibility for reusing the elastomers should they fail within a device.

This work demonstrates that tuning the size of the grafted polar group can provide superior electromechanical properties for energy harvesting and actuation device. In addition, this chapter demonstrates that the pursuit of solely enhancing the relative permittivity without considering other factors such as mechanical properties and the nature of the polymer chains, does not necessarily lead to enhancements in actuation or energy harvesting performance.

5.2 Results and Discussion

5.2.1 Intrinsic modification of SBS with methyl-3-mercaptopropionate

The grafting of methyl-3-mercaptopropionate (M3M) to SBS was firstly conducted following the optimised conditions for MG-SBS synthesis. Briefly, a 4× excess of methyl-3-mercaptopropionate was calculated based on the concentration of vinyl groups in SBS from section 4.2.1 and used. However, during the photoinitiated thiol-ene reaction, the polymer solution gelled due to a high concentration of interchain crosslinking between polymer chains. This indicated that the grafting rate of methyl-3-mercaptopropionate to SBS was lower than previously observed for MG-SBS.

Therefore, the reaction conditions were modified to increase the excess of methyl-3-mercaptopropionate to a 5× excess. This was based on the observations for the synthesis of MG-SBS with different thiol ratios in section 4.2.1 and based on extensive investigations into thiol-ene reactions by Silverstein *et al.*²³ Nonetheless, the resultant modified elastomer from this reaction also gelled during the photoinitiation step.

To overcome the problem of gelation of methyl-3-mercaptopropionate modified SBS (M3M-SBS), an investigation into the solvent ratio used for the reaction was conducted. For all prior reactions, a 9:1 weight ratio was used between THF/SBS. In

a series of reactions, the solvent ratio was increased to 20:1, 25:1 and 40:1 THF and SBS with a 5× excess of methyl-3-mercaptopropionate and a 20 minute UV light exposure. The reactions involving 20:1 and 25:1 THF/SBS ratio gelled during the photoinitiation step, whilst 40:1 THF/SBS did not and a product was obtained. Once dry, this M3M-SBS elastomer was yellow in colour and did not melt, nor dissolve. This indicated that the reaction between methyl-3-mercaptopropionate and SBS was slow and a high degree of interchain crosslinking had taken place between the polymer chains

To confirm this, the UV-light exposure time was reduced to 15 minutes whilst maintaining a 40:1 THF/SBS ratio and 5× excess of methyl-3-mercaptopropionate. This resultant M3M-SBS was still yellow in colour, albeit not as strongly coloured yellow, and not dissolvable nor able to melt. Therefore, it was concluded that increasing the solvent/polymer ratio was not beneficial for the promotion of the thiol-ene reaction, and instead promoted the interchain crosslinking reaction. Due to the increased solvent volume, there was a decrease in the concentration of methyl-3-mercaptopropionate and SBS, increasing the rate of intra- and interchain crosslinking as free alkene sites were available to react.^{24, 25}

Therefore, based on this experimentation, the excess of thiol used was increased to 10× excess, whilst the THF:SBS ratio was maintained at 9:1 under a 15 minute UV exposure time. This yielded a white elastomer, which was both dissolvable and meltable. ¹H NMR spectra, Figure 5.2a, demonstrated the successful reaction through the reduction of the peaks at 5.4 ppm and 4.8 ppm, whilst new peaks at 3.7 ppm and 2.7 ppm arose due to CH₃ and CH₂ groups either side of the ester respectively as well as a new peak at 2.6 ppm associated with CH environment adjacent to the sulphur from methyl-3-mercaptopropionate and on the polymer backbone. From ¹H NMR, using equations 4.5 and 4.6, the grafting of methyl-3-mercaptopropionate from the thiol peaks was 96.7% and the reduction in the alkene peak was 98.6%, indicating that the reaction proceeded with a high grafting efficiency and a low rate of side reactions.

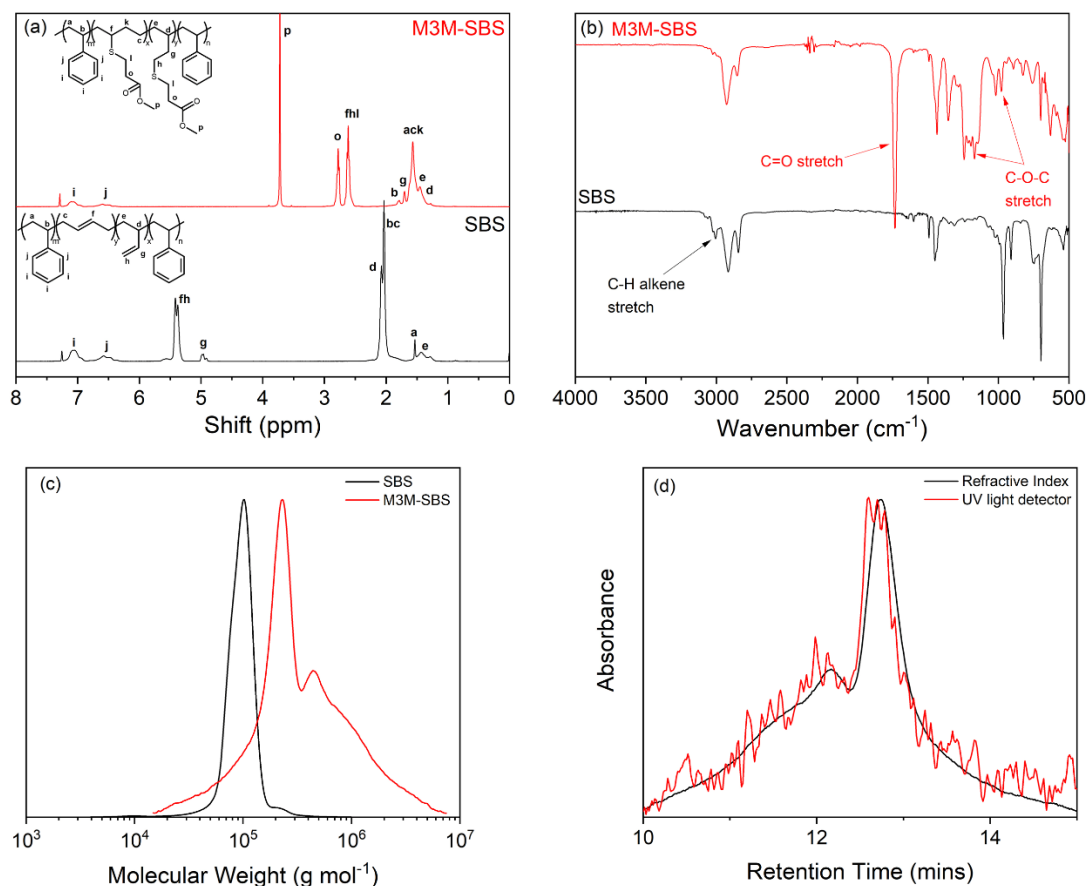


Figure 5.2 (a) ^1H NMR spectra at 400 MHz in CDCl_3 of SBS and M3M-SBS with assigned peaks, (b) FTIR spectra of SBS and M3M-SBS with key peaks highlighted, (c) GPC trace of SBS and M3M-SBS in THF and (d) GPC trace of M3M-SBS in THF with the UV light detector at 254 nm and Refractive Index against retention time

The associated FTIR spectrum of M3M-SBS is shown in Figure 5.2b. As similar to MG-SBS in section 4.2.1, the C-H alkene stretch at 3001 cm^{-1} of SBS disappears, and replaced by a C=O stretch at 1728 cm^{-1} . Additionally, there are symmetric and asymmetric C-O stretches present in the FTIR spectrum of M3M-SBS. However, there are 2 visible for each stretching vibration, at 1169 and 1243 cm^{-1} for the asymmetric C-O stretch which overlaps slightly with a CH_3 and CH_2 bend at 1195 and 1145 cm^{-1} , and at 979 and 1018 cm^{-1} for the symmetric C-O stretch, indicating two different vibrational energies.² This behaviour has been observed previously for methyl-3-mercaptopropionate.^{26, 27} Based on recent *ab-initio* modelling,²⁸ the two peaks are ascribed to the two most common conformers of methyl-3-mercaptopropionate, seen in Figure 5.3. Each conformer has a different bond energy associated with the ester group

depending on its environment. Therefore, the FTIR assists with confirmation that the polar group was successfully grafted.

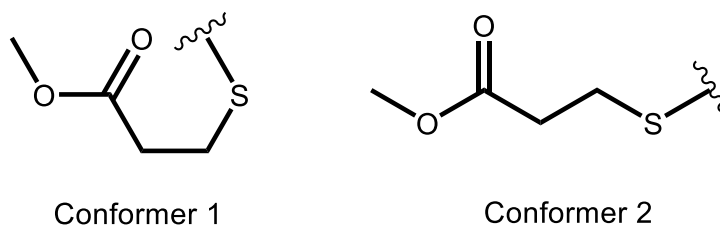


Figure 5.3 The two most common conformers of methyl-3-mercaptopropionate

GPC shows that after modification, the M_n , M_w and \bar{D} all increased significantly due to the grafting, see Figure 5.2c. Prior to grafting, SBS had an M_n of 86,000 g mol⁻¹, an M_w of 101,000 g mol⁻¹ and a \bar{D} of 1.17. Comparatively M3M-SBS had a M_n of 193,000 g mol⁻¹, M_w of 603,442 g mol⁻¹ and a \bar{D} of 3.13. The greater M_n and M_w of M3M-SBS compared to MG-SBS was attributed to the larger sized grafting group enabling the elastomer to elute faster from the GPC column. Furthermore, the larger \bar{D} was also attributed to UV light induced polymer chain scission in the butadiene block of M3M-SBS, as the UV response for at higher retention times is low, see Figure 5.2d.

Upon scaling up the reaction to using 10 g SBS, the UV light exposure time was increased from 15 minutes to 20 minutes to ensure that the thiol-ene reaction was complete and the obtained M3M-SBS had as high a grafting efficiency as possible. ¹H NMR confirmed that M3M-SBS produced by large scale synthesis was unaffected and had a thiol grafting efficiency of 95.2%. The alkene peak was not observable in the spectra, indicating that a high degree of alkene groups had been converted.

5.2.2 Mechanical and electrical characterisation of M3M-SBS

The effect of the intrinsic modification of SBS with methyl-3-mercaptopropionate on the mechanical properties is shown in Figure 5.4. Compared to SBS, M3M-SBS exhibited a reduced tensile strength of 4.7 ± 0.7 MPa, as well as a significantly reduced Young's modulus of 2.5 ± 0.8 MPa, which is similar to the change in mechanical behaviour after modification to form MG-SBS. This was ascribed to the grafted methyl-3-mercaptopropionate inhibiting chain entanglement and altering the polymer chain structure. However, in M3M-SBS, the strain at break unexpectedly increased from $857\% \pm 45.8\%$ to $1000 \pm 126\%$. This is associated with the longer chained

methyl-3-mercaptopropionate more easily able to electrostatically interact with the styrenic block of SBS, increasing the strength between the polymer chains and preventing mechanical failure.

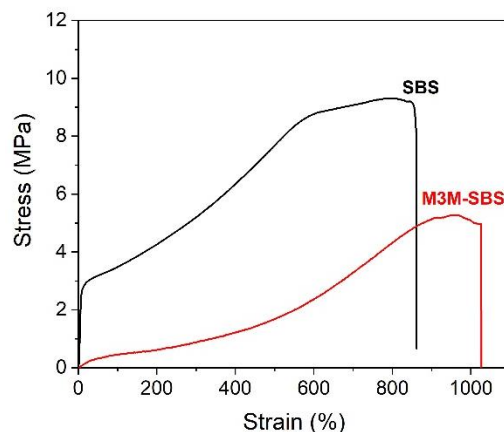


Figure 5.4 Stress strain curve of SBS and M3M-SBS

Cyclic stress softening of M3M-SBS in Figure 5.5a-d demonstrated that it has a significantly lower hysteresis loss at 100%, 300% and 500% strain extension. Additionally, the hysteresis loops were smaller due to a more elastic nature of the polymer and exhibited a linear response. Over the course of five cycles, the hysteresis loss for M3M-SBS was 18.8% at 100% strain, 20.3% at 300% strain and 27.7% at 500% strain. Compared to SBS (discussed in section 4.2.5), the loss of M3M-SBS is between 50 – 66% lower for each of the strains, with the greatest difference between the two polymers at 300% strain. From 500% strain onwards, crystallisation of polymer chains increased the tensile strength of M3M-SBS. This is realised further in the stress strain curve of Figure 5.4 where the strain induced polymer chain crystallisation²⁹ appears strongly between 500% and 1000% until failure. This effect was not observed in MG-SBS in section 4.2.2 and is related to the increased length of the polar groups in M3M-SBS, freeing them and not inhibiting polymer chain crystallisation.

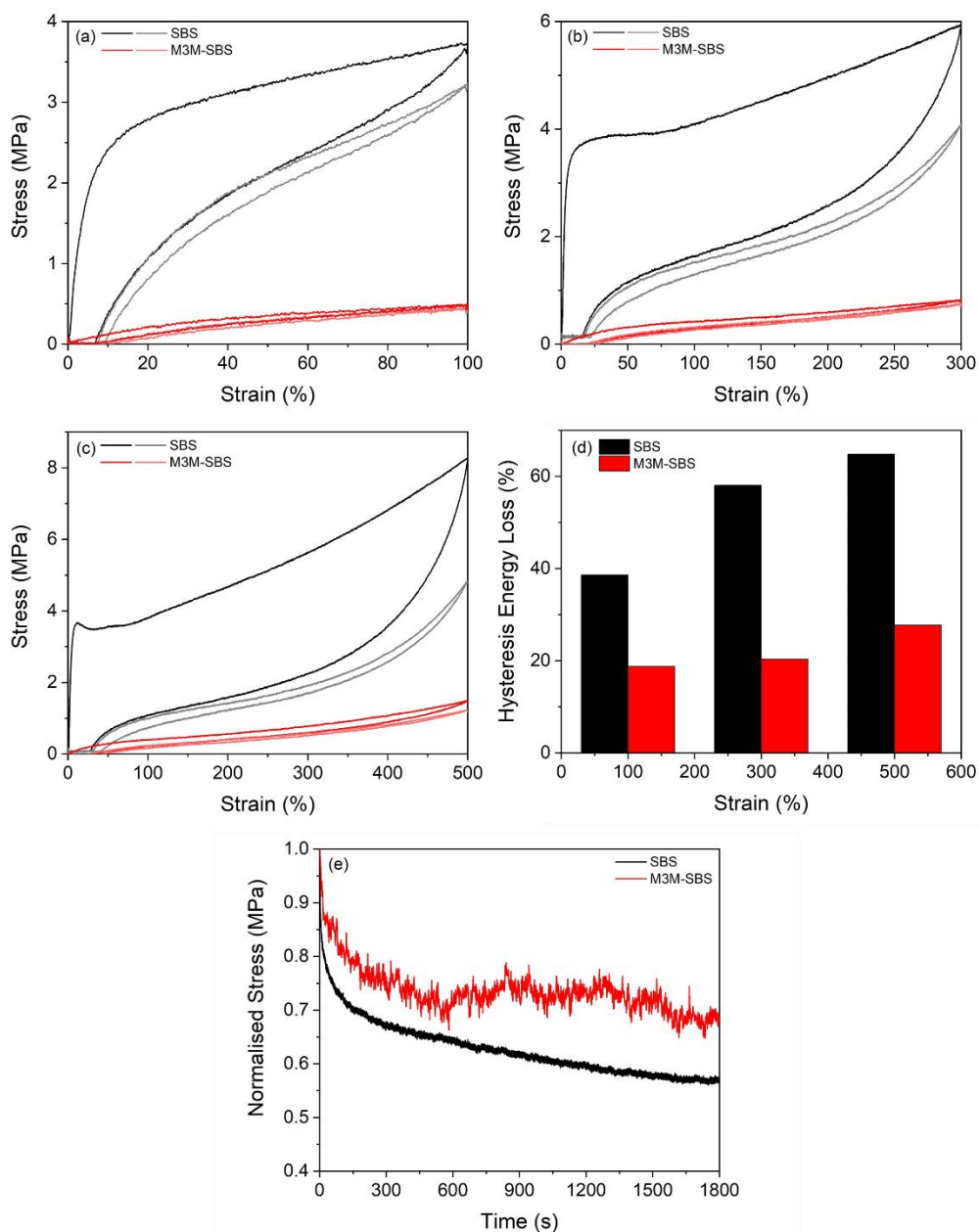


Figure 5.5 Cyclic stress softening curves of SBS and M3M-SBS at (a) 100%, (b) 300% and (c) 500% strain. The darker colour is the first cycle and the lighter colour is the fifth cycle for each material. (d) Hysteresis loss for SBS and M3M-SBS after five cycles. (e) Stress relaxation of SBS and M3M-SBS up to 30 minutes.

Stress relaxation testing of M3M-SBS, Figure 5.5e, demonstrates that the electrostatic interchain interaction previously observed in MG-SBS in section 4.2.5 is present in M3M-SBS as well. After 30 minutes at 100% strain, M3M-SBS exhibited a normalised stress of 0.65-0.70 MPa. In comparison, the normalised stress of SBS decreased to 0.55-0.60 MPa due to greater polymer chain slippage. This higher value

was ascribed to the electrostatic interaction in M3M-SBS preventing the polymer chains from moving under strain, thus maintaining a higher stress.

The grafting of methyl-3-mercaptopropionate enhanced the relative permittivity up to $\epsilon_r \approx 7.5$ at 10^3 Hz, compared to 2.8 for SBS in Figure 5.6. This is a reduction in the enhancement of the relative permittivity compared to MG-SBS because the longer carbon chain between the thiol group and the ester group of methyl-3-mercaptopropionate reduced the polarity difference across on the backbone of SBS. Additionally, the $\tan \delta$ loss for M3M-SBS was low, 0.03 at 10^3 Hz and only slightly higher than for SBS. Furthermore, the AC conductivity for M3M-SBS was an order of magnitude higher at 10^3 Hz than SBS, with a conductivity of $1.3 \times 10^{-8} \text{ S m}^{-1}$ compared to $1.4 \times 10^{-9} \text{ S m}^{-1}$ for SBS.

However, at 1 Hz the difference in conductivity between the two polymer is greater than 3 orders of magnitude. M3M-SBS was almost frequency independent in this region, demonstrating that it has a dc conductivity close to $3 \times 10^{-9} \text{ S m}^{-1}$ whereas SBS exhibited a frequency dependent behaviour. This indicated that the dc conductivity of SBS was significantly lower than M3M-SBS, and was lower than $2.4 \times 10^{-12} \text{ S m}^{-1}$ at 1 Hz.

Finally, the phase angle of M3M-SBS demonstrated an insulating response of -90° by M3M-SBS. The deviation from -90° in the frequency range of 1 to 100 Hz was also observed in the $\tan \delta$ loss and relative permittivity as an increase is due to electrode polarisation. This is where electrons get trapped at the electrode, enhancing the measured response. Additionally, there was a small deviation in phase angle once more between 10^5 and 10^6 Hz, observed as an increase in the $\tan \delta$ loss but a decrease in the relative permittivity. This was attributed to atomic polarisation of M3M-SBS, where the polymer chains are no longer able to respond to the alternating electric field. This occurred in M3M-SBS but not MG-SBS most likely due to the inability of larger methyl-3-mercaptopropionate to respond to the changing electric field at a lower frequency.²

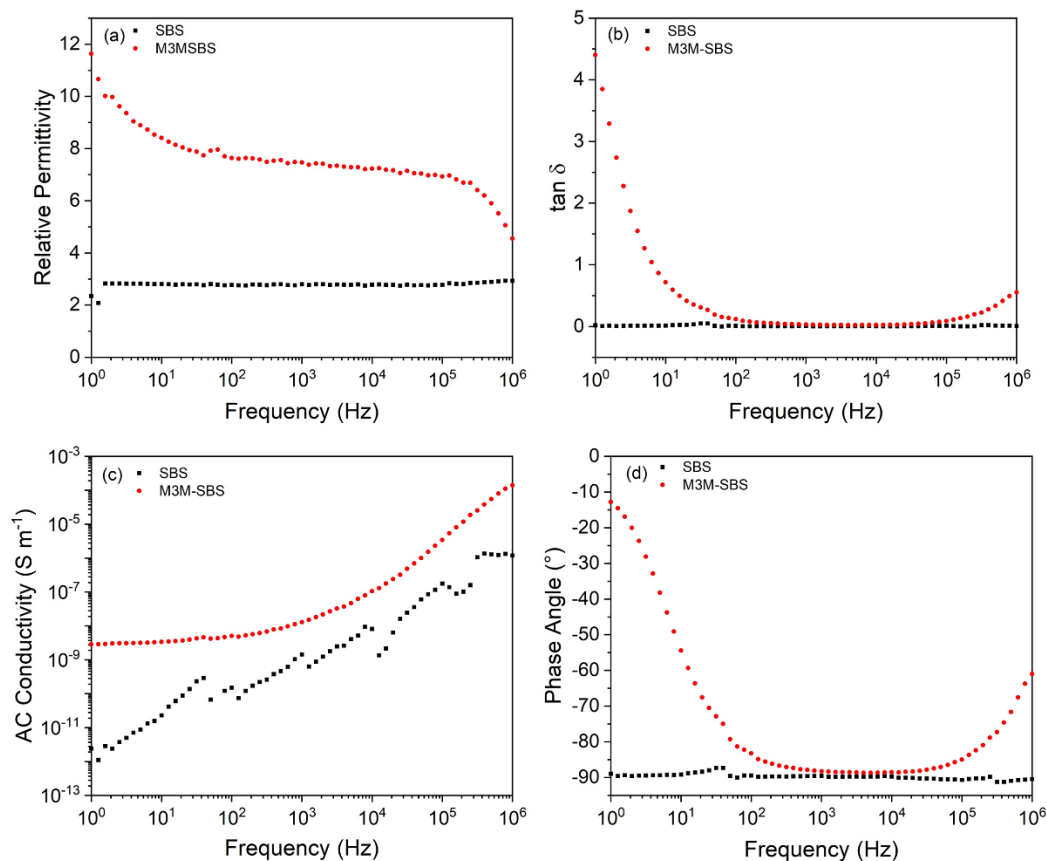


Figure 5.6 Impedance spectroscopy of SBS and M3M-SBS with (a) relative permittivity, (b) $\tan \delta$, (c) AC conductivity and (d) phase angle

5.2.3 Self-healing ability and structural rationalisation of M3M-SBS

As seen in section 5.2.2, the cyclic stress softening and stress relaxation testing demonstrated that the grafting of methyl-3-mercaptopropionate was able to also introduce an electrostatic interchain interaction similar to MG-SBS. To understand the degree of self-healing possible with M3M-SBS, two freshly cut dogbone pieces were reconnected and allowed to self-heal for different time periods, Figure 5.7 and Appendix Figure 8. When M3M-SBS was tested immediately after reattaching the two pieces together, a strain at break recovery of 6.1% was observed, corresponding to an actual strain at break of $55 \pm 4.8\%$. Additionally, this also led to a similar recovery in the tensile strength of 5.4% (0.25 ± 0.06 MPa). After 15 minutes of self-healing, M3M-SBS was able to recover 11.8% of its strain at break ($106 \pm 6.6\%$) and 7.2% of its tensile strength (0.34 ± 0.07 MPa). This demonstrated that after the initial connection of the two polymers, chain entanglement took place according to the theory by Kim and Wool.³⁰ After M3M-SBS was left for a three day time period for healing, the

recovery for the strain at break increased to 26% ($234 \pm 21\%$) whilst the tensile strength recovered by 12.8% (0.60 ± 0.08 MPa). The strain at break recovery was similar to that of MG-SBS, however the strain at break was significantly higher due to the greater strain at break of the elastomer compared to MG-SBS. Thus, M3M-SBS is able to be strained further after self-healing before failure occurs.

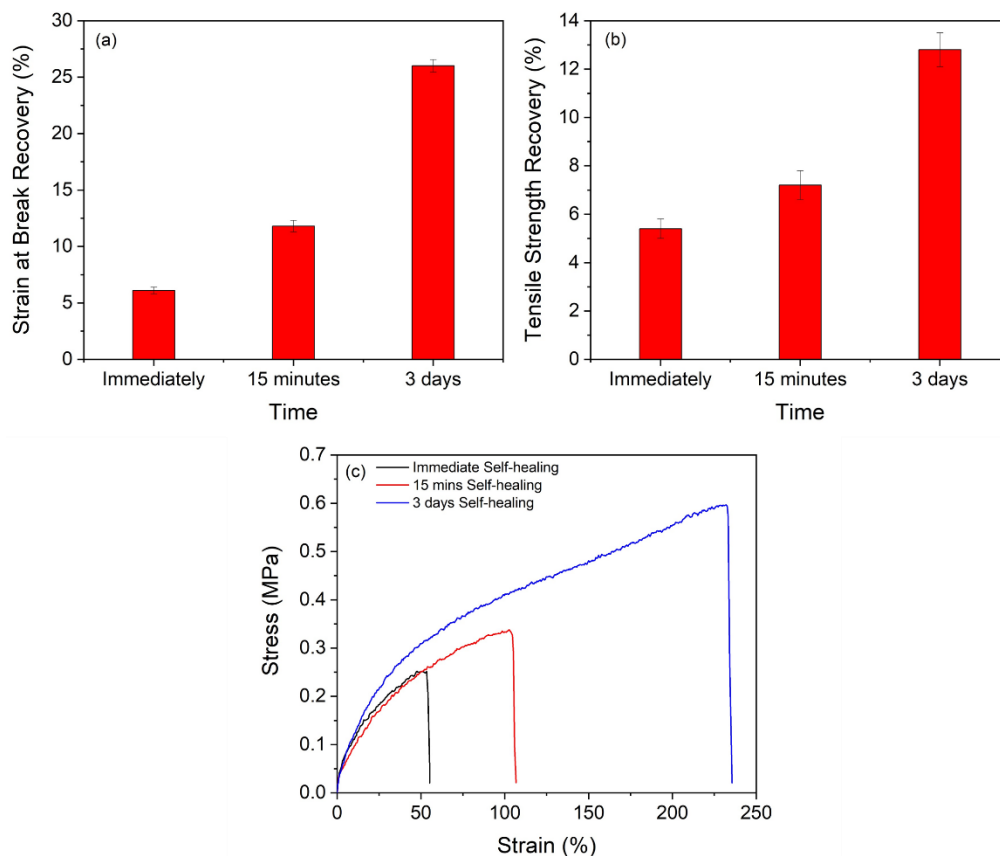


Figure 5.7 (a) Recovery for the strain at break at various times compared to the strain at break for pristine M3M-SBS, (b) recovery for the tensile strength at various times compared to the tensile strength for pristine M3M-SBS and (c) stress strain curves for the self-healing of M3M-SBS at various times

To understand further the self-healing nature of M3M-SBS, the structure of M3M-SBS was probed using DMTA. The $\tan \delta$ loss of M3M-SBS showed that there was only one glass transition after modification compared to two for the phase separated structure of SBS, Figure 5.8a. M3M-SBS followed the same previously observed behaviour of MG-SBS and the single glass transition was due to the compatibilisation of the butadiene block with the styrene block through the methyl-3-mercaptopropionate ester. Above 50 °C, the $\tan \delta$ loss displayed some noise due to the

softness of the material. Additionally, the storage modulus and loss modulus are shown in Appendix Figure 9. They show a decrease of three orders of magnitude after the glass transition temperature. Additionally, above 100 °C, the storage modulus begins to drop further whilst the loss modulus increases, indicating that the material is beginning to display as more viscous behaviour, most likely due to the loss of any π - π stacking present in the elastomer.

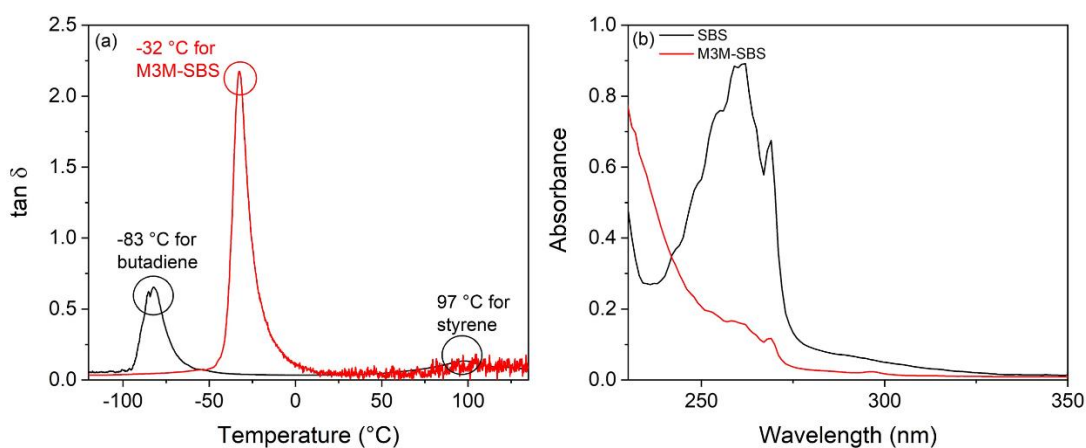


Figure 5.8 (a) DMTA $\tan \delta$ and (b) Solution state UV-Vis spectroscopy of SBS and M3M-SBS in DCM

Solution state UV-Vis spectroscopy provided further evidence of a similar electrostatic interaction between the grafted ester and the styrenic block of SBS. Figure 5.8b shows that the π - π^* transition for free styrene occurred at 262 nm in SBS. However, after the reaction, the π - π^* transition for the aromatic groups blue shifted below the solvent cut off of 230 nm, instead leaving the edge of a peak which increased in intensity from 250 nm. Compared to methyl thioglycolate, the longer length of the methyl-3-mercaptopropionate side-group assists with greater polymer chain entanglement, increasing the ease for the δ^+ proton from the ester of methyl-3-mercaptopropionate to remove electron density from the δ^- aromatic centre of styrene. This increased the π - π^* orbital band-gap, thus decreasing the wavelength of light for promotion.

To investigate the interactions behind the self-healing behaviour within M3M-SBS, variable temperature FTIR was utilised to determine the specific bonds affected by disrupting the electrostatic interaction through temperature, see Figure 5.9. Upon heating, it was observed that three peaks shifted their wavenumber. From Figure 5.9a

the C=O stretch at 1734 cm^{-1} shifted by 4 cm^{-1} to 1738 cm^{-1} in the temperature range of $30\text{ }^{\circ}\text{C}$ – $150\text{ }^{\circ}\text{C}$. The higher energy indicated that the C=O bond required more energy for stretching. The second peak which shifted was the CH_3 bend in the ester of methyl-3-mercaptopropionate at 1356 cm^{-1} as seen in Figure 5.9b, shifting to a lower wavenumber whilst broadening upon heating. This demonstrated that it is easier for the bending vibration of the CH_3 group to occur, as the δ^+ proton is no longer interacting with the styrene group. Finally, in Figure 5.10c, the asymmetric C-O-C stretch at 1244 cm^{-1} decreased by 2 cm^{-1} . The C-O-C bond is not directly involved in the electrostatic interaction, however the decrease in wavenumber indicated that it is easier to stretch at a lower energy. This was rationalised by the overcoming the of the CH_3 bend at 1356 cm^{-1} . Therefore, the variable temperature FTIR reinforced the results from DMTA and UV-Vis spectroscopy as to the nature of the self-healing interaction in M3M-SBS. Additionally, the variable temperature FTIR of SBS for the same regions are shown in Appendix Figure 10 as a comparison but show no peak shifts in these regions.

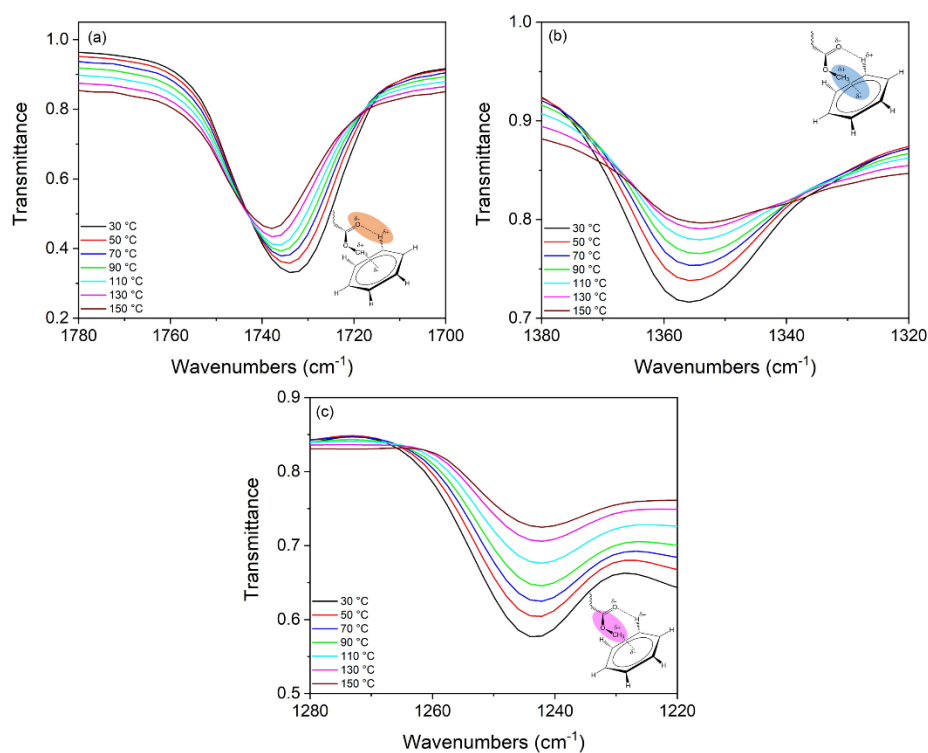


Figure 5.9 Temperature dependent FTIR for M3M-SBS between $30\text{ }^{\circ}\text{C}$ and $150\text{ }^{\circ}\text{C}$ for (a) 1734 cm^{-1} , (b) 1356 cm^{-1} and 1244 cm^{-1}

5.2.4 Actuation performance of M3M-SBS

The electroactive abilities of M3M-SBS was first investigated through its actuation performance. Despite the lower relative permittivity of M3M-SBS, the comparison of actuation properties between MG-SBS and M3M-SBS is important to determine which elastomer is superior. Thus, the $FoM_{Actuation}$ value from equation 4.7 was calculated to be 226.2 when normalised to SBS, 40% greater than for MG-SBS. This was attributed to the higher breakdown strength and slightly lower Young's modulus of M3M-SSB, see Table 5.1 for a summary of the properties of M3M-SBS.

Table 5.1 Table of experimentally determined properties of M3M-SBS and the theoretically determined $FoM_{Actuation}$

Young's modulus (MPa)	Elongation at break (%)	Elongation at break after self-healing (%)	Elongation recovery (%)	Normalised stress relaxation (MPa)	ϵ_r at 1 kHz	E_b (MV m ⁻¹)	$FoM_{Actuation}$
2.4	1000	230% at RT for 3 days	27	0.7	7.5	39.6	226.2

Therefore, the experimental determination of the actuation abilities of M3M-SBS followed the same procedure as for the actuation testing of MG-SBS in section 4.2.6. M3M-SBS was pre-strained biaxially 33% onto a rigid frame as shown in Figure 5.10a and the electric field was calculated as the true electric field from equation 4.8.

Therefore, the actuation abilities of M3M-SBS are shown in Figure 5.10b-c. M3M-SBS failed under an electric field of 39.6 MV m⁻¹ whilst actuating 9.3% radially. This corresponded to an areal actuation of 19.5%. This was significantly improved compared to MG-SBS, and demonstrated that the enhanced actuation abilities of M3M-SBS was correctly predicted by the $FoM_{Actuation}$. The actuation behaviour of M3M-SBS is somewhat different to that of MG-SBS. MG-SBS actuated linearly with respect to the electric field. However, the actuation of M3M-SBS deviated from linearity above 25 MV m⁻¹, where the actuation behaviour became exponential with respect to electric field. This change in behaviour is attributed to the stronger electric field increasing the Maxwell's pressure on the elastomer, overcoming the elastic

forces of the material. This behaviour has been observed in the literature for actuation previously.³¹⁻³³

After mechanical damage was inflicted upon M3M-SBS *via* a needle probe, M3M-SBS was healed and its actuation abilities were retested. Healed M3M-SBS was able to recover its electrical breakdown strength to 33.8 MV m⁻¹, a recovery of 85.3%. Additionally, M3M-SBS was able to actuate 4.2% radially and an areal strain of 8.5%, the same actuation performance as pristine MG-SBS. This corresponded with a 44.8% recovery in radial actuation strain and demonstrated that M3M-SBS has superior actuation abilities compared to both SBS and MG-SBS.

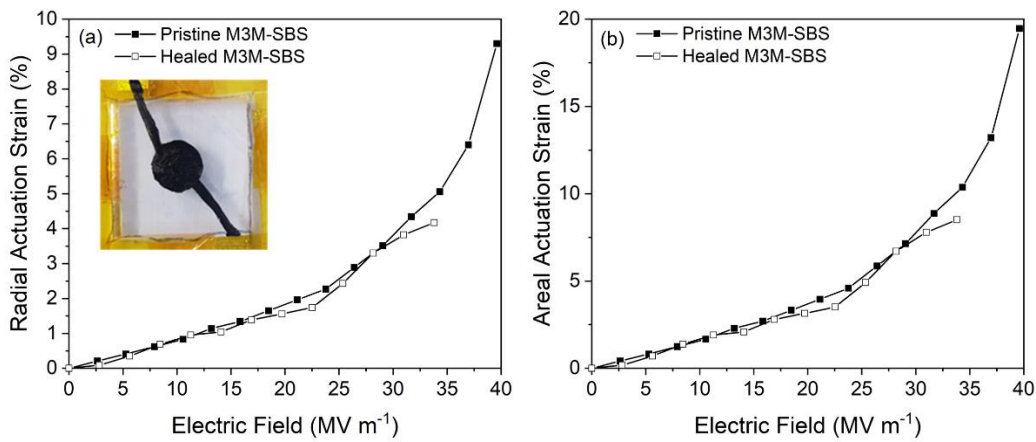


Figure 5.10 (a) Radial actuation and (b) areal actuation of pristine M3M-SBS and healed M3M-SBS under different electric fields, the inset image shows the set-up of actuation testing of M3M-SBS.

5.2.5 Energy harvesting abilities of MG-SBS and M3M-SBS

Thus far, only electrical energy transduction into mechanical energy has been considered. Therefore, in this next section, the mechanical energy transduction into electrical energy was investigated for both MG-SBS and M3M-SBS. As with actuation, the theoretical energy harvesting ability was calculated using $FOM_{Harvesting}$, shown in Equation 5.1:

$$FOM_{Harvesting} = \epsilon_0 \epsilon_r E_b^2 \quad (5.1)$$

where ϵ_0 is the permittivity of a vacuum, ϵ_r is the relative permittivity and E_b is the breakdown strength of the material. The equation is similar to the equation for $FOM_{Actuation}$ but does not take into account the Young's modulus of the elastomer. This is because the Young's modulus is assumed to be sufficiently low enough that a

mechanical force will be able to deform the elastomer. The normalised values of $FoM_{Harvesting}$ for MG-SBS and M3M-SBS against $FoM_{Harvesting}$ value of SBS are 9 and 10.5, respectively, an order of magnitude greater than SBS, indicating that the modified elastomers would exhibit better energy harvesting abilities.

An energy harvesting device was fabricated by clamping the elastomer MG-SBS or M3M-SBS onto a frame over an air chamber in an unstrained state. Air pressure was applied to simulate mechanical deformation of the elastomers and depressurisation of the system was used to remove the mechanical deformation. The energy harvesting cycle is shown in Figure 5.11. In state A, the elastomer was undeformed with only a resting voltage of 1.5 kV applied. The elastomer was stretched under air pressure to inflate the elastomer and simulate mechanical deformations in state B whilst maintaining an applied voltage of 1.5 kV. After this, the applied voltage was increased to 2.0 kV whilst maintaining a constant mechanical deformation in state C and then the depressurisation of the system relaxes the elastomer in state D, increasing the repulsion in the system and increasing the voltage further, which was harvested before returning to the initial cycle state in A.

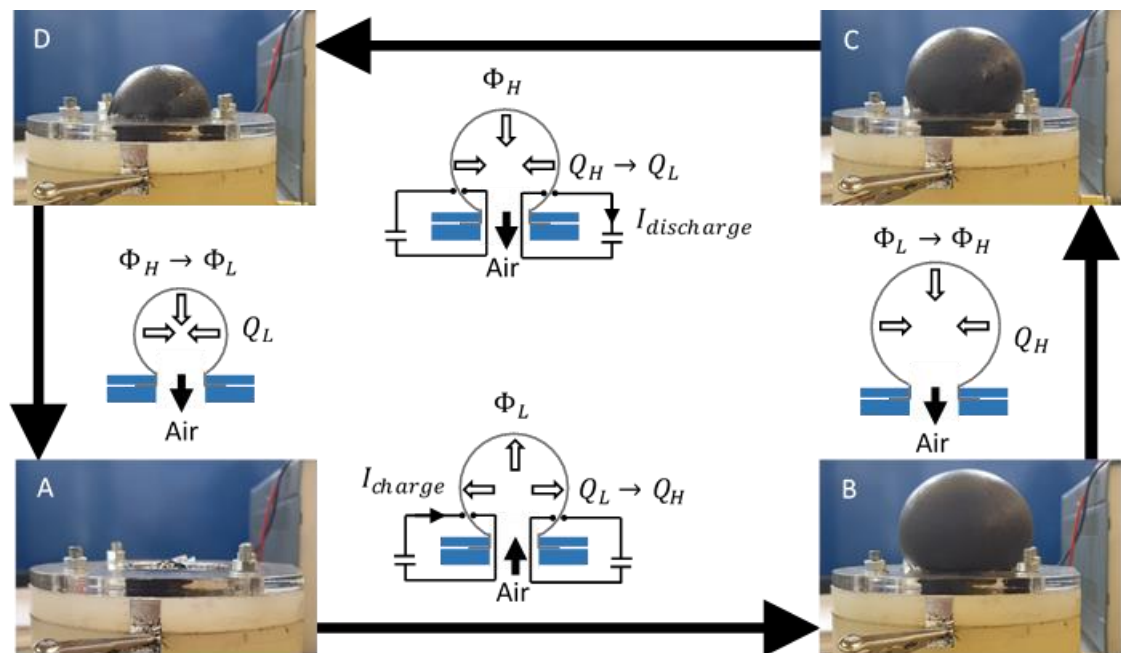


Figure 5.11 Schematic energy harvesting cycle of elastomers using air pressure. In state A, the elastomer is in the undeformed state with no applied voltage. In state B, the application of air pressure has deformed the elastomer to its stretched state. In state

C, the voltage is applied and in state D the air pressure is removed to bring the elastomer to the undeformed state.

The schematic for the electric circuitry for the energy harvesting device and the schematic for the application of voltage are shown in Figure 5.12 and shows how mechanical energy was converted in the device. This showed that 1.5 kV is supplied through diode D1 in state A, in Figure 5.12a. When deformed in state B, the capacitance of the elastomer increased as thickness decreased and increased the stored charge in the elastomer under a fixed voltage, due to equation 1.14.

When the elastomer returns to its unstrained state, the capacitance of the material decreases, increasing the voltage as the charge in the elastomer remains static. The charge was removed *via* diode D2 and then the voltage decreases to the initial applied voltage of 1.5 kV.

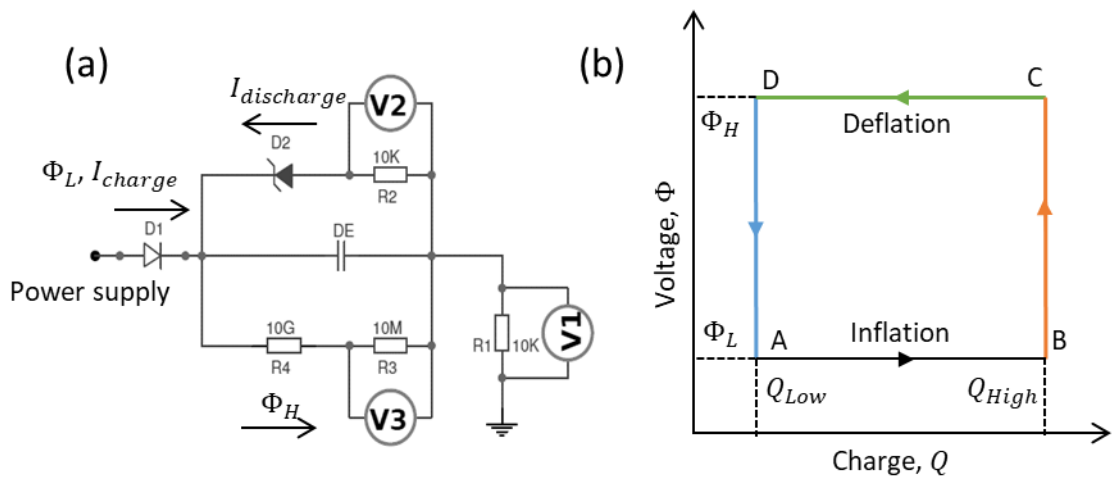


Figure 5.12 (a) Electrical circuitry schematic for the dielectric elastomer generator and (b) application of voltage during the different states of the energy harvesting cycle

An example energy harvesting cycle is given in Figure 5.13 which followed the change in pressure and volume flow rate of air in Figure 5.13a and the change in current and voltage in Figure 5.13b. In this example, a single energy harvesting cycle for M3M-SBS is shown where the biaxial deformation was 300% ($\lambda_a = 3$). The first half of the cycle, between 0-10 seconds, is attributed to pressurisation of the chamber and until the correct volumetric change was achieved. This is denoted by equation 5.2:

$$\Delta V_a = \int_0^{10} Q_a(t) dt \quad (5.2)$$

where ΔV_a is the volumetric change, $Q_a(t)$ is the volumetric flow of air into the air chamber and dt is the change in time. Therefore, Figure 5.13a showed that the air pressure reached a maximum pressure of 0.06 bar within 1.5 seconds, at which point $Q_a(t)$ decreased to zero and no further increase in pressure was observed. When the time was 10 seconds, the pressure in the system decreased to 0.05 bar from the elastomer relaxing. The increase in the capacitance of the elastomer in this state is observed from equation 1.11. Therefore, as the area increased and the thickness decreased, the capacitance increased.

During the time of 10-20 seconds in the cycle, the pressure decreased as the chamber depressurised. Depressurisation took four times longer than the pressurisation step as the difference in pressure between the surrounding environment and in the air chamber was only 0.05 bar.

Figure 5.13b showed how the current and voltage changed within the cycle. Focussing on the pressurisation step, the current flowed to the electrode in the elastomer steady state between 2 and 10 seconds as a positive current remains, where $I(t)$ is $\approx 5 \mu\text{A}$. The leakage current, $I_{leak}(t)$, was considered to be proportional to the deformation of the elastomer during the pressurisation step, and constant during relaxation, whilst the leakage charge was calculated as the area between the voltage and $I_{leak}(t)$. The charging current, I_{charge} , and the charge increased due to the increase in capacitance, Q_{charge} , are calculated from equations 5.3 and 5.4 respectively:

$$I_{charge}(t) = I(t) - I_{leak}(t) \quad (5.3)$$

$$Q_{charge} = \int I_{charge}(t)dt \quad (5.4)$$

The final ten seconds in the cycle saw the voltage increase from 1.5 kV to 2.0 kV between 10 – 12.5 seconds. The voltage remained constant for a further 2.5 seconds before decreasing to 1.5 kV once more. Whilst under a constant voltage of 2 kV, a discharge current, $I_{discharge}(t)$, was released into the energy harvesting circuit, observed as a negative current. The harvested charge, $Q_{discharge}$, was calculated from equation 5.5:

$$Q_{discharge} = \int I_{discharge}(t)dt \quad (5.5)$$

However some of the energy generated in the elastomer was dissipated due to the presence of leakage current, leading to the harvested energy being less than the charges supplied to the electrodes. This loss was expressed in equation 5.6:

$$Q_{leak} = Q_{charge} - Q_{discharge} \quad (5.6)$$

where Q_{leak} is the leakage charge. The pressure, air flow, current and voltage graphs for MG-SBS and M3M-SBS at different strains ($\lambda_a = 1.3 - 3.0$) as well as after healing are found in Appendix Figure 11 - 14.

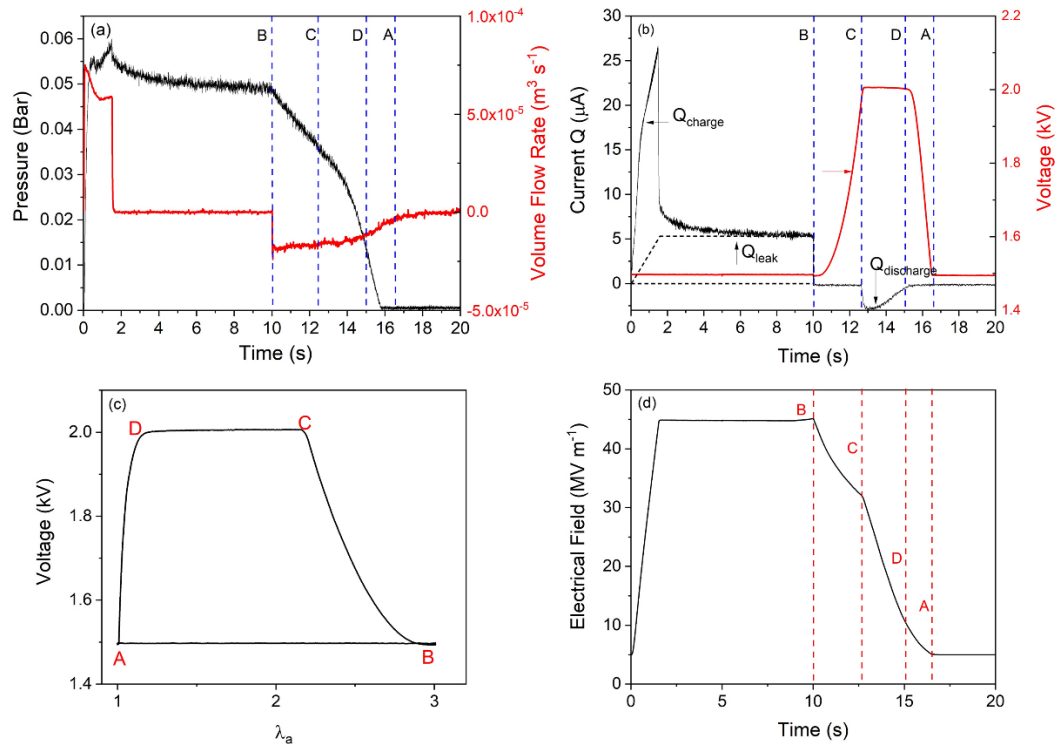


Figure 5.13 (a) Change in pressure and air volume flow rate compared to time for an energy harvesting cycle, (b) change in current and voltage compared to time for an energy harvesting cycle, (c) change in applied voltage as a function of strain and (d) change in electric field over one complete energy harvesting cycle

The change in applied voltage as a function of strain and the change in electric field over the harvesting cycle are shown in Figure 5.13c-d, where electric field was calculated as true electric field. The graphs show that the applied voltage remained fixed upon axial deformation, whilst the electric field increased from 5 MV m^{-1} to 45 MV m^{-1} . The applied voltage increased to 2.0 kV whilst experiencing a decrease in the axial deformation. Due to this, the electric field also decreased to 30 MV m^{-1} . When the axial deformation was removed, the applied voltage remained at 2 kV whilst the

electric field decreased further due to an increase in thickness of the elastomer. After reducing the applied voltage to 1.5 kV, the electric field decreased to the resting state of A at 5 MV m^{-1} .

To calculate the energy harvested by the energy harvesting device, the total converted electrical energy, W_e , and the generated electrical energy, $W_{harvest}$, were calculated from the electrical work-conjugated plane diagram of the energy harvesting cycle from Figure 5.14a. The overall dotted line area is calculated as W_e and the enclosed area is the generated electrical energy, $W_{harvest}$, and these were calculated using equations 5.7 and 5.8:

$$W_e = (\Phi_H - \Phi_L)Q_{charge} \quad (5.7)$$

$$W_{harvest} = (\Phi_H - \Phi_L)Q_{discharge} \quad (5.8)$$

Subsequently, the expended mechanical energy *via* air pressure in the energy harvesting cycle was calculated from the mechanical work-conjugate plane diagram of the energy harvesting cycle, as shown in Figure 5.14b using equation 5.9:

$$W_{mech} = \int P_a(t)dV_a(t) \quad (5.9)$$

Finally, the efficiency for energy conversion, η , is seen from equation 5.10:

$$\eta = \frac{W_{harvest}}{W_{mech}} = \frac{(\Phi_H - \Phi_L)Q_{discharge}}{\int P_a(t)dV_a(t)} \quad (5.10)$$

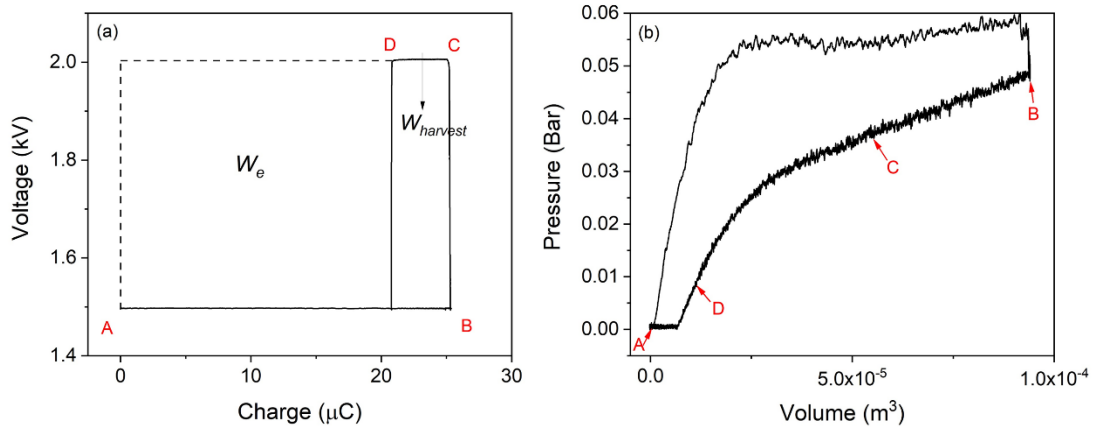


Figure 5.14 Measured energy harvesting cycles for M3M-SBS with the axial deformation of $\lambda_a = 3$ for (a) electrical and (b) mechanical work-conjugate plane. The enclosed to (a) the total converted electrical energy, W_e , of [13 mJ (52 mJ g^{-1})] and the

actual harvested electrical energy, $W_{harvest}$, of [2.3 mJ (9.2 mJ g⁻¹)] and (b) the expended mechanical energy, W_{mech} , of [178 mJ (324 mJ g⁻¹)].

From the energy harvesting cycles, the specific energies generated during the cycles were calculated at different axial deformations for both M3M-SBS and MG-SBS to show the total converted electrical energy, W_e , and the generated electrical energy, $W_{harvest}$, in Figure 5.15a-b respectively. The difference between W_e and $W_{harvest}$ is the W_e takes into account the energy loss through I_{leak} . From Figure 5.15a, both elastomers generated a similar specific energy per cycle up until $\lambda_a = 2.5$. Where $\lambda_a > 2.5$, M3M-SBS generated a higher specific energy up until 51.8 mJ g⁻¹ at $\lambda_a = 3.0$. Comparatively, MG-SBS could generate only 29.0 mJ g⁻¹ when $\lambda_a = 2.8$. The MG-SBS elastomer failed at $\lambda_a = 3.0$.

However, when energy loss through I_{leak} was taken into account, both elastomers generated significantly less specific energy, and produced no energy when $\lambda_a < 1.6$. MG-SBS harvested the greatest energy at $\lambda_a = 2.2$, with $W_{harvest} = 2.3$ mJ g⁻¹. In comparison, M3M-SBS harvested the greatest energy when $\lambda_a = 2.8$ with $W_{harvest} = 11.5$ mJ g⁻¹. The harvested energy does not follow the same trend as the total energy harvested as the leakage current increased as the axial deformation increases.³⁴

After damage, M3M-SBS showed a reduced ability for energy harvesting, with M3M-SBS only able to harvest 0.89 mJ g⁻¹ when $\lambda_a = 2.0$. However, the harvested energy for MG-SBS remained constant and was able to harvest 3.3 mJ g⁻¹ when $\lambda_a = 2.2$. This indicated that under harvesting, M3M-SBS was only able to recover 44% of its electrical breakdown strength, as it failed under an electric field of 20 MV m⁻¹ compared to its original electric field of 45 MV m⁻¹. It was difficult to maintain the thickness of the elastomer at the healed site during the healing process. In a dielectric elastomer generator, air pressure is applied uniformly across the elastomer, instead of planar stresses from pre-strain in an actuator. This means that if the healed site is thinner than the surrounding elastomer, the air pressure can deform the healed region excessively, inducing a premature breakdown despite a low average electric field across the elastomer. The combination of high biaxial strain and high electric field resulted in a lower self-healing performance in a dielectric elastomer generator compared to an actuation device.

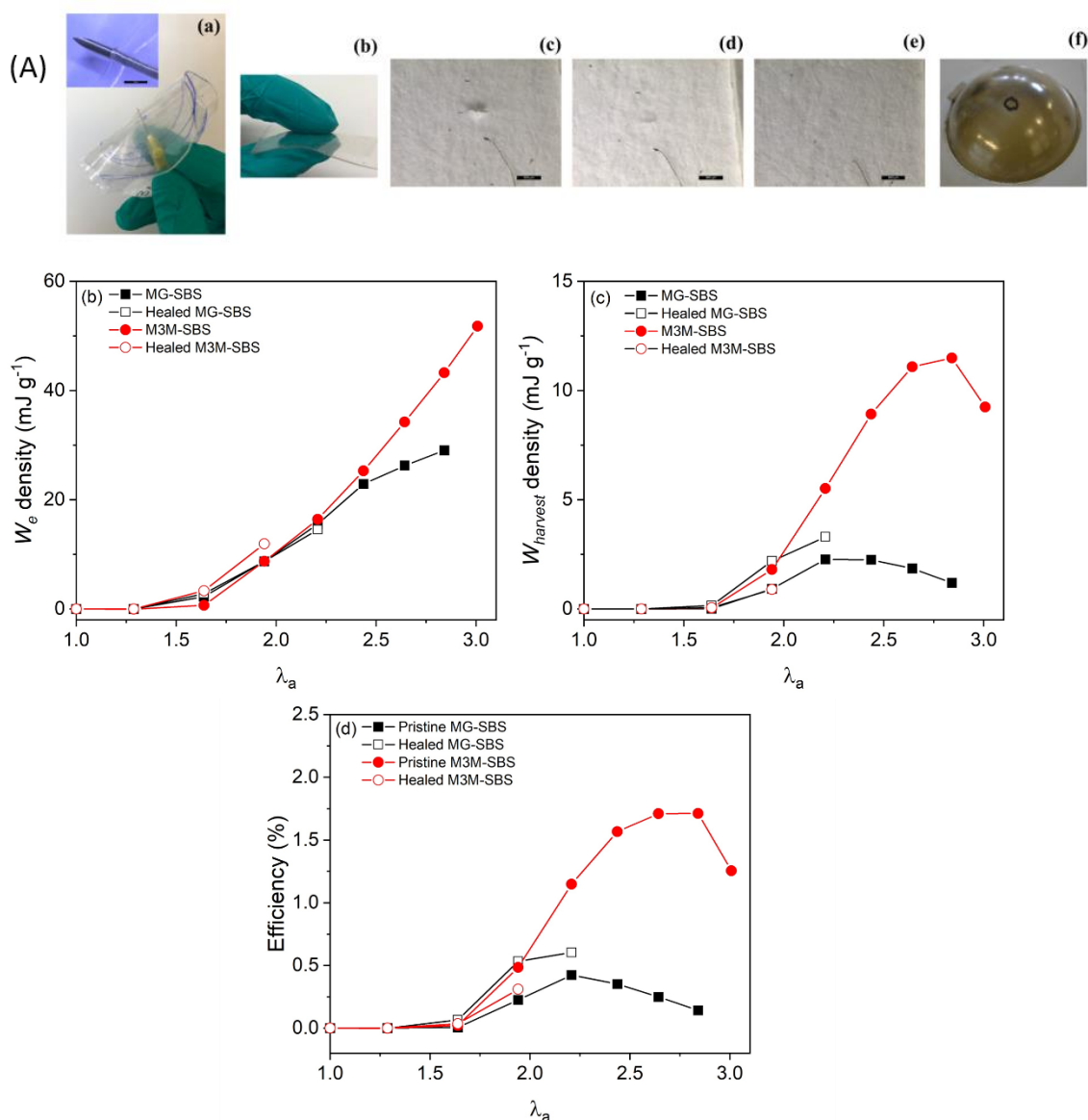


Figure 5.15 (a) The mechanical damage process on the elastomers (b) total converted electrical energy density, (c) generated electrical energy density and (d) energy harvesting efficiency of M3M-SBS and MG-SBS

The energy harvesting efficiencies for MG-SBS and M3M-SBS are shown in Figure 5.15d. Due to a high dissipation of energy, M3M-SBS exhibited an efficiency of 1.7% at $\lambda_a = 2.8$ whilst MG-SBS had an efficiency of 0.4% at $\lambda_a = 2.0$. The energy was dissipated through a large leakage current that arose from the defects within the elastomers as well as the slow depressurisation step in the energy harvesting cycle. To improve this efficiency further, reducing the defects present in the elastomers and increasing the depressurisation speed are key.

However, the efficiency of the energy harvesting device is controlled by other factors as well. This includes the energy harvesting configuration, including the harvesting voltage and the driving voltage, the mechanical loading set-up, such as the duration of each harvesting cycle and the method of mechanical loading, circuitry design and application of electrodes. Therefore, these results are not directly comparable with literature obtained values from dielectric energy generators in the literature, however MG-SBS and M3M-SBS are of similar value to reported VHB 4910 energy harvesting values, which are between $2.1 - 400 \text{ mJ g}^{-1}$.³⁵⁻³⁷

5.3 Conclusion

Methyl-3-mercaptopropionate grafted SBS (M3M-SBS) was synthesised and confirmed *via* ^1H NMR and FTIR with a grafting efficiency of 95.2%. The grafting of the longer polar group reduced the Young's modulus of the elastomer to 2.5 MPa compared to SBS and MG-SBS, whilst leading to a higher strain at break up to 1000%. The cyclic mechanical testing and the stress relaxation of M3M-SBS showed that at high elongations, the elastomer had a low hysteresis loss from a highly elastic behaviour and a lower stress relaxation compared to SBS. However, the stress relaxation was greater when compared to MG-SBS due to greater polymer chain slippage in M3M-SBS.

For the electrical properties, the relative permittivity of M3M-SBS was enhanced compared to SBS to 7.5 whilst maintaining a low $\tan \delta$ loss and retaining its insulating properties. The increase in the relative permittivity was lower than for MG-SBS ($\epsilon_r \approx 11.4$) due to the smaller change in polarity across the polymer backbone.

M3M-SBS exhibited a strong self-healing ability and was able to recover its strain at break to 234%, showing a recovery of 26%, greater than MG-SBS, which demonstrated a strain at break recovery of 21%. The self-healing nature was identified due to a δ^+ proton adjacent to the ester of the grafted polar group interacted with the δ^- aromatic centre of the styrene block of SBS. This intrachain interaction promoted the phase compatibilisation of SBS.

The actuation abilities of M3M-SBS far surpassed those of MG-SBS, despite its lower relative permittivity. M3M-SBS was able to actuate up to 9.3% radially under an electrical field of 39.6 MV m^{-1} . The superior actuation abilities of M3M-SBS were

attributed to its lower Young's modulus and its higher breakdown strength. In addition, the comparison of the experimental actuation abilities of MG-SBS and M3M-SBS were correctly predicted theoretically by the $FoM_{Actuation}$, which indicated that M3M-SBS had a superior actuation performance. Furthermore, M3M-SBS was still able to actuate up to 4.2% radially and recovered 85.3% of its electrical breakdown strength, failing under an electrical field of 33.8 MV m^{-1} .

The energy harvesting performance of M3M-SBS was higher than that of MG-SBS, which was able to harvest 11.5 mJ g^{-1} under an axial deformation of $\lambda_a = 2.8$; in comparison with 2.3 mJ g^{-1} under an axial deformation of $\lambda_a = 2.2$ for MG-SBS. Above these axial deformations, the harvested energy decreased due to an increase in the leakage current.

In addition, the self-healed MG-SBS was able to harvest up to 3.3 mJ g^{-1} under an axial deformation of $\lambda_a = 2.2$, whereas the maximum harvested energy for healed M3M-SBS was 0.89 mJ g^{-1} under an axial deformation of $\lambda_a = 2.0$. The lower healing properties of M3M-SBS based energy harvesting device compared to the actuators was attributed to inhomogeneous thickness at the defect site, which caused strained non-uniformly compared to the bulk elastomer.

Due to the simplicity of the energy harvesting device and circuitry set up, large leakage currents were observed from elastomer defects and from the slow depressurisation step after the removal of air pressure. Therefore, only low harvesting efficiencies were found of up to 1.7% when $\lambda_a = 2.8$ for M3M-SBS and 0.4% when $\lambda_a = 2.2$ for MG-SBS. However, the overall specific energy densities of MG-SBS and M3M-SBS are in the correct range for literature reported values.

Overall, this chapter successfully demonstrated that the chain length of the grafted polar groups has a key role in determining the electromechanical properties and the self-healing properties of the elastomer. The mechanical properties and electrical breakdown strength of a dielectric elastomer should be considered for achieving high actuation and energy harvesting performance, alongside a high relative permittivity.

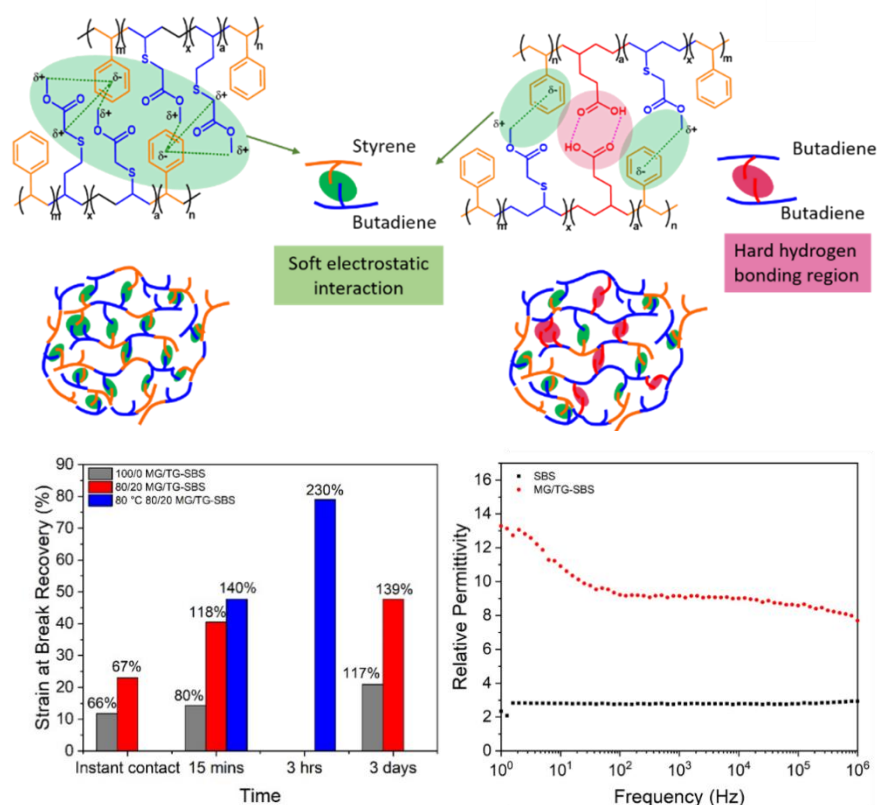
5.4 References

1. H. U. Rehman, Y. Chen, M. S. Hedenqvist, R. Pathan, H. Liu, H. Wang, T. Chen, X. Zhang and H. Li, *Mater. Des.*, 2019, **182**, 108010.
2. C. Ellingford, R. Zhang, A. M. Wemyss, Y. Zhang, O. B. Brown, H. Zhou, P. Keogh, C. Bowen and C. Wan, *ACS Appl. Mater. Interfaces*, 2020, **12**, 7595–7604 .
3. Y. Pan, J. Hu, Z. Yang and L. Tan, *ACS Appl. Polym. Mater.*, 2019, **1**, 425-436.
4. C.-J. Fan, Z.-C. Huang, B. Li, W.-X. Xiao, E. Zheng, K.-K. Yang and Y.-Z. Wang, *Sci. China Mater.*, 2019, **62**, 1188-1198.
5. J. Chen, F. Li, Y. Luo, Y. Shi, X. Ma, M. Zhang, D. W. Boukhvalov and Z. Luo, *J. Mater. Chem. A*, 2019, **7**, 15207-15214.
6. J.-F. Mei, X.-Y. Jia, J.-C. Lai, Y. Sun, C.-H. Li, J.-H. Wu, Y. Cao, X.-Z. You and Z. Bao, *Macromol. Rapid Commun.*, 2016, **37**, 1667-1675.
7. L. Liu, S. Yan and L. Zhang, *Macromol. Rapid Commun.*, 2018, **39**, 1800349.
8. A. Das, A. Sallat, F. Böhme, M. Suckow, D. Basu, S. Wießner, K. W. Stöckelhuber, B. Voit and G. Heinrich, *ACS Appl. Mater. Interfaces*, 2015, **7**, 20623-20630.
9. L. Du, Z.-Y. Xu, C.-J. Fan, G. Xiang, K.-K. Yang and Y.-Z. Wang, *Macromolecules*, 2018, **51**, 705-715.
10. Q. Zheng, Z. Ma and S. Gong, *J. Mater. Chem. A*, 2016, **4**, 3324-3334.
11. M. Suckow, A. Mordvinkin, M. Roy, N. K. Singha, G. Heinrich, B. Voit, K. Saalwächter and F. Böhme, *Macromolecules*, 2018, **51**, 468-479.
12. A. Campanella, D. Döhler and W. H. Binder, *Macromol. Rapid Commun.*, 2018, **39**, 1700739.
13. N. I. Khan, S. Halder, S. B. Gunjan and T. Prasad, *IOP Conf. Ser.: Mater. Sci. Eng.*, 2018, **377**, 012007.
14. Y.-L. Liu and T.-W. Chuo, *Polym. Chem.*, 2013, **4**, 2194-2205.
15. J. Bai, H. Li, Z. Shi, M. Tian and J. Yin, *RSC Adv.*, 2015, **5**, 45376-45383.
16. L. Zhang, T. Qiu, Z. Zhu, L. Guo and X. Li, *Macromol. Rapid Commun.*, 2018, **39**, 1800121.
17. L. Ling, J. Li, G. Zhang, R. Sun and C.-P. Wong, *Macromol. Res.*, 2018, **26**, 365-373.
18. S.-H. Lee, S.-R. Shin and D.-S. Lee, *Mater. Des.*, 2019, **172**, 107774.
19. R. Mo, J. Hu, H. Huang, X. Sheng and X. Zhang, *J. Mater. Chem. A*, 2019, **7**, 3031-3038.
20. R. Purohit, N. K. Gupta, M. R. Purohit, A. Patil, R. K. Bhariya and S. K. Singh, *Mater. Today: Proc.*, 2015, **2**, 3371-3377.
21. W. Wang, Y. Zhang and W. Liu, *Prog. Polym. Sci.*, 2017, **71**, 1-25.
22. J. W. Steed and J. L. Atwood, in *Supramol. Chem.*, John Wiley & Sons, 2009, pp. 1-48.
23. J. S. Silverstein, B. J. Casey, M. E. Natoli, B. J. Dair and P. Kofinas, *Macromolecules*, 2012, **45**, 3161-3167.
24. M. Wright, in *An Introduction to Chemical Kinetics*, ed. M. Wright, John Wiley & Sons, Ltd, 2004, pp. 263-316.
25. L. Wilhelmy, *Ann. Phys.*, 1850, **157**, 499-526.
26. B. Korthals, M. C. Morant-Miñana, M. Schmid and S. Mecking, *Macromolecules*, 2010, **43**, 8071-8078.

27. Y. Gao, X. Wang, L. Tong, A. Qin, J. Z. Sun and B. Z. Tang, *Polym. Chem.*, 2014, **5**, 2309-2319.
28. W. G. D. P. Silva, L. Evangelisti and J. van Wijngaarden, *J. Phys. Chem. A*, 2019, **123**, 9840-9849.
29. K. Kojio, M. Furukawa, Y. Nonaka and S. Nakamura, *Materials*, 2010, **3**, 5097-5110.
30. R. P. Wool and K. M. O'Connor, *J. Polym. Sci., Polym. Lett. Ed.*, 1982, **20**, 7-16.
31. D. M. Opris, *Adv. Mater.*, 2018, **30**, 1703678.
32. E. Perju, Y. S. Ko, S. J. Dünki and D. M. Opris, *Mater. Des.*, 2020, **186**, 108319.
33. S. J. Dünki, Y. S. Ko, F. A. Nüesch and D. M. Opris, *Adv. Funct. Mater.*, 2015, **25**, 2467-2475.
34. C. Chiang Foo, S. Cai, S. Jin Adrian Koh, S. Bauer and Z. Suo, *J. Appl. Phys.*, 2012, **111**, 034102.
35. R. Pelrine, R. D. Kornbluh, J. Eckerle, P. Jeuck, S. Oh, Q. Pei and S. Stanford, presented in part at the SPIE Smart Structures and Materials, 2001.
36. C. Jean-Mistral, S. Basrour and J.-J. Chaillout, presented in part at the SPIE Smart Structures and Materials + Nondestructive Evaluation and Health Monitoring, 2008, 148-156.
37. C. Graf and J. Maas, *Evaluation and Optimization of Energy Harvesting Cycles Using Dielectric Elastomers*, SPIE, 2011.

Chapter 6

Modification of SBS with mixed pendant polar groups for enhancement of both self-healing and electromechanical properties



Publications:

C. Ellingford, A. M. Wemyss, R. Zhang, I. Prokes, T. Pickford, C. Bowen, V. A. Coveney and C. Wan*, Understanding the enhancement and temperature-dependency of the self-healing and electromechanical properties of dielectric elastomers containing mixed pendant polar groups, *J. Mater. Chem. C*, 2020, **8**, 16, 5426

6.1 Introduction

Different types of interactions between polymer chains can be used to tune the electromechanical properties, the self-healing properties and the operational temperature of a dielectric elastomer. This allows the optimal operating conditions to be configured by the ratio of polar groups and interactions introduced into a dielectric elastomer, thus allowing an energy harvesting or actuation device to operate under hostile conditions.

As seen in the previous chapter in Figure 5.1, a range of various noncovalent interactions are possible, all with different strength binding energies. Thus far, MG-SBS and M3M-SBS have been synthesised containing solely noncovalent electrostatic interactions which has introduced a self-healing ability into the dielectric elastomers, but were readily overcome at elevated temperatures.¹

Hydrogen bonding introduces higher strength noncovalent interactions, introducing the ability for self-healing and temperature resistance. Typically, hydrogen bonding introduces a temperature resistance up to 60 °C, beyond which the thermal energy of the system allows the hydrogen bonding to easily break and reform.²

Hydrogen bonding takes place between hydrogen atoms and electronegative atoms such as oxygen or nitrogen which behave as hydrogen bond acceptors and donors, dictated by the type of functional group. Hydrogen bond acceptors donate electron density to the hydrogen bond and consist of esters, aldehydes, ethers and ketones, whereas hydrogen bond donors provide a hydrogen atom for the hydrogen bond and include amines, alcohols and amides. Carboxylic acids are unique as they are able to behave as both a hydrogen bond acceptor and donor as it is able to stabilise itself through the formation of a resonance structure and can form reciprocal dimers.

Increasing the number of hydrogen bonding acceptors and donors on a polymer chain increases the strength of the hydrogen bonding formed and can be used to tailor the properties of a polymer.³ This idea has been used by Cao *et al.* to develop self-healing flexible sensors designed for human-machine interaction able to read facial movements for real-time speaking applications. After self-healing, a minimal loss in the electronic output signal was observed, thus ensuring a reliable sensor even after failure.⁴

However, for actuation and energy harvesting applications, increasing the hydrogen bonding groups can affect its performance by increasing the stiffness and brittleness of the elastomer. Therefore, it is key to balance the strength of the hydrogen bonding network, and thus the strength of self-healing.

Previously developed self-healing dielectric elastomers have primarily focussed on silicone based materials. Hydrogen bonding in silicone elastomers has been introduced through carboxylic acid and amine groups by Sun *et al.* show in Figure 6.1. They found that self-healing after mechanical damage led to a recovery in the tensile strength of 115%, when allowed to heal at 80 °C for five hours. This was because the hydrogen bonds were able to freely break and reform, and therefore interacting with polymer chains across the polymer divide. Interestingly, if the silicone elastomer was self-healed at 100 °C, the breakdown strength increased, the relative permittivity increased to 4.4 and the silicone elastomer was able to actuate up to 8.3% under an electric field of 15 kV mm⁻¹. This change in behaviour was due the hydrogen bonding being converted to stronger ionic bonding. However, this was at the expense of the strain at break as the brittleness of the elastomer increased.⁵

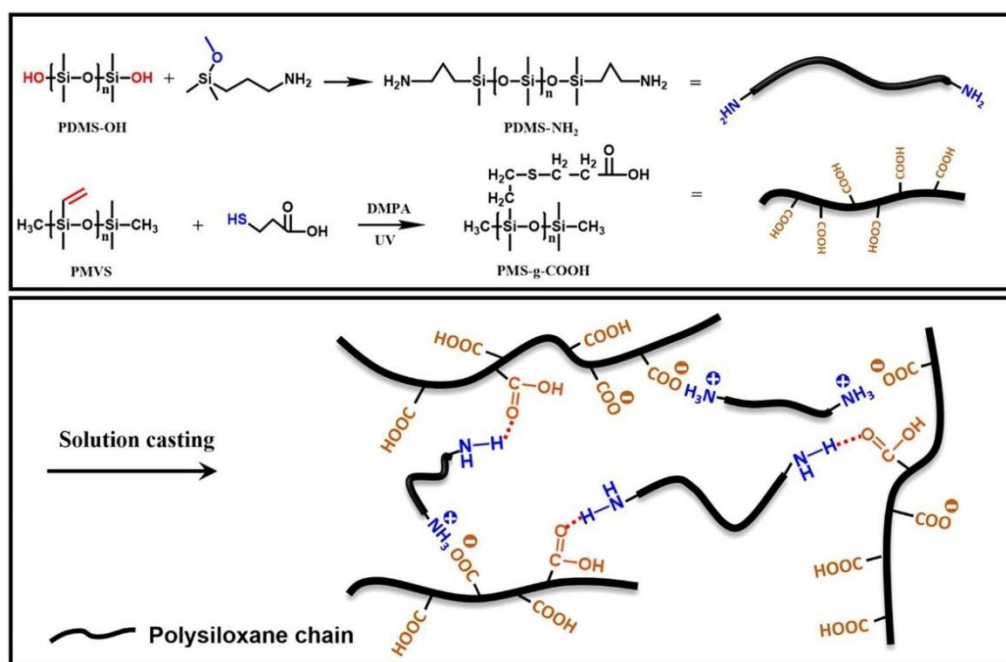


Figure 6.1 Formation of hydrogen bonding between carboxylic acid and amine groups on a polysiloxane chain as well as the ionic bonds formed when converted at 100 °C. Reproduced from Sun *et al.*⁵

Madsen *et al.* used an alternative approach of forming an interpenetrating polymer network which also contained ionic crosslinking through proton exchange between amines and carboxylic acids. When self-healed for 12 hours at 120 °C, the elastomer could recover up to 77% of its strain at break, and failed at 300% strain. The higher temperature for healing was required because of the increase binding energy exhibited by ionic bonds compared to hydrogen bonds. Furthermore, the modified elastomer exhibited a relative permittivity of up to 4.3 and a high breakdown strength of 57 MV m⁻¹.⁶

Therefore, in this chapter hydrogen bonding is introduced into SBS in different ratios to enhance the self-healing abilities of SBS and enhance the ability for SBS to operate as an actuator or energy harvester in hostile environments. To introduce hydrogen bonding an analogous polar group to methyl thioglycolate was used, thioglycolic acid (TG). Thioglycolic acid is similar to methyl thioglycolate except that it contains carboxylic acid functionality instead of an ester.

Thus thioglycolic acid was introduced into SBS in a graded approach whereby the strength of the hydrogen bonding network was tuned by the ratio of grafting between methyl thioglycolate and thioglycolic acid. This was conducted as a one pot synthesis whereby both thiols were added in the desired ratio and the resulting elastomer called MG/TG-SBS. The ratio between MG and TG was varied between 100/0 and 80/20, and further increases in the hydrogen bonding strength were deemed not desirable due to the degradation of the mechanical properties.

The successful synthesis of a range of MG/TG-SBS elastomers was confirmed *via* ¹H NMR and FTIR and the effect on the strength, stiffness and failure investigated. This is followed by the electrical properties of the MG/TG-SBS elastomers.

To understand the effect of the hydrogen bonding on the temperature properties of the elastomers, variable temperature FTIR, ¹H NMR and impedance spectroscopy was conducted, alongside self-healing testing of the MG/TG-SBS elastomers at both room temperature and at 80 °C.

Finally, the actuation properties of 80/20 MG/TG-SBS was investigated and compared to both MG-SBS and M3M-SBS. This work demonstrates the effect the introduction of a hydrogen bonding network has on the temperature properties of SBS elastomers for use in actuation and energy harvesting devices in hostile conditions.

6.2 Results and Discussion

6.2.1 Intrinsic modification of SBS with methyl thioglycolate and thioglycolic acid

By altering the grafting of the hydrogen bonding thioglycolic acid group, the self-healing performance and the temperature resistance of the elastomer can be balanced depending on the environmental conditions required for an actuation or energy harvesting device. Therefore, both methyl thioglycolate and thioglycolic acid were grafted utilising photoinitiated thiol-ene chemistry between 100/0 and 80/20 respectively and characterised *via* ^1H NMR and FTIR in Figure 6.2 and Appendix Figure 16 and 17. For clarity, MG-SBS is referred to as 100/0 MG/TG-SBS in this chapter, to make clearer the ratios of the two thiols present in the elastomer.

From ^1H NMR in Figure 6.2a and Appendix Figure 16, the characteristic alkene peak for SBS at 5.4 ppm decreased substantially after the photoreaction. In its place, two new peaks arose, a CH_3 for the terminus of methyl thioglycolate at 3.7 ppm, and a CH_2 peak at 3.2 ppm for both methyl thioglycolate and thioglycolic acid. Therefore, from equation 4.5, the total grafting ratio of both methyl thioglycolate and thioglycolic acid to SBS was 97.2%, 97.5%, 97.8% and 93.4% for 100/0, 95/5, 90/10 and 80/20 MG/TG-SBS respectively. Additionally, the thiol grafting was compared to the reduction in the vinyl groups at 5.4 ppm to determine the ratio of methyl thioglycolate and thioglycolic acid grafting. Therefore the absolute grafting ratio of 95/5, 90/10 and 80/20 MG/TG-SBS was 94.9/5.1%, 87.9/12.1% and 73.4/26.6% respectively.

Additionally, the FTIR spectra in Figure 6.2b and Appendix Figure 17 show the introduction of new bonds in the elastomers. After the reaction, the alkene group of SBS at 3006 cm^{-1} disappeared and new carboxylic acid and ester $\text{C}=\text{O}$ stretches appeared at 1730 cm^{-1} . In addition, an asymmetric $\text{C}-\text{O}-\text{C}$ stretch and symmetric $\text{C}-\text{O}-\text{C}$ stretch from the methyl thioglycolate ester are observed at 1277 cm^{-1} and 1007 cm^{-1} respectively. Furthermore, an $\text{O}-\text{H}$ stretch in the region of $3200 - 3400\text{ cm}^{-1}$ appears, observed most strongly in 80/20 MG/TG-SBS and ascribed to the thioglycolic acid carboxylic acid.

The GPC trace for 90/10 MG/TG-SBS is shown in Figure 6.2c. Prior to modification, SBS had an M_n of $86,000\text{ g mol}^{-1}$, M_w of $101,000\text{ g mol}^{-1}$ and a Đ of 1.17. After modification, the M_n increased to $273,000\text{ g mol}^{-1}$, the M_w increased to $656,000\text{ g mol}^{-1}$

1 and the \bar{D} increased to 2.41, once again due to polymer chain scission. The increase in the M_n and M_w also confirms the successful grafting reaction. However, 95/5 and 80/20 MG/TG-SBS could not be ran *via* GPC due to solubility issues in THF arising from the acid groups grafted.

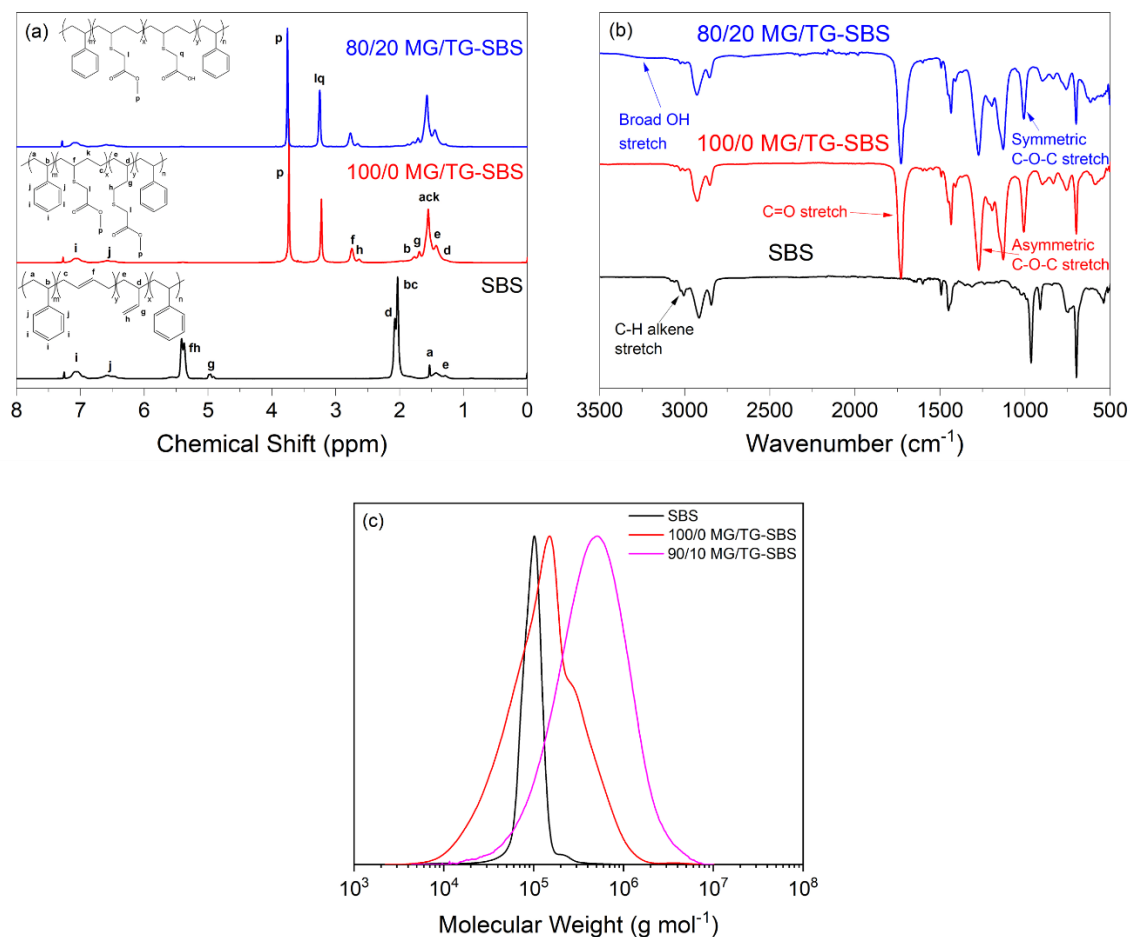


Figure 6.2 (a) ^1H NMR spectra at 400 MHz in CDCl_3 , (b) FTIR spectroscopy of SBS, 100/0 MG/TG-SBS and 80/20 MG/TG-SBS and (c) GPC trace of 90/10 MG/TG-SBS in THF with a Refractive Index detector.

6.2.2 Synergistic effects of methyl thioglycolate and thioglycolic acid on elastomer morphology and electromechanical properties

The effect of the grafted polar group ratios on the mechanical properties are shown through the stress strain curves of Figure 6.3, and summarised in Table 6.1. Prior to modification, the tensile strength of SBS was 8.9 ± 0.7 MPa and had a strain at break of $857 \pm 45.8\%$. As mentioned in section 4.2.2, 100/0 MG/TG-SBS exhibited a reduced tensile strength of 3.1 ± 0.1 MPa and a reduced strain at break of $569 \pm 25.9\%$.

Table 6.1 Summary of mechanical properties for SBS and MG/TG-SBS elastomers with grafting ratios between 100/0 and 80/20 respectively

Elastomer	Tensile strength (MPa)	Strain at break (%)
SBS	8.9 ± 0.7	857 ± 45.8
100/0 MG/TG-SBS	3.1 ± 0.1	569 ± 25.9
95/5 MG/TG-SBS	4.4 ± 0.3	602 ± 35.8
90/10 MG/TG-SBS	2.8 ± 0.1	315 ± 26.6
80/20 MG/TG-SBS	3.3 ± 0.3	270 ± 47

Through the introduction of hydrogen bonding, the tensile strength of the elastomers increased for both 95/5 and 80/20 MG/TG-SBS, to 4.4 ± 0.3 MPa and 3.3 ± 0.3 MPa respectively compared to 100/0 MG/TG-SBS. However, the tensile strength for 90/10 MG/TG-SBS decreased to 2.8 ± 0.1 MPa, attributed to a change in the polymer microstructure and phase morphology due to the presence of a larger hydrogen bonding network. This effect is further confirmed in AFM imaging in Figure 6.5.

A stronger hydrogen bonding network also decreased the strain at break exhibited in the elastomers. The strain at break decreased to $270 \pm 47\%$ for 80/20 MG/TG-SBS. This demonstrates that the mechanical properties can be tuned by tuning the hydrogen bonding network for the optimal strain at break and tensile strength properties for use in actuation or energy harvesting device applications.

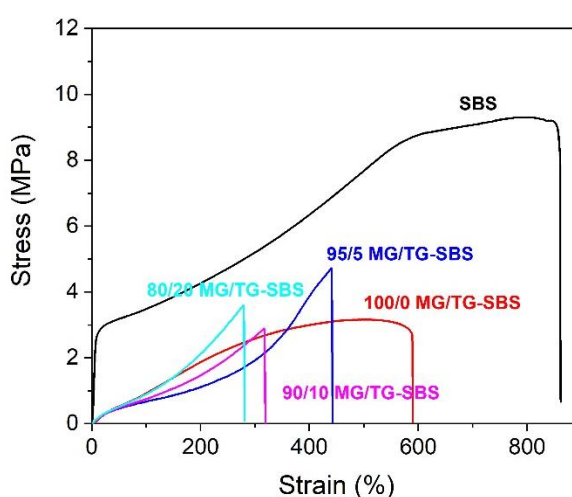


Figure 6.3 Stress strain curves of SBS, 100/0, 95/5, 90/10 and 80/20 MG/TG-SBS

The dynamic hydrogen bonding networks from thioglycolic acid introduces a stronger interaction between polymer chains compared to the electrostatic interaction from methyl thioglycolate. This affects the interchain behaviour and the polymer chain mobility, and was observed in the cyclic stress softening profiles. In Figure 6.4a-b, the cyclic stress softening curves for the first cycle and fifth cycle are shown for 95/5, 90/10 and 80/20 MG/TG-SBS, with the cyclic stress softening curves of SBS and 100/0 MG/TG-SBS in section 4.2.5. As seen from Figure 6.4a, c, modification of SBS with methyl thioglycolate and thioglycolic acid resulted in a hysteresis loss of less than 20% when cyclically strained 100%. Comparatively, SBS exhibited a larger hysteresis loss of 39%. The difference in mechanical behaviour arose from the interchain electrostatic interactions of methyl thioglycolate compatibilising the block co-polymerisation of SBS and preventing hysteresis energy loss.

Increasing the strain for cyclic stress softening increased the hysteresis loss for all elastomers. SBS exhibited a hysteresis loss of 58% after five 300% strain cycles. 100/0, 95/5 and 90/10 MG/TG-SBS all exhibited lower hysteresis loss compared to SBS, however, the elastomers showed a difference in behaviour depending on the degree of hydrogen bonding present. As such, 90/10 MG/TG-SBS had the greatest hysteresis energy loss of 29% compared to 95/5 and 100/0 MG/TG-SBS, which both exhibited hysteresis losses below 20%. The difference in behaviour was attributed to the rigid behaviour of the stronger hydrogen bonding network formed. In contrast, 80/20 MG/TG-SBS could not be tested at 300% strain as it failed at 270% strain.

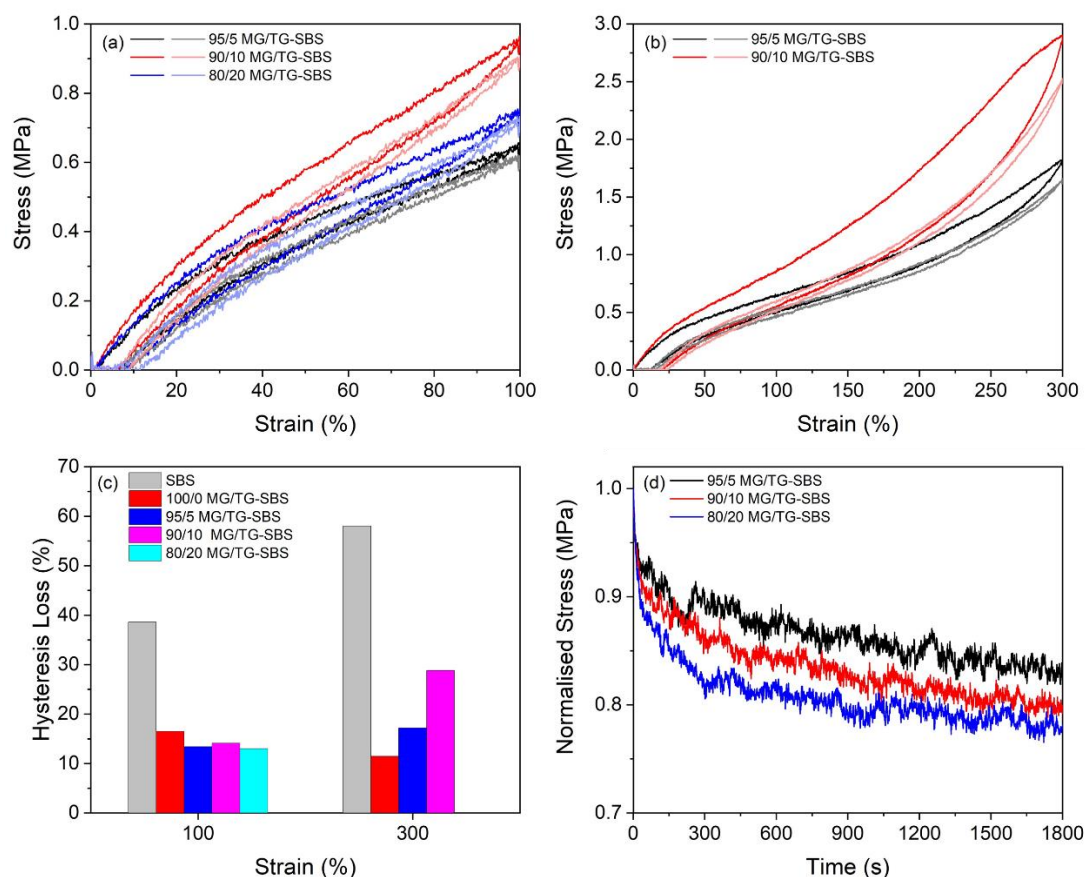


Figure 6.4 (a) Cyclic stress softening of 95/5, 90/10 and 80/20 MG/TG-SBS at 100%, (b) cyclic stress softening of 95/5, 90/10 and 80/20 MG/TG-SBS at 300%, (c) a summary of hysteresis loss from cyclic stress softening for SBS, 100/0, 95/5, 90/10 and 80/20 MG/TG-SBS. Darker colour is cycle 1, lighter colour is cycle 5. (d) Stress relaxation of 95/5, 90/10 and 80/20 MG/TG-SBS

The stress relaxation behaviour of the hydrogen bonding elastomers is shown in Figure 6.4d, whilst stress relaxation for SBS and 100/0 MG/TG-SBS can be found in section 4.2.5. The stress relaxation of all MG/TG-SBS elastomers remained low, with all elastomers retaining 75-85% of their stress after 30 minutes. However, the stress relaxation of the MG/TG-SBS elastomers increased with increasing hydrogen bonding network within the elastomers. This was attributed to the interchain interactions present within the elastomer and the effect that this has on the polymer phase morphology. In comparison, SBS exhibited a significantly greater stress relaxation due to polymer chain slippage.

AFM imaging demonstrated the effect of altering the strength of the hydrogen bonding had on the phase morphology, Figure 6.5a. In unmodified SBS, microphase separation

was observed between the styrene and butadiene blocks, whereby the dark cylindrical styrene phase is surrounded a lighter butadiene matrix. After modification with 95/5 MG/TG-SBS, the ordered phase morphology of SBS was lost due to compatibilisation by methyl thioglycolate¹ and a disordered spherical arrangement within the matrix became present, attributed to a small amount of uncompatibilised styrene. Further increases in the strength of the hydrogen bonding network increased the number of spheres present in 90/10 MG/TG-SBS but decreased the difference in ‘hard/soft’ regions in the elastomer until an ordered arrangement of sphere is observed in 80/20 MG/TG-SBS. The disordered spherical network was attributed to a change in microstructure for 90/10 MG/TG-SBS and is the reason behind its decrease in tensile strength in section 6.2.1. However, the presence of the spheres was not attributed to the presence of uncompatibilised styrene due to the reduction of grafted methyl thioglycolate. As is observed for 90/10 MG/TG-SBS, the height distribution within the contour maps is significantly lower than for SBS, 100/0 and 95/5 MG/TG-SBS, thus not indicating that phase separation is taking place. Therefore, the presence of the spheres was attributed to ordered regions of thioglycolic acid groups as the hydrogen bond network grows. This was further reinforced in 80/20 MG/TG-SBS, whereby the height distribution decreased further, and a phase morphology transition occurred to show a regular microstructure arrangement in place of a disordered phase morphology. This process is shown in Figure 6.5b.

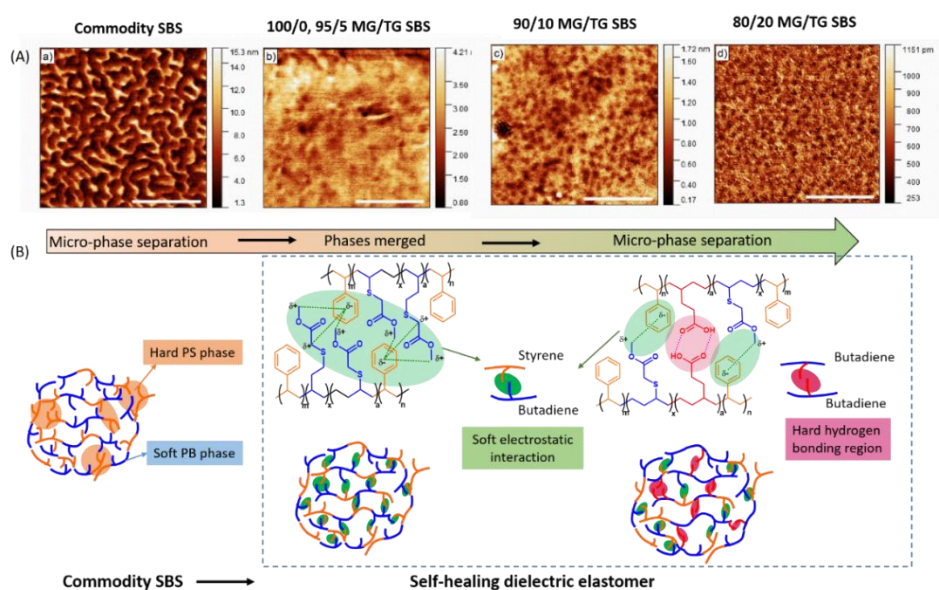


Figure 6.5 (a) AFM images of SBS, 95/5, 90/10 and 80/20 MG/TG-SBS with height distribution scales. Scale bar shown is 200 nm and (b) schematic diagram to explain

to ordered microstructure phase transition upon increase in hydrogen bonding content. The increase in compatibility between styrene and butadiene results from electrostatic interactions (shown in green). Increase the hydrogen bonding network introduces a disorder-to-order phase transition of hydrogen bonding regions (shown in red). Reproduced from Ellingford et. al.⁷

The increased strength of the hydrogen bonding network affected the glass transition temperatures for MG/TG-SBS elastomers, Figure 6.6a. Prior to modification, SBS exhibited two glass transition temperatures, one for butadiene at $-83\text{ }^{\circ}\text{C}$ and one for styrene at $97\text{ }^{\circ}\text{C}$ as explained in section 4.2.3. After modification, 95/5 MG/TG-SBS exhibited a strong, single glass transition temperature at $-24.8\text{ }^{\circ}\text{C}$ as both styrene and butadiene blocks were compatibilised by the modification. Increasing the thioglycolic acid ratio increased the glass transition temperature to $-22.4\text{ }^{\circ}\text{C}$ and $-18.5\text{ }^{\circ}\text{C}$ for 90/10 and 80/20 MG/TG-SBS respectively. The increase in the glass transition temperature was associated with the increased strength of the hydrogen bonding network, requiring more energy to overcome it. As the thioglycolic acid content increased, small broad peaks are observed in the region of $40\text{ }^{\circ}\text{C} - 100\text{ }^{\circ}\text{C}$ associated with the hydrogen bonding. As the thermal energy in the system increased, the hydrogen bonds were able to freely break and reform. As this reduced the strength of the interchain interactions, the polymer chain motions increased and lead to the relaxations observed. This supports the observations from AFM imaging in Figure 6.5.

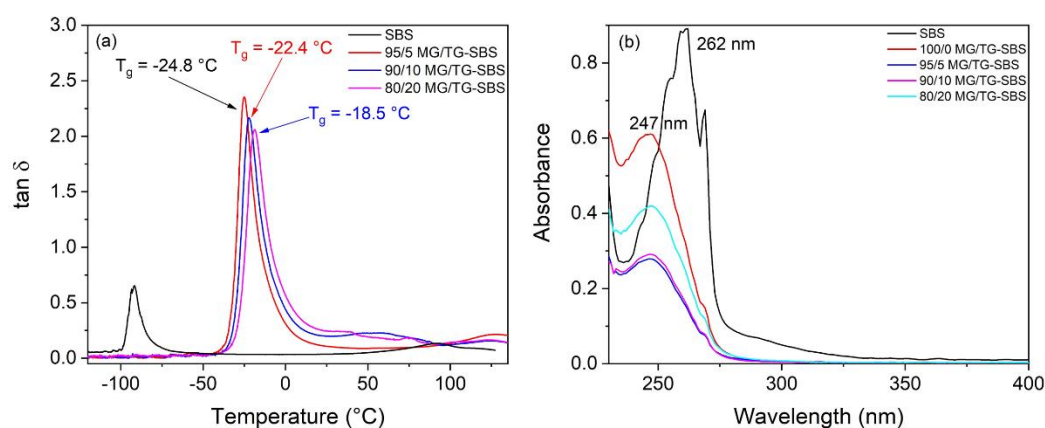


Figure 6.6 (a) DMTA $\tan \delta$ for SBS, 95/5, 90/10 and 80/20 MG/TG-SBS and (b) solution state UV-Vis spectroscopy for SBS, 100/0, 95/5, 90/10 and 80/20 MG/TG-SBS in DCM

The effect of the hydrogen bonding network on the methyl thioglycolate/styrene electrostatic interaction was investigated *via* solution state UV-Vis spectroscopy in Figure 6.6b. Before the introduction of thioglycolic acid, SBS exhibited a π - π^* transition at 262 nm, from free styrene rings which blue shifted to 247 nm after grafting of methyl thioglycolate, see section 4.2.3 for more information. After grafting with increased ratios of thioglycolic acid, the absorption wavelength for the π - π^* transition of styrene remained at 247 nm. This indicated that the interaction between methyl thioglycolate and styrene was unaffected by the addition of thioglycolic acid and remained fully interacting, despite the change in microstructure to an ordered arrangement. This also provided further evidence for the rationalisations of the AFM imaging in Figure 6.5, whereby the ordered arrangement of spheres was attributed to thioglycolic acid groups instead of a phase separation between the styrenic block and the methyl thioglycolate modified butadiene block.

Finally, the effect of the change in polymer composition and morphology was investigated using impedance spectroscopy in Figure 6.7. Prior to grafting, SBS exhibited a relative permittivity of 2.8 at 10^3 Hz. After modification, the relative permittivity of 95/5, 90/10 and 80/20 increased to $\epsilon_r \approx 9.2$ at 10^3 Hz. This increase was due to the polar groups increasing the polarity of the polymer backbone. However, this increase was not as high as for 100/0 MG/TG-SBS in section 4.2.2 ($\epsilon_r \approx 11.4$). Whilst thioglycolic acid is more polar than methyl thioglycolate, the carboxylic acid of thioglycolic acid hydrogen bonds through dimerization to form the spheres observed in the AFM imaging of Figure 6.5. The dimerization reduced the change in polarity as the charge difference was decreased across the carboxylic acid of thioglycolic acid. Thus purely thioglycolic acid modified SBS demonstrated lower relative permittivities of 7.2 at 10^3 Hz in the literature.⁸⁻¹⁰

The $\tan \delta$ loss of the MG/TG-SBS elastomers remained low after modification. In SBS, the $\tan \delta$ loss was 0.009 at 10^3 Hz. In 95/5, 90/10 and 80/20 MG/TG-SBS, the $\tan \delta$ loss also remained low and was between 0.01 and 0.02 at 10^3 Hz. This indicated that these elastomers have a high efficiency for energy harvesting due to a low energy dissipation. The $\tan \delta$ rose below 10^2 Hz due to electrode polarisation, where electrons became blocked at the electrode.¹¹ Meanwhile, the AC conductivity of the MG/TG-SBS elastomers increased to 1×10^{-9} S m⁻¹, and become frequency independent at low frequency. Contrastingly, SBS displayed much lower AC conductivity, which

decreased to $1 \times 10^{-12} \text{ S m}^{-1}$ at 1 Hz. Finally, the MG/TG-SBS elastomers maintained an insulating phase angle of -90° , also seen in SBS. However, due to electrode polarisation the phase angle tends towards 0° below 10^2 Hz and an additional small deviation from -90° was observed above 10^5 Hz. This was ascribed to the beginning of a relaxation peak due to atomic polarisation, where part of or all of the polymer chains are unable to respond quickly enough to the alternating electric field.

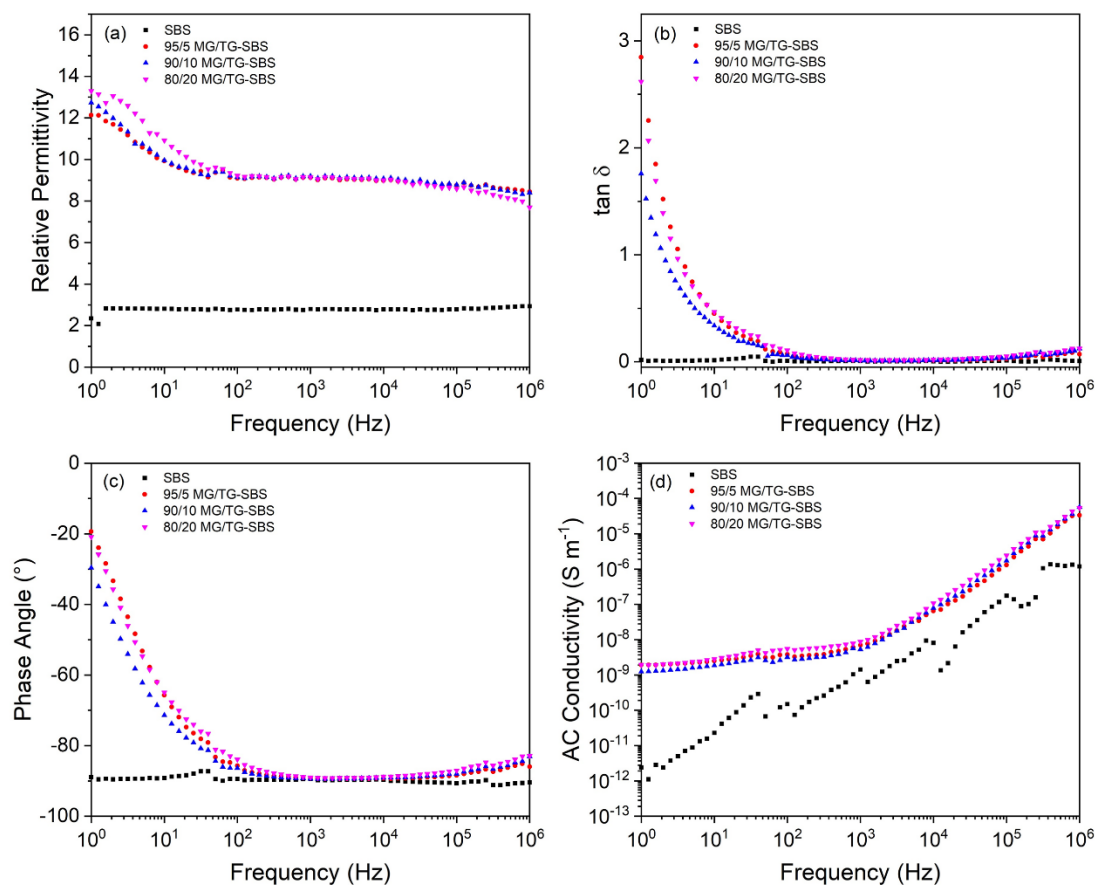


Figure 6.7 Impedance spectroscopy for SBS, 95/5, 90/10 and 80/20 MG/TG-SBS for (a) relative permittivity, (b) $\tan \delta$, (c) phase angle and (d) AC conductivity

6.2.3 Temperature dependency of self-healing and electric properties

Variable temperature FTIR allows the interactions present within MG/TG-SBS elastomers to be investigated, to determine the nature of the exhibited interactions within the elastomers and at which temperature they are affected. Therefore, the FTIR of MG/TG-SBS elastomers was ran between 30°C and 150°C , Figure 6.8 and Appendix Figure 17.

As the temperature increased from 30 to 150 °C, the wavenumber of the C=O ester at 1730 cm⁻¹ increased by 6 cm⁻¹ to 1736 cm⁻¹ in all four variations of MG/TG-SBS elastomers. In addition to this, a shoulder peak at 1700 cm⁻¹ was observed in 90/10 and 80/20 MG/TG-SBS attributed to the carboxylic acid C=O dimer present in the hydrogen bonding network. As expected, the shoulder peak is strongest in 80/20 MG/TG-SBS, which has the largest hydrogen bonding network present. However, the dimer peak flattens with increasing temperature and is not visible in 80/20 MG/TG-SBS beyond 90 °C. Comparatively, the C=O hydrogen bonding peak disappeared above 50 °C in 90/10 MG/TG-SBS due to the presence of a weaker hydrogen bonding network. Finally, no hydrogen bonding C=O peak can be observed in 95/5 MG/TG-SBS.

The O-H peak in 80/20 MG/TG-SBS elastomers is strongly visible, and shifts from 3200 cm⁻¹ to 3300 cm⁻¹ as the temperature increased. This shift is attributed to the breaking of the hydrogen bonding, and freeing of the OH groups on the carboxylic acid of thioglycolic acid, as the increased thermal energy allowed these groups to freely break and reform. In 90/10 MG/TG-SBS, the OH-peak was only observed until 90 °C, due to the weaker hydrogen bonding network present. Above this temperature, the hydrogen bonding network is completely lost. This demonstrated that a balance in tunability of the mechanical properties and the hydrogen bonding network can be struck, depending on the environment for the application. Comparatively, the hydrogen bonding was not visible in this range for 95/5 MG/TG-SBS.

Further temperature dependence of the hydrogen bonding network was observed in variable temperature solution state ¹H NMR for 80/20 MG/TG-SBS. In Appendix Figure 18 the change in the chemical shift of the acid proton from thioglycolic acid was monitored. At 25 °C, the peak appeared at 8.9 ppm. At 50 °C, the peak shifted upfield to 8.3 ppm due to the breaking of hydrogen bonding, deshielding the acid proton. Nonetheless, a downfield tail on the peak was observed at this temperature indicating that some hydrogen bonding remained. After increasing to 70 °C, the tail disappeared suggesting that the hydrogen bonding interaction had been thermally overcome.

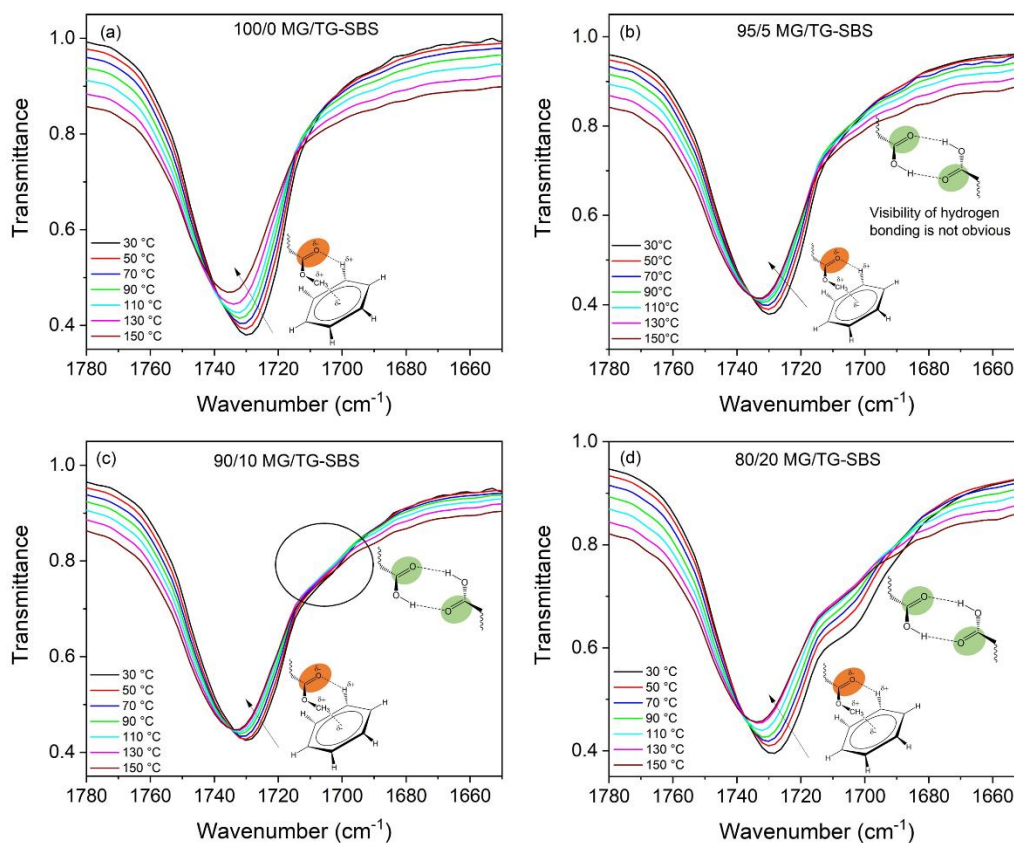


Figure 6.8 Temperature-dependent FTIR spectroscopy for MG/TG-SBS at 1730 cm^{-1} : (a) 100/0, (b) 95/5, (c) 90/10 and (d) 80/20

Variable temperature impedance spectroscopy was implemented to investigate the effect of the electrostatic interactions and hydrogen bonding interactions on the electrical properties of SBS, 100/0 MG/TG-SBS and 80/20 MG/TG-SBS, and how thermal energy affects this further, see Figure 6.9. SBS could only be investigated at 30 °C as the elastomer began to flow at 50 °C and reduced the adhesion of the electrode to the surface. Nonetheless, a relaxation peak was observed for SBS at 12 kHz in both the phase angle and the $\tan \delta$. The relaxation peak was ascribed to the frequency at which the polymer chains could not respond to the alternating electric field.

For 100/0 MG/TG-SBS, a relaxation peak was observed at 9 kHz in both the phase angle and the $\tan \delta$, once again ascribed to the inability of the polymer chains to respond to the alternating electric field. The frequency of this peak was lower than for SBS, due to the grafting of methyl thioglycolate to the polymer chains, inhibiting the polymer chains responding to the electric field. In addition, this relaxation peak is coupled with a decrease in the relative permittivity for the elastomer. However, this

relaxation peak was lost at 90 °C and above, because the weak interchain electrostatic interaction had been thermally disrupted and overcame the dipole present in the elastomer. The low frequency range of 1 to 100 Hz showed an increase in the relative permittivity between 30 °C and 70 °C, attributed to the increase in electron transfer due to increased thermal energy of the polymer matrix. In addition, this was observed in the phase angle as it tended towards 0° in this frequency region. However, once the dipole had been thermally disrupted, a lower relative permittivity was observed between 1 to 100 Hz.

Comparatively, 80/20 MG/TG-SBS exhibited a relaxation peak across all temperatures investigated. At 30 °C, the relaxation peak was at 4 kHz, lower than for both SBS and 100/0 MG/TG-SBS due to the additional hydrogen bonding restricting and retarding the movement of the polymer chains further. However, increasing the temperature to 130 °C shifted the relaxation peak to 64 kHz. Increasing the thermal energy reduced the intensity of the relaxation peak as the hydrogen bonding was overcome from an increase in the rate of hydrogen bond breaking and reformation, and a lower hydrogen bond lifetime. However, it is never fully overcome at 130 °C, thus a dipole remains in the elastomer. Nonetheless, the faster rate of breaking and reforming of hydrogen bonding from thermal energy meant that the polymer chains are able to respond to higher electric fields, thus increasing the relaxation peak to 64 kHz. Finally, electrode polarisation was observed once more at frequencies lower than 100 Hz, but was present at all temperatures. The source of the electrode polarisation is attributed to the greater thermal energy increasing the flow of ions.

Based on the variable temperature impedance spectroscopy, the time-frequency superposition principle¹² can be applied to both the relative permittivity and the phase angle of 80/20 MG/TG-SBS to create master curves, as seen in Figure 6.10. The frequency range of 70 °C was used as a reference temperature and extended its frequency range from 10⁻¹ to 10⁷ Hz by shifting the curves according to equation 6.1:

$$a(t) = \frac{t_t}{t_r} \quad (6.1)$$

where $a(t)$ is the shifting factor, t_t is the relaxation time at a specific temperature and t_r is the relaxation time at the reference temperature. Therefore, the curves show that electrode polarisation increased greatly for both relative permittivity and phase angle,

especially between 10^{-1} and 10^2 Hz. Furthermore, the relaxation peak attributed to the restriction of the polymer chains from hydrogen bonding was observed at 10^4 Hz. Beyond this, in the region of 10^5 - 10^7 Hz, no further relaxation peaks from structural transitions are observed, and the phase angle remains at -90° to indicate the insulating, capacitive nature of the polymer.

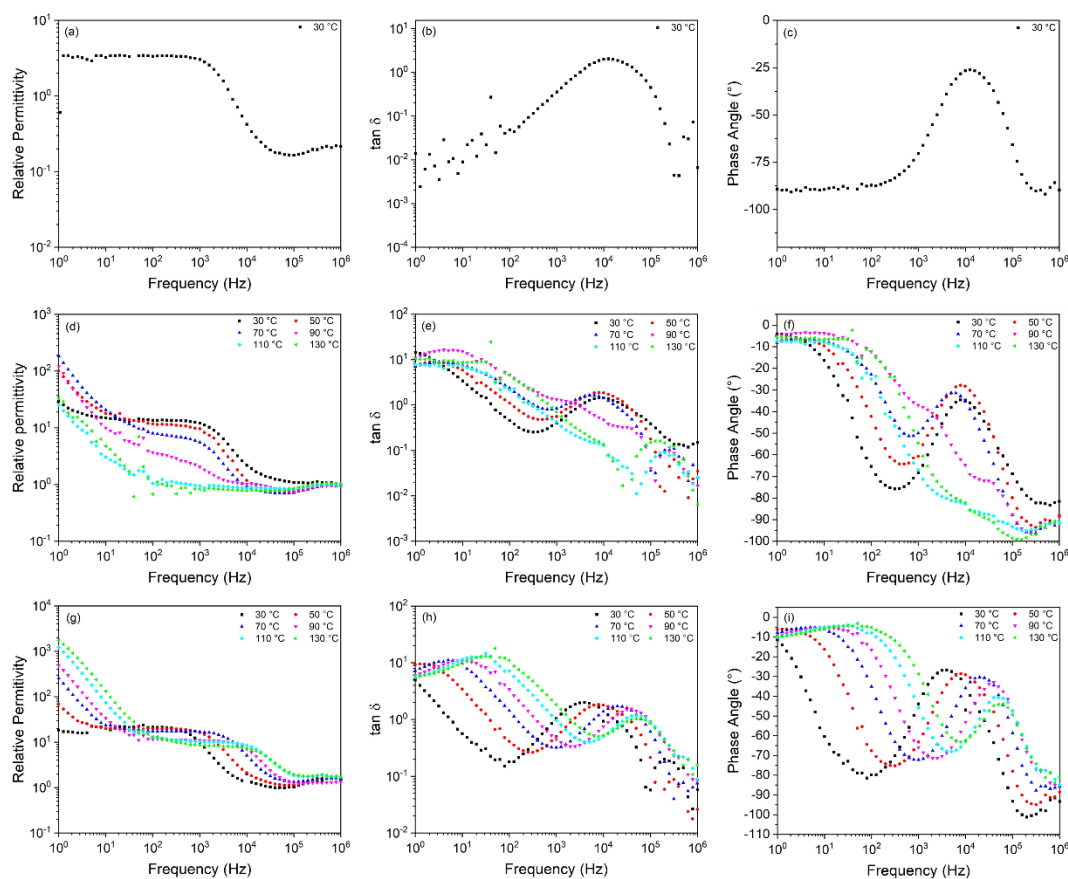


Figure 6.9 Variable temperature impedance spectroscopy showing the relative permittivity, $\tan \delta$ and phase angle of SBS (a-c), 100/0 MG/TG-SBS (d-f) and 80/20 MG/TG-SBS (g-i) in the temperature range of 30 °C to 130 °C

Thus, the temperature tunability of the hydrogen bonding networks indicates that the self-healing of MG/TG-SBS elastomers could also be temperature dependent. Therefore, the self-healing of MG/TG-SBS elastomer was investigated at room temperature and at 80 °C, to determine whether the increased breaking and reforming of the hydrogen bonding network enhanced the self-healing ability.

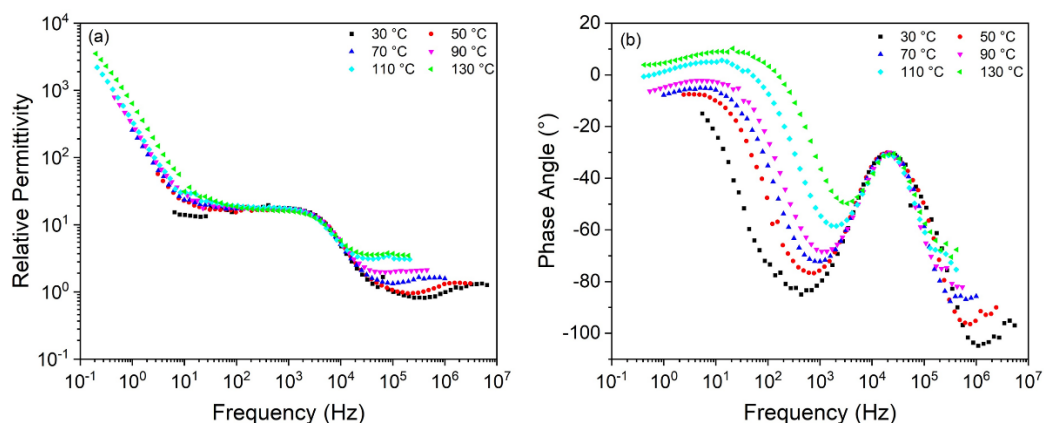


Figure 6.10 Master curves of 80/20 MG/TG-SBS at a reference temperature of 70 °C for (a) relative permittivity and (b) phase angle

80/20 MG/TG SBS was able to recover 48% of its strain at break after three days at room temperature, and exhibited a strain at break of $139 \pm 5.6\%$, Figure 6.11. However, 80/20 MG/TG-SBS could also recover 48% of its strain at break in just 15 minutes when self-healed at 80 °C. When allowed to heal at 80 °C for three hours the strain at break recovery increased to 79%, corresponding to a strain at break failure at $230 \pm 6.4\%$. This demonstrated that the interchain electrostatic interaction and hydrogen bonding interaction could work synergistically to enhance the self-healing to a more significant degree.

Decreasing the hydrogen bonding network demonstrated a reduction in the temperature dependency of self-healing and a total reduction in the ability of MG/TG-SBS elastomers to self-heal, Appendix Figure 19. 95/5 MG/TG-SBS had poorer self-healing ability (33% strain at break recovery at 80 °C) compared to 90/10 MG/TG-SBS (50% strain at break recovery at 80 °C) which in turn was not able to self-heal to the same extent as 80/20 MG/TG-SBS.

Furthermore, the recovery in the tensile strength for the MG/TG-SBS elastomers is shown in Appendix Figure 20. The greatest tensile strength recovery was for 80/20 MG/TG-SBS after three hours of self-healing at 80 °C, whereby the tensile strength healed up to 0.9 ± 0.06 MPa, a 28% recovery. Comparatively, after three days at room temperature, 80/20 MG/TG-SBS exhibited a tensile strength of 0.7 ± 0.05 MPa. The tensile strengths for 95/5 and 90/10 MG/TG-SBS healed to a similar strength compared to 80/20 MG/TG-SBS.

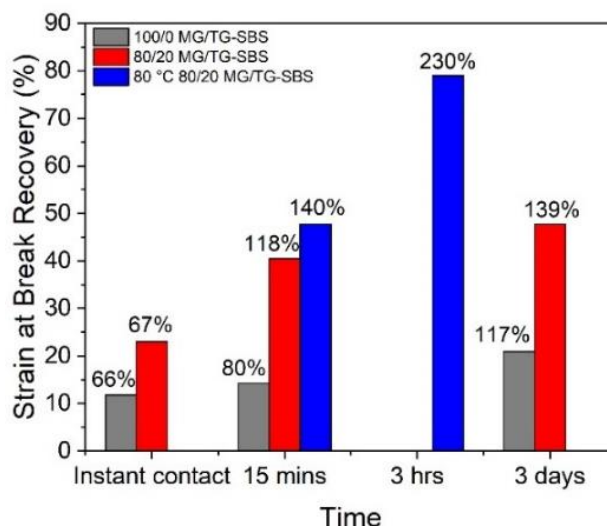


Figure 6.11 Comparative self-healing recovery of 100/0 and 80/20 MG/TG-SBS at room temperature at 80/20 MG/TG-SBS at 80 °C at different time intervals

The effect of phase morphology on the self-healing of MG/TG-SBS elastomers played a key role in the efficiency of self-healing. Softer elastomers with a low glass transition temperature allow close contact to occur and facilitate intermolecular diffusion.¹³⁻¹⁶ Furthermore, the ‘wetting’ stage of self-healing is aided by intermolecular interactions between polymer chains and enables the growth of the contact area with time. Thus, SBS was unable to self-heal due to the hard styrenic block, accounting for 30 wt% of the polymer, which had an experimentally determined glass transition temperature of 97 °C. The glassy styrenic block therefore inhibited intermolecular diffusion and the wetting stage. Through modification of SBS to form 100/0 MG/TG-SBS, the elastomer softens and the butadiene and styrene blocks are compatibilised, and 95/5 MG/TG-SBS exhibits a similar behaviour to 100/0 MG/TG-SBS due to their similar structures. By introducing a greater hydrogen bonding network into MG/TG-SBS, a disorder-to-order microstructure arrangement was promoted, from hard regions of hydrogen bonding. Thus, the modification of SBS with methyl thioglycolate and thioglycolic acid introduced an interchain electrostatic interaction and hydrogen bonding, to allow intermolecular diffusion and wetting to occur for self-healing.

The difference in the self-healing performance at room temperature and at 80 °C can be ascribed to the hydrogen bonding using the theory from Wool & O’Connor.¹³⁻¹⁶ At room temperature, the hydrogen bonding enhances the wetting stage of self-healing, whilst also inhibiting interchain diffusion, and indicates that with enough time 100/0

MG/TG-SBS will self-heal to a greater degree at room temperature than for 80/20 MG/TG-SBS. However, as hydrogen bonding is influenced by the thermal environment around it, at 80 °C it is able to both facilitate wetting and interchain diffusion. This enhances the rate of self-healing significantly.

6.2.4 Actuation testing of MG/TG-SBS

To investigate the actuation properties of 80/20 MG/TG-SBS, the theoretical $FOM_{actuation}$ was calculated to determine how its physical properties affect the actuation performance. The $FOM_{actuation}$ for 80/20 MG/TG-SBS was 21.2, an order of magnitude lower than the predicted actuation abilities of MG-SBS and M3M-SBS. This is attributed to the higher Young's modulus of the elastomer.

An investigation into the actuation properties of 80/20 MG/TG-SBS under 33% biaxial prestrain before and after self-healing through mechanical damage at room temperature is shown in Figure 6.12. Pristine 80/20 MG/TG-SBS was able to actuate radially 1.5% and areally by 3.1% before failure under an 18.0 MV m^{-1} electric field. This confirms that the $FOM_{actuation}$ correctly predicted the decrease in actuation performance for this elastomer. Whilst the actuation performance of 80/20 MG/TG-SBS was low at room temperature, based on the temperature dependency properties in section 5.2.3, 80/20 MG/TG-SBS could demonstrate enhanced actuation abilities at elevated temperatures due to thermal energy increasing the rate of hydrogen bond breaking and reforming, allowing the polymer chains to move.

80/20 MG/TG-SBS was also punctured with a small hole and subsequently rehealed at room temperature for 24 hours. When actuated, it was able to recover its actuation abilities to 1.3% radially and 2.6% areally, a recovery of 85.0%. The elastomer broke down under an electric field of 14.4 MV m^{-1} , demonstrating an 80.0% recovery in the electrical breakdown strength. Overall this suggests that 80/20 MG/TG-SBS is more suited to actuation and energy harvesting devices under elevated temperatures rather than at room temperature, due to its lower performance.

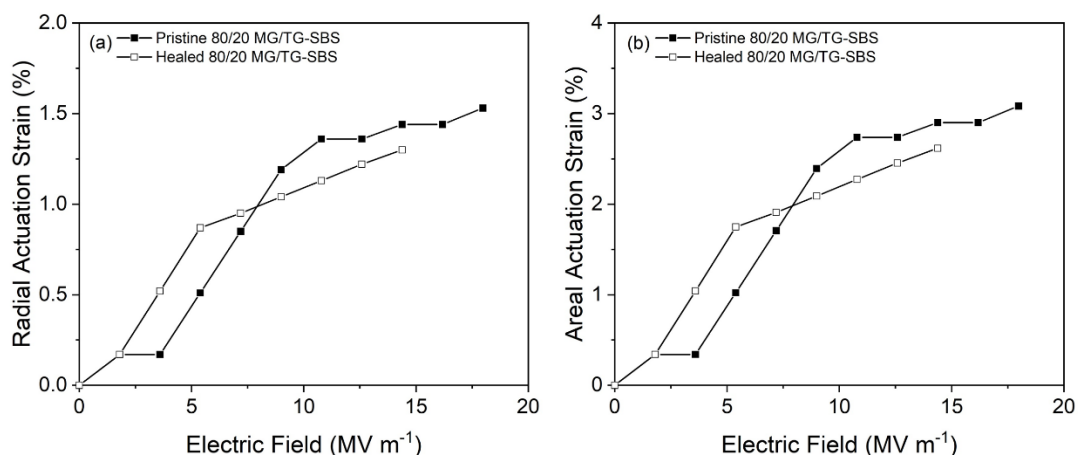


Figure 6.12 (a) Radial actuation strain and (b) areal actuation strain for pristine 80/20 MG/TG-SBS and healed 80/20 MG/TG-SBS

6.3 Conclusion

In conclusion, this chapter demonstrated the successful synthesis of SBS elastomers containing varying degrees of both electrostatic interactions and hydrogen bonding to enhance both the self-healing ability of the elastomer and the resistance of the elastomer to hostile environments. The structures and the grafting ratios of the elastomers were characterised using ¹H NMR as well as FTIR for further confirmation. The absolute grafting ratios of 95/5, 90/10 and 80/20 MG/TG-SBS were 94.9/5.1%, 87.9/12.1% and 73.4/26.6% respectively. In addition, the grafting efficiency of the thiol groups to the SBS backbone was over 93% for all elastomers.

The effect of the hydrogen bonding networks was investigated and an increase in brittleness was observed for an increasing hydrogen bonding network strength. However, an increase in strength was not uniformly observed due to a change in the polymer phase morphology. As observed by AFM, a disorder to order transition was observed as the thioglycolic acid ratio increased and spherical regions of hydrogen bonding were formed. Further, a decrease in the relative permittivity for all MG/TG-SBS elastomers was observed to 9.2 at 10³ Hz. This was attributed to the dimerization of thioglycolic acid groups decreasing the change in polarity across the polymer backbone.

Further investigations were conducted on the structure of MG/TG-SBS elastomers. It was found that the glass transition temperature of the elastomers increased upon

increasing hydrogen bonding network strength. Furthermore, variable temperature FTIR confirmed the nature of both electrostatic and hydrogen bonding interactions present in MG/TG-SBS, and discovered that hydrogen bonding was not visible in 80/20 MG/TG-SBS above 90 °C. This was further confirmed *via* variable temperature ^1H NMR. In addition to this, variable temperature impedance spectroscopy demonstrated the electrical behaviour of the polymer chains at different temperatures. It showed that without the hydrogen bonding network, the relative permittivity of the elastomer decreased substantially above 90 °C due to the loss of polarisation within 100/0 MG/TG-SBS. However, for 80/20 MG/TG-SBS the elastomer retained its high relative permittivity across all temperature ranges, demonstrating the effect that the hydrogen bonding has on temperature reinforcement of the elastomer.

Finally, the actuation abilities of 80/20 MG/TG-SBS were investigated. It was found that the actuation performance of the elastomer were significantly affected by the hydrogen bonding network. This was because of the increase in the Young's modulus of the elastomer. Thus 80/20 MG/TG-SBS was only able to actuate 1.5% radially before failure under an electric field of 18.0 MV m^{-1} . However, 80/20 MG/TG-SBS was able to exhibit excellent self-healing, and recovered 80% of its electrical breakdown strength. Therefore, the elastomer failed under an electric field of 14.4 MV m^{-1} and was still able to actuate 1.3% radially, a recovery of 85%.

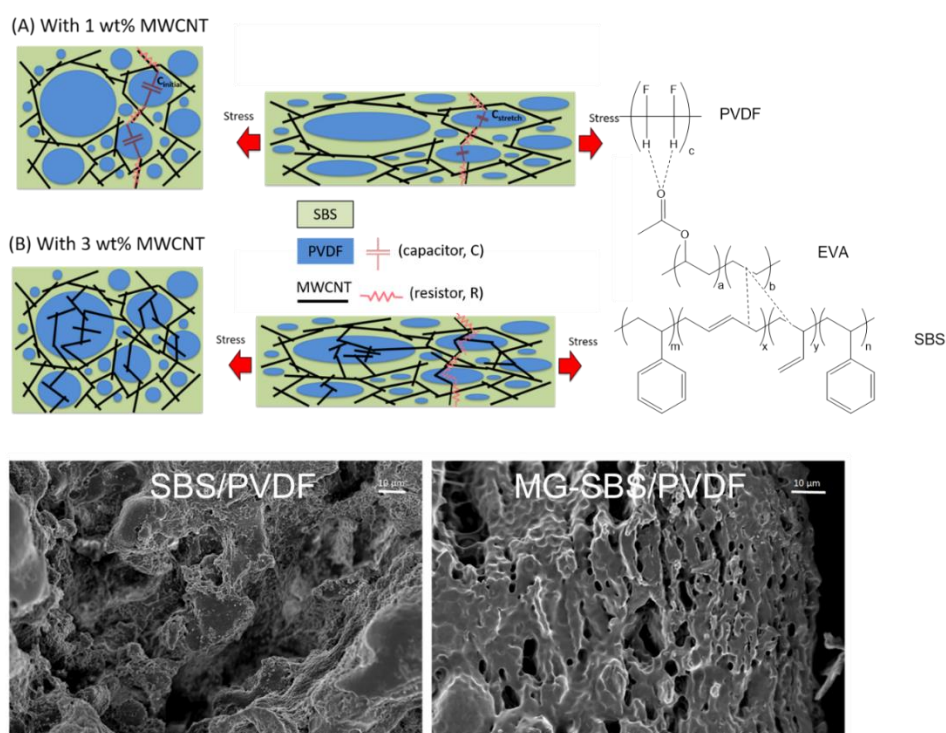
Overall, this chapter demonstrates that the hydrogen bonding network strength of MG/TG-SBS elastomers can be tuned to develop an elastomer which can be used successfully in an actuation and energy harvesting device under hostile conditions such as elevated temperature. Further work is required to optimise the specific hydrogen bonding network strength for balancing of the mechanical properties and actuation and energy harvesting performance, potentially through altering the ester group from methyl thioglycolate to methyl-3-mercaptopropionate. In addition, the grafting of hydrogen bonding groups with two or more hydrogen bonding sites could lower the required grafting to form a strong hydrogen bonding network. This in turn could enhance the mechanical strain at break and lower the Young's modulus whilst developing a dielectric elastomer for use in hostile temperature conditions.

6.4 References

1. C. Ellingford, R. Zhang, A. M. Wemyss, C. Bowen, T. McNally, Ł. Figiel and C. Wan, *ACS Appl. Mater. Interfaces*, 2018, **10**, 38438-38448.
2. E. Wittenberg, A. Meyer, S. Eggers and V. Abetz, *Soft Matter*, 2018, **14**, 2701-2711.
3. Z. Jiang, A. Bhaskaran, H. M. Aitken, I. C. G. Shackelford and L. A. Connal, *Macromol. Rapid Commun.*, 2019, **40**, 1900038.
4. J. Cao, C. Lu, J. Zhuang, M. Liu, X. Zhang, Y. Yu and Q. Tao, *Angew. Chem. Int. Ed.*, 2017, **56**, 8795-8800.
5. H. Sun, X. Liu, S. Liu, B. Yu, N. Ning, M. Tian and L. Zhang, *Chem. Eng. J.*, 2020, **384**, 123242.
6. F. B. Madsen, L. Yu and A. L. Skov, *ACS Macro Lett.*, 2016, **5**, 1196-1200.
7. C. Ellingford, A. M. Wemyss, R. Zhang, I. Prokes, T. Pickford, C. Bowen, V. Coveney and C. Wan, *J. Mater. Chem. C*, 2020, **8**, 5426-5436.
8. M. Tian, H. Yan, H. Sun, L. Zhang and N. Ning, *RSC Adv.*, 2016, **6**, 96190-96195.
9. C. Ellingford, C. Wan, Ł. Figiel and T. McNally, *Compos. Commun.*, 2018, **8**, 58-64.
10. C. Ellingford, R. Zhang, A. M. Wemyss, C. Bowen, T. McNally, Ł. Figiel and C. Wan, *ACS Appl. Mater. Interfaces*, 2018, **10**, 38438-38448.
11. J. I. Roscow, C. R. Bowen and D. P. Almond, *ACS Energy Lett.*, 2017, **2**, 2264-2269.
12. C. Hyung Kim and J. Shin, *Bull. Korean Chem. Soc.*, 2002, **23**.
13. Y. H. Kim and R. P. Wool, *Macromolecules*, 1983, **16**, 1115-1120.
14. R. P. Wool and K. M. O'Connor, *J. Appl. Phys.*, 1981, **52**, 5953-5963.
15. R. P. Wool and K. M. O'Connor, *J. Polym. Sci., Polym. Lett. Ed.*, 1982, **20**, 7-16.
16. S. Prager and M. Tirrell, *J. Chem. Phys.*, 1981, **75**, 5194-5198.

Chapter 7

Extrinsic modification of SBS with PVDF and multi-walled carbon nanotubes



Publications:

C. Ellingford, H. Smith, X. Yan, C. Bowen, L. Figiel, T. McNally and C. Wan*, Electrical dual-percolation in MWCNTs/SBS/PVDF based thermoplastic elastomer (TPE) composites and the effect of mechanical stretching, *Eur. Polym. J.*, 2019, **112**, 504

C. Ellingford, C. Wan*, L. Figiel and T. McNally, Mechanical and dielectric properties of MWCNT filled chemically modified SBS/PVDF blends, *Compos. Commun.*, 2018, **8**, 58-64

7.1 Introduction

Extrinsic modification of SBS is an industrially viable approach to produce enhanced permittivity nanocomposites for actuation and energy harvesting applications. This is because extrinsic modification approaches can be scaled up easily to the kilogram or tonne scale, the production can be fast and continuous as well as a solvent free approach. However, significant challenges remain for the production of nanocomposites, primarily associated with the addition of nanoparticles to form the composites. This is because nanoparticles, such as graphene or carbon nanotubes typically have a poor interfacial compatibility with the polymer, and they prefer to agglomerate instead of disperse homogeneously.

The use of poly(vinylidene fluoride) (PVDF) in energy harvesting devices is highly desirable due to its inherently high relative permittivity ($\epsilon_r \approx 12$) and piezoelectric properties, thus allowing it to be used in dielectric elastomer harvesters and piezoelectric harvesters.¹ The high relative permittivity and piezoelectric coefficient arise from the semi-crystalline nature of PVDF. PVDF exhibits three different crystalline structures,^{2,3} the α , β and γ phase as shown in Figure 7.1. The α phase is paraelectric and does not contribute to enhancing the relative permittivity or the piezoelectric properties of PVDF. This is because of the hexagonal arrangement of the crystal phase, where polymer chains are aligned anti-parallel to each other. The β phase contributes to the piezoelectric properties and polarity of PVDF. This is because the crystal phase is orthorhombic, with the polymer chains arranged in a trans planar zigzag conformation with all dipoles parallel to each other. The β phase has the highest contribution to the polarity of PVDF of all possible crystal phases.⁴ The γ phase is less polar but still contributes to the polarity of PVDF.² Therefore, the promotion or preservation of the β phase in PVDF is crucial towards its high permittivity.

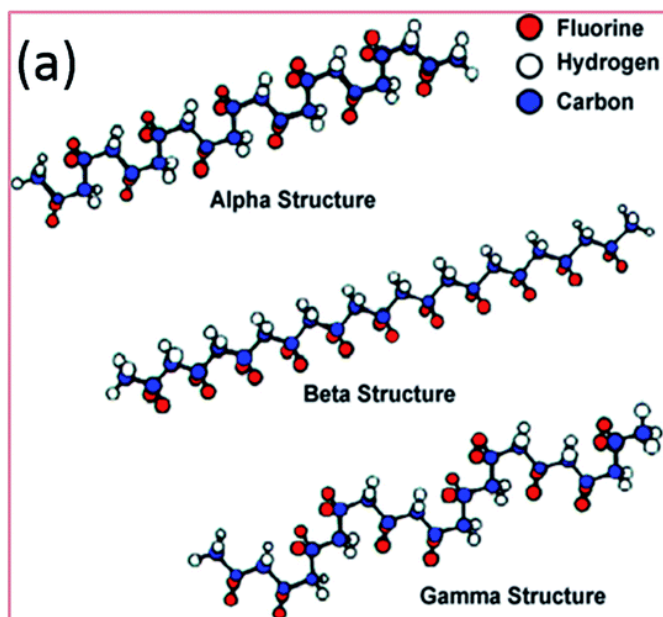


Figure 7.1 The three crystalline structures of PVDF, the α phase, β phase and γ phase. Reproduced from Wan *et al.*²

However, due to its semi-crystalline nature, the mechanical properties of PVDF make it unsuitable for direct use in a dielectric energy harvester device.⁵ Therefore, the blending of PVDF with other polymers to enhance the mechanical properties of PVDF whilst retaining the electrical properties have been investigated. Typically, PVDF is incompatible with many dielectric elastomers, and poor mechanical properties have been observed due to poor phase mixing and large phase dimensions.⁶ Therefore, to compatibilise two polymers, a third compatibilising polymer can be utilised. For example, 20-40 wt% polymethylmethacrylate (PMMA) was used to compatibilise a polycarbonate and PVDF blend.⁷ To lower the addition of compatibilising polymer, methyl methacrylate-co-glycidyl methacrylate (MMA-co-GMA) was utilised for compatibilising a blend of PVDF and polyamide 6 (PA6). Epoxy groups on GMA compatibilised PA6 through hydrogen bonding with carboxylic acid and amino groups. The successful compatibilisation was observed *via* a reduction in the crystallinity of both PVDF and PA6 and a significant increase in the strain at break, from 20% to 250%.⁸ Alternatively, compatibilising a polyamide 11 and PVDF blend using vinyl acetate-co-maleic anhydride was demonstrated.⁹

A second approach is to functionalise PVDF to enhance its compatibility. Blending PVDF-g-malic anhydride enhanced its compatibility with polyurethane and a thin film

of it was successfully demonstrated in a piezoelectric wind harvesting device, exhibiting an energy density of 200 mW m^{-2} .^{10, 11}

Finally, a third alternative is to form thermoplastic vulcanates by crosslinking two polymers together.¹² One example demonstrated PVDF dynamically vulcanised with acrylonitrile butadiene rubber *via* melt mixing to produce a polymer blend with enhanced mechanical properties and phase mixing.¹³

The addition of conducting nanoparticles can enhance the relative permittivity of a polymer matrix by acting as microcapacitors to store charge when below the percolation threshold.² However, the fillers can have a negative effect on the $\tan \delta$ loss due to an increase in the leakage current from internal conductive pathways.^{14, 15} As well, the breakdown strength can be reduced due to the increase in interfacial defects affecting the homogeneity of the electric field through the polymer matrix.¹⁵⁻¹⁸ Finally, nanoparticles typically act to reinforce the mechanical properties by reducing the elasticity and increasing the strength of the composite.¹⁹ Examples of compositing using thermally expanded graphene nanoplatelets and partially reduced graphene oxide increased the relative permittivity of composites up to 225.^{20, 21} In addition, multi-walled carbon nanotubes (MWCNTs) have shown excellent enhancement in relative permittivity whilst requiring a low weight fraction addition compared to graphene and ceramic fillers.²²⁻²⁴

In this chapter, two approaches to compatibilise PVDF and SBS are investigated and presented. In the first section, a 50/50 SBS/PVDF blend was compatibilised using a compatibilising third polymer of ethylene vinyl acetate (EVA) to improve the mechanical properties and reduce phase separation. The mechanism of compatibilisation was investigated through the change in glass transition temperatures from DMTA with further evidence of compatibilisation shown through SEM imaging.

After compatibilisation, up to 3 wt% MWCNTs were used to composite the polymer blend and the effect on the mechanical and electrical properties was investigated. The changes in the composite behaviour are rationalised by understanding the locality of the MWCNTs using contact angle measurements, and the effect on the polymer composite structure from MWCNTs through DSC and FTIR. The rheological properties were investigated as well as the electrical properties under strain to observe the change in behaviour of the nanocomposite for different MWCNT additions.

In the second section, increasing the compatibility between SBS and PVDF by modification of SBS was investigated. SBS was modified to form MG-SBS, reported in chapter 4. The increased polarity of MG-SBS allowed it to interact more strongly with PVDF. Thus the effect of blending was investigated on the electrical and mechanical properties of blends between 30 wt% MG-SBS to 70 wt% MG-SBS and compared to the behaviour of SBS/PVDF blends in the same weight ratio.

Following this, the effect of 1 wt% MWCNTs for compositing of four chosen polymer blends was investigated *via* DSC, FTIR and SEM imaging. Finally, the effect of compositing on the mechanical and electrical properties was investigated and the nature of the observed percolation threshold was defined.

Overall, this chapter demonstrates two routes for compatibilising SBS and PVDF to improve the electrical properties of SBS whilst retaining an elastic behaviour. It also demonstrates the effect of MWCNTs on the behaviour of these composites and demonstrates that elastomeric SBS/PVDF blends for actuation and energy harvesting devices can be produced *via* extrinsic modification methods.

7.2 Results and discussion for extrinsic modification of SBS through compositing to produce thermoplastic elastomer nanocomposites with an electrical dual percolation threshold

7.2.1 Structural characterisation of SBS/PVDF thermoplastic elastomers

SBS was melt mixed with PVDF in a 50/50 wt% ratio followed by the addition of 20 wt% EVA to assist with the compatibilisation of the polymer blend, and to retain the elastic behaviour of SBS. In subsequent formulations, multi-walled carbon nanotubes (MWCNTs) were introduced in different wt% ratios between 0.3 and 3 wt% to enhance the electrical properties of the nanocomposites, by increasing their relative permittivity until the percolation threshold was reached. Thus, the mechanical properties of the SBS/PVDF blends and nanocomposites are shown in Figure 7.2. Individually, SBS and PVDF have a strain at break of $857 \pm 45.8\%$ and $15 \pm 0.2\%$ respectively. However, the blending of the two polymers to produce SBS/PVDF (50/50) led to a decrease in strain at break to $10.5 \pm 0.3\%$. This was attributed to poor compatibility between the two polymers, leading to phase separation and reduced

mechanical behaviour. Thus, the compatibilisation of SBS/PVDF was facilitated by the introduction of 20 wt% EVA. As observed in Figure 7.2, SBS/PVDF/EVA 50/50/20 exhibited an increased strain at break of $205 \pm 36\%$, as well as a tensile strength of 2.95 ± 0.2 MPa. Lower additions of EVA was found to incompletely compatibilise SBS/PVDF, causing some phase separation to remain.

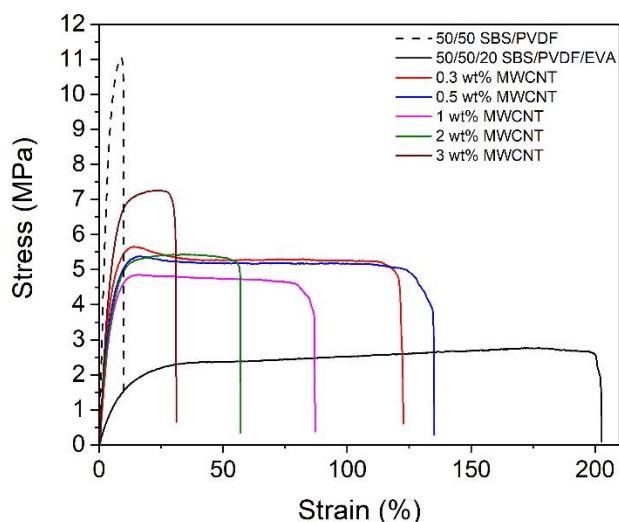


Figure 7.2 Stress strain curve of SBS/PVDF, SBS/PVDF/EVA and SBS/PVDF/EVA with between 0.3 wt% and 3 wt% MWCNTs

The effect of the compatibilisation of SBS and PVDF through EVA was observed through the glass transition temperature (T_g) via DMTA in Figure 7.3a. SBS/PVDF exhibited four separate T_g 's at -83.8 °C, -37.6 °C, 92.4 °C and 118.6 °C. These were attributed to the T_g for the butadiene block of SBS, the T_g of PVDF, the T_g of the styrene block of SBS and the α -relaxation peak of PVDF respectively.²⁵ Upon the addition of EVA as a compatibilising polymer, the T_g for the butadiene block of SBS shifted from -83.8 °C to -80.4 °C, attributed to a Van der Waals electrostatic interaction between the butadiene block of SBS and ethylene from EVA. Additionally, the T_g for PVDF disappeared and instead a broad hump at -6.8 °C appeared due to the interaction between the acetyl groups of EVA hydrogen bonding with the fluoride groups of PVDF.²⁶ In addition to the broadness of the peak, the original T_g for EVA was -17.4 °C. The shift by this peak to a higher temperature provided further evidence for a stronger interaction type present in the polymer blend. This series of interactions is summarised in Figure 7.3b, and the storage and loss modulus for these polymers is shown in Appendix Figure 21.

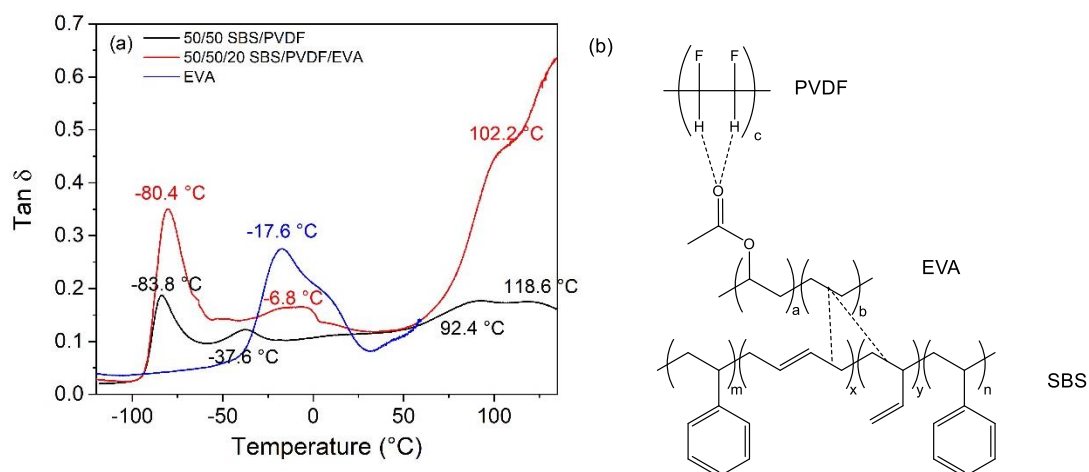


Figure 7.3 (a) $\tan \delta$ graph of 50/50 SBS/PVDF, 50/50/20 SBS/PVDF/EVA and EVA with glass transition temperatures shown and (b) diagram of the compatibilisation interaction present within SBS/PVDF/EVA

SBS/PVDF/EVA blends were visualised before and after compatibilisation to determine the effect on the phase morphology. Prior to compatibilisation, SBS and PVDF exhibited phase separation, with the individual phases measuring hundreds of micrometres, Figure 7.4. With 20 wt% of EVA incorporated into the polymer blend, a compatibilised phase morphology, with ovoid and worm-like PVDF structures in smaller dimensions within the SBS matrix was observed. EVA resides at the interface between SBS and PVDF, to ensure that the ethylene units interact with SBS and the fluoride groups hydrogen bond with the carbonyls,²⁶ and thus shows good phase mixing. This is the reason behind the decrease in the tensile strength but the increase in the strain at break for SBS/PVDF/EVA in Figure 7.2.

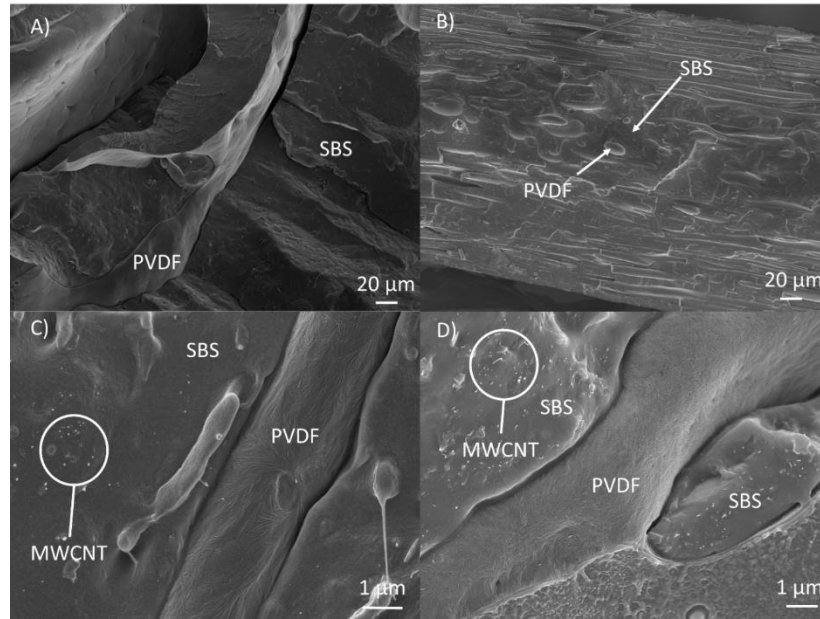


Figure 7.4 SEM imaging of (a) 50/50 SBS/PVDF, (b) 50/50/20 SBS/PVDF/EVA, and SBS/PVDF/EVA/MWCNT (c) 50/50/20/1 and (d) 50/50/20/3

7.2.2 Selective localisation of MWCNTs in SBS/PVDF thermoplastic elastomers

The selective location of MWCNTs within in either phase of the SBS/PVDF TPE affects the nanoparticle dispersion and alters the electrical and mechanical performance. To theoretically determine the locality of the MWCNTs within the SBS/PVDF TPE, contact angle measurements were utilised. MWCNTs interact differently with the two polymer phases, as interactions such as electrostatic Van der Waals interactions or π - π stacking create a different affinity. Thus, the wetting coefficient, ω_a , was calculated for MWCNTs and SBS, EVA and PVDF using the equation shown in Equation 7.1²⁷:

$$\omega_a = \frac{\gamma_{MWCNTs-polymer1} - \gamma_{MWCNTs-polymer2}}{\gamma_{polymer1,2}} \quad (7.1)$$

where $\gamma_{MWCNT-polymer1}$ is the interfacial tension between MWCNTs and ‘polymer 1’, $\gamma_{MWCNT-polymer2}$ is the interfacial tension between MWCNTs and ‘polymer 2’ and $\gamma_{polymer1,2}$ is the interfacial tension between ‘polymer 1’ and ‘polymer 2.’ Therefore, three conditions can arise:

1. if $\omega_a < -1$, the MWCNTs preferentially reside in polymer 1
2. if $\omega_a > 1$, the MWCNTs preferentially reside in polymer 2

3. if ω_a is < 1 but > -1 , then the MWCNTs reside at the interface between both polymers.

To calculate the interfacial tension, the geometric mean equation is applied in equation 7.2:²⁸

$$\gamma_{1,2} = \gamma_1 + \gamma_2 - 2 \left(\sqrt{\gamma_1^d \gamma_2^d} + \sqrt{\gamma_1^p \gamma_2^p} \right) \quad (7.2)$$

where γ_i is the total surface energy of component i and γ_i^d and γ_i^p are the dispersive and polar parts of the surface energy from component i respectively. For calculation of the surface energy, equations 7.3 and 7.4 are used based on the geometric mean:²⁹

$$\gamma_{LV} = (1 + \cos\theta) = 2 \left(\sqrt{\gamma_{SV}^d \gamma_{LV}^d} + \sqrt{\gamma_{SV}^p \gamma_{LV}^p} \right) \quad (7.3)$$

$$\gamma_{SV} = \gamma_{SV}^d + \gamma_{SV}^p \quad (7.4)$$

where θ is the experimentally determined contact angle, γ_{SV} and γ_{LV} are interfacial surface-vapour and interfacial liquid-vapour respectively, the superscripts d and p are to differentiate between the dispersive and polar components of surface tension. The liquids selected for contact angle measurements were distilled H₂O and CH₂I₂. Their literature surface energy data is shown in Table 7.1.

Table 7.1 Surface energy data for H₂O and CH₂I₂ for the total surface energy, the dispersive part of surface energy and polar part of surface energy.^{30, 31}

Solvent	γ_{LV} (N m ⁻¹)	γ_{LV}^d (N m ⁻¹)	γ_{LV}^p (N m ⁻¹)
H ₂ O	72.8	21.8	51.0
CH ₂ I ₂	50.8	48.5	2.3

The experimentally determine contact angles for SBS, PVDF and EVA from both H₂O and CH₂I₂ are shown in Table 7.2 and are used to calculate the ω_a 's using the theoretical interfacial tension of MWCNTs³² and the equations 7.1 – 7.4. The preferred locality of MWCNTs is shown in Table 7.3.

Table 7.2 Experimental contact angles of H₂O and CH₂I₂ for SBS, PVDF and EVA

Material	$\theta_{\text{H}_2\text{O}}$ (°)	$\theta_{\text{CH}_2\text{I}_2}$ (°)
SBS	98.8	72.4
PVDF	102.2	67.2
EVA	94.2	63.9

Table 7.3 Calculated wetting coefficient, ω_a , between polymer phases and the preferential locality of MWCNTs.

Polymer 1	Polymer 2	ω_a	Preferred locality of MWCNTs
PVDF	SBS	1.3190	SBS
EVA	SBS	0.6658	SBS/EVA interface
PVDF	EVA	5.82	EVA

Therefore, theoretically the preferred locality of MWCNTs was the SBS phase and the SBS/EVA interface.

Observation of the MWCNTs locality is shown in Figure 7.4c-d. The MWCNTs reside within the SBS phase at 1 wt% concentration, and show a homogeneous dispersion. As the weight fraction of MWCNTs increased to 3 wt%, phase separation occurs between SBS matrix and the EVA/PVDF phase. Additionally an increase in the phase dimensions of EVA/PVDF is observed, but a homogeneous dispersion of MWCNTs is maintained with no visible agglomeration. Therefore, the presence of the MWCNTs at the SBS/EVA interface decreases the compatibility between SBS and EVA. Normally, MWCNTs interact through π - π stacking with the aromatic styrene rings from the styrene block of SBS. However, under melt mixing oxidative degeneration of the butadiene block forms free radicals which can react with the open ends and defects present in MWCNTs.^{33, 34} As the ratio of MWCNTs increased from 1 wt% to 3 wt%, the degree of MWCNT bonding to the butadiene backbone increased, reducing the number of available sites and space for the ethylene groups of EVA to interact with butadiene.

The effect on the morphology of SBS/PVDF TPE's was observed in the stress strain curves as the weight fraction of MWCNTs increased, in Figure 7.2. Increasing the

addition of MWCNTs from 0.3 wt% to 0.5 wt% and 1 wt% led to an increase in the tensile strength from 2.95 to 4.50 ± 0.45 MPa but a decrease in the strain at break from 205% to $111 \pm 19\%$. This was attributed to the MWCNTs reducing the elasticity of the SBS/PVDF TPE by π - π stacking with the styrene block and free radical addition to the butadiene block to decrease the interactions between SBS and EVA.^{33,34}

When 2 wt% of MWCNT was added into the SBS/PVDF TPE matrix, the strain at break decreased further to $62 \pm 11\%$ whilst an increase in MWCNT concentration to 3 wt% further decreased the strain at break to $31 \pm 6\%$, due to the further reduction in compatibility within the SBS/PVDF TPE. The tensile strength increased to a maximum of 7.5 ± 0.42 MPa at 3 wt% MWCNT.

Stress relaxation is shown in Figure 7.5 for samples with a MWCNT weight fraction of up to 1% due to limits of the strain at break. All samples exhibited a similar stress relaxation, whereby the normalised stress for the TPEs decreased to 0.5 MPa after 30 minutes. Thus, the MWCNTs had a minimal impact on the entanglement of the polymer chains. Further investigations into the mechanical behaviour of the SBS/PVDF TPE composites considered their hysteresis loss through cyclic stress softening. As observed from Figure 7.5b, the hysteresis loops for all materials was large. For 50/50/20 SBS/PVDF/EVA, the hysteresis energy loss was 55.4% after five cycles, demonstrating a large viscoelastic behaviour. After compositing with 0.3 wt% MWCNTs, the viscous portion of the TPE increased as the hysteresis energy loss increased drastically to 70.1%. Further increases in the viscoelastic losses were observed, as with 1 wt% addition of MWCNTs the hysteresis loss increased to 75%. The cause of the increase in the viscous losses was due to the incompatibility MWCNTs introduced into the composite, thus causing more damage to the composite upon elongation.^{35,36}

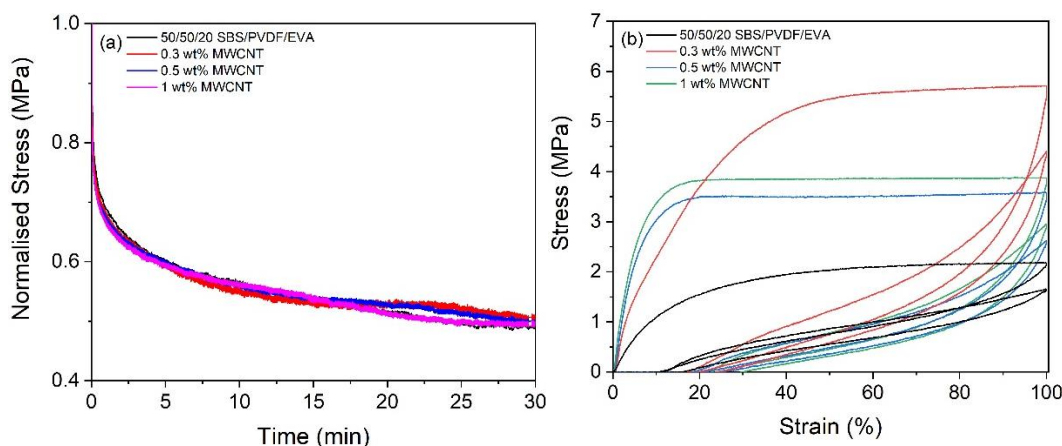


Figure 7.5 (a) Normalised stress intensity for SBS/PVDF/EVA with 0-1 wt% MWCNTs and (b) cyclic stress softening of SBS/PVDF/EVA with 0-1 wt% MWCNTs

Using EVA as a compatibiliser and incorporating MWCNTs selectively into the composite affects the crystallinity of PVDF. Differential scanning calorimetry (DSC) allowed the change in percentage crystallinity, $X_c(\%)$, of PVDF and EVA to be observed when MWCNT concentration was increased, as shown in Table 7.4. Literature values used for the heat of fusion for 100% crystalline PVDF and EVA were 104.7 J g^{-1} and 277.1 J g^{-1} respectively.^{37, 38}

Table 7.4 Percentage crystallinity of PVDF and EVA in SBS/PVDF TPE blends and composites

Material	$X_c(\%)$ PVDF	$X_c(\%)$ EVA
PVDF	48.7	-
EVA	-	22.0
SBS/PVDF/EVA (50/50/20)	42.7	8.51
0.3 wt% MWCNT	45.1	8.70
0.5 wt% MWCNT	45.2	9.42
1 wt% MWCNT	45.0	11.0
2 wt% MWCNT	46.3	11.4
3 wt% MWCNT	47.7	11.8

Both PVDF and EVA experienced a decrease in $X_c(\%)$ when blended into 50/50/20 SBS/PVDF/EVA compared to $X_c(\%)$ for neat PVDF and EVA. Therefore, $X_c(\%)$

PVDF decreased by 12.3% from 48.7% to 42.7%. In addition, the $X_c(\%)$ of EVA decreased by 61.3% from 22.0% to 8.5%. This was because of the compatibilisation effect between SBS and PVDF EVA introduced, and thus the phase mixing between the polymers led to large amorphous regions.

Upon incorporation of MWCNTs into SBS/PVDF TPEs, the $X_c(\%)$ increased. MWCNTs acted as heterogeneous sites for crystallisation³⁹ and thus the inclusion of 0.3 wt% MWCNTs enhanced the $X_c(\%)$ from 42.7% to 45.1% for PVDF, whilst the $X_c(\%)$ was not affected for EVA. However, addition of 0.5 wt% and 1 wt% MWCNTs increased the $X_c(\%)$ in the EVA phase to 9.42% and 11.0%, whilst no change in PVDF occurred. Thus, this fits well with the results from contact angle measurements, as MWCNTs disrupt the compatibility between SBS and EVA, reducing the amorphous regions present. Beyond 1 wt%, increasing the MWCNT concentration further increased the $X_c(\%)$ for PVDF to a significant degree whilst EVA exhibited a slower increase. This change in behaviour for the crystallinity is observed in the tensile testing stress strain curves where the strain at break decreases significantly upon the addition of 2 wt% and 3 wt% MWCNTs.

In addition to DSC, the change in α -phase and β -phase crystallinity with the change in $X_c(\%)$ within PVDF was investigated by FTIR, as shown in Figure 7.6a. Two α -phase crystallinity peaks and two β -phase crystallinity peaks are observed in PVDF at 615 cm^{-1} , 763 cm^{-1} , 840 cm^{-1} and 1275 cm^{-1} respectively. Appendix Table 1 shows how the β/α phase ratio changes between the peaks in transmission mode upon change in MWCNT concentration, as well as the origins of crystallinity within the composite. As a lower peak intensity indicates a stronger peak in the FTIR, PVDF therefore has a greater intensity of β -phase than α -phase before incorporation within the TPE. After formation of the SBS/PVDF TPE, the non-polar α -phase increased whilst the ferroelectric β -phase decreased. This was due to two effects, firstly some of the β -phase was converted to α -phase crystallinity and secondly, some crystalline content in PVDF transformed into amorphous regions, as observed by DSC in Table 7.4

Figure 7.6b showed how the ratio of β/α phase crystallinity was affected by different concentrations of MWCNTs into SBS/PVDF/EVA. 0.3 wt% of MWCNTs decreased the β -phase ratio in PVDF slightly, demonstrating that the ratio of β -phase increased. However, further increases in the MWCNT concentration up to 2 wt% showed a small

increase in the β/α phase intensity due to a greater proportion of α crystallinity with respect to the β -phase within PVDF. However, there was a large difference between the β/α ratio between the addition of 2 wt% and 3 wt% MWCNTs, attributed to MWCNTs residing in the PVDF phase which simultaneously disrupted the β -phase whilst increasing the α -phase.

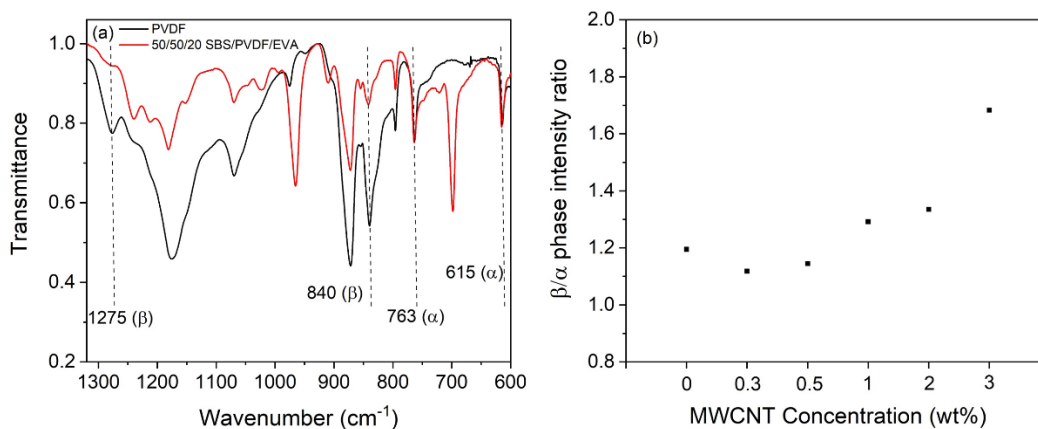


Figure 7.6 (a) α -phase and β -phase analysis of PVDF crystallinity from FTIR and (b) the effect of MWCNT concentration in the β/α phase ratio of PVDF from FTIR

7.2.3 Rheological dual percolation of SBS/PVDF/EVA/MWCNT nanocomposites

To investigate the microstructure of the nanocomposites, oscillatory rheology was used to observe the storage modulus and complex viscosity, $|\eta^*|$, as shown in Figure 7.7. Between SBS/PVDF/EVA/MWCNT (50/50/20/0.5) and (50/50/20/1), a large increase was seen between the two samples for all frequencies in the storage modulus and $|\eta^*|$, attributed to the formation of a percolated network, restricting polymer chain movement. Thus, as the MWCNTs reside in the SBS phase, the percolation was achieved within this phase between 0.5 wt% and 1 wt% MWCNTs. The percolation event was most observable at low frequencies as the samples showed a convergence at high frequencies.⁴⁰

Furthermore, a second percolation event was observed between 2 wt% and 3 wt% addition MWCNTs in SBS/PVDF/EVA, characterised by a large increase in the storage modulus and $|\eta^*|$. The second percolation event was ascribed to percolation within the PVDF phase after some MWCNTs reside in PVDF due to the high concentration with the SBS phase. The change in the phase morphology was

demonstrated from SEM imaging in Appendix Figure 22 where the phase structure showed increasing phase dimensions and a reduced compatibility.

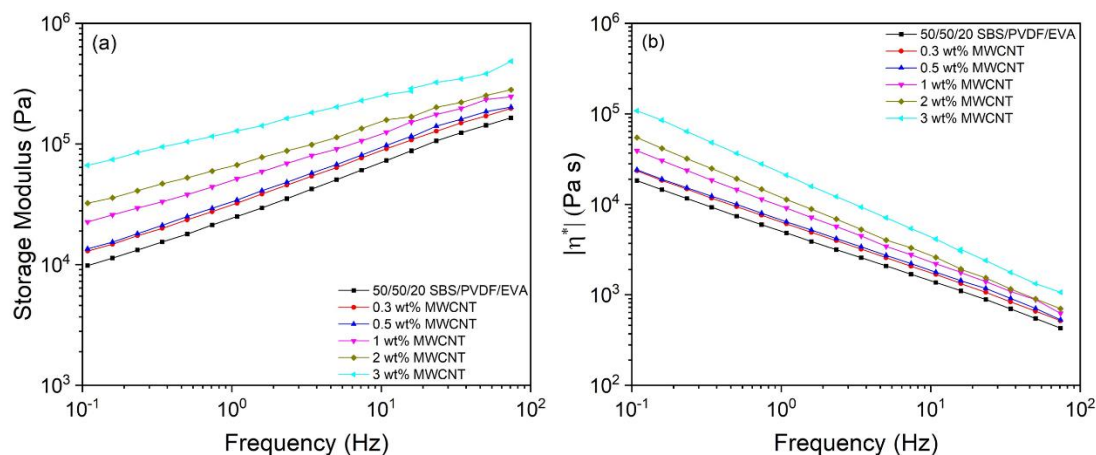


Figure 7.7 Rheological properties of SBS/PVDF/EVA blends and nanocomposites showing (a) storage modulus and (b) complex viscosity ($|\eta^*|$)

7.2.4 Electrical dual-percolation in SBS/PVDF/EVA TPE composites

Prior to blending, PVDF had a relative permittivity of 13.2 at 10^3 Hz, Appendix Figure 23. The blending of 50/50/20 SBS/PVDF/EVA resulted in a polymer blend with a relative permittivity of 3.8 at 10^3 Hz, only marginally higher than pure SBS, see Figure 7.8a. Despite a high PVDF content, the blending together of the three polymers reduced the crystallinity present in the blend, increasing the amorphous phase content. In addition, for PVDF some of the β -phase content was converted to α -phase content, reducing the polarity of the crystalline phase additionally. The addition of 0.3 wt% MWCNTs increased the relative permittivity of the composite up to 5.6 at 10^3 Hz, attributed to the increase in crystallinity of the composite and the ability of the MWCNTs to act as microcapacitors. Furthermore, an increased addition of MWCNTs to 0.5 wt% enhanced the relative permittivity of the elastomer to 13.4, whilst maintaining a low $\tan \delta$ loss as seen in Figure 7.8b, indicating that 0.5 wt% of MWCNTs is close to the percolation threshold of SBS/PVDF/EVA nanocomposites.

After the addition of 1 wt% MWCNTs, the first electrical percolation event occurred and the permittivity increased to 22.5, but the $\tan \delta$ loss increased to 0.5 at 10^3 Hz. Furthermore, the addition of 2 wt% MWCNTs increased the relative permittivity to 34.9, whilst maintaining a constant $\tan \delta$ loss. The lack of increase in the $\tan \delta$ loss indicated that the leakage current in the composite is suppressed. The suppression is

also observed by the increase in the frequency dependent nature of the SBS/PVDF/EVA composites as MWCNT content increases, due to Maxwell-Wagner-Sillars polarisation from charge build up at the interfaces.⁴¹ An additional cause of the frequency dependent nature is the increase in space charge from voids and defects as a direct result of the MWCNTs. The electrical properties of SBS/PVDF/EVA/MWCNTs (50/50/20/2), with high relative permittivity and suppressed $\tan \delta$ loss, indicate that it is a suitable material for vibration control sensors and variable impedance devices, energy harvesters and actuation devices.^{1, 31}

Finally, a second percolation threshold was reached after loading 3 wt% MWCNTs into SBS/PVDF/EVA (50/50/20). This was characterised by a large increase in the relative permittivity to 395.0 at 10^3 Hz, whilst a similarly large increase in the $\tan \delta$ was observed, up to 123.8. This is due to the residence of a second percolation network, located in the PVDF/EVA phase. Thus the existence of a dual percolation network was present in both the rheological and electrical properties of SBS/PVDF/EVA, and the MWCNTs affected the rheological and electrical properties of the composites.

In addition, the SBS/PVDF/EVA composites exhibit further the electrical dual percolation nature through the AC conductivity and the phase angle. Compared to the polymer blend of SBS/PVDF/EVA, the addition of 0.3 wt% MWCNTs increased the AC conductivity from 1.8×10^{-9} S m⁻¹ to 9.4×10^{-9} S m⁻¹, less than a one order of magnitude increase, whilst the phase angle remained insulating at -90° . Further increases in the MWCNT concentration to 0.5 wt% introduced a frequency dependent nature in the phase angle below 10^2 Hz, whilst the AC conductivity increased by an order of magnitude to 7.6×10^{-8} S m⁻¹. The addition of 1 wt% and 2 wt% MWCNTs to SBS/PVDF/EVA further increased the AC conductivity by an order of magnitude to 6.3×10^{-7} S m⁻¹ and 9.2×10^{-7} S m⁻¹ respectively. The increase in the AC conductivity between 0.5 wt% and 1 wt% MWCNTs was due to the formation of the first percolation network. However, the increase in AC conductivity between 1 wt% and 2 wt% MWCNTs was very low due to the suppression of the percolation network. This was reinforced by the phase angle at high frequency, where both SBS/PVDF/EVA/MWCNT (50/50/20/1) and (50/50/20/2) showed an insulating nature as they tended towards -90° but at low frequencies tended towards 0° due to electrode polarisation. Finally, after the second percolation event from the addition of

3 wt% MWCNTs, the AC conductivity increased drastically by four orders of magnitude to $2.7 \times 10^{-3} \text{ S m}^{-1}$ at 10^3 Hz , and demonstrated a conducting phase angle. Therefore, this composite is now fully conducting.

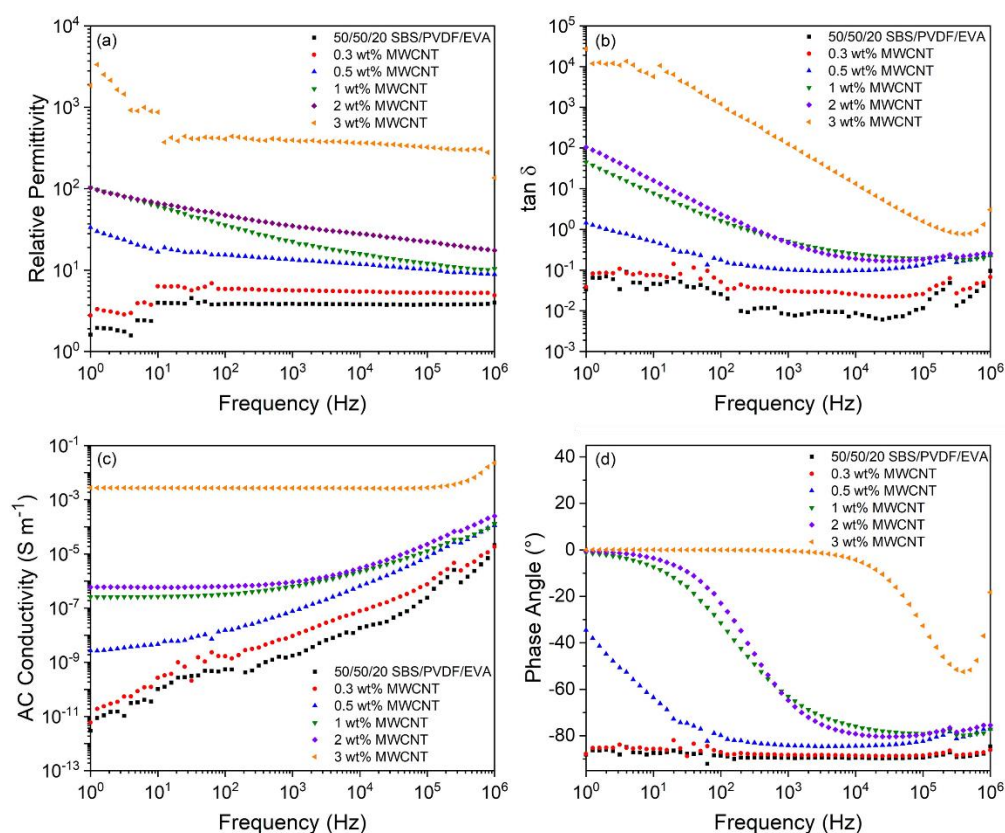


Figure 7.8 Impedance spectroscopy of SBS/PVDF/EVA/MWCNTs between 0 wt% and 3 wt% for (a) relative permittivity, (b) $\tan \delta$, (c) AC conductivity and (d) phase angle

Furthermore, polarisation-electric field (P-E) loops of the SBS/PVDF/EVA composites shown in Figure 7.9 show how the electrical nature of the composite changes up to the first percolation threshold. In Figure 7.9a, the response of SBS/PVDF/EVA TPE was linear with a constant gradient, indicative of its capacitive nature, as the polarisation is related to the voltage. This agrees well with the low loss and phase angle from impedance spectroscopy results in Figure 7.8, despite a much higher electric field used. P-E loops of SBS/PVDF/EVA/MWCNTs (50/50/20/0.3) in Figure 7.9b showed that the linearity and constant gradient was lost upon an increasing electric field due to the presence of the MWCNTs. This is typical of a ‘lossy dielectric,’ originating from the electrical conductivity within the sample and not ferroelectricity.⁴² As the MWCNT concentration was increased in Figure 7.9c, the P-

E loop opened further and exhibited a more circular response. This was due to the composite transitioning from ‘lossy dielectric’ to conductor and indicated that the first percolation threshold was close. Finally, at 1 wt% MWCNT concentration, the SBS/PVDF/EVA TPE displayed a circular response due to its conducting nature.

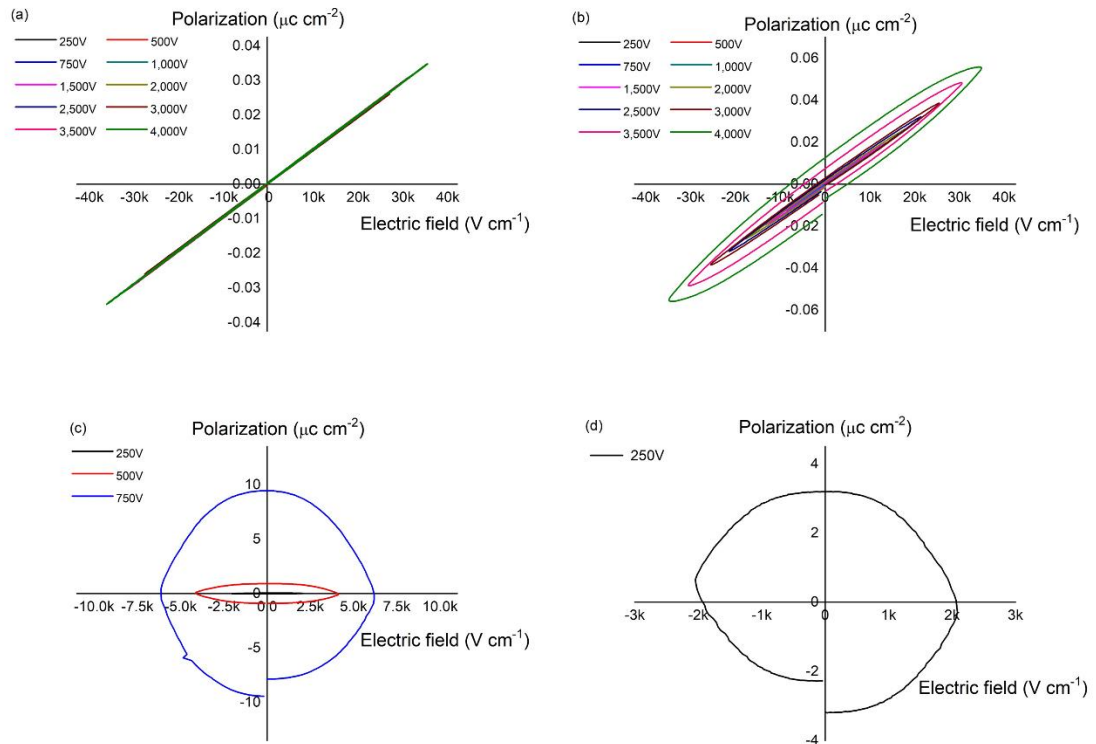


Figure 7.9 Polarisation – electric field loops (P-E) loops for SBS/PVDF/EVA containing 0 wt% - 1 wt% MWCNTs under different electric fields

7.2.5 Electrical dual-percolation behaviour of SBS/PVDF/EVA TPEs under mechanical stretching

The effect of deformation on the microstructure and electrical properties was investigated by measuring the capacitance and phase angle under different strains, shown in Figure 7.10. Deformation can induce changes on the geometry and microstructure, and the capacitance of a material is dependent on both whilst the phase angle is dependent on solely the microstructure, and unaffected by changes in the sample geometry, as shown from equation 1.11 and 7.5:

$$\theta = \tan^{-1} \left(\frac{Z''}{Z'} \right) \quad (7.5)$$

where θ is phase angle, Z' is the real impedance and Z'' is the imaginary impedance. Therefore, for the capacitance of SBS/PVDF/EVA in Figure 7.10a, the TPE was

frequency independent at low frequencies, whilst a relaxation was overserved at higher frequencies. The capacitance increased in line with increasing strain, however the phase angle remained unaffected at low frequencies, indicating that the differences observed in the capacitance are solely because of thickness and area changes, and the material behaved as a dielectric.

The addition of 1 wt% MWCNT in the SBS/PVDF/EVA TPE resulted in a percolation threshold in solely the SBS phase. As seen from Figure 7.10c, the capacitance exhibited a high frequency dependency at low frequencies attributed to the increased electrical conductivity in the elastomer from the percolation network of MWCNTs,⁴³ also characterised by the deviation of the phase angle at low frequencies from -90° . As the low frequency region for capacitance exhibited a strain independence, the percolated network of MWCNTs was unaffected by variations in strain. However, the intermediate frequency region demonstrated a change in behaviour, whereby the capacitance is strain dependant and the phase angle also exhibited a strain dependency when approaching -90° . Therefore, the change in phase angle indicated that a change in microstructure occurs under strain.

The addition of 3 wt% of MWCNTs into SBS/PVDF/EVA TPE introduced two percolation networks into the elastomer, where one resides in the SBS phase and the second resides in the PVDF phase. Under strain, neither the capacitance nor the phase angle exhibited a varied response, indicating that the MWCNT network was unaffected. Finally, the large deviation in the phase angle from -90° towards 0° demonstrated the increased conductivity of the material.

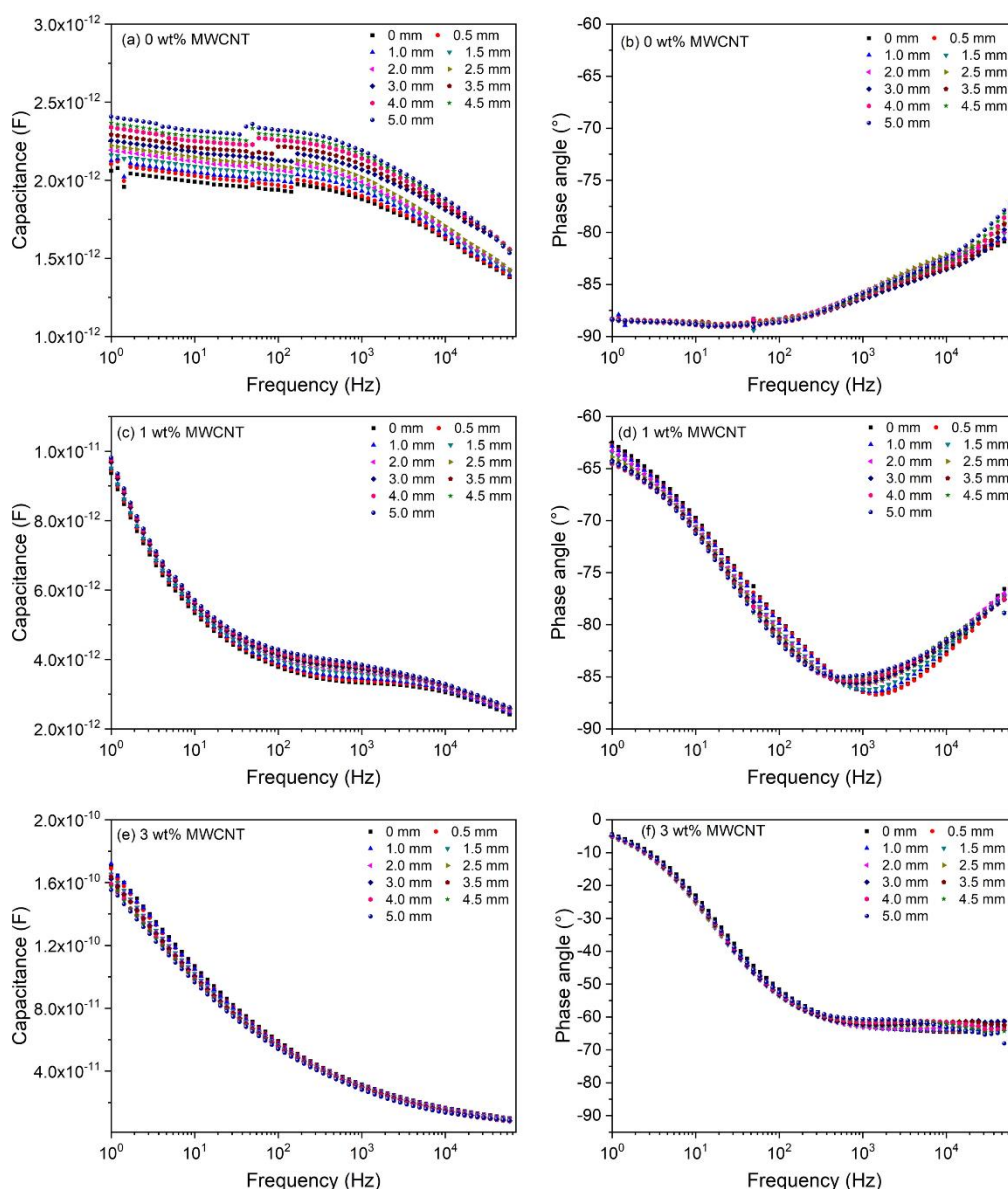


Figure 7.10 Change in capacitance and phase angle respectively under various extensions for SBS/PVDF/EVA TPEs containing (a-b) 0 wt% MWCNTs, (c-d) 1 wt% MWCNTs and (e-f) 3 wt% MWCNTs

Therefore, Figure 7.11 introduced a schematic mechanism to describe the response from the dual percolated SBS/PVDF/EVA/MWCNT composite by considering a network of capacitors and resistors⁴⁴ where resistors, R , were considered as the conductive phase and capacitors, C , were considered as the capacitive/insulating phase. After the first percolation event in SBS/PVDF/EVA/MWCNT (50/50/20/1), the composite had a percolated network of MWCNTs residing in the SBS phase, acting as resistors, combined with capacitive islands of PVDF with no MWCNTs present. Under low frequency, f , conditions, the AC current flowed through the conducting

SBS phase, since $R^{-1} \gg 2\pi fC$ and the phase angle deviated from -90° to 0° . As the frequency increased, the AC conductivity of the capacitive PVDF islands and under the conditions of $R^{-1} \sim 2\pi fC$, the capacitive PVDF islands contributed to the AC current and the phase angle approached -90° .³¹ In the unstrained state, the PVDF islands in the 1 wt% composite were considered to have a relatively low capacitance as they had a high thickness. Upon deformation, the thickness of the PVDF islands decreased and an increase in the capacitance was observed and thus $R^{-1} \sim 2\pi fC$ was achieved at a lower frequency. This behaviour was observed in Figure 7.10d where the minimum for the phase angle shifted to a lower frequency upon increasing strain deformations.

However, when 3 wt% of MWCNTs were incorporated into the matrix, the second percolation threshold was achieved and percolation networks existed in both polymer phases. Therefore, the network was only resistive, as observed in Figure 7.11b, and the capacitance and phase angle were unaffected by increasing strain deformations. Therefore, under a 3 wt% loading, the electrically conducting MWCNT network was unaffected until the material experienced mechanical failure under a 30% strain.

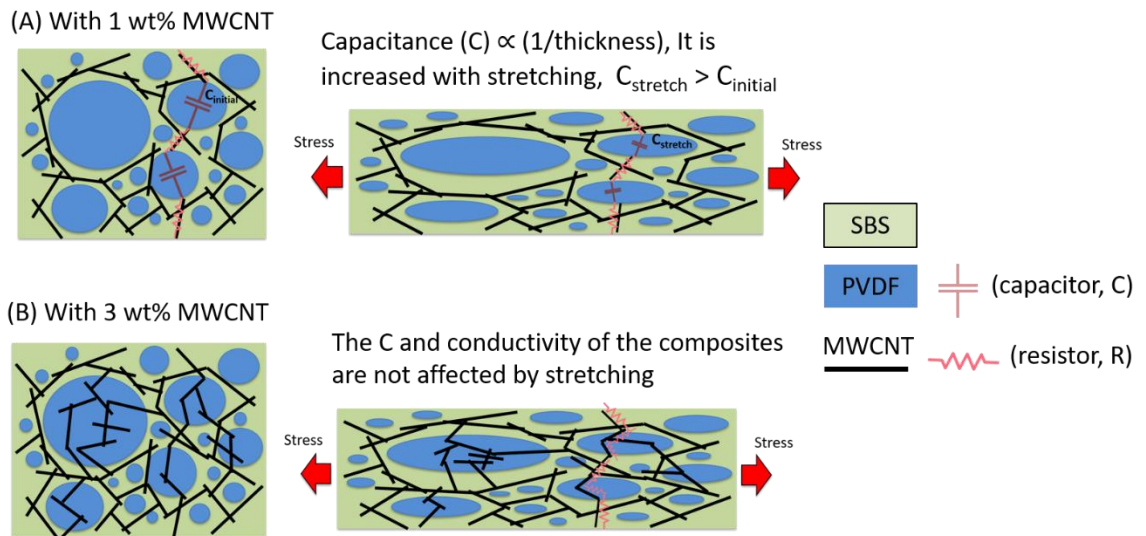


Figure 7.11 Schematic diagram of resistor/capacitor network in the unstrained and strained state for (a) SBS/PVDF/EVA/MWCNT (50/50/20/1) and (b) SBS/PVDF/EVA/MWCNT (50/50/20/3). Reproduced from Ellingford et al.³¹

7.3 Results and discussion for extrinsic modification of intrinsically modified SBS composites with PVDF and MWCNTs

7.3.1 Electrical properties of SBS/PVDF and MG-SBS/PVDF blends

The effect of blending SBS/PVDF and MG-SBS/PVDF in ratios between 70/30 and 30/70 wt% on the electrical properties is shown in Figure 7.12. As seen previously in section 4.2.2, SBS has a relative permittivity of 2.8 at 10^3 Hz. Upon the formation of SBS/PVDF (70/30) the relative permittivity increased to 5.8 at 10^3 Hz due to the increased polarity of PVDF, Appendix Figure 23. Increasing the PVDF fraction further increases the relative permittivity up to 8.8 at 10^3 Hz for SBS/PVDF (30/70). Comparatively, MG-SBS has a relative permittivity of 11.4 at 10^3 Hz. However, as can be seen from Figure 7.12a, as the relative permittivity of the two materials was close, very little differentiation was observed between the ratios MG-SBS/PVDF (70/30) to (30/70). For all SBS/PVDF and MG-SBS/PVDF the $\tan \delta$ loss remained low at 10^3 Hz, exhibiting a $\tan \delta$ of $\sim 0.01 - 0.06$. Additionally, a relaxation peak was observed for the SBS/PVDF blends at 10^5 Hz due to atomic polarisation. The intensity of the peak decreased as the ratio of SBS decreased, however the frequency remained the same. This is attributed to the SBS chains unable to respond to the alternating electric field. Additionally, the relaxation peak is not observed in MG-SBS/PVDF blends, indicating that the cause behind the atomic polarisation was only present on the SBS polymer chains, and that the grafting of methyl thioglycolate removed this. As all of the polymer blends were insulating, the AC conductivity response is within an order of magnitude at all frequencies for all samples. This is regardless of whether SBS or MG-SBS was used, or the ratio between the elastomer and PVDF. This is because both PVDF, SBS and MG-SBS exhibit a capacitive response and thus poorly conductive pathways are formed in the polymer blends. Finally, the phase angle in Figure 7.12d remained at -90° for all elastomers, however a relaxation peak from atomic polarisation was observed at 10^5 Hz for SBS/PVDF blends.

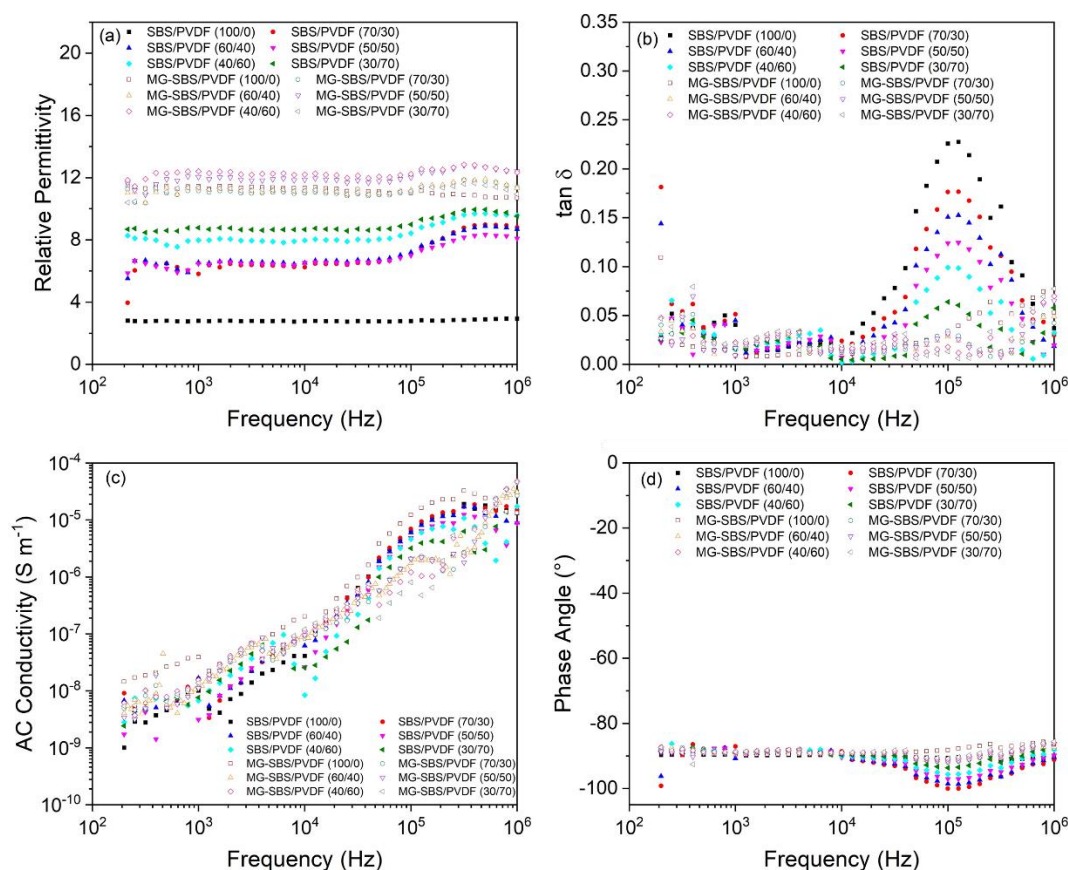


Figure 7.12 Impedance spectroscopy of SBS/PVDF and MG-SBS/PVDF blends for (a) relative permittivity, (b) $\tan \delta$, (c) AC conductivity and (d) phase angle

7.3.2 Mechanical properties of SBS/PVDF blends

The mechanical properties of SBS/PVDF blends and MG-SBS/PVDF blends are shown in Figure 7.13. For the SBS/PVDF blends, SBS/PVDF (70/30) exhibited the largest strain at break of $92.5 \pm 1.5\%$, a large decrease compared to the strain at break for pristine SBS. However, all other blends containing an increased portion of PVDF and reduced SBS exhibited a sharp decrease in their strain at breaks to between 15–20%. This was similar to the strain at break for PVDF, as seen in Figure 7.13a. The sharp decrease in strain at break demonstrates the incompatibility between SBS and PVDF. In addition, the decrease in strain at break between SBS/PVDF (70/30) and SBS/PVDF (60/40) was attributed to a morphological change in the blend. Comparatively, the tensile strength for the elastomer blends increased with increasing PVDF content. SBS/PVDF (70/30) exhibited a tensile strength of 9.6 ± 0.3 MPa, whereas for SBS/PVDF (30/70) the tensile strength increased to 22.5 ± 1.4 MPa. Finally, the Young's modulus of the elastomers exhibited a significant increase as the

PVDF content increased and the SBS content decreased. In SBS/PVDF (70/30) the Young's modulus was 102.3 ± 12.6 MPa, which increased drastically to 677.4 ± 9.6 MPa for SBS/PVDF (30/70). For MG-SBS/PVDF blends, the largest strain at break was for MG-SBS/PVDF (60/40) of $267.2 \pm 3.7\%$ rather than for MG-SBS/PVDF (70/30) which exhibited a strain at break of $145.2 \pm 22.6\%$. Only MG-SBS/PVDF (30/70) exhibited a strain at break similar to PVDF ($\sim 20\%$).

Additionally, the tensile strengths for MG-SBS/PVDF blends were significantly lower than for PVDF. As established in section 4.2.2, MG-SBS chains do not undergo strain induced polymer chain crystallisation due to the addition of methyl thioglycolate groups. In addition, MG-SBS demonstrated increased compatibility between the methyl thioglycolate ester and the fluoro groups of PVDF thus increasing the amorphous regions present in PVDF and lowering the tensile strength. However, the tensile strength increased between MG-SBS/PVDF (60/40) and MG-SBS/PVDF (30/70) from 2.1 ± 0.1 MPa to 5.5 MPa due to the increased PVDF content. MG-SBS/PVDF (70/30) exhibited a slightly higher tensile strength of 3.4 ± 0.9 MPa. Finally, the Young's modulus of MG-SBS/PVDF blends increased upon increasing PVDF content. In MG-SBS/PVDF (70/30) the Young's modulus was 15.6 ± 6.3 MPa, however, for MG-SBS/PVDF (30/70) the Young's modulus increased to 163.0 ± 18.8 MPa.

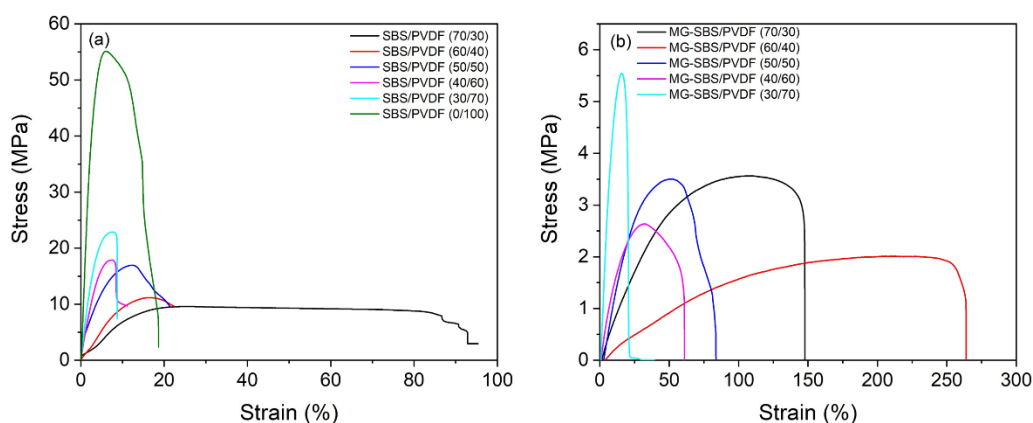


Figure 7.13 Stress strain curves for (a) SBS/PVDF (70/30) ~ (0/100) and (b) MG-SBS/PVDF (70/30) ~ (30/70)

The increased compatibility between MG-SBS and PVDF was further confirmed by visualisation of the polymer phase morphologies *via* SEM in Figure 7.14 and interactions from normalised FTIR spectra in Figure 7.15. In Figure 7.14, the left hand

SEM image demonstrates SBS/PVDF (50/50) in which the PVDF phase was removed. This image demonstrated the large phase dimensions and phase separation within SBS/PVDF due to a lack of compatibility and explains the poor mechanical properties in Figure 7.13. For MG-SBS/PVDF (50/50), the removal of the PVDF phase led to the composite disintegrating as MG-SBS was also soluble in N,N-dimethylacetamide. Thus MG-SBS was removed instead using chloroform and shown in the right-hand SEM image in Figure 7.14. The phase dimensions of MG-SBS (represented by the holes) are much smaller than for SBS, indicating that the compatibility between MG-SBS and PVDF was improved compared to SBS and PVDF.

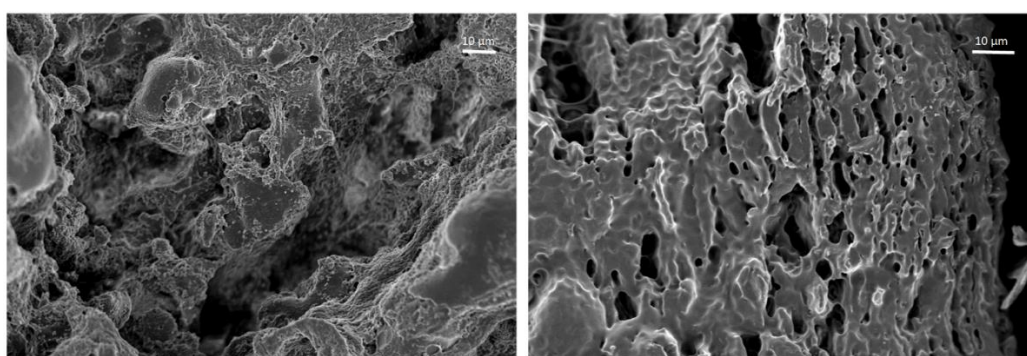


Figure 7.14 SEM imaging of left SBS/PVDF (50/50) with the PVDF phase removed using N,N-dimethylacetamide and right MG-SBS/PVDF (50/50) with the MG-SBS phase removed using chloroform

Furthermore, normalised FTIR spectra to compare peak intensities between SBS and PVDF and MG-SBS and PVDF are shown in Figure 7.15. The shift in the peak intensities indicated whether two polymers are interacting with each other. As can be seen from Figure 7.15a, the peak intensity for the C-F peak at 1177 cm^{-1} in PVDF remained identical before and after mixing with SBS, with a transmission intensity of 0.81, as seen in Appendix Table 2. Comparatively, Figure 7.15c showed the peak at 1177 cm^{-1} in MG-SBS/PVDF increasing in intensity to 0.72 due to a stronger interaction between the PVDF and MG-SBS taking place. In addition, Figure 7.15b showed that MG-SBS exhibited a difference in intensity between the C=O peak at 1732 cm^{-1} and C-O peak at 1272 cm^{-1} after mixing with PVDF. Comparatively, no difference in intensity was observed for a C-H peak for MG-SBS at 1130 cm^{-1} after PVDF is mixed into MG-SBS. This indicated that MG-SBS interacts with PVDF through the ester of methyl thioglycolate to hydrogen bond with PVDF.

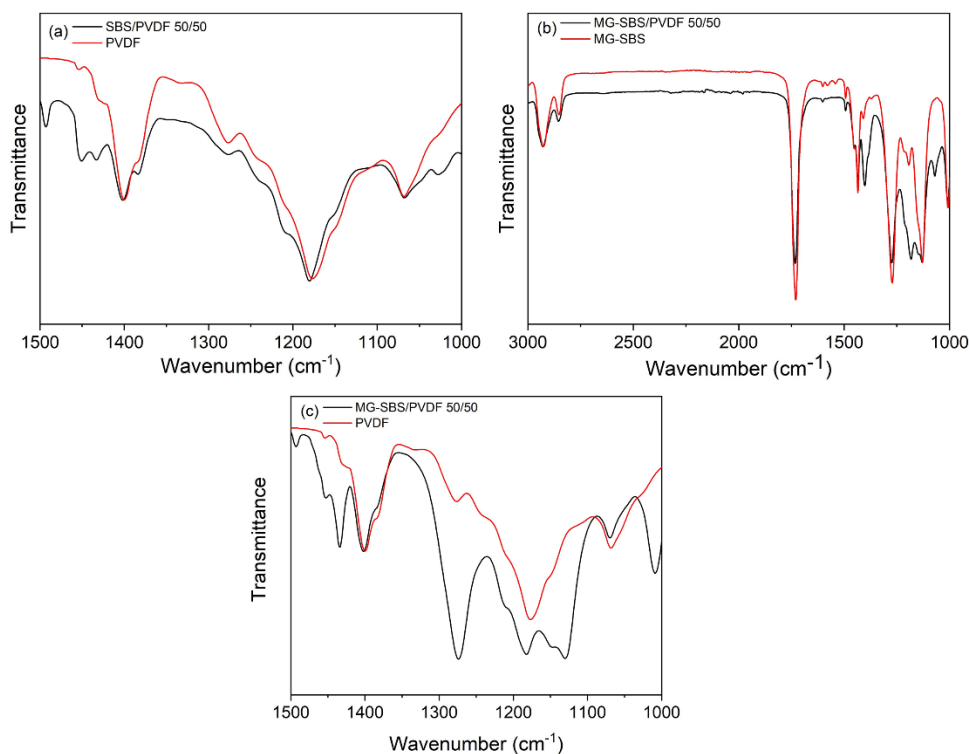


Figure 7.15 Normalised FTIR spectra for comparing peaks intensities in (a) SBS/PVDF 50/50 and PVDF, (b) MG-SBS/PVDF 50/50 and MG-SBS and (c) MG-SBS/PVDF 50/50 and PVDF

7.3.3 Formation of SBS/PVDF and MG-SBS/PVDF composites with MWCNTs

To further develop the electrical properties of SBS/PVDF 50/50, SBS/PVDF 70/30, MG-SBS/PVDF 50/50 and MG-SBS/PVDF 70/30, 1 wt% MWCNTs was added to extrinsically modify the polymer blends. The effect on the mechanical properties is shown in the stress-strain curves of Figure 7.16. For SBS/PVDF 50/50, the addition of 1 wt% of MWCNTs reduced the tensile strength from 17.7 ± 1.4 MPa to 14.1 ± 4.0 MPa, as well as decreasing the Young's modulus from 472 ± 22 MPa to 337 ± 23 MPa. Finally, the strain at break for SBS/PVDF/MWCNT 50/50/1 remained low at 20%. For SBS/PVDF 70/30, the addition of 1 wt% MWCNT yielded a minimal effect on the tensile strength, decreasing it slightly to 8.6 ± 0.7 MPa. However, the Young's modulus of SBS/PVDF 70/30 increased from 102.3 ± 12.6 MPa to 267 ± 19 MPa upon the incorporation of 1 wt% MWCNTs. Interestingly, the strain at break for the composite increased from $92.5 \pm 1.5\%$ to $122 \pm 5.6\%$.

In comparison, the addition of 1 wt% MWCNTs to MG-SBS/PVDF 50/50 resulted in a reinforcing effect on the composite. The tensile strength increased from 3.9 ± 0.4

MPa to 7.9 ± 0.2 MPa and decreased the strain at break from $67 \pm 5.1\%$ to $44 \pm 4.0\%$. Additionally, the Young's modulus of the composite increased from 33 ± 4.6 MPa to 93 ± 17.5 MPa. However the reinforcement effect in MG-SBS/PVDF/MWCNT 70/30/1 was not fully observed. The Young's modulus decreased marginally from 15.6 ± 2.4 MPa to 13.4 ± 3.4 MPa, the tensile strength decreased from 3.0 ± 0.6 MPa to 2.8 ± 0.3 MPa whilst the strain at break increased from $145 \pm 22.6\%$ to $181 \pm 8.5\%$.

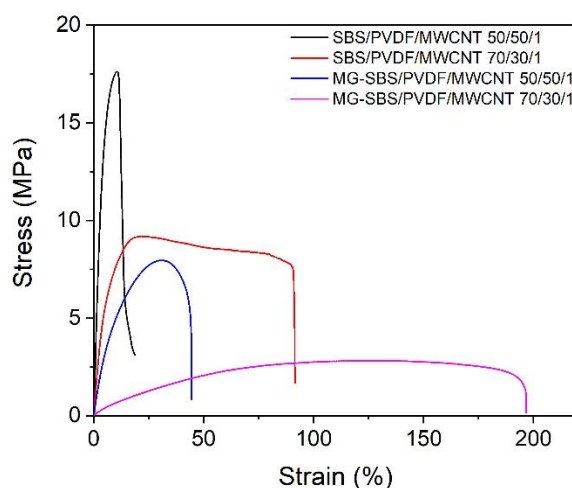


Figure 7.16 Stress-strain curves of SBS/PVDF 50/50, SBS/PVDF 70/30, MG-SBS/PVDF 50/50 and MG-SBS/PVDF 70/30 all containing 1 wt% MWCNT

The effect on the percentage crystallinity, $X_c(\%)$, of the PVDF phase was measured from DSC alongside the crystallisation temperature (T_c) and melting temperature (T_m) via DSC in Appendix Table 3. However, the T_c and T_m of PVDF were largely unaffected by the variations in samples. By blending MG-SBS with PVDF, the $X_c(\%)$ of PVDF decreased up to 14% due to the increased compatibility increasing the presence of amorphous regions in PVDF. Comparatively, the blending of SBS with PVDF increased $X_c(\%)$ due to the poor compatibility between the two polymers. The addition of MWCNTs into MG-SBS/PVDF recovered the $X_c(\%)$ to close to the $X_c(\%)$ for PVDF as MWCNTs can act as heterogeneous nucleation sites for crystallisation within a polymer matrix.³⁹

SEM imaging, Figure 7.17, showed SBS/PVDF/MWCNT and MG-SBS/PVDF/MWCNT 50/50/1, demonstrating the polymer phase in which the MWCNTs are residing in. The SEM images are similar to Figure 7.14 where the PVDF phase was removed in SBS/PVDF and the MG-SBS phase was removed in MG-SBS/PVDF. A large quantity of white dots are observed in the SBS phase of

SBS/PVDF/MWCNT and in the PVDF phase of MG-SBS/PVDF/MWCNT, attributed to the charging ends of the MWCNTs under the SEM electron beam and represent the locality of MWCNTs within the composites. Therefore, the locality of the MWCNTs explains the observed mechanical behaviour present in Figure 7.15. For MG-SBS/PVDF/MWCNT composites, the mechanical properties were reinforced with mechanical degradation. This illustrated that it is easier to obtain a homogenous dispersion of MWCNTs within the composite, and the general higher strain at break indicated that MG-SBS remained compatible with PVDF after the addition of MWCNTs. Additionally, the reinforcement effect of the mechanical properties was more significant in MG-SBS/PVDF/MWCNT 50/50/1 compared to 70/30/1. After compositing, the $X_c(\%)$ of MG-SBS/PVDF/MWCNT 50/50/1 was almost identical to pure PVDF, and the mechanical properties exhibited a reduction in the ductility and an increase in the tensile strength after compositing MG-SBS/PVDF 50/50. As the $X_c(\%)$ increased from MWCNT nucleation sites and mechanical reinforcement was observed, the MG-SBS/PVDF 50/50 blend containing more PVDF, compared to MG-SBS/PVDF 70/30, was more able to disperse the MWCNTs, indicating that the MWCNTs reside in the PVDF phase.

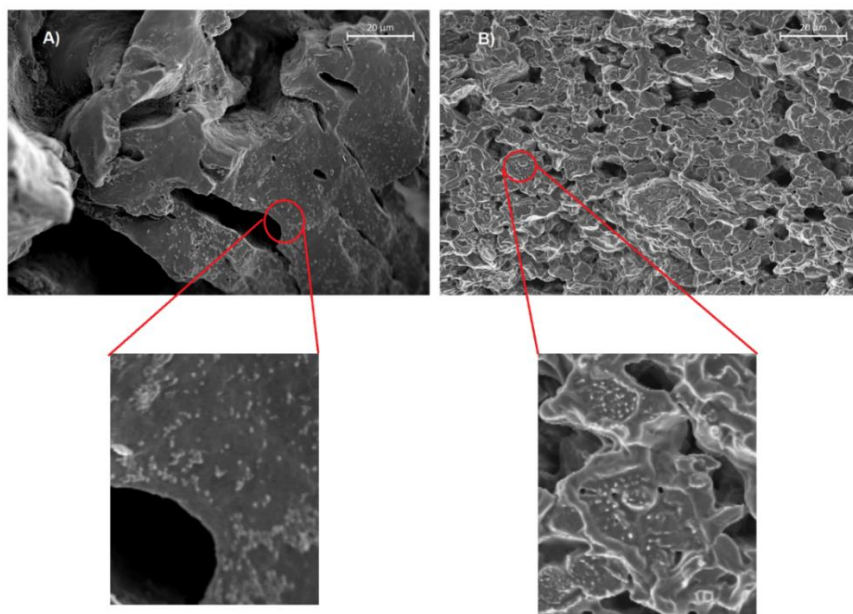


Figure 7.17 SEM imaging of (a) the SBS of SBS/PVDF/MWCNT 50/50/1 and (b) the PVDF phase in MG-SBS/PVDF/MCNT 50/50/1

Conversely, the addition of MWCNTs to SBS/PVDF reduced the mechanical properties in both the 50/50 and 70/30 blends. Whilst the $X_c(\%)$ was greater for

SBS/PVDF 50/50 compared to SBS/PVDF 70/30 due to the greater PVDF content assisting crystallisation formation in SBS/PVDF 50/50, after compositing the $X_c(\%)$ for both decreased significantly. This was due to poor dispersion of the MWCNTs and explained the reduction in the mechanical properties observed.

As observed in section 7.2, the MWCNTs preferentially resided in the SBS phase compared to the PVDF phase and this is reinforced in Figure 7.17a whereby a large quantity of MWCNTs were observed unlike for the MG-SBS/PVDF composites. SBS is able to π - π stack through the styrenic groups with MWCNTs⁴⁵ and the butadiene chain is able to react with the open ends and defects on MWCNTs *via* a free radical reaction.^{33, 34} Comparatively, the grafting of the polar side group in MG-SBS introduced an ester which interacted with both the styrenic block and the PVDF phase. However, the packing of the polymer chains was affected by the grafted polar group and the increased phase mixing of the styrenic and butadiene blocks⁴⁶ reduced the ability for MWCNTs to interact with MG-SBS favourably compared to SBS. Therefore, the MWCNTs formed a stronger interaction with PVDF and preferentially resided in this polymer phase.

Finally, the electrical properties of the SBS/PVDF and MG-SBS/PVDF composites are observed in Figure 7.18. For SBS, the highest relative permittivity was for SBS/PVDF/MWCNT 50/50/1 at 11.7 at 10^3 Hz. However, MG-SBS containing composites demonstrated enhanced relative permittivities of 16.3 and 24.3 at 10^3 Hz for MG-SBS/PVDF/MWCNT 50/50/1 and MG-SBS/PVDF/MWCNT 70/30/1 respectively. The higher relative permittivity was attributed to the increased polarity of MG-SBS compared to SBS. However, the AC conductivity of MG-SBS/PVDF/MWCNT 70/30/1 demonstrated a frequency independent response of 10^{-4} S m⁻¹ and a phase angle deviated from -90° at high frequencies and tending towards 0° at low frequencies. In addition, an increase in the $\tan \delta$ loss was observed due to electrode polarisation observed below 10^3 Hz. This indicated that 70/30 MG-SBS/PVDF had reached the percolation threshold at 1 wt% addition of MWCNT. However, the percolation threshold was not reached in MG-SBS/PVDF/MWCNT 50/50/1, and it exhibited a low $\tan \delta$ of 0.03 at 10^3 Hz. This provides further confirmation of the preferential locality of MWCNTs in the PVDF phase of MG-SBS/PVDF composites as the percolation network was formed more easily with a reduced content of PVDF. A similar observation was not found in SBS/PVDF

composites, and it indicates that the increased compatibility between MG-SBS and PVDF assisted conductive network formation.

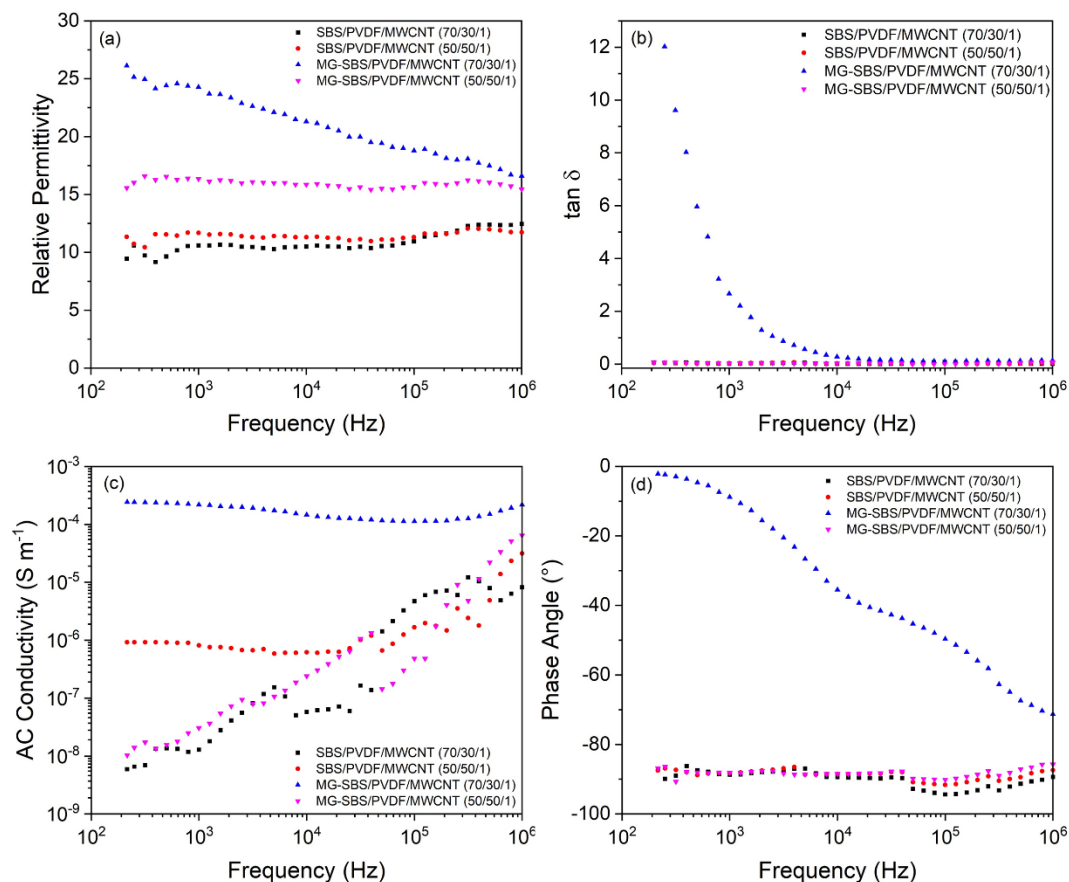


Figure 7.18 Impedance spectroscopy for SBS/PVDF 50/50 and 70/30 and MG-SBS/PVDF 50/50 and 70/30 all containing 1 wt% MWCNTs with (a) relative permittivity, (b) $\tan \delta$, (c) AC conductivity and (d) phase angle

7.4 Conclusion

In conclusion, this chapter presented two methods for compatibilising PVDF and SBS polymer blends to enhance the strain at break, followed by subsequent compositing *via* MWCNTs to enhance their electrical properties.

The first method compatibilised SBS and PVDF using 20 wt% EVA as a compatibilising third polymer *via* melt mixing. This was able to increase the strain at break of 50/50 SBS/PVDF up to 200% as well as observing a small increase in the relative permittivity.

The addition of MWCNTs increased the relative permittivity but at the expense of the elasticity of the composite. It was observed that SBS/PVDF/EVA experienced a dual percolation behaviour at 1 wt% and 3 wt% addition of MWCNTs. The first percolation threshold was attributed to percolation of MWCNTs selectively localised in the SBS/EVA phase and the second percolation threshold was observed in the PVDF phase, characterised by theoretical contact angle measurements, DSC and FTIR. The dual percolation threshold suppressed the increase in the $\tan \delta$ loss of the composite at 1 wt% and 2 wt% MWCNTs concentration. In addition, a rheological dual percolation threshold was observed in the SBS/PVDF/EVA composites.

Finally, the electrical dual percolation threshold was investigated whilst under stretching up to 30% strain. Under a high electric field, polarisation-electric field loops showed that SBS/PVDF/EVA containing 1 wt% MWCNTs exhibited a conducting response due to the higher electric field. Below this, the nanocomposite at 0.3 wt% and 0.5 wt% MWCNTs demonstrated a ‘lossy’ dielectric response. Under stretching, the electrical response of SBS/PVDF/EVA containing 1 wt% MWCNTs was affected by strain, whereas 0 wt% MWCNTs and 3 wt% MWCNTs remained unaffected. The effect on the electrical properties was rationalised using the resistor and capacitor model as a change in the microphase structure. The effect of the stretching affected the thickness of the PVDF islands in the composite, and thus affected their capacitance and phase angle.

The second section investigated the compatibilisation of SBS and PVDF by blending MG-SBS with PVDF. MG-SBS/PVDF exhibited a significantly higher strain at break than for SBS/PVDF at all blending ratios. In addition, MG-SBS/PVDF demonstrated higher relative permittivity and low $\tan \delta$ loss for all polymer blends than SBS/PVDF. This was because the relative permittivity of SBS was 2.8 and for MG-SBS was 11.4.

The addition of 1 wt% MWCNTs to both 50/50 and 70/30 MG-SBS/PVDF and SBS/PVDF increased the brittleness of the nanocomposites and increased the tensile strength, whilst the relative permittivity of all composites was enhanced. For SBS, 50/50 SBS/PVDF exhibited the highest relative permittivity of 11.7 at 10^3 Hz. For MG-SBS, 70/30 MG/TG-SBS exhibited the highest relative permittivity and reached the percolation threshold. SEM imaging and DSC confirmed the locality of the MWCNTs in the different composites. In SBS containing composites, the MWCNTs

preferentially resided in the SBS phase, whilst in MG-SBS containing composites, the MWCNTs resided in the PVDF phase.

Overall, this chapter demonstrated two methods to extrinsically modify SBS for elastomers with increased electromechanical properties for actuation and energy harvesting device. It showed that PVDF can be realistically incorporated into polymer blends to enhance the electrical properties without complete loss of the elastomeric behaviour. Furthermore, it demonstrated that MWCNTs can be successfully utilised to additionally enhance the relative permittivity however an optimum MWCNTs concentration must be found to balance its destructive effect on the strain at break and the elasticity of the composite.

7.5 References

1. C. Ellingford, C. Bowen, T. McNally and C. Wan, *Macromol. Rapid Commun.*, 2018, **39**, 1800340.
2. C. Wan and C. R. Bowen, *J. Mater. Chem. A*, 2017, **5**, 3091-3128.
3. B. Ameduri, *Chem. Rev.*, 2009, **109**, 6632-6686.
4. A. J. Lovinger, *J. Appl. Phys.*, 1981, **52**, 5934-5938.
5. L. F. Malmonge, S. d. C. Langiano, J. M. M. Cordeiro, L. H. C. Mattoso and J. A. Malmonge, *Mater. Res.*, 2010, **13**, 465-470.
6. C. Ellingford, C. Wan, Ł. Figiel and T. McNally, *Compos. Commun.*, 2018, **8**, 58-64.
7. N. Moussaif and R. Jérôme, *Polymer*, 1999, **40**, 3919-3932.
8. D. Li, S. Song, C. Li, C. Cao, S. Sun and H. Zhang, *J. Polym. Res*, 2015, **22**, 102.
9. D. Kuang, R. Li and J. Pei, *Polymers*, 2014, **6**, 2146.
10. H. Mutsuda, J. Miyagi, Y. Doi, Y. Tanaka, H. Takao and Y. Sone, *Int. J. Energy Eng.*, 2014, **4**, 67.
11. H. Ma and Y. Yang, *Polym. Test.*, 2008, **27**, 441-446.
12. Y. Li, Y. Oono, Y. Kadowaki, T. Inoue, K. Nakayama and H. Shimizu, *Macromolecules*, 2006, **39**, 4195-4201.
13. X. Jiang, C. Xu, Y. Wang and Y. Chen, *J. Macromol. Sci., Part B: Phys.*, 2015, **54**, 58-70.
14. M. Li, Y. Deng, Y. Wang, Y. Zhang and J. Bai, *Mater. Chem. Phys.*, 2013, **139**, 865-870.
15. H. Stoyanov, D. Mc Carthy, M. Kolloosche and G. Kofod, *Appl. Phys. Lett.*, 2009, **94**, 232905.
16. J. I. Roscow, C. R. Bowen and D. P. Almond, *ACS Energy Lett.*, 2017, **2**, 2264-2269.
17. F. B. Madsen, A. E. Daugaard, S. Hvilsted and A. L. Skov, *Macromol. Rapid Commun.*, 2016, **37**, 378-413.

18. S. Nayak, T. K. Chaki and D. Khastgir, *Ind. Eng. Chem. Res.*, 2014, **53**, 14982-14992.
19. H. Zhao, Y.-J. Xia, Z.-M. Dang, J.-W. Zha and G.-H. Hu, *J. Appl. Polym. Sci.*, 2013, **127**, 4440-4445.
20. M. Tian, Z. Wei, X. Zan, L. Zhang, J. Zhang, Q. Ma, N. Ning and T. Nishi, *Compos. Sci. Technol.*, 2014, **99**, 37-44.
21. X.-l. Xu, C.-j. Yang, J.-h. Yang, T. Huang, N. Zhang, Y. Wang and Z.-w. Zhou, *Composites, Part B*, 2017, **109**, 91-100.
22. S. Zhao, J. Li, D. Cao, Y. Gao, W. Huang, G. Zhang, R. Sun and C.-P. Wong, *J. Mater. Chem. C*, 2016, **4**, 6666-6674.
23. S. Zhao, G. Zhang, Y. Gao, L. Deng, J. Li, R. Sun and C.-P. Wong, *ACS Appl. Mater. Interfaces*, 2014, **6**, 22823-22829.
24. K. Shehzad, A. A. Hakro, Y. Zeng, S.-H. Yao, Y. Xiao-Hong, M. Mumtaz, K. Nadeem, N. S. Khisro and Z.-M. Dang, *Appl. Nanosci.*, 2015, **5**, 969-974.
25. L. Keun Yoon and B. Kyu Kim, *J. Appl. Polym. Sci.*, 2000, **78**, 1374-1380.
26. M. H. Lang and J. Zhang, *Plast., Rubber Compos.*, 2014, **43**, 8-14.
27. R.-C. Zhang, Y. Xu, Z. Lu, M. Min, Y. Gao, Y. Huang and A. Lu, *J. Appl. Polym. Sci.*, 2008, **108**, 1829-1836.
28. J. Chen, Y.-y. Shi, J.-h. Yang, N. Zhang, T. Huang, C. Chen, Y. Wang and Z.-w. Zhou, *J. Mater. Chem.*, 2012, **22**, 22398-22404.
29. D. K. Owens and R. C. Wendt, *J. Appl. Polym. Sci.*, 1969, **13**, 1741-1747.
30. L. Cao, S. Deng and Z. Lin, *Polymers*, 2016, **8**, 50.
31. C. Ellingford, H. Smith, X. Yan, C. Bowen, Ł. Figiel, T. McNally and C. Wan, *Eur. Polym. J.*, 2019, **112**, 504-514.
32. L. Zonder, S. McCarthy, F. Rios, A. Ophir and S. Kenig, *Adv. Polym. Tech.*, 2014, **33**.
33. L. Lu, Z. Zhou, Y. Zhang, S. Wang and Y. Zhang, *Carbon*, 2007, **45**, 2621-2627.
34. S. Inukai, K.-i. Niihara, T. Noguchi, H. Ueki, A. Magario, E. Yamada, S. Inagaki and M. Endo, *Ind. Eng. Chem. Res.*, 2011, **50**, 8016-8022.
35. S. Yu, X. Wang, H. Xiang, L. Zhu, M. Tebyetekerwa and M. Zhu, *Carbon*, 2018, **140**, 1-9.
36. X. Wang, S. Meng, M. Tebyetekerwa, Y. Li, J. Pionteck, B. Sun, Z. Qin and M. Zhu, *Composites, Part A*, 2018, **105**, 291-299.
37. V. Kochervinskii, I. Malyshkina, N. Gavrilova, S. Sulyanov and N. Bessonova, *J. Non-Cryst. Solids*, 2007, **353**, 4443-4447.
38. X. M. Shi, J. Zhang, J. Jin and S. J. Chen, *Express Polym. Lett.*, 2008, **2**, 623-629.
39. K. Ke, Y. Wang, K. Zhang, Y. Luo, W. Yang, B.-H. Xie and M.-B. Yang, *J. Appl. Polym. Sci.*, 2012, **125**, E49-E57.
40. S. J. Chin, S. Vempati, P. Dawson, M. Knite, A. Linarts, K. Ozols and T. McNally, *Polymer*, 2015, **58**, 209-221.
41. Z. Chen, L. Xie, X. Huang, S. Li and P. Jiang, *Carbon*, 2015, **95**, 895-903.
42. J. F. Scott, *J. Phys.: Condens. Matter*, 2008, **20**, 021001.
43. D. P. Almond and C. R. Bowen, *J. Phys. Chem. Lett.*, 2015, **6**, 1736-1740.
44. D. P. Almond and C. R. Bowen, *Phys. Rev. Lett.*, 2004, **92**, 157601.
45. T. Fujigaya and N. Nakashima, *Sci. Technol. Adv. Mater.*, 2015, **16**, 024802.
46. C. Ellingford, R. Zhang, A. M. Wemyss, C. Bowen, T. McNally, Ł. Figiel and C. Wan, *ACS Appl. Mater. Interfaces*, 2018, **10**, 38438-38448.

Chapter 8

Intrinsic modification of alternative commercial elastomers

Publications:

C. Ellingford, A. Pengchaicharoen, A. M. Wemyss and C. Wan,* Structure and dielectric properties of electroactive tetraaniline grafted non-polar elastomers, *J. Compos. Sci*, 2020, **4**, 1, 25

8.1 Introduction

The development of dielectric elastomers with enhanced electromechanical properties has so far utilised an SBS block copolymer for both intrinsic and extrinsic modification methods. The separation of styrene and butadiene into blocks created a phase separated morphology consisting of ‘hard’ glassy styrene regions and ‘soft’ butadiene regions. This results in a strong but elastic mechanical behaviour from only polymer chain entanglement and π - π stacking.¹

However, the mechanical properties of styrenic dielectric elastomers can be tuned by altering the ratio of styrene and butadiene, as well as removing the block structure of styrene and butadiene. Therefore, using styrene-butadiene rubber (SBR) as an alternative to SBS introduces a statistical arrangement of styrene and butadiene groups along a polymer chain, to decrease the mechanical strength and increase the deformability of the dielectric elastomer.¹ Furthermore, removal of the styrenic block entirely results in a weak, soft polymer with high deformability and very high strain at break.

Therefore both intrinsic and extrinsic approaches have been utilised to enhance the strength of these polymers. Extrinsically, 2.5 phr bacterial cellulose nanowhiskers were mixed into SBR and enhanced the tensile strength of SBR from 2.4 MPa up to 9.9 MPa, whilst also increasing the strain at break from 464% to 513%. The bacterial cellulose nanowhiskers acted as multifunction crosslinkers, increasing the crosslinking density of SBR. This reinforced the mechanical properties, however further increases beyond 2.5 phr of bacterial cellulose nanowhiskers increased the brittleness of the rubber.² Surface modified cellulose nanofibers with thiol and vinyl functionality were introduced into SBR and provided crosslinking sites during vulcanisation. The tensile strength of the elastomer was increased from 3.2 MPa to 8.1 MP, whilst the strain at break increased from 714% to 786% with 7 wt% cellulose nanofibers.³ Alternatively the addition of nanocopper *via* a twin roll mill enhanced the tensile strength of SBR from 1.6 MPa to 2.9 MPa.⁴ For polybutadiene, a palygorskite filler was compatibilised using a silane coupling agent. 15% addition of the silane coupling agent optimally enhanced the tensile strength for the composite from 5 MPa to 11 MPa.⁵

One form of intrinsic modification of polybutadiene to enhance the mechanical properties was to incorporate Diels-Alder reversible crosslinking. For Diels-Alder bonding, furan groups were grafted indirectly to the polybutadiene backbone followed by the mixing of bismaleimide into the polymer. The introduction of dynamic crosslinking enhanced the tensile strength up to 9.6 MPa but at the expense of the strain at break. In addition, the reversible dynamic covalent bonds introduced a self-healing nature to polybutadiene.⁶ The grafting was further simplified by grafting furfuryl mercaptan *via* thiol-ene chemistry to the backbone of polybutadiene to introduce the dynamic Diels-Alder crosslinking, see Figure 8.1. This process made the polybutadiene recyclable upon heating as the Diels-Alder bonding underwent the retro Diels-Alder reaction. The tensile strength was increased to 5.6 MPa, however, once again the strain at break was negatively affected and failed at only 45%.⁷

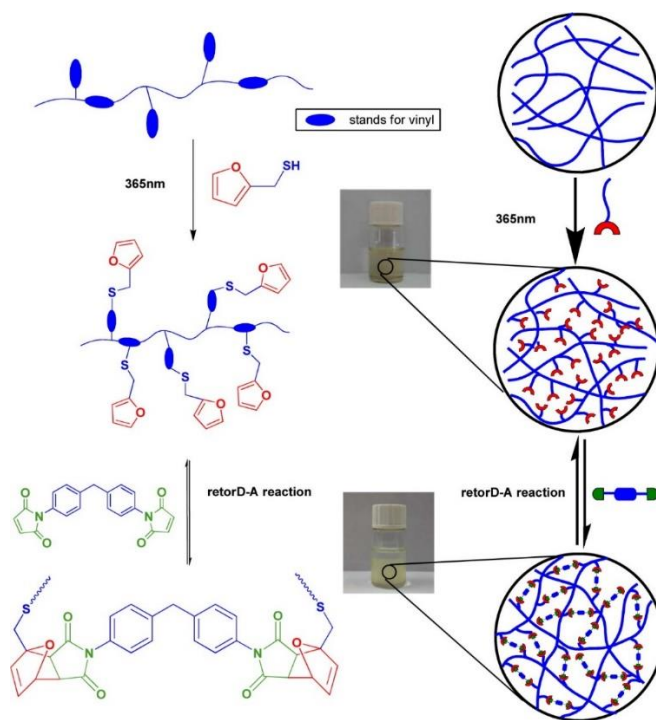


Figure 8.1 Introduction of dynamic covalent diels-alder crosslinking into polybutadiene to increase the tensile strength and introduce a self-healing and recyclable nature. Reproduced from Bai *et al.*⁷

Thus far, non-conducting polar groups have been intrinsically grafted to the backbone of SBS. However the grafting of conducting polymers can be utilised to enhance the relative permittivity of a non-polar dielectric elastomer. Polyaniline (PANI) is one such example which was grafted to styrene-ethylene-butadiene-styrene.⁸ This

increased the relative permittivity up to 10 at 10^4 Hz with 2.1 vol% grafting. However, above this grafting the PANI chains percolated and formed a conducting network.⁸ The drawbacks of using conductive PANI is that it suffers from poor solubility and processability.⁹

The basic conductive repeat unit of PANI consists of four aniline units and is called tetraaniline (TANI). It is the smallest conductive oligomer of aniline, but only conductive in the emeraldine salt oxidation state, up to 1 S m^{-1} . However, TANI in the emeraldine salt oxidation state also suffers from issues of solubility and processability.¹⁰

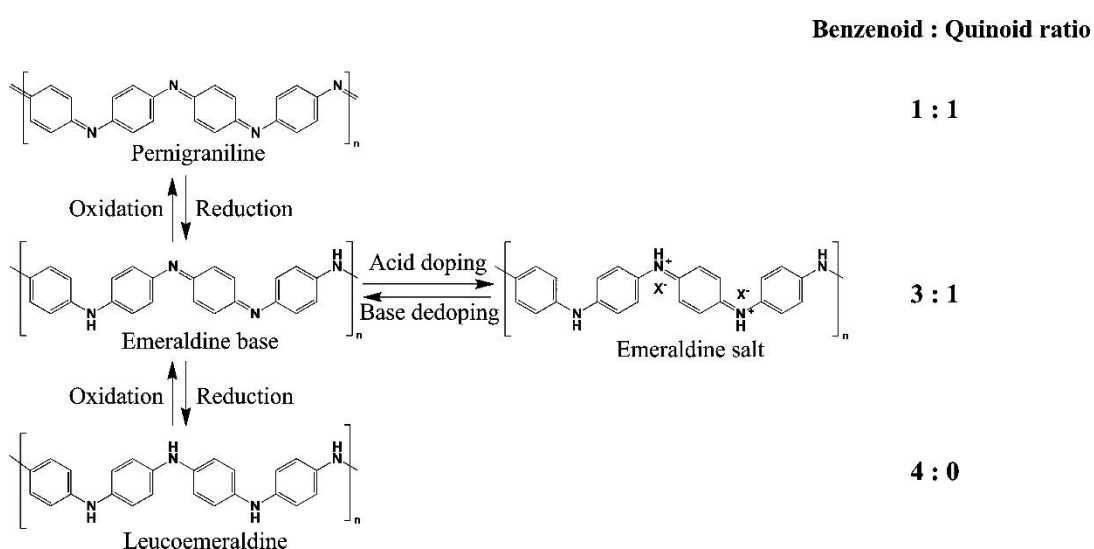


Figure 8.2 The different oxidation states of TANI and the benzene ring to quinoid ring ratio. Reproduced from Wang *et al.*¹⁰

All of the different oxidation states of TANI are shown in Figure 8.2. The emeraldine oxidation state of TANI consists of three benzene rings and one quinoid ring, and can be doped using a strong acid and dedoped using a strong base between the emeraldine salt and emeraldine base oxidation state. The difference in oxidation state is visible as TANI in the emeraldine base form is blue, whilst TANI in the emeraldine salt form is green. In addition, a reduced oxidation state of TANI can be synthesised known as the leucoemeraldine oxidation state, consisting of four benzene rings, whilst an oxidised oxidation state of TANI is called the pernigraniline oxidation state and consists of two benzene rings and two quinoid rings. However, neither the leucoemeraldine, pernigraniline or emeraldine base oxidation state are conductive.^{10, 11} Furthermore, self-healing has been observed in grafting of TANI. This was observed in a sebacic

acid and citric acid polymer *via* hydrogen bonding on the polymer chain and π - π stacking from TANI groups.¹²

Therefore, in this chapter alternative polymers of SBR and polybutadiene (PB) were used for grafting both methyl thioglycolate and thioglycolic acid to. Utilising the statistical arrangement of styrene and butadiene in SBR and removing the styrenic block in PB, the aim was to produce a more mechanically deformable and less brittle hydrogen bonding elastomer which also had enhanced electrical properties for actuation and energy harvesting devices. Therefore, in SBR, an electrostatic interaction and hydrogen bonding interaction is present after grafting both polar groups whilst in PB only a hydrogen bonding interaction is present.

The results for both modified SBR and polybutadiene rubbers are split over two different sections. The first section focusses on the synthesis of modified SBR rubbers and the successful grafting of methyl thioglycolate and thioglycolic acid. The structural properties of the modified SBR elastomers were investigated by UV-Vis spectroscopy and DMTA to determine the effect that grafting the two polar group has on SBR. Finally, the electrical and mechanical properties of modified SBR elastomers were investigated by tensile testing and impedance spectroscopy. In the second section, the modification of PB with methyl thioglycolate and thioglycolic acid is presented and follows the same structure for characterisation and analysis.

The final section investigates the grafting of different ratios of conducting TANI to both SBS and PB to enhance the electrical properties of the elastomers *via* a three step grafting procedure. This allowed a series of microcapacitors to be grafted to the polymer backbones without issues of agglomeration or dispersion arising, whilst retaining solubility and processability of the modified elastomer.

This chapter represents the development of alternative elastomers for energy harvesting and actuation devices. An incorporated hydrogen bonding network was used to tune the mechanical properties for increased strength whilst retaining a high strain at break, and improve on the mechanical behaviour observed in MG/TG-SBS. Furthermore, this chapter also demonstrates that conducting oligomeric groups can be introduced to polymer backbones for enhanced actuation and energy harvesting performance, instead of intrinsic modification solely utilising non-conductive polar groups.

8.2 The grafting of polar groups to styrene-butadiene-rubber (SBR)

8.2.1 Grafting of methyl thioglycolate and thioglycolic acid to styrene-butadiene rubber.

To react SBR under a photoinitiated thiol-ene reaction, the concentration of vinyl groups in the rubber was first established, using ^1H NMR shown in Figure 8.3a. From the spectrum, the peaks for the aromatic styrene region were observed at 7.3 ppm and 7.2 ppm, representing two protons and three protons respectively for styrene. However, the peak at 7.3 ppm overlaps with the CDCl_3 solvent peak and thus cannot be used for the calculation of the ratio between styrene and the aromatic region. Comparatively, the alkene region exhibited three vinyl peaks. The peak at 5.6 ppm was attributed to the single proton environment on the exo vinyl group, whilst the two proton environment for the exo vinyl group was at 5.0 ppm. Finally, the two protons for the endo vinyl group are at 5.4 ppm. Thus the vinyl/styrene ratio in SBR was calculated using the endo and exo peaks at 5.4 ppm and 5.0 ppm respectively in equation 4.1 and 4.2. The composition of SBR was 82.4 mol% butadiene and 17.6 mol% styrene and from equations 4.3 and 4.4, the weight fraction of butadiene and styrene groups was 70.9 wt% vinyl and 29.1 wt% styrene, and a similar ratio of vinyl groups and styrene groups compared to SBS. Per gram of SBR, there was 13.1 mmols of vinyl groups present.

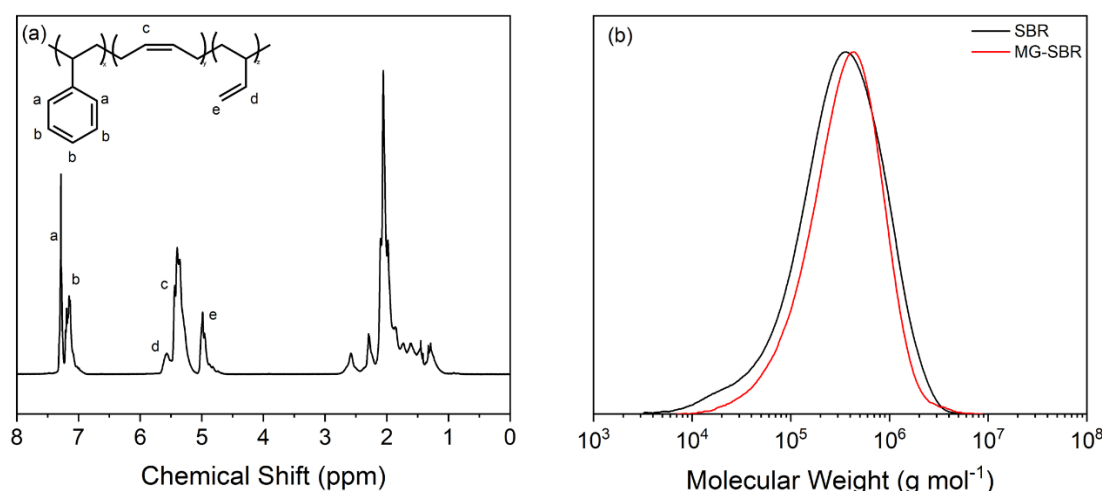


Figure 8.3 (a) ^1H NMR spectrum at 400 MHz in CDCl_3 and (b) GPC trace of SBR and MG-SBR in THF using a Refractive Index detector

GPC in Figure 8.3b provides further information on the nature of the polymer chains in SBR. The M_w of SBR was $148000 \text{ g mol}^{-1}$, higher than for SBS but the M_n of SBR was lower compared to SBS, with a M_n of 46000 g mol^{-1} . This variation was due to the high \bar{D} of SBR rubber, 3.22, which indicated that the polymer chains are not uniform and vastly vary in size.

Therefore, the grafting of methyl thioglycolate to SBR initially followed the optimised conditions for methyl thioglycolate grafting to SBS, where methyl thioglycolate was in a 4× excess, 0.6 mol% photoinitiator with respect to vinyl group concentration was used and 20 minutes UV light exposure was applied. However, a significant quantity of product was lost during the purification step as the polymer formed a cloudy solution upon addition of hexane and only 0.6 g of polymer was obtained from 1 g of starting product. Analysis of ^1H NMR demonstrated that the grafting of methyl thioglycolate was low, with a thiol grafting of 21.3% and 23.3% of the vinyl groups had reacted. Thus, due to the low grafting, many polymer chains did not precipitate during purification and remained in solution. The low grafting was attributed to a slow grafting rate instead of the reaction termination.

A series of experiments to enhance the grafting of methyl thioglycolate were conducted. Firstly, the excess of methyl thioglycolate was increased to a 5× excess. However, only 0.4 g of product was obtained and ^1H NMR confirmed that the grafting of methyl thioglycolate was 19.4% and 20.1% reacted vinyl groups. Therefore, under these conditions, increasing the thiol excess had little effect on the grafting. Additionally, the photo exposure time was increased from 20 minutes to 30 minutes to increase the time for the reaction to proceed. ^1H NMR analysis demonstrated that the grafting of methyl thioglycolate was 28.3% and 29.8% of the vinyl groups were reacted. Overall, 0.9 g product was obtained.

Alongside this, the effect of increasing the photoinitiator concentration on the grafting rate was investigated. Under the conditions of 1.2 mol% photoinitiator concentration, 5× excess methyl thioglycolate and 20 minutes photo exposure, the methyl thioglycolate grafting increased to 31.3% whilst 32.8% of the vinyl groups were reacted. In line with the increase in grafting, the weight of product obtained also increased to 1.1 g.

Overall, it was experimentally determined that the controllable factors for the grafting of methyl thioglycolate were the length of the reaction and the photoinitiator concentration. Therefore, the following set of reaction conditions were used to boost the grafting reaction: 5× excess methyl thioglycolate, 60 minutes UV exposure time and 1.5 mol% photoinitiator concentration. ^1H NMR indicated that the reaction had progressed further, but not to completion as the methyl thioglycolate grafting was 69.1% and the vinyl groups reacted was 69.9%. The yield of modified elastomer was 1.7 g from 1 g of SBR

The conditions were further modified to ensure that the grafting reaction reached completion. Therefore, 5× methyl thioglycolate excess, three hour photo exposure and 3 mol% photoinitiator with respect to the butadiene block was used. At both the 1 g scale and 10 g scale, 98.1% methyl thioglycolate grafted according to ^1H NMR and 98.1% of the vinyl groups reacted as well. The methyl thioglycolate modified SBR polymer was referred to as MG-SBR and the yield from the reaction was 22.7 g from 10 g of SBR.

These conditions were also used for dual grafting of both methyl thioglycolate and thioglycolic acid to SBR in an 80/20 ratio. The total grafting was determined to be 85.7% methyl thioglycolate and 14.3% thioglycolic acid and the overall grafting to SBR was 98.0%. This was matched by 99.4% the vinyl groups reacting. This product was referred to as 80/20 MG/TG-SBR and 23.4 g product was obtained from 10 g SBR. The ^1H NMR spectra are observed in Figure 8.4a for MG-SBR and 80/20 MG/TG-SBR. The ^1H NMR spectra for MG-SBR shows two new peaks at 3.7 ppm and 3.2 ppm ascribed to the CH_3 and CH_2 environment on the methyl thioglycolate ester, respectively. In addition, the presence of the three vinyl peaks between 5.5 ppm and 5.0 ppm disappeared due to the high grafting efficiency of the reaction. In 80/20 MG/TG-SBR, the CH_3 peak for the methyl thioglycolate ester was found at 3.7 ppm and the CH_2 peak for thioglycolic acid carboxylic acid and methyl thioglycolate ester was found at 3.2 ppm. Finally, the vinyl peaks are unobservable, further confirming the high grafting degree of the reaction.

The FTIR of SBR, MG-SBR and 80/20 MG/TG-SBR is shown in Figure 8.4b. The structure of SBR demonstrated the presence of vinyl groups though a weak C-H stretch at 3006 cm^{-1} and a series of peaks between 1634 cm^{-1} and 1540 cm^{-1} attributed to

various alkene stretches including the C=C alkene disubstituted (cis) stretch and C=C conjugated alkene stretch. Finally, two peaks at 958 cm^{-1} and 906 cm^{-1} were attributed to an out of plane CH_2 wag near a trans alkene and an out of plane CH_2 wag near a vinyl alkene respectively. In addition, the FTIR of SBR confirmed the presence of the aromatic styrene groups due to the C-H bending aromatic overtones in between $2400 - 1950\text{ cm}^{-1}$. Finally, an aromatic C-H stretch was observed at 3073 cm^{-1} and a C-H bend at 695 cm^{-1} from all five protons oscillating in the ring was observed.¹³ After the reaction for both MG-SBR and 80/20 MG/TG-SBR, the peaks associated with the vinyl groups disappeared. In their place, a C=O stretch appeared at 1730 cm^{-1} , an asymmetric C-O-C stretch at 1272 cm^{-1} and a symmetric C-O-C stretch at 1008 cm^{-1} . Finally, a very broad O-H stretch was observed between $3700 - 3300\text{ cm}^{-1}$ for 80/20 MG/TG-SBR due to the grafting of thioglycolic acid. Overall, ^1H NMR and FTIR confirmed the successful grafting of methyl thioglycolate and thioglycolic acid to SBR with a high grafting efficiency.

GPC in Figure 8.3b shows how the grafting reaction affected the M_n , M_w and \bar{D} of MG-SBR. In MG-SBR, the M_n increased to 170000 g mol^{-1} and the M_w increased to $1074541\text{ g mol}^{-1}$. In addition, the \bar{D} increased to 6.31. Unlike in SBS in Chapter 4 and 5, a lack of a low molecular weight tail indicates that a low degree of polymer chain scission took place. 80/20 MG/TG-SBR could not be investigated *via* GPC due to solubility issues arising from the grafting of the acid groups to the polymer backbone.

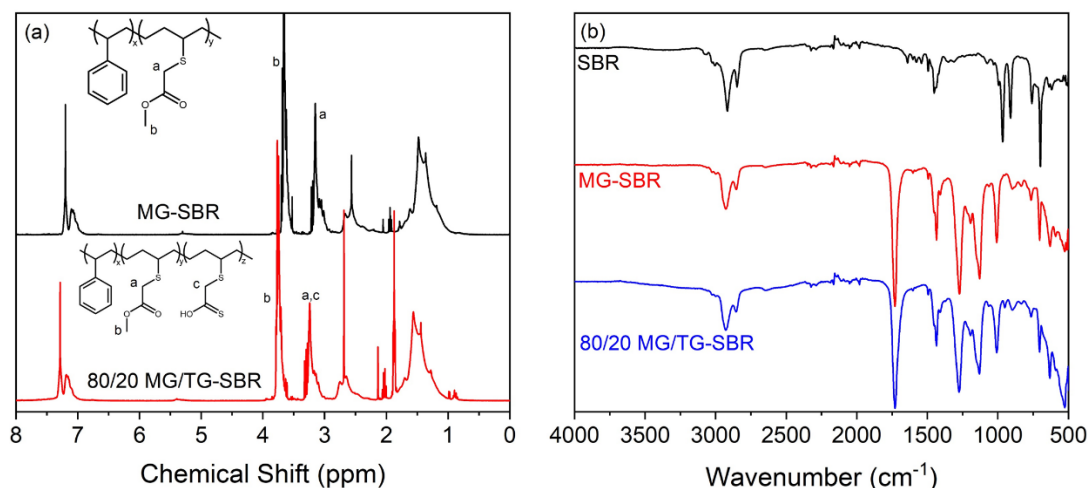


Figure 8.4 (a) Partially assigned ^1H NMR spectra of MG-SBR and 80/20 MG/TG-SBR and (b) FTIR spectra of SBR, MG-SBR and 80/20 MG/TG-SBR

8.2.2 Structural characterisation of MG-SBR and 80/20 MG/TG-SBR

The effect on the T_g from modification was observed in the $\tan \delta$ loss from DMTA for SBR, MG-SBR and 80/20 MG/TG-SBR and shown in Figure 8.5a. Prior to modification, a single T_g for SBR at -31.5°C was observed, unlike the observation of two T_g 's for SBS in the block copolymer form. This indicated that the SBR did not exhibit a phase separated structure due to the statistical configuration of styrene and butadiene on the polymer chain. After modification, MG-SBR exhibited a shift in the T_g to -5.9°C as a result of the increased compatibility and interchain interaction between the styrene and methyl thioglycolate butadiene groups. Furthermore, the T_g for 80/20 MG/TG-SBR was unaffected by the addition of hydrogen bonding into the elastomer and remained at -6.1°C . From 25°C onwards, the $\tan \delta$ loss increased steadily in SBR and MG-SBR, attributed to increased flexibility and transition towards melting as the temperature increased. However, the same increase in the $\tan \delta$ was not observed in 80/20 MG/TG-SBR. This was because the hydrogen bonding network behaved as reversible crosslinking, and inhibited the melting of the polymer. The small rise in the $\tan \delta$ for 80/20 MG/TG-SBR was attributed to the loosening of the polymer chains from overcoming the methyl thioglycolate/styrene electrostatic interaction. The loss modulus and storage modulus for these elastomers is found in Appendix Figure 24.

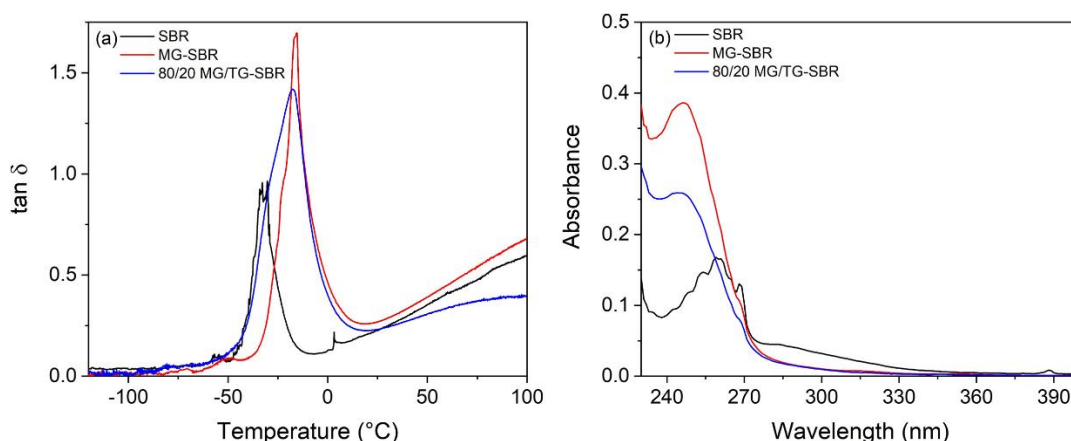


Figure 8.5 (a) DMTA $\tan \delta$ loss of SBR, MG-SBR and 80/20 MG/TG-SBR and (b) UV-Vis spectroscopy of SBR, MG-SBR and 80/20 MG/TG-SBR in DCM with the UV active range of the polymers shown

The behaviour of modified SBR elastomers was further characterised *via* solution state UV-Vis spectroscopy in Figure 8.5b. In SBR, a peak at 260 nm was attributed to the π - π^* transition for free styrene, whilst the broad peak between 270 – 330 nm was attributed to the π - π^* transition for π -stacking styrene. The π - π stacking styrene peak was broad and low in intensity due to the solution state disrupting the π -stacking. After modification, both MG-SBR and 80/20 MG/TG-SBR exhibited only one blue shifted transition to 246 nm, ascribed to the π - π^* transition for styrene in the elastomers. The blue shift was similar in degree to the observed blue shifts of MG-SBS and 80/20 MG/TG-SBS and thus was attributed to the increase in the transition energy for electron promotion within the π - π^* band due to the electrostatic methyl thioglycolate/styrene interaction removing delocalised aromatic electron density away from the styrene ring. This increased the energy required to promote a remaining aromatic electron in the delocalised aromatic system.^{14, 15}

8.2.3 Electromechanical properties of SBR elastomers

The mechanical stress strain curves of SBR, MG-SBR and 80/20 MG/TG-SBR show how the grafting affected the mechanical properties of the elastomers. From Figure 8.6, SBR had a low strain at break of $226 \pm 10\%$, a low tensile strength of 0.30 ± 0.02 MPa and a Young's modulus of 4.0 ± 0.8 MPa. However, after modification, the tensile strength and Young's modulus of MG-SBR decreased to 0.14 ± 0.02 MPa and 1.91 ± 0.4 MPa respectively. This was attributed to the grafted group inhibiting polymer chain entanglement, making the elastomer more 'gel-like.' This was further confirmed by the large increase in the strain at break to $1623 \pm 192\%$. In addition to the 'gel-like' nature, based on DMTA and UV-Vis spectroscopy it is feasible that the methyl thioglycolate/styrene interaction present also contributes to the increase in the strain at break. After the introduction of a hydrogen bonding network, the strain at break decreased compared to MG-SBR but was still enhanced compared to pristine SBR and 80/20 MG/TG-SBR failed at $598 \pm 40\%$. This was directly attributed to the hydrogen bonding network present, which behaved like dynamic crosslinking at room temperature and restricted the polymer chains, increasing the brittleness of the dielectric elastomer. The polymer chain restriction was observed in the large increase in the tensile strength for the elastomer to 0.78 ± 0.17 MPa and an increased Young's modulus of 2.9 ± 0.3 MPa.

Impedance spectroscopy for SBR elastomers demonstrated how the grafting of the polar groups enhanced their electrical properties. From Figure 8.7a, the relative permittivity of SBR was 3.4 at 10^3 Hz. After introduction of methyl thioglycolate to the polymer backbone, the relative permittivity increased to 12.6 at 10^3 Hz. Beyond 10^3 Hz, the relative permittivity of MG-SBR decreased rapidly due to atomic polarisation. Comparatively, the relative permittivity for 80/20 MG/TG-SBR increased slightly to 13.9 at 10^3 Hz and also exhibited atomic polarisation beyond 10^3 Hz, albeit delayed by approximately a further 4 kHz. Finally, there is an increase in the relative permittivity below 10^2 Hz due to electrode polarisation and the trapping of electrons at the electrode interface.

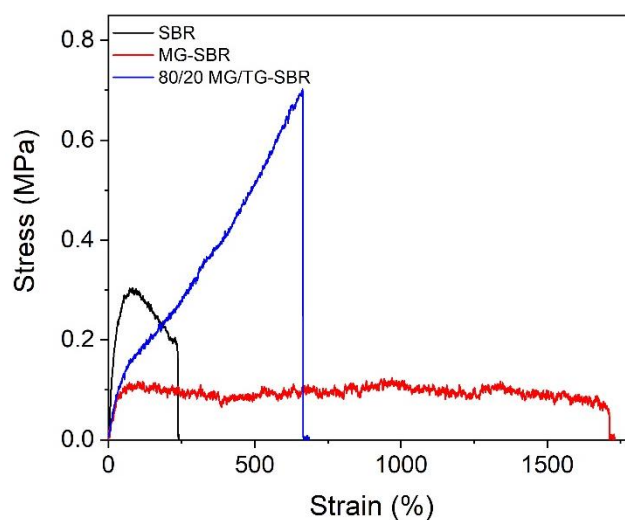


Figure 8.6 Stress strain curves of SBR, MG-SBR and 80/20 MG/TG-SBR

The $\tan \delta$ loss of SBR was low, 0.017 at 10^3 Hz as shown in Figure 8.7b. However, an atomic polarisation peak was observed and further highlighted in Appendix Figure 25. The atomic polarisation peak appeared at 126 kHz, although it began at 10 kHz. This was due to the SBR polymer chains unable to respond to the alternating electric field. A higher $\tan \delta$ loss was observed in MG-SBS with $\tan \delta \sim 0.29$ at 10^3 Hz. The higher $\tan \delta$ loss was due to the tail of the atomic polarisation peak extending beyond 10^3 Hz. In fact, from Appendix Figure 25 the atomic polarisation peak began at 300 Hz and reached its maxima at 18 kHz. The MG-SBR polymer chains stopped responding to the electric field at a much lower frequency than SBR, attributed to the increased size of the polymer chain hindering its ability to respond.¹⁶ Thus the $\tan \delta$ loss reached a plateau in the frequency region of 30 – 300 Hz, where the $\tan \delta$ loss was 0.06. Finally,

in 80/20 MG/TG-SBR a high $\tan \delta$ loss is also reported of 0.24 at 10^3 Hz. However, 80/20 MG/TG-SBR appeared to display overlapping electronic polarisation and atomic polarisation. Thus a broad atomic polarisation peak exhibited a maxima at 34 kHz, and electronic polarisation was observed from below 800 Hz.

The AC conductivity of the SBR elastomers was similar between 50 kHz and 1 MHz, however, at lower frequencies the curves diverge. The AC conductivity for SBR decreased to 1×10^{-13} S m⁻¹ at 1 Hz and exhibited a highly frequency dependent response. Comparatively, MG-SBR exhibited a largely frequency independent response below 10^2 Hz and exhibited an AC conductivity of 2×10^{-9} S m⁻¹. The increased conductivity was attributed to the grafting of the polar groups to the polymer backbone. For 80/20 MG/TG-SBR, a frequency independent response was exhibited from below 10^3 Hz and the shift in position of the frequency independent range was attributed to the electrode polarisation observed during electrical testing.

Finally, the phase angle of the SBR elastomers is shown in Figure 8.7d. The phase angle of SBR was -90° up until 10^3 Hz. At higher frequencies, a deviation from -90° was realised through the atomic relaxation peak, which had a maxima matching SBR at 126 kHz. In MG-SBR, at less than 10^2 Hz a deviation away from -90° was observed attributed to electrode polarisation, and agreed well with the increase in $\tan \delta$ for MG-SBR at low frequencies as well. Additionally, the summit of the atomic polarisation peak in the phase angle matched the $\tan \delta$ loss at 18 kHz. Only the frequency range between 100 Hz – 300 Hz showed a fully insulating response. For 80/20 MG/TG-SBR, no frequency exhibited a fully insulating response due to electrode polarisation and atomic polarisation overlapping. The maxima of the atomic polarisation peak also matched the $\tan \delta$ loss maxima at 34 kHz.

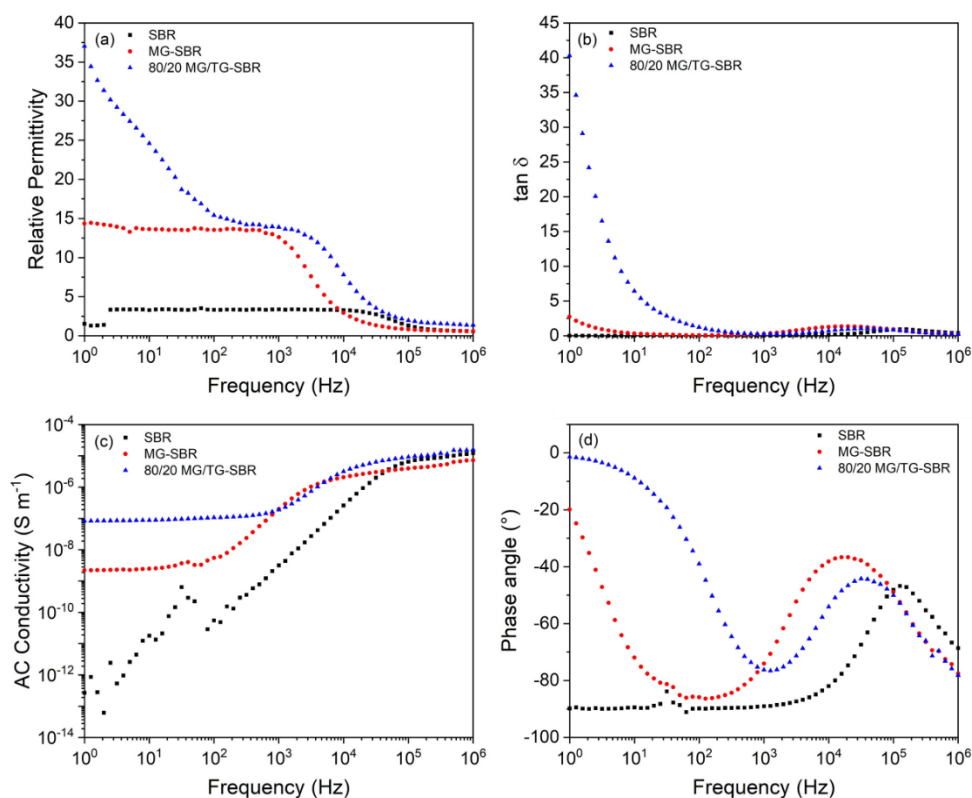


Figure 8.7 Impedance spectroscopy for SBR, MG-SBR and 80/20 MG/TG-SBR showing (a) relative permittivity, (b) $\tan \delta$, (c) AC conductivity and (d) phase angle

8.3 The grafting of polar groups to polybutadiene (PB)

8.3.1 Grafting of methyl thioglycolate and thioglycolic acid to polybutadiene

For the grafting of methyl thioglycolate to polybutadiene, ^1H NMR of pristine polybutadiene (PB) in Figure 8.8a showed two peaks at 5.4 ppm and 2.1 ppm attributed to the vinyl groups and alkyl groups of PB respectively. The vinyl group environment contained two protons and the alkyl group environment had four protons, and thus the expected integration ratio between these peaks was expected to be 1:2 respectively. From Figure 8.8a, the integration ratio between the vinyl and alkyl is 1:2, thus the polymer chain was fully unsaturated.

Therefore, the concentration of vinyl groups within 1 g of PB, and thiol excesses for the grafting reaction was determined theoretically from equation 4.3 and 1 g PB contained 1.8×10^{-2} mol of vinyl groups.

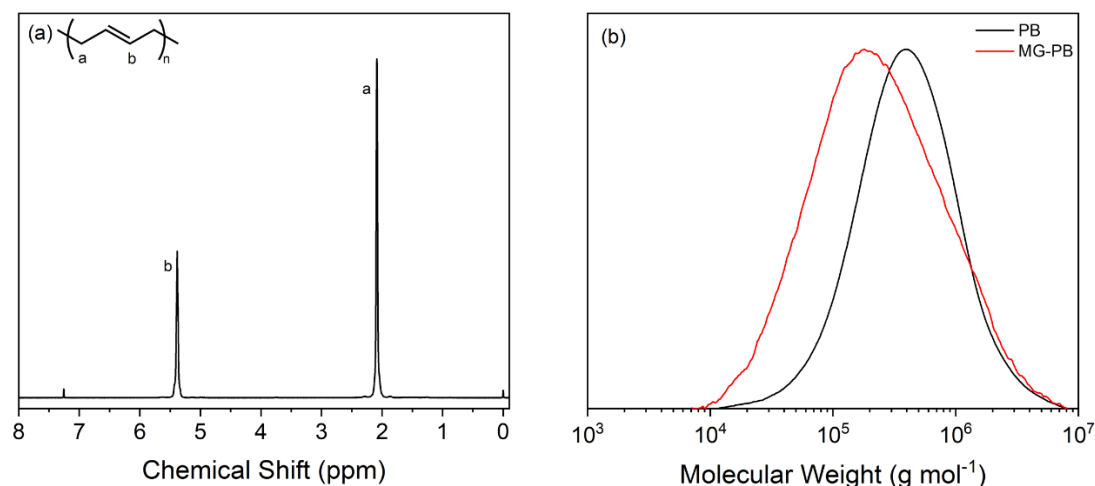


Figure 8.8 (a) ¹H NMR spectrum at 400 MHz in CDCl₃ of PB with assigned peaks and (b) GPC trace of the molecular weight of PB and MG-PB in THF with a Refractive Index detector

To further investigate the nature of the polymer chains of PB, the GPC of PB is shown in Figure 8.8b. The curve of PB was broad, showing the presence of both high and low molecular weight chains. The Đ of PB reflected this and was 2.4. Compared to SBS and SBR, PB had significantly longer polymer chains and the M_n was 248000 g mol⁻¹ whilst the M_w was 604000 g mol⁻¹.

Therefore, the initial grafting of methyl thioglycolate to PB to synthesise MG-PB followed the optimised conditions for the synthesis of MG-SBS. However, due to the high molecular weight chains, the PB solution became viscous and saturated during the reaction under a 9:1 solvent:polymer weight ratio. Therefore, the thiol excess was increased from 4× to 5× excess of methyl thioglycolate to reduce any increase in viscosity from interchain crosslinking during the reaction. However, the increased thiol excess caused PB to precipitate as the solvent ratio was too low to maintain PB solubility. Therefore, the thiol ratio was maintained at 5× excess and the solvent ratio was increased to 20:1. The solution during the reaction maintained a low viscosity and remained free flowing. After the reaction, a white sticky polymer was obtained. From this reaction, 1 g starting PB resulted in 2.3 g of MG-PB. However, only 87% methyl thioglycolate grafting was obtained as the reaction did not go to completion. Therefore, the concentration of photoinitiator was increased from 0.42 mol% to 0.84 mol% however the solution gelled during the reaction due to increased interchain crosslinking. Thus, the methyl thioglycolate ratio was also increased to 6× excess and

a solid white product was obtained with a yield of 2.5 g of MG-PB. ^1H NMR confirmed that the grafting of methyl thioglycolate was 99.4%. The production of MG-PB was successfully scaled up to 10 g of PB and resulted in 19.4 g of MG-PB obtained with a grafting of 99.5% of methyl thioglycolate. The ^1H NMR of MG-PB is shown in Figure 8.9a.

The addition of a hydrogen bonding network to PB was realised through grafting of both methyl thioglycolate and thioglycolic acid. The synthesis of 80/20 MG/TG-PB utilised the same conditions for the synthesis of MG-PB. However, during the purification step hexane would not precipitate the modified elastomer due to the change in the polarity of 80/20 MG/TG-PB elastomer and thus it was precipitated in methanol. When scaled up to 10 g starting PB, 80/20 MG/TG-PB could not be precipitated in methanol and water was used for purification. The resulting polymer was 20.2 g and from ^1H NMR in Figure 8.9a, the overall grafting of 80/20 MG/TG-PB was 99.2% with 88% methyl thioglycolate and 12% thioglycolic acid grafting.

From Figure 8.8a and Figure 8.9a, the alkene peak of PB at 5.4 ppm disappeared after the reaction and in Figure 8.9a, three new peaks appeared at 3.7 ppm, 3.2 ppm and 2.8 ppm, attributed to the CH_3 of methyl thioglycolate, CH_2 of methyl thioglycolate and thioglycolic acid and polymer backbone CH for the carbon which covalently bonded with the thiols respectively. In addition to this, the FTIR of MG-PB and 80/20 MG/TG-PB in Figure 8.9b showed that the C-H vinyl stretch in PB at 3000 cm^{-1} disappeared after the reaction. After the reaction, in MG-PB and 80/20 MG/TG-PB a C=O stretch appeared at 1724 cm^{-1} and asymmetric and symmetric C-O-C stretches were observed at 1263 cm^{-1} and 1004 cm^{-1} respectively. Furthermore, a broad O-H stretch was observed in 80/20 MG/TG-PB from $3100 - 3600\text{ cm}^{-1}$. The broadness of the peak was attributed to free OH groups on thioglycolic acid between $3400 - 3600\text{ cm}^{-1}$, and the hydrogen bonding network between $3100 - 3400\text{ cm}^{-1}$. Therefore, FTIR and ^1H NMR confirmed the successful grafting of methyl thioglycolic and thioglycolic acid to PB. Finally, GPC of MG-PB shows how the M_n , M_w and \bar{D} were affected by the grafting reaction. The M_n and M_w both decreased to 120000 and 464000 respectively, whilst the \bar{D} increased to 3.86. This indicates that polymer chain scission took place along the polybutadiene

chain, similar to the observations in MG-SBS and M3M-SBS in Chapter 4 and 5.

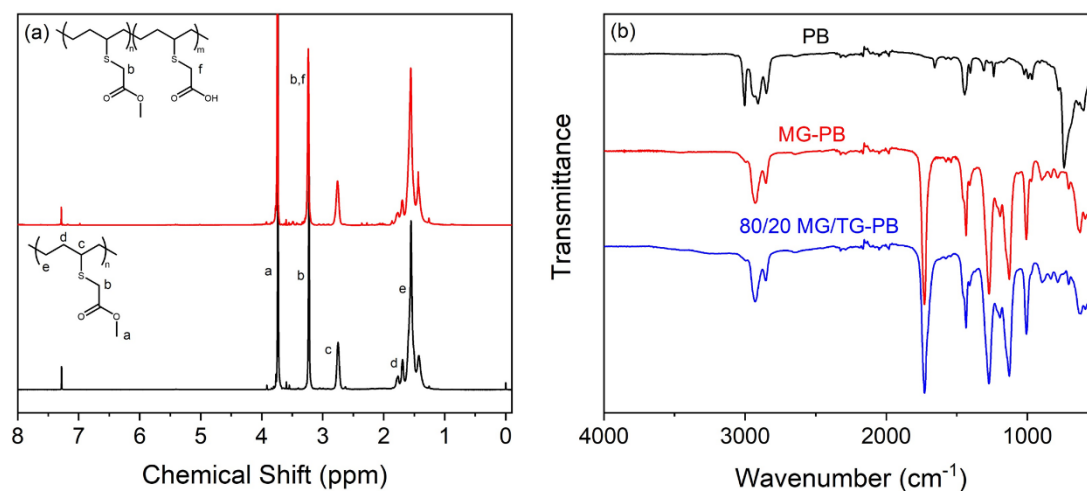


Figure 8.9 (a) Assigned ^1H NMR spectra of MG-PB and 80/20 MG/TG-PB and (b) FTIR spectra of PB, MG-PB and 80/20 MG/TG-PB

8.3.2 Structural characterisation of MG-PB and 80/20 MG/TG-PB

The structure of MG-PB and 80/20 MG/TG-PB was investigated through DMTA and UV-Vis spectroscopy in Figures 8.10a and 8.10b respectively. DMTA revealed that the T_g for butadiene shifted from $-83\text{ }^\circ\text{C}$, Figure 4.9, shifted to $-24\text{ }^\circ\text{C}$ after modification with methyl thioglycolate. The broadness of the peak was attributed to the high dispersity of PB prior to the reaction, thus the different polymer chain lengths exhibited a slightly different T_g . After modification with both methyl thioglycolate and thioglycolic acid, the T_g shifted further to $-15\text{ }^\circ\text{C}$ due to the incorporation of the hydrogen bonding network. However, there was also a small shoulder peak remaining at $-22\text{ }^\circ\text{C}$, attributed to regions of high methyl thioglycolate modification on the polybutadiene chains. Finally, the storage modulus and loss modulus are seen in Appendix Figure 26 and show a decrease in the storage modulus by three orders of magnitude and a decrease of two orders of magnitude for the loss modulus in the temperature range of $-120\text{ }^\circ\text{C} - 60\text{ }^\circ\text{C}$.

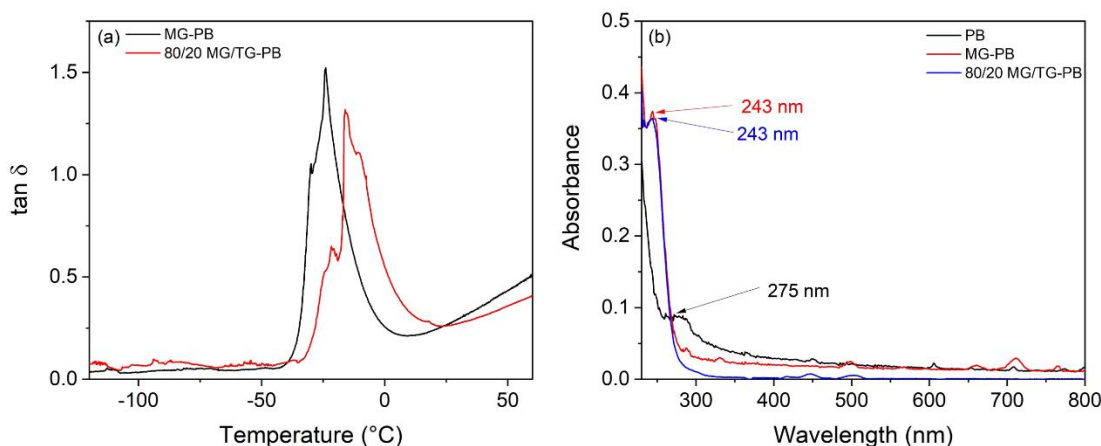


Figure 8.10 (a) DMTA $\tan \delta$ graphs for MG-PB and 80/20 MG/TG-PB and (b) UV-Vis spectra of PB, MG-PB and 80/20 MG/TG-PB

From the UV-Vis spectra, Figure 8.10b, a small peak was observed at 275 nm for PB which was associated with the a transition from the conjugated vinyl groups.¹⁷ Additionally, identical peaks for MG-PB and 80/20 MG/TG-PB were observed at 243 nm. This was three nm lower than observed in MG-SBR, and four nm lower than MG-SBS. Thus methyl thioglycolate is UV-active, and the lower promotion wavelength was because more energy is required to promote an electron in methyl thioglycolate when it is not interacting with styrene. Therefore this demonstrates that in MG-SBR and MG-SBS, methyl thioglycolate received electron density from styrene, thus making electron promotion easier, and red shifting the promotion of an electron in methyl thioglycolate.

8.3.3 Electromechanical properties of PB elastomers

Stress strain curves of PB, MG-PB and 80/20 MG/TG-PB are shown in Figure 8.11. PB exhibited a high strain at break of $2442 \pm 333\%$, a low tensile strength of 0.15 ± 0.04 MPa and a Young's modulus of 1.5 ± 0.2 MPa. A slight increase in the observed tensile strength between 1000% and 2442% was attributed to the crystallisation of the polymer chains under strain. By grafting methyl thioglycolate to PB, MG-PB had a slightly lower tensile strength and Young's modulus of 0.12 ± 0.01 MPa and 1.1 ± 0.3 MPa respectively and a decreased strain at break of $522 \pm 85\%$. The weakening of the mechanical properties was due to the bulky polar group inhibiting chain entanglement of the PB chains. MG-PB was also very weak due to a lack of 'hard' block in the polymer structure, unlike in SBS. Finally, 80/20 MG/TG-PB showed that a hydrogen

bonding network provided reinforcement of the polymer chains by increasing the Young's modulus and tensile strength to 2.3 ± 0.4 MPa and 0.27 ± 0.03 MPa respectively. In addition, the hydrogen bonding network prevented mechanical failure by increasing the interchain interactions and increased the strain at break compared to MG-PB to $1263 \pm 122\%$.

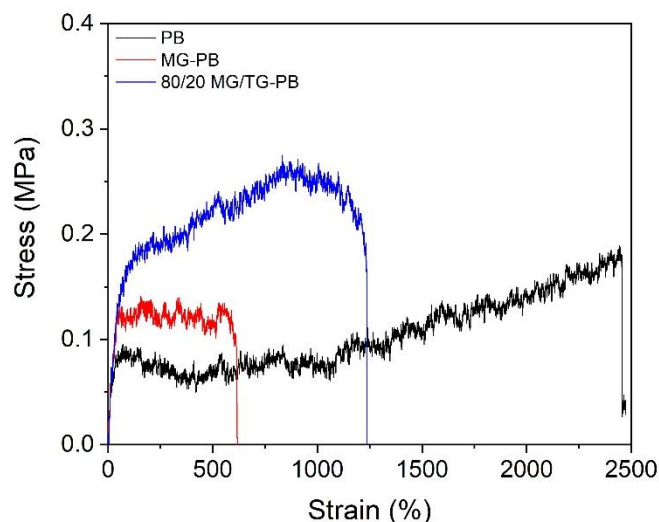


Figure 8.11 Stress strain curve of PB, MG-PB and 80/20 MG/TG-PB

The relative permittivity of MG-PB showed a significant enhancement compared to PB. Before modification, PB exhibited a relative permittivity of 3.3 at 10^3 Hz, as shown in Figure 8.12a, however this increased for MG-PB to 12.3 from the increased polarity of the PB backbone. At frequencies between 10^5 Hz and 10^6 Hz, the relative permittivity for PB dropped from 3.7 to 3.0, due to the beginning of an atomic polarisation response from the long PB chains unable to respond to the high frequency alternating field. For MG-PB, a decrease in the relative permittivity due to atomic polarisation began at approximately 20 kHz, due to the bulky side groups inhibiting the polymer chains from responding to the electric field. 80/20 MG/TG-PB had a similar relative permittivity to MG-PB at 10^3 Hz, however its response across all other frequencies of electric field was different. Atomic polarisation in 80/20 MG/TG-PB was present from 2 kHz and was represented by a decrease in the relative permittivity. Atomic polarisation occurred at a lower frequency due to the additional hydrogen bonding network inhibiting the polymer chain response further at room temperature. Finally, 80/20 MG/TG-PB showed a small increase in the relative permittivity at frequencies lower than 10^2 Hz, associated with electrode polarisation.

The $\tan \delta$ loss for PB was low, 0.009 at 10^3 and frequency independent. For MG/TG-PB, the $\tan \delta$ loss remained low at 10^3 Hz at 0.02. At high frequencies, atomic polarisation in MG-PB had a maxima at 147 kHz, whilst electronic polarisation was observed below 10 Hz. For 80/20 MG/TG-PB, the $\tan \delta$ loss was higher than for PB and MG-PB at 10^3 Hz and was 0.36. Additionally, the maxima for the atomic polarisation peak was at 12 kHz and electronic polarisation was observed for frequencies below 10^2 Hz.

The AC conductivity and phase angle in Figure 8.12c-d for all three elastomers showed they are all insulating. PB exhibited an AC conductivity of 3×10^{-12} S m⁻¹ at 1 Hz, whilst MG-PB and 80/20 MG/TG-PB showed higher conductivities of 3×10^{-9} Hz and 5×10^{-8} Hz respectively. PB showed a frequency dependent response across all frequencies indicating that PB had a much lower DC conductivity. For MG-PB and 80/20 MG/TG-PB, the AC conductivity response plateaus and became frequency independent at 10^2 Hz from electronic polarisation. PB and MG-PB exhibited an insulating response with a phase angle of -90° at 10^3 Hz. However, the phase angle deviated from -90° for MG-PB at 10^2 Hz due to the increase in conductivity from electronic polarisation. In addition, the atomic polarisation peak in MG-PB agreed well with the maxima from the $\tan \delta$ loss. Finally, 80/20 MG/TG-PB never displayed a truly insulating phase angle response. This was also due to electronic polarisation and atomic polarisation overlapping to a small degree and thus the phase angle at 10^3 Hz was -70° . The atomic polarisation peak maxima for the phase angle agreed well with the $\tan \delta$ loss additionally.

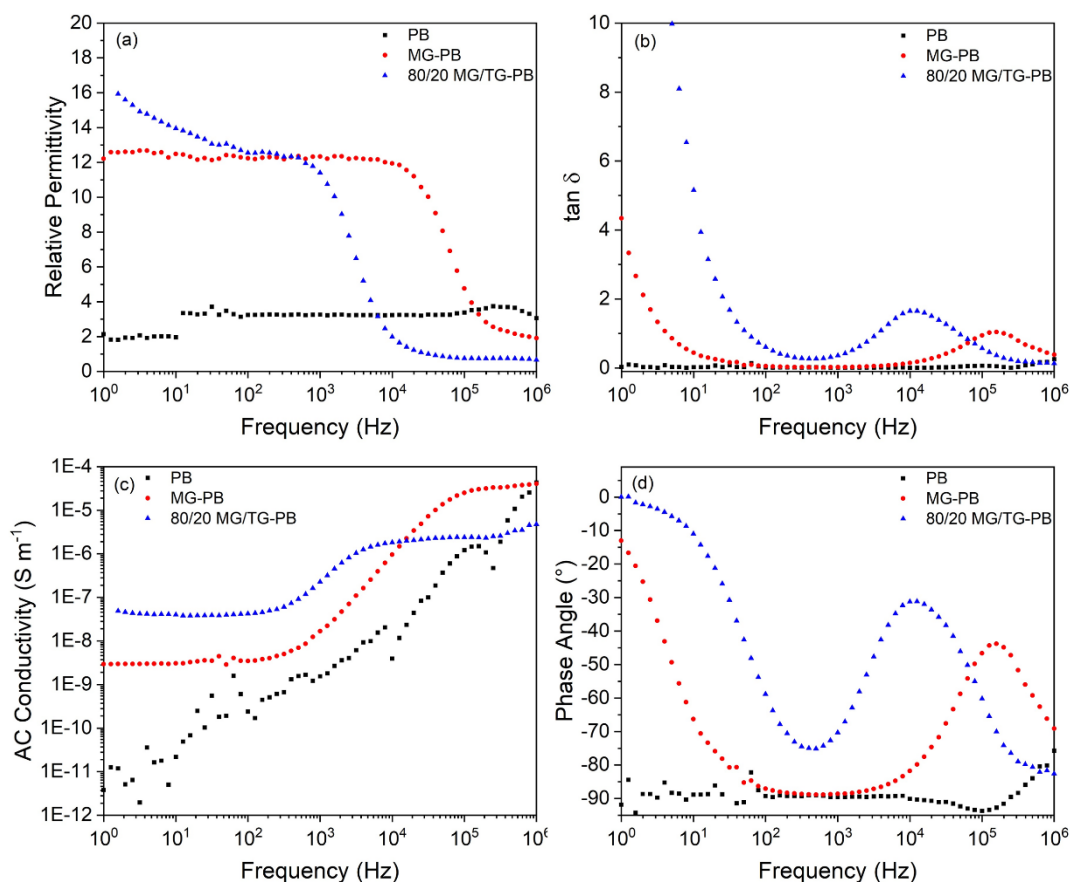


Figure 8.12 Impedance spectroscopy for PB, MG-PB and 80/20 MG/TG-PB with (a) relative permittivity, (b) $\tan \delta$ loss, (c) AC conductivity and (d) phase angle

8.4 Intrinsic modification of SBS and PB with conducting groups

8.4.1 The synthesis of emeraldine base tetraaniline

Polyaniline (PANI) is normally synthesised through oxidative polymerisation, yielding a long polymer chain.¹¹ However, an oxidative coupling reaction using *N*-phenyl-*p*-phenylenediamine is used to synthesise an oligomeric form of PANI, consisting of four aniline units called tetraaniline (TANI).^{18, 19} The initial synthesis of TANI followed the synthesis from Zhao *et al.*²⁰ and resulted in the formation a dark blue powder, indicating the emeraldine base oxidation state, and contained two products. As seen from Figure 8.13a, the GPC for TANI formed from a 2 hour reaction showed a major peak and a broad peak at a higher molecular weight. GPC indicated that there were two products formed, the major product attributed to tetraaniline and the secondary, broad peak attributed to higher molecular weight oligomers such as

octaaniline. However, due to the similarity in solubility arising from the similarity in structure, higher molecular weight oligomers cannot be separated from TANI. Therefore, the reaction time for the synthesis of TANI was decreased from two hours to 1.5 hours to reduce the possibility for higher molecular weight oligomer formation. As seen from Figure 8.13a, the reduction of the reaction time increased the major TANI peak and the degree of higher molecular weight oligomers synthesised decreased. The M_n , M_w and \bar{D} of both syntheses of TANI are shown in Appendix Table 4. The \bar{D} of TANI decreased from 2.05 to 1.58 by reducing the reaction time. Thus TANI reacted for 90 minutes was used for the subsequent grafting reactions.

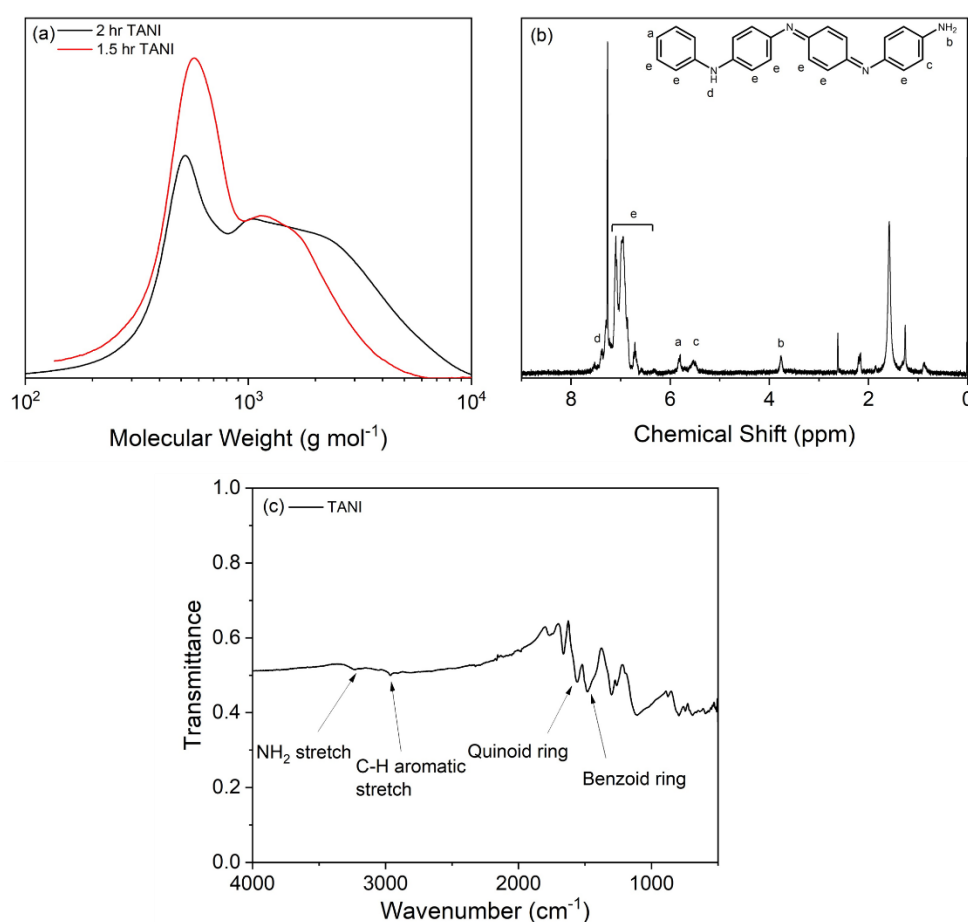


Figure 8.13 (a) GPC trace of TANI with a two hour reaction time and a 1.5 hour reaction time (b) assigned ¹H NMR spectrum of TANI and (c) FTIR spectrum of TANI with key peaks are highlighted

TANI was further characterised *via* ¹H NMR, shown in Figure 8.13b. The ¹H NMR spectrum showed that aromatic protons are found at 7.1 ppm, 7.0 ppm, 5.8 ppm and 5.5 ppm. In addition, a downfield proton attached to a nitrogen between aromatic rings

appeared at 7.4 ppm, and the proton attached to the amine at the terminus of the oligomer appeared at 3.8 ppm.²¹ Thus, ¹H NMR indicated the correct structure for TANI.^{20,22} FTIR of synthesised TANI is shown in Figure 8.13c and demonstrated that an NH₂ stretch and a C-H stretch from aromatic rings are present. Also, the stretches associated with the quinoid and benzoid rings in TANI are present in FTIR at 1558 cm⁻¹ and 1480 cm⁻¹ respectively.²³⁻²⁵ Therefore, the structure of TANI is confirmed and it was successfully synthesised.

In the literature, acidification of TANI to the emeraldine salt state using HCl results in a nanowire morphology.²⁶ However, as seen from the SEM image in Appendix Figure 27, the morphology of TANI *via* our synthesis method resulted in an agglomerated form. The lack of defined morphology was attributed to the large counter ion size of trifluoroacetic acid disrupting the structure formed. However, trifluoroacetic was used as both it and TANI-SBS were soluble in THF.

8.4.2 Grafting of TANI to unsaturated backbones

In order to graft TANI to the unsaturated backbones of SBS and PB, a two step-grafting reaction was utilised. The first step formed an epoxide ring through oxidation of the vinyl groups of both SBS and PB to synthesise E-SBS and E-PB. However, both E-SBS and E-PB could only be precipitated using methanol, which slowly ring opens epoxide rings under room temperature conditions. In addition, the epoxide rings slowly ring opened and form covalent interchain crosslinking over a several day period, rendering an insoluble product. Therefore, to remove as much methanol as possible without ring opening occurring, E-SBS and E-PB were allowed to dry for two hours under air before reacting with TANI. ¹H NMR of E-SBS and E-PB are shown in Figure 8.14 and ¹³C NMR and HSQC for E-SBS are shown in Appendix Figure 28 and 29. After the epoxidation reaction, two small peaks associated with inequivalent protons attached to the two carbons in the epoxide ring appeared in the ¹H NMR of E-SBS at 2.96 ppm and 2.72 ppm. In ¹³C NMR, two small peaks at 56.9 ppm and 58.6 ppm appeared, in the expected region for carbons in an epoxide ring. Through HSQC, resonance peaks indicated that these hydrogens were attached to the carbons on the epoxide rings. The peak in ¹H NMR at 3.52 ppm was attributed to residual methanol,²⁷ and also appeared at 50.8 ppm in ¹³C NMR and the resonance peak between these peaks was observed in HSQC in Appendix Figure 29. For PB, the epoxide peak

appeared as a single overlapped peak for the two protons at 2.95 ppm. Overall, three versions of E-SBS were synthesised with different levels of epoxidation on the polymer backbone. These were 25 mol% E-SBS, 35 mol% E-SBS and 50 mol% E-SBS. For PB, the epoxidation on the polymer backbone consisted of 1 mol% E-PB, 25 mol% E-PB, 35 mol% E-PB and 50 mol% E-PB.

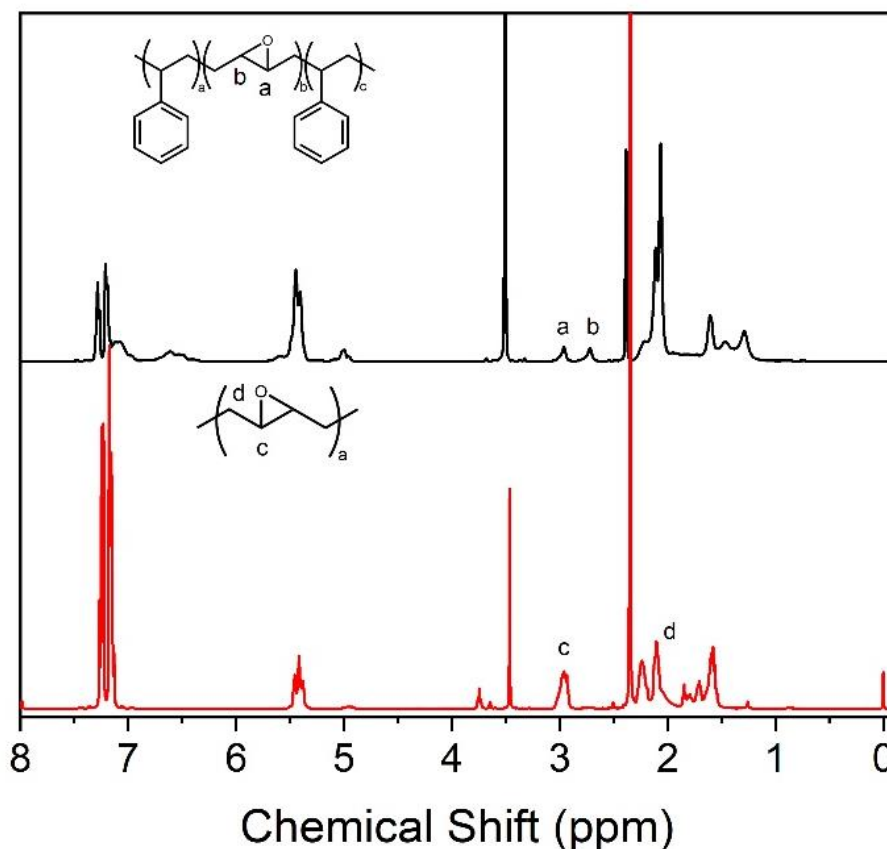


Figure 8.14 Assigned ¹H NMR spectra at 400 MHz in CDCl₃ of E-SBS and E-PB

The grafting of TANI through ring opening of the epoxide rings was successfully confirmed using ¹H NMR and FTIR, Figure 8.15 and ¹³C NMR, HSQC and HMBC in Appendix Figure 30 – 32 respectively. After the reaction, TANI-SBS had one epoxide peak at 2.7 ppm, attributed to the newly formed hydroxyl group from the opened epoxide peak. The other peak shifted downfield to 4.4 ppm as the carbon was attached to an electronegative nitrogen atom from TANI. HSQC showed that these two protons were attached to carbons at 59 ppm and 68 ppm respectively. The peak at 59 ppm was seen clearly in the ¹³C NMR and the peak at 68 ppm was observable marginally above the background noise. The undefined broad peaks in the region of 3 – 4 ppm were attributed to methanol grafting side reactions. Finally HMBC showed that the proton

attached to the hydroxyl carbon from the epoxide ring had a strong resonance association with an alkyl group and a weak resonance with the adjacent carbon covalently bound to TANI.

FTIR provided additional confirmation of the grafting of TANI to SBS. After the reaction, a broad OH stretch appeared in TANI-SBS between $3300 - 3600 \text{ cm}^{-1}$, indicating that the ring opening reaction had taken place. In addition, a strong C-N stretch appeared at 1783 cm^{-1} indicating that the grafting reaction had taken place between the polymer backbone and TANI. Furthermore the benzoid and quinoid ring from TANI were observed at 1494 cm^{-1} and 1577 cm^{-1} respectively. Thus the successful grafting of TANI to SBS was confirmed.

For the grafting of TANI to PB, a doublet was observed at 3.0 ppm attributed to the ring opened epoxide ring. Furthermore, a peak at 4.4 ppm was also observed attributed with the grafting of TANI to PB. Thus the ^1H NMR of TANI-PB is similar to the ^1H NMR of TANI-SBS. In addition, the FTIR of TANI-PB showed that an NH stretch present at 3242 cm^{-1} attributed to a secondary amine. In addition, the C-N stretch, quinoid ring and benzoid ring were found at 1776 cm^{-1} , 1565 cm^{-1} and 1498 cm^{-1} respectively. Therefore, the grafting of TANI to PB was also successfully confirmed.

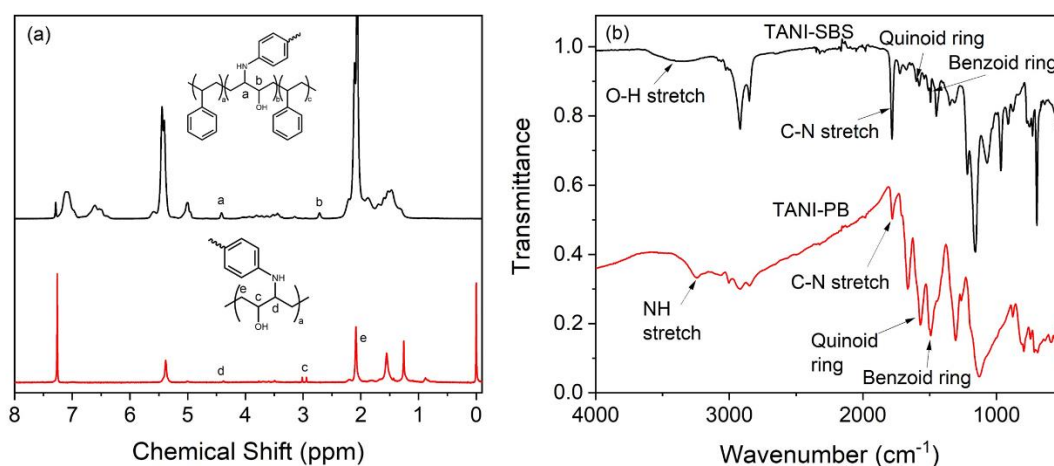


Figure 8.15 (a) Assigned ^1H NMR for TANI-SBS and TANI-PB and (b) FTIR of TANI-SBS and TANI-PB with key peaks highlighted

After the reaction, grafted TANI was acidified using trifluoroacetic acid to convert it to the conductive emeraldine salt oxidation state, to enhance the electrical properties of the elastomers. However, the effect on the physical properties from the introduction of TANI was also noticeable. The morphology of 25 mol%, 35 mol% and 50 mol%

TANI-SBS and 25 mol% and 50 mol% TANI-PB was visualised through SEM imaging in Figure 8.16. As seen between Figures 8.16a-c, a phase morphology change took place as more TANI was grafted. After grafting of 25 mol% TANI to SBS, a phase separated structure was observed between the butadiene block and styrene block. Due to the low grafting of TANI, the butadiene chain retained control over the properties of the butadiene block. Upon increasing the grafting to 35 mol% TANI, a compatibilised phase morphology was observed and phase separation was not clearly observable. This is because the increase in TANI groups enabled the compatibilisation of the butadiene and styrene block through π - π stacking. Furthermore, increasing the TANI grafting to 50 mol% resulted in a phase separated morphology observed once more. This is attributed to TANI dominating butadiene block and styrene block regions.

For TANI-PB, grafting of 25 mol% TANI and 50 mol% TANI yielded a phase separated structure between TANI and butadiene in Figure 8.16d-e. This was due to the TANI groups and butadiene being incompatible with each other, resulting in a TANI/butadiene phase separated structure.²⁸

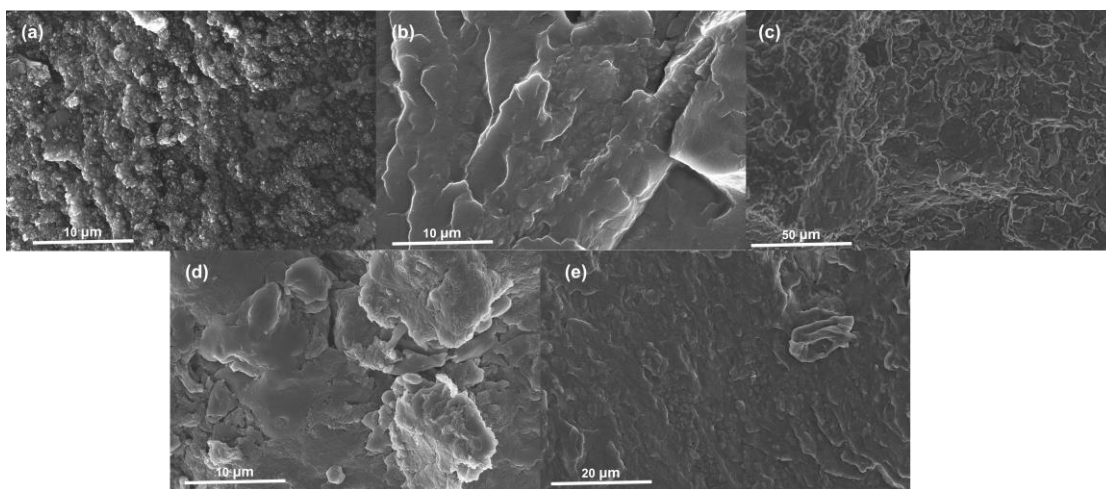


Figure 8.16 SEM imaging of (a) 25 mol% TANI-SBS, (b) 35 mol% TANI-SBS, (c) 50 mol% TANI-SBS, (d) 25 mol% TANI-PB and (e) 50 mol% TANI-PB

To further understand the observations from the SEM imaging, DMTA of 25 mol%, 35 mol% and 50 mol% TANI-SBS and 50 mol% TANI-PB were investigated to determine the T_g 's of polymer phases in Figure 8.17 and Appendix Figure 33. After modification with 25 mol% TANI, three glass transition temperatures were observed, one more than SBS. The T_g at -52 °C was attributed to the partially modified butadiene

backbone, with the TANI groups increasing the temperature of this transition. A small T_g at $-15\text{ }^\circ\text{C}$ was observed associated with TANI domains and a final T_g at $76\text{ }^\circ\text{C}$ was attributed to the styrenic block. This agrees well with the phase separated TANI-SBS morphology observed for 25 mol% grafting.

For 35 mol% TANI-SBS, two distinct T_g 's were observed, attributed to the TANI dominating butadiene backbone at $-1\text{ }^\circ\text{C}$ and $88\text{ }^\circ\text{C}$ for the styrene block of SBS. The decrease in the number of T_g 's was due to TANI groups controlling the properties of the butadiene block. Finally, for 50 mol% TANI-SBS, only two T_g 's are observable. These occur at $46\text{ }^\circ\text{C}$ and $88\text{ }^\circ\text{C}$, indicating that this material was in a glassy state at room temperature.

For 50 mol% TANI-PB, shown in Appendix Figure 33, there were two T_g 's observed at $-39\text{ }^\circ\text{C}$ and a broad plateau peak which began at $40 - 60\text{ }^\circ\text{C}$. The peak at $-39\text{ }^\circ\text{C}$ was attributed to the polybutadiene chain and the broad increase transition was due to the TANI groups. However, as there were two T_g temperatures it indicated that there was a lack of compatibility between the two regions and indicated why a phase separated structure exists for TANI-PB from the SEM images.

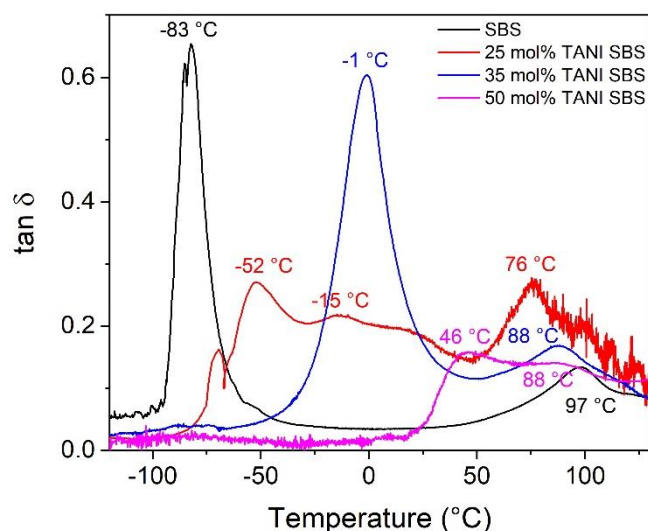


Figure 8.17 DMTA $\tan \delta$ for SBS, 25 mol% TANI-SBS, 35 mol% TANI-SBS and 50 mol% TANI-SBS

Further characterisation of the structure of TANI-SBS and TANI-PB was performed using UV-Vis spectroscopy. The solution state UV-Vis spectrum of TANI in the emeraldine salt form is observed in Appendix Figure 34. Three peaks appeared at 299

nm, 416 nm and 600-800 nm. These were attributed to the π - π^* benzoid ring transition in TANI, the polaron transition from the quinoid ring from emeraldine salt form TANI and the bipolaron (exciton) transition also located on the quinoid ring respectively.^{29, 30}

After grafting 25 mol% TANI to SBS, the benzoid and polar transitions transition red shifted to a high wavelength, requiring less energy to promote an electron as shown in Figure 8.18. This suggested that π - π stacking took place solely between TANI groups, creating an electron rich environment. Additionally, the bipolaron transition disappeared and was replaced by sharp peaks further demonstrating that the quinoid ring was involved in the TANI π - π stacking,

Upon increasing the grafting level to 35 mol% TANI in SBS, the bipolaron and π - π benzoid transition blue shifted to a lower wavelength of 550 – 700 nm and 291 nm, respectively. However, the polaron transition remained unaffected. The π - π^* styrenic peak blue shifted by 9 nm indicating that electron density was removed from the aromatic regions and π - π stacking occurred between the benzoid ring and styrene block. The blue shift for the bipolaron transition demonstrated the benzoid ring/styrene interaction further as less electron density was shared with the quinoid ring from adjacent benzoid rings. This confirmed the observations from SEM and DMTA that a shift in the phase morphology occurred and that TANI and styrene interacted *via* the benzoid ring. 50 mol% TANI-SBS could not be investigated due to poor solubility.

For 25 mol% TANI-PB, the benzoid and polaron transitions in TANI were unaffected by grafting and no electron rich environment was created. However, two peaks for the bipolaron transition were observed at 500 – 600 nm and 700 – 800 nm. This indicated that no π - π stacking was present between TANI groups in the solution state. The cause of this was attributed to the longer chain length of polybutadiene inhibiting the TANI interaction. Additionally, the π - π^* transition from the polybutadiene vinyl groups was hidden by the π - π benzoid transition.

Transitions for 1 mol% TANI-PB were not clearly observed due to the low grafting content of TANI, and only the π - π^* transition for the PB vinyl groups was observed. This peak was broader than in pristine PB due to a shoulder peak from the benzoid transition of TANI. Furthermore, the solubility of 35 mol% TANI-PB and 50 mol% TANI-PB was too low for investigation *via* solution state UV-Vis spectroscopy.

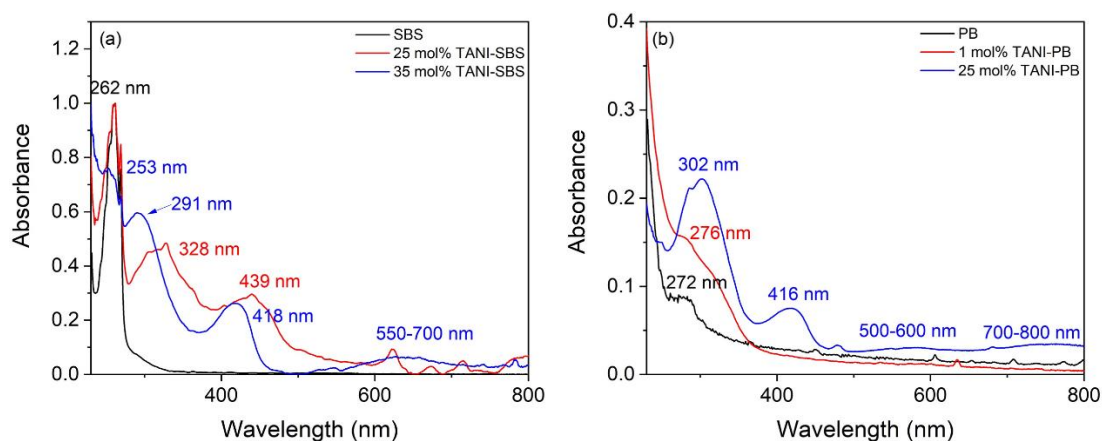


Figure 8.18 Solution state UV-Vis spectroscopy in chloroform for (a) SBS, 25 mol% TANI-SBS and 35 mol% TANI-SBS and (b) PB, 1 mol% TANI-PB and 25 mol% TANI-PB

8.4.3 Electromechanical properties of TANI modified elastomers

The effect on the mechanical properties of SBS and PB after grafting with different molar ratios of TANI are shown *via* stress strain curves in Figure 8.19. Prior to modification, SBS exhibited a tensile strength of 8.9 MPa, Young's modulus of 2.9 MPa and a strain at break of 857%, whilst PB had a tensile strength of 0.15 MPa, a Young's modulus of 1.5 MPa and a strain at break of 2442%.

Modification of SBS with 25 mol% and 35 mol% TANI led to a sharp decrease in the strain at break, $186 \pm 28.7\%$ and $167 \pm 29.8\%$ respectively. This was due to the increase in brittleness of the elastomer from the increase in 'hard' regions. However, the strain at break remained similar between the two elastomers due to the change in polymer morphology whereby 35 mol% TANI-SBS exhibited a more compatibilised polymer phase structure. The Young's modulus demonstrated a loss of deformability as the TANI grafting was increased, as the Young's modulus increased up to 7.7 ± 0.5 MPa and 64.9 ± 0.8 MPa for 25 mol% TANI-SBS and 35 mol% TANI-SBS respectively. Finally, the tensile strength for 25 mol% TANI-SBS was lower than for SBS and was 2.9 ± 0.4 MPa. This decrease was attributed to the decrease in polymer chain entanglement from the grafting of oligomeric TANI. In addition, the interactions between TANI groups were not strong enough to recover the tensile strength from the decrease in chain entanglement at this grafting level. For 35 mol% TANI-SBS, the tensile strength recovered to 8.7 ± 1.1 MPa due to a polymer phase morphology change

allowing TANI to π - π stack with the styrene block and form ‘hard’ regions which enhanced the tensile strength. For 50 mol% TANI-SBS, the material was too brittle for tensile testing and mechanically failed at $\sim 1\%$.

However, grafting of 25 mol% and 35 mol% TANI to PB had a markedly different effect on the mechanical properties. The strain at break decreased for both elastomers to $4.7 \pm 1.6\%$ and $3.4 \pm 1.2\%$ respectively. 25 mol% TANI-PB exhibited a large increase in tensile strength and Young’s modulus up to 8.8 ± 1.2 MPa and 692 ± 61.5 MPa respectively, whilst for 35 mol% TANI-PB the strength of the polymer was much weaker. This occurred due to the polybutadiene backbone and TANI group’s incompatibility with each other and resulted in a phase separated structure. However, a reduced grafting of 1 mol% TANI to PB decreased the tensile strength and Young’s modulus of the modified elastomer to 0.22 ± 0.04 MPa and 3.9 ± 0.3 MPa, whilst enhancing the strain at break to $156 \pm 35.4\%$. This was still a large decrease in the strain at break, demonstrating the detrimental effect of phase separation between TANI and PB on the mechanical properties.

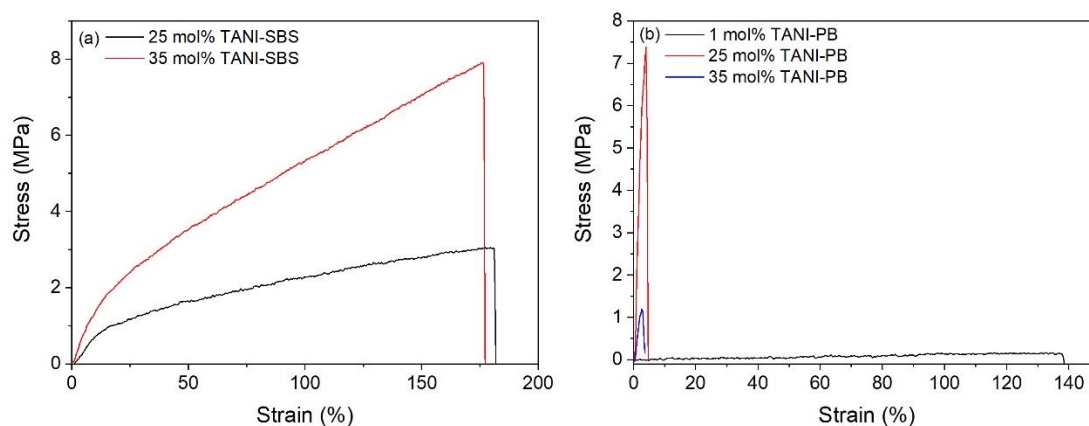


Figure 8.19 Stress strain curves of (a) 25 mol% TANI-SBS and 35 mol% TANI-SBS and (b) 1 mol% TANI-PB, 25 mol% TANI-PB and 35 mol% TANI-PB

The effect of grafting TANI on the electrical properties of SBS and PB are shown in Figure 8.20 and Appendix Figure 35. As previously observed, the relative permittivity was 2.8 at 10^3 Hz and displayed a largely frequency independent response. Comparatively, 25 mol% TANI-SBS and 35 mol% TANI-SBS exhibited an increased relative permittivity of 6.2 and 9.2 at 10^3 Hz respectively. Both 25 mol% TANI-SBS and 35 mol% TANI-SBS exhibited electronic polarisation due to electrode blocking, occurring below 10^2 Hz for 25 mol% TANI-SBS but from 10^1 Hz for 35 mol% TANI-

SBS. In addition, 35 mol% TANI-SBS exhibited a decrease in relative permittivity at 300 Hz due to atomic polarisation preventing the polymer chains from responding to the alternating electric field.

The $\tan \delta$ loss of TANI-SBS elastomers was higher than for SBS due the losses introduced from the conducting TANI groups. Thus, 25 mol% TANI-SBS and 35 mol% TANI-SBS had $\tan \delta$ losses of 0.25 and 0.30 at 10^3 Hz compared to 0.009 at 10^3 Hz for SBS. In addition, in 25 mol% TANI-SBS, a relaxation peak attributed to electrode blocking had a maxima at 12 Hz, whilst 35 mol% TANI-SBS exhibited an atomic relaxation peak at 23 kHz and the beginning of an electrode polarisation relaxation peak at lower than 10 Hz.

The insulating nature of TANI-SBS elastomers is shown in the phase angle for SBS and 25 mol% TANI-SBS where they exhibited a phase angle response of -90° , except 25 mol% TANI-SBS where a deviation towards 0° was observed from electronic polarisation. 35 mol% TANI-SBS exhibited a phase angle response deviated away from -90° indicating that the elastomer was near the percolation threshold for conducting TANI groups. Further deviations towards 0° were observed due to electrode blocking and atomic polarisation. Final confirmation of the insulating nature of TANI-SBS elastomers was observed in the AC conductivity in Appendix Figure 35, whereby the TANI-SBS elastomers exhibited an increased conductivity compared to SBS but all remain below $1 \times 10^{-7} \text{ S m}^{-1}$ at 1 Hz.

For PB, an initial relative permittivity of 3.3 Hz was observed in Figure 8.20b. After modification with 1 mol% TANI, PB exhibited a relative permittivity of 5.9 at 10^3 Hz. Both forms of PB maintained a largely frequency independent response. However, 25 mol% TANI-PB and 35 mol% TANI-PB exhibited highly frequency dependent relative permittivities, indicative of a conducting elastomer.

The $\tan \delta$ loss of 1 mol% TANI-PB remained low, 0.03 at 10^3 Hz, and only increased marginally compared to pristine PB, which exhibited a $\tan \delta$ loss of 0.008 at 10^3 Hz. However, the $\tan \delta$ loss for 25 mol% and 35 mol% TANI-PB was large due to the conductive nature of TANI. The conductive nature was further observed in the phase angle and AC conductivity of 25 mol% TANI-PB and 35 mol% TANI-PB which remained close to 0° across all frequencies lower than 10^5 Hz. The AC conductivity response for 25 mol% TANI-PB and 35 mol% TANI-PB was also frequency

independent due to its conductive nature from a conductive TANI pathway. Comparatively, 1 mol% TANI-PB exhibited a phase angle response of -90° due to its highly insulating nature. However, a small atomic polarisation relaxation peak was observed at 86 kHz due to grafted TANI inhibiting the PB chain response.

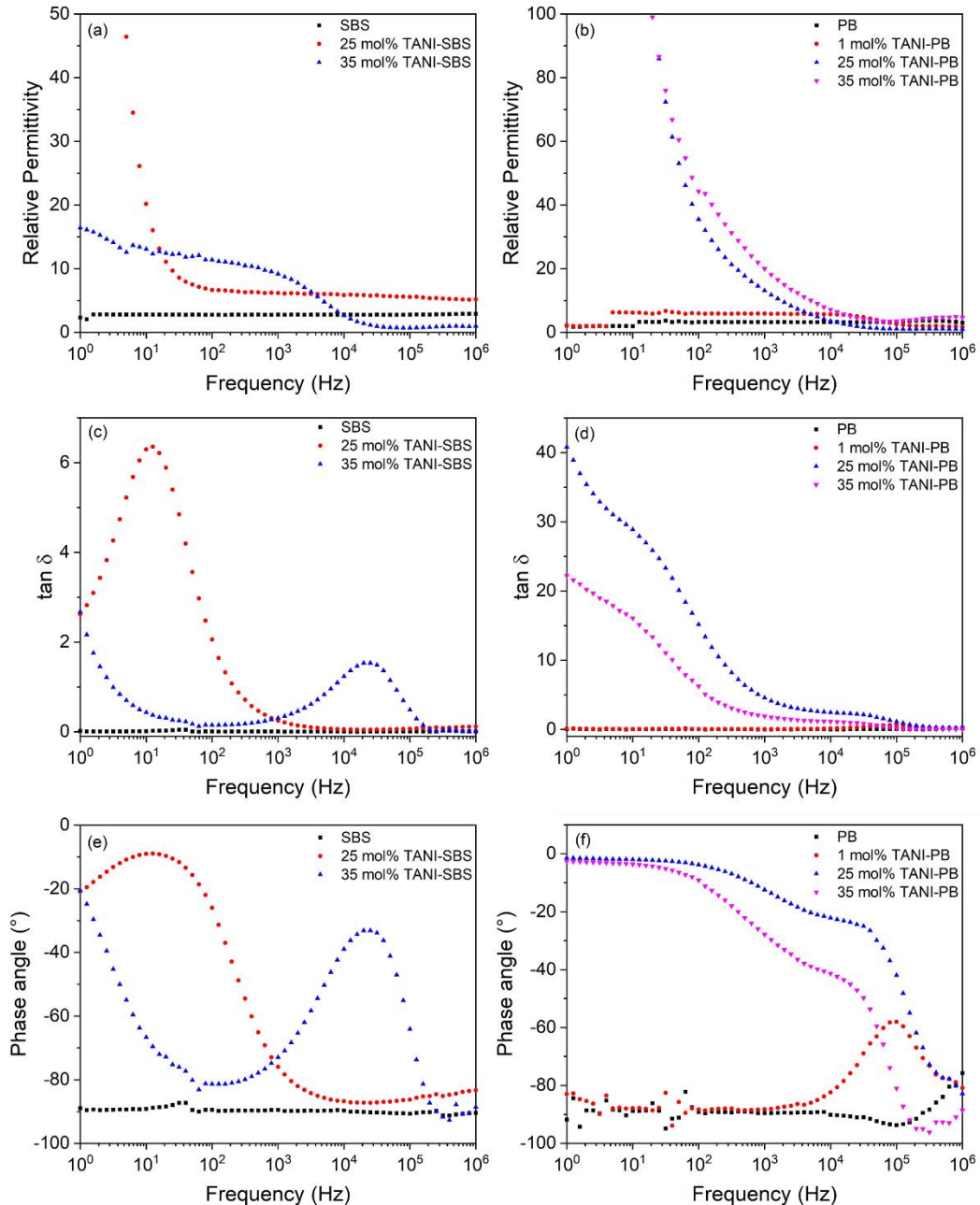


Figure 8.20 Impedance spectroscopy of SBS, 25 mol% TANI-SBS and 35 mol% TANI-SBS and the (a) relative permittivity, (c) $\tan \delta$ loss and (e) phase angle and of PB, 1 mol% TANI-PB, 25 mol% TANI-PB and 35 mol% TANI-PB and the (b) relative permittivity, (d) $\tan \delta$ loss and (f) phase angle

8.5 Conclusions

Overall, this chapter demonstrated the successful grafting of methyl thioglycolate and thioglycolic acid to alternative polymers of SBR and PB. The purpose of this was to introduce hydrogen bonding for increased self-healing ability whilst maintaining a high deformability of elastomer and high strain at break as well as enhanced electrical properties. Therefore, MG-SBR and 80/20 MG/TG-SBR were synthesised in the first section of this chapter. ^1H NMR confirmed the grafting of 98% of polar groups to the polymer backbone.

The structural characterisation of SBR MG-SBR and 80/20 MG/TG-SBR showed that the glass transition temperature increased after grafting. However, both SBR and MG-SBR had an increasing $\tan \delta$ as temperature increased beyond the glass transition temperature. This was attributed to transitioning towards melting for the elastomer. However, 80/20 MG/TG-SBR did not exhibit this due its hydrogen bonding network.

The stress strain curves showed that the grafting of methyl thioglycolate to SBR reduced the tensile strength of the elastomer. This was because any increase in tensile strength from the electrostatic interaction between methyl thioglycolate and styrene was lost from the decrease in tensile strength from the reduction in polymer chain entanglement. However, the strain at break increased to 1623%. By introducing the hydrogen bonding network, the tensile strength increased to 0.78 MPa, a Young's modulus of 2.9 MPa and a strain at break of 598%. Furthermore, 80/20 MG/TG-SBR had an enhanced relative permittivity of 13.9 at 10^3 Hz. This elastomer represents an excellent candidate for further investigation into its self-healing abilities, as well as use in an actuation and energy harvesting device.

The grafting of methyl thioglycolate and thioglycolic acid to PB was also confirmed by ^1H NMR and FTIR and a grafting of 99% was achieved. Whilst the relative permittivity was similarly enhanced, the mechanical properties of MG-PB and 80/20 MG/TG-PB remained too low for successful use actuation and energy harvesting devices.

Finally, the last section of this chapter investigated the grafting of TANI to SBS and PB to enhance its electromechanical properties. TANI was grafted *via* a three step grafting process to ensure that TANI was in the conductive emeraldine salt oxidation

state. TANI-SBS and TANI-PB were characterised by NMR and FTIR, with TANI grafting to SBS of 25 mol%, 35 mol% and 50 mol% whilst TANI grafting to PB was 1 mol%, 25 mol% and 35 mol%.

TANI-SBS exhibited enhanced electrical properties, but a reduction in strain at break and an increased Young's modulus upon increasing TANI grafting. This was because TANI could π - π stack with both itself and styrene. However, for 25 mol% and 35 mol% TANI-PB a highly phase separated structure was observed, and resulted in a highly brittle polymer. This was because TANI and polybutadiene are not compatible with each other. Therefore, 1 mol% TANI-PB was synthesised and exhibited an increased strain at break. However, this was at expense of the relative permittivity increase.

Overall, this chapter presents an alternative choice of elastomers for intrinsic modification to improve actuation and energy harvesting performance. Additionally, the grafting of conductive oligomers was presented as an alternative to the use of non-conducting polar groups.

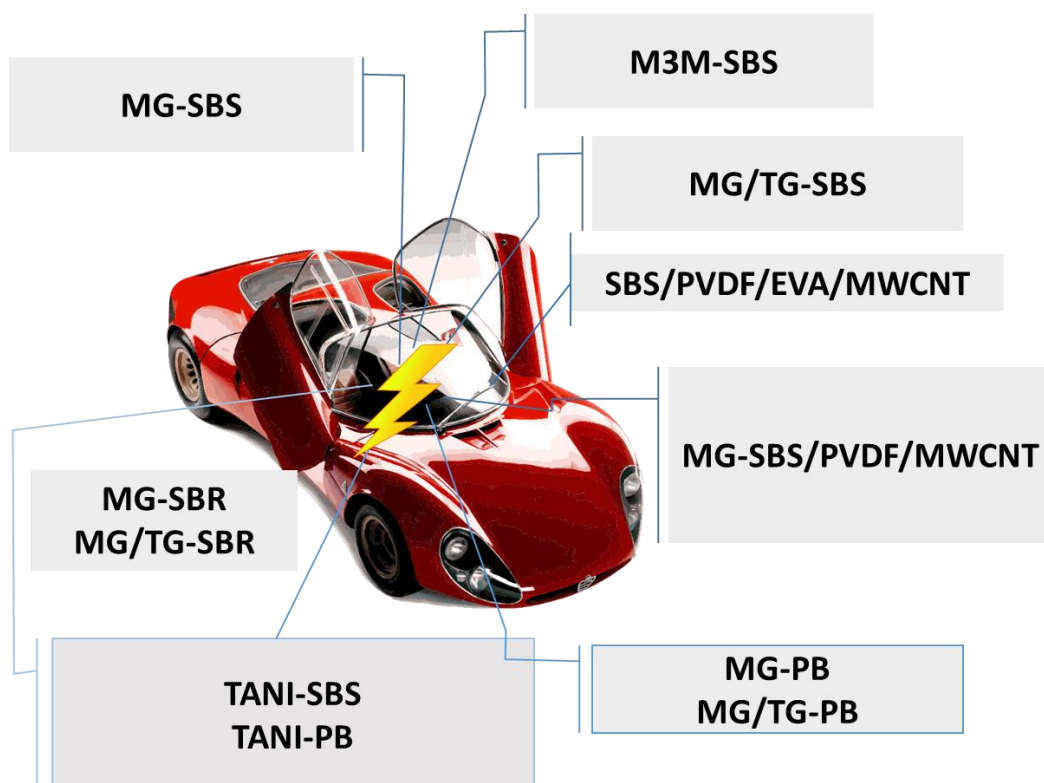
8.6 References

1. F. Zhang and C. Hu, *Constr. Build. Mater.*, 2013, **43**, 461-468.
2. B. Yin, G. Li, D. Wang, L. Wang, J. Wang, H. Jia, L. Ding and D. Sun, *Adv. Polym. Tech.*, 2018, **37**, 1323-1334.
3. A. Sinclair, X. Zhou, S. Tangpong, D. S. Bajwa, M. Quadir and L. Jiang, *ACS Omega*, 2019, **4**, 13189-13199.
4. M. H. Harandi, F. Alimoradi, G. Rowshan, M. Faghihi, M. Keivani and M. Abadyan, *Results Phys.*, 2017, **7**, 338-344.
5. F. Wang, L. Feng, Q. Tang, H. Liu and H. Liu, *J. Nanomater.*, 2013, **2013**.
6. P. Berto, A. Pointet, C. Le Coz, S. Grelier and F. Peruch, *Macromolecules*, 2018, **51**, 651-659.
7. J. Bai, H. Li, Z. Shi and J. Yin, *Macromolecules*, 2015, **48**, 3539-3546.
8. H. Stoyanov, M. Kolloosche, D. N. McCarthy and G. Kofod, *J. Mater. Chem.*, 2010, **20**, 7558-7564.
9. B. Wessling, *Polymers*, 2010, **2**, 786-798.
10. Y. Wang, H. D. Tran, L. Liao, X. Duan and R. B. Kaner, *J. Am. Chem. Soc.*, 2010, **132**, 10365-10373.
11. H. D. Tran, J. M. D'Arcy, Y. Wang, P. J. Beltramo, V. A. Strong and R. B. Kaner, *J. Mater. Chem.*, 2011, **21**, 3534-3550.
12. L. Liu, S. Yan and L. Zhang, *Macromol. Rapid Commun.*, 2018, **39**, 1800349.
13. S. Munteanu and C. Vasile, *J. Optoelectron. Adv. Mater.*, 2005, **7**, 3135.

14. L. Sobczyk, S. J. Grabowski and T. M. Krygowski, *Chem. Rev.*, 2005, **105**, 3513-3560.
15. C. Ellingford, R. Zhang, A. M. Wemyss, C. Bowen, T. McNally, Ł. Figiel and C. Wan, *ACS Appl. Mater. Interfaces*, 2018, **10**, 38438-38448.
16. C. Ellingford, R. Zhang, A. M. Wemyss, Y. Zhang, O. B. Brown, H. Zhou, P. Keogh, C. Bowen and C. Wan, *ACS Appl. Mater. Interfaces*, 2020, **12**, 7595–7604.
17. V. T. Kagiya and K. Takemoto, *J. Macromol. Sci., Chem.*, 1976, **10**, 795-810.
18. C. U. Udeh, N. Fey and C. F. J. Faul, *J. Mater. Chem.*, 2011, **21**, 18137-18153.
19. W. J. Zhang, J. Feng, A. G. MacDiarmid and A. J. Epstein, *Synth. Met.*, 1997, **84**, 119-120.
20. W. Zhao, L. Glavas, K. Odelius, U. Edlund and A.-C. Albertsson, *Polymer*, 2014, **55**, 2967-2976.
21. Q.-C. Lv, Y. Li, Z.-K. Zhong, H.-J. Wu, F.-A. He and K.-H. Lam, *Appl. Surf. Sci.*, 2018, **441**, 945-954.
22. A. Thota, R. Arukula, R. Narayan, P. Sripadi, S. Bojja and C. R. K. Rao, *J. Electrochem. Soc.*, 2017, **164**, F1090-F1099.
23. B. Butoi, A. Groza, P. Dinca, A. Balan and V. Barna, *Polymers*, 2017, **9**, 732.
24. X. Du, Y. Xu, L. Xiong, Y. Bai, J. Zhu and S. Mao, *J. Appl. Polym. Sci.*, 2014, **131**.
25. T. Ohsaka, Y. Ohnuki, N. Oyama, G. Katagiri and K. Kamisako, *J. Electroanal. Chem. Interfacial Electrochem.*, 1984, **161**, 399-405.
26. W. Lyu, J. Feng, W. Yan and C. F. J. Faul, *J. Mater. Chem. C*, 2015, **3**, 11945-11952.
27. H. E. Gottlieb, V. Kotlyar and A. Nudelman, *J. Org. Chem.*, 1997, **62**, 7512-7515.
28. C. Ellingford, A. Pengchaicharoen, A. M. Wemyss and C. Wan, *J. Compos. Sci.*, 2020, **4**, 25.
29. S. Gul, A.-u.-H. A. Shah and S. Bilal, *J. Phys.: Conf. Ser.*, 2013, **439**, 012002.
30. A. O. Patil, A. J. Heeger and F. Wudl, *Chem. Rev.*, 1988, **88**, 183-200.

Chapter 9

Conclusions and future perspectives



9.1 Conclusions

This thesis introduces intrinsic and extrinsic approaches to modify styrenic and butadiene based dielectric elastomers to enhance their electromechanical performance for DEA and DEG applications. The purpose of this was to tune their relative permittivity, $\tan \delta$ loss, electrical breakdown strength and Young's modulus in order to enhance the capacitance of the dielectric elastomers for applications as capacitors, actuators and energy generators. To achieve this, an array of different approaches were investigated and the main outcomes were summarised as follows:

In Chapter 4, triblock copolymer SBS was chemically modified by grafting polar methyl thioglycolate to form MG-SBS *via* thiol-ene chemistry. MG-SBS had an enhanced relative permittivity of 11.4, high strain at break and low Young's modulus. MG-SBS exhibited an unexpected instantaneous self-healing ability at room temperature which strengthened with time. This was attributed to an electrostatic interaction between the δ^+ protons adjacent to the ester of methyl thioglycolate interacting with the δ^- aromatic centre of styrene. Owing to the weak electrostatic interactions, when the grafting level of MG-SBS decreased, the self-healing ability decreased. Additionally, when the temperature for self-healing was increased to 37 °C the self-healing decreased as well. Furthermore, an investigation into the electrical recovery due to self-healing of the elastomer was investigated as well. It was found that the electrical recovery could be significantly enhanced by clearing the pinhole defect formed upon breakdown with a needle probe to remove conductive material. The actuation properties of MG-SBS were investigated in pristine MG-SBS and in MG-SBS after failure. Pristine MG-SBS actuated radially 4.2% under a 29.8 MV m⁻¹ electric field and could recover up to 90% of its actuation abilities after failure and recover 79% of its original breakdown strength. Finite element modelling was conducted to support the experimental observations that the defects at the polymer surface and voids within the original failure channel should be avoided in order to enhance the self-healing ability.

In Chapter 5, SBS was intrinsically modified with an alternative polar thiol-group, methyl-3-mercaptopropionate to form M3M-SBS. The size of the grafted polar group was larger, thus it reduced the Young's modulus to allow easier deformation of the elastomer and provided more free space for the polar group to move and interact with styrene to increase the strength of self-healing exhibit by the dielectric elastomer.

However, the increased length of the polar group meant that the relative permittivity of M3M-SBS was not as high as for MG-SBS, but the lower Young's modulus and higher breakdown strength of M3M-SBS meant that its actuation performance was significantly greater. Therefore, M3M-SBS was able to actuate 9.3% radially under a 39.6 MV m^{-1} electric field, recover its electrical breakdown strength by 85.3% and recover its actuation performance by 44.8%. Furthermore, the energy harvesting abilities of both MG-SBS and M3M-SBS were investigated and it was found that MG-SBS could harvest 2.3 mJ g^{-1} under a λ_a of 2.2, whereas M3M-SBS was able to harvest 11.5 mJ g^{-1} under a λ_a of 2.8. After failure, healed MG-SBS was able to retain its energy harvesting abilities whereas M3M-SBS suffered a large decrease in its performance.

In Chapter 6, hydrogen bonding was introduced in varying degrees by combining the grafted polar groups of methyl thioglycolate and thioglycolic acid to SBS in a one-pot synthesis to form MG/TG-SBS. The purpose of the hydrogen bonding was to enhance the self-healing ability of the elastomer and also increase its temperature resistance to operate in a DEA or DEG at high temperature. The modified dielectric elastomers exhibited enhanced electrical properties but stronger hydrogen bonding networks increased the stiffness and decreased the strain at break under room temperature testing. However, self-healing at $80 \text{ }^\circ\text{C}$ demonstrated a significant enhancement in the mechanical recovery and 80/20 MG/TG-SBS was able to recover up to 79% of its strain at break after 3 hours. Comparatively, 90/10 MG/TG-SBS and 95/5 MG/TG-SBS were able to recover only up to 50% and 33% their strain at break respectively. The actuation performance of the elastomer at room temperature was the lowest of the three intrinsically modified SBS elastomers, MG-SBS, M3M-SBS and MG/TG-SBS, 1.5% radially under an 18 MV m^{-1} electric field. However, this elastomer holds great promise for actuation and energy harvesting under elevated temperature conditions as the elastomer will retain a high self-healing ability and soften due to the overcoming of the elastic interchain interactions and increased mobility of hydrogen bonding.

In Chapter 7, two different extrinsic modification approaches of SBS were implemented by blending SBS and PVDF to enhance the electric properties of the polymer blend, and the subsequent addition of MWCNTs to further enhance the relative permittivity. Firstly, the use of EVA as a third, compatibilising polymer between SBS and PVDF was introduced. EVA was able to interact through Van der

Waals forces with SBS and it was able to hydrogen bond with PVDF. This meant that the polymer blend exhibited high mechanical strain and increased relative permittivity due to its enhanced compatibility. The introduction of MWCNTs further increased the relative permittivity of the composite and exhibited a double electrical and rheological percolation threshold at 1 wt% and 3 wt% addition of MWCNTs. However, the addition of MWCNTs increased the brittleness of the composite and reduced the strain at break as a result. This occurred because the MWCNTs resided at the interface between SBS and EVA, hindering the weak Van der Waals interaction and reducing the effectiveness of the EVA compatibility.

An alternative method to this was to increase the polarity of SBS *via* grafting of methyl thioglycolate and blend PVDF and MG-SBS together. This resulted in an elastic polymer blend with high permittivity as the ester was able to interact with the PVDF backbone. 1 wt% MWCNTs were added to 50/50 and 70/30 MG-SBS/PVDF and percolation was achieved in the 70/30 MG-SBS/PVDF composite, indicating that the MWCNTs resided in the PVDF phase of the composite due to the increased size of the butadiene block on MG-SBS from the polar groups preventing it from residing in that polymer phase.

Finally, in Chapter 8, alternative polymers were selected to graft both methyl thioglycolate and thioglycolic acid in an attempt to decrease the Young's modulus of the hydrogen bonding elastomers. The alternative polymers selected were SBR, where the block structure of styrene and butadiene is replaced with a statistical arrangement, and PB, where the 'hard' styrenic block was removed entirely. SBR showed excellent promise in 80/20 MG/TG-SBR with high relative permittivity, high strain at break and low Young's modulus as an alternative to SBS for future dielectric elastomers. For the PB based elastomers, the tensile strength of these remained too low even upon the addition of the hydrogen bonding network, and further enhancements in the tensile strength need to be considered to further this elastomer viability.

A final alternative approach was through the grafting of conductive emeraldine salt TANI to SBS and PB. It was found that grafting TANI to PB resulted in phase separation and a brittle polymer. Promise was shown by grafting TANI to SBS, however the aromatic system of TANI also behaved like an additional 'hard' styrenic

region and thus the electrical gain is required to be balanced and optimised with the reinforcement of the mechanical properties for its future use.

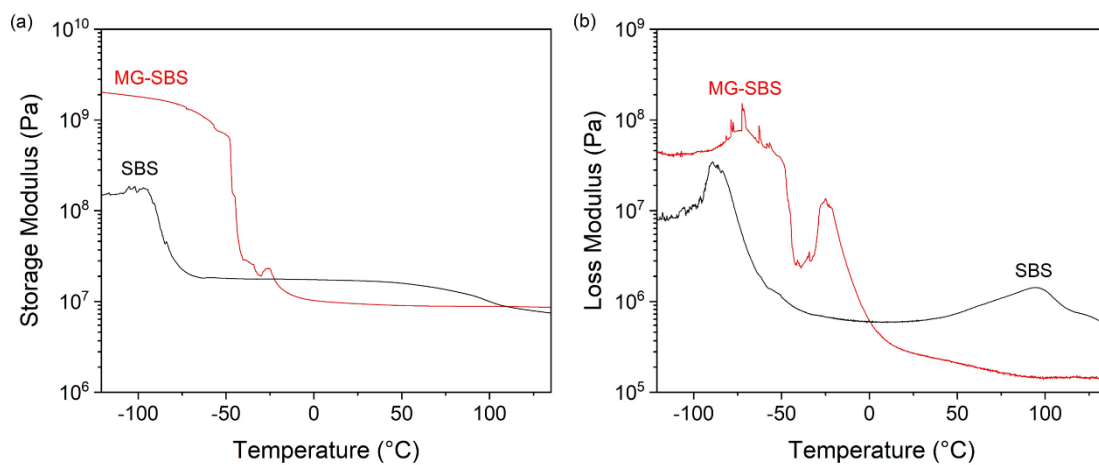
9.2 Future perspectives

1. The grafting of polar groups to intrinsically modify the polymer backbone resulted in high permittivity, high strain at break and low Young's modulus. However, whilst the introduction of hydrogen bonding increased the self-healing exhibited by these elastomers, it also stiffened the elastomers at room temperature, which reduced its actuation performance at room temperature. Therefore, the hydrogen bonding modified elastomer is only suitable for actuation at elevated temperatures. Further work into testing MG/TG-SBS at 60 – 80 °C could yield excellent properties for its mechanical, actuation and energy harvesting performance.
2. Extrinsic modification of dielectric elastomers with MWCNTs increased the electrical properties of composites but had a negative effect on their overall mechanical properties. Chemical modification of the MWCNTs to enhance their residency in the PVDF phase could yield better mechanical properties, or by changing the conductive filler to a graphene based filler such as rGO, which has oxygen based functional groups for hydrogen bonding with PVDF.
3. 80/20 MG/TG-SBR is an excellent candidate to take forward for self-healing applications due to its hydrogen bonding network. Additionally, it is an excellent candidate for DEA and DEG applications due to its deformability and high strain at break and should be further investigated.
4. PB based elastomers require further work to make them a viable future option. Currently, their tensile strength and Young's modulus are too low. Increasing the hydrogen bonding content or introducing crosslinking present future paths of progression to have high permittivity, deformable and elastic materials.
5. The grafting of emeraldine salt TANI presents excellent increases in permittivity however the degradation of the mechanical properties remains a big challenge. Alternatively utilising SBR as a polymer, where no block structure exists, could enable an elastomer to be synthesised which balances

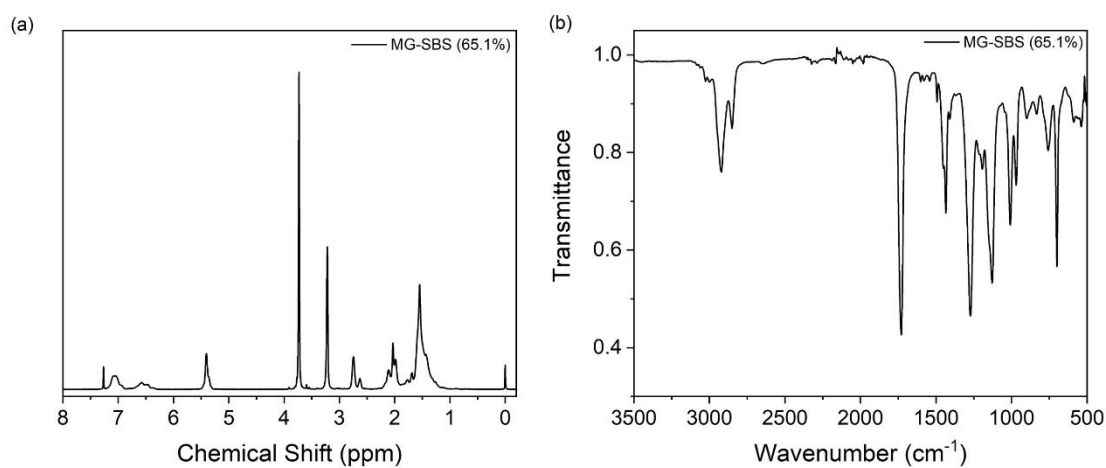
the electrical and mechanical properties better. Alternatively, using SBS with a small styrenic composition could also be a viable future pathway.

6. The development of a DEG is challenging and requires the device fabrication, the circuitry, the energy storage method and the dielectric elastomer used to be considered as a whole to make this successful. Improvements to the design of our DEG would increase the efficiency in which energy was harvested by the materials presented in this thesis. Furthermore, the use of an electret material to charge the dielectric elastomer could make the DEG self-sustainable and require no external voltage input.
7. There is the potential to use other elastomers in addition to SBS, SBR and PB for the intrinsic and extrinsic modification approaches used in this work. These include, but are not limited to, PVMS and natural rubber, which have unsaturation *via* alkene groups along the polymer backbone. Natural rubber represents a renewable alternative to crude-oil based elastomers, and is a key candidate for future dielectric elastomers for energy harvesting. Choosing a suitable starting elastomer is essential to achieve high performance electromechanical properties from modified elastomers.

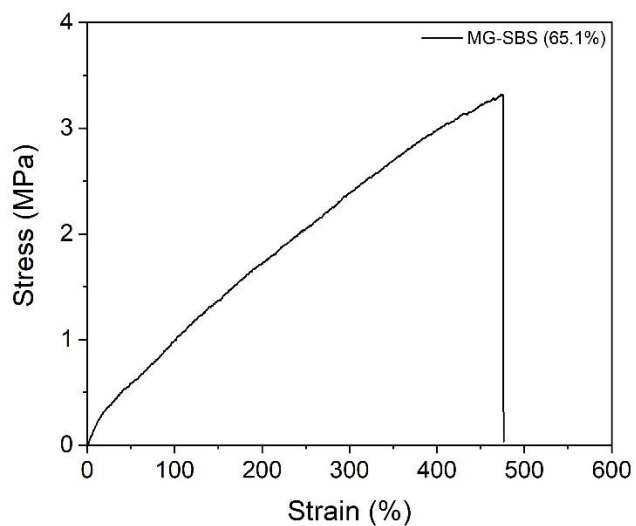
Appendix



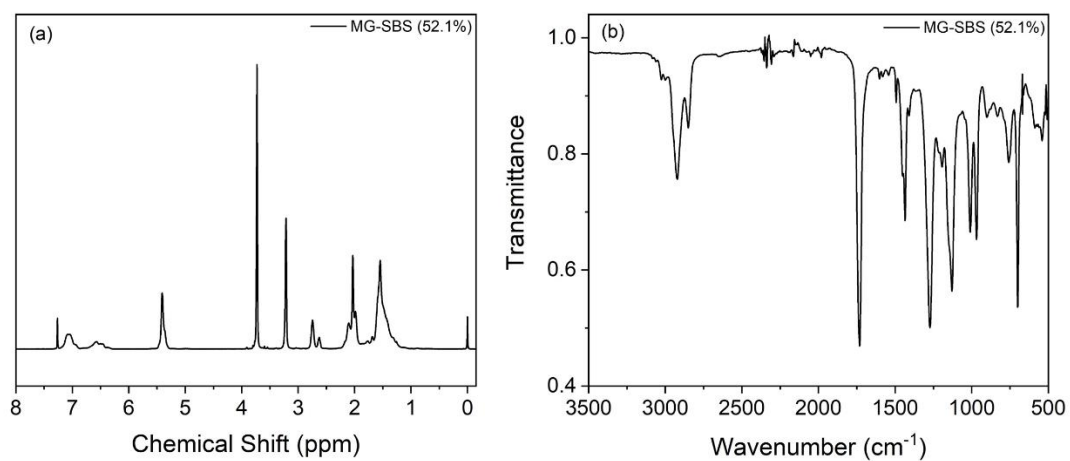
Appendix Figure 1 (a) Storage modulus of SBS and MG-SBS, (b) loss modulus of SBS and MG-SBS

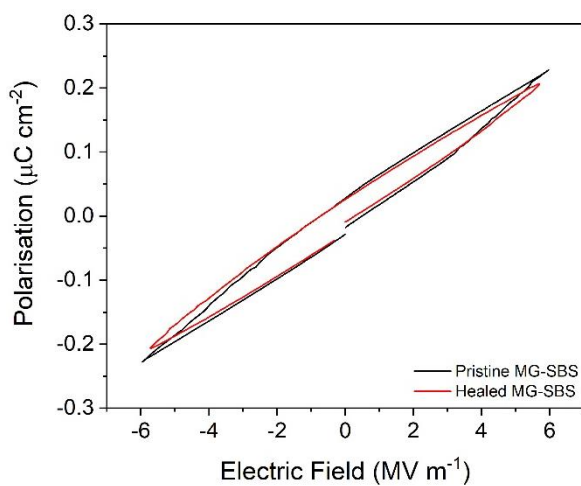


Appendix Figure 2 (a) ^1H NMR of MG-SBS (65.1%), (b) FTIR of MG-SBS (65.1%)

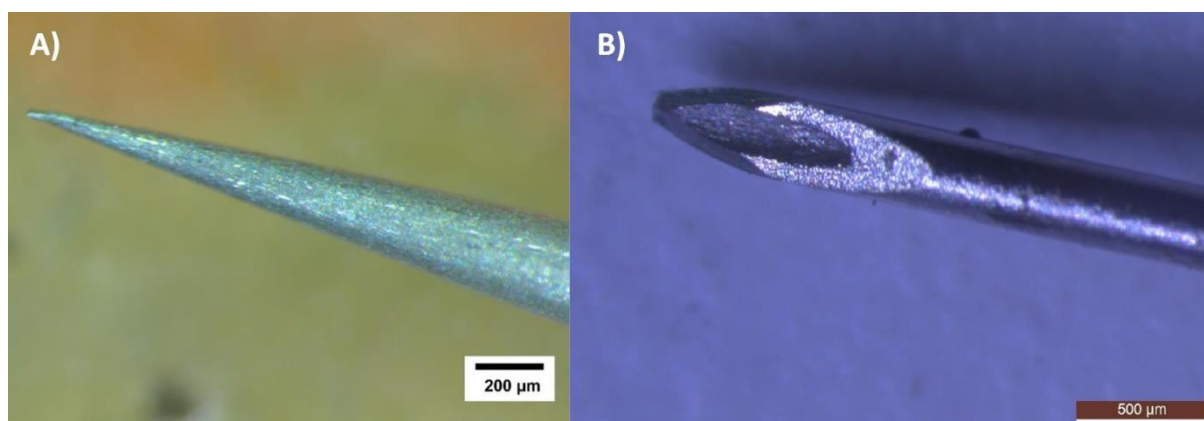


Appendix Figure 3 Stress-Strain curve of MG-SBS (65.1%)

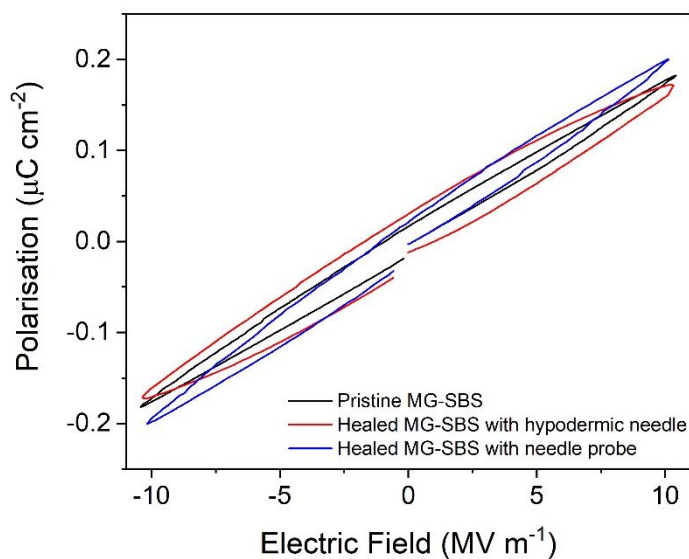
Appendix Figure 4 (a) ¹H NMR of MG-SBS (52.1%) and (b) FTIR of MG-SBS (52.1%)



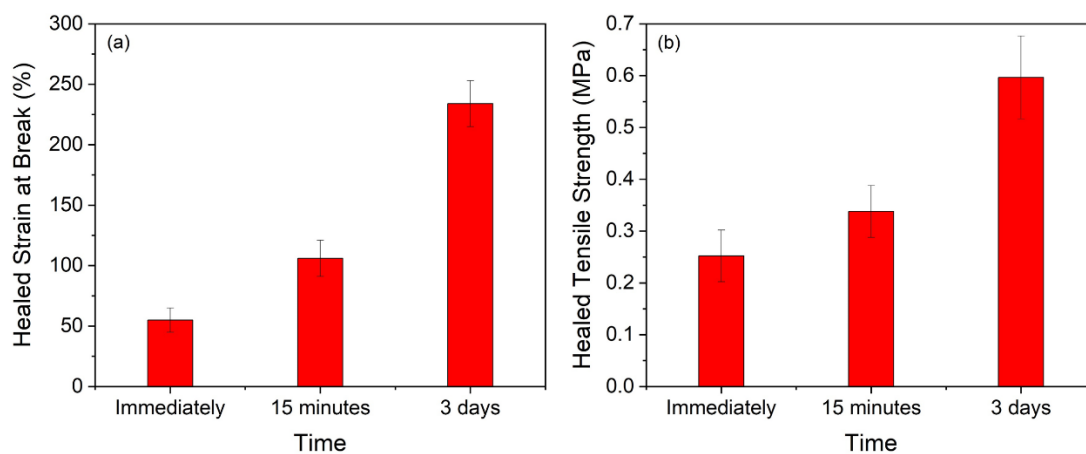
Appendix Figure 5 Polarisation electric field loops of pristine MG-SBS and healed MG-SBS under an electric field with a maxima of 5.9 MV m^{-1}



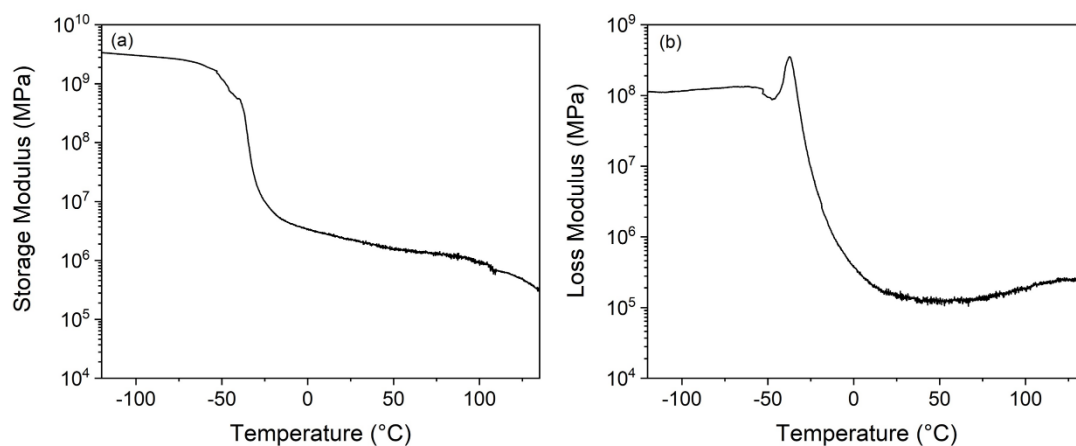
Appendix Figure 6 Optical images of (a) thin needle on a Needle Probe and (b) a hypodermic needle used to clear the pinhole defect site of MG-SBS after electrical breakdown



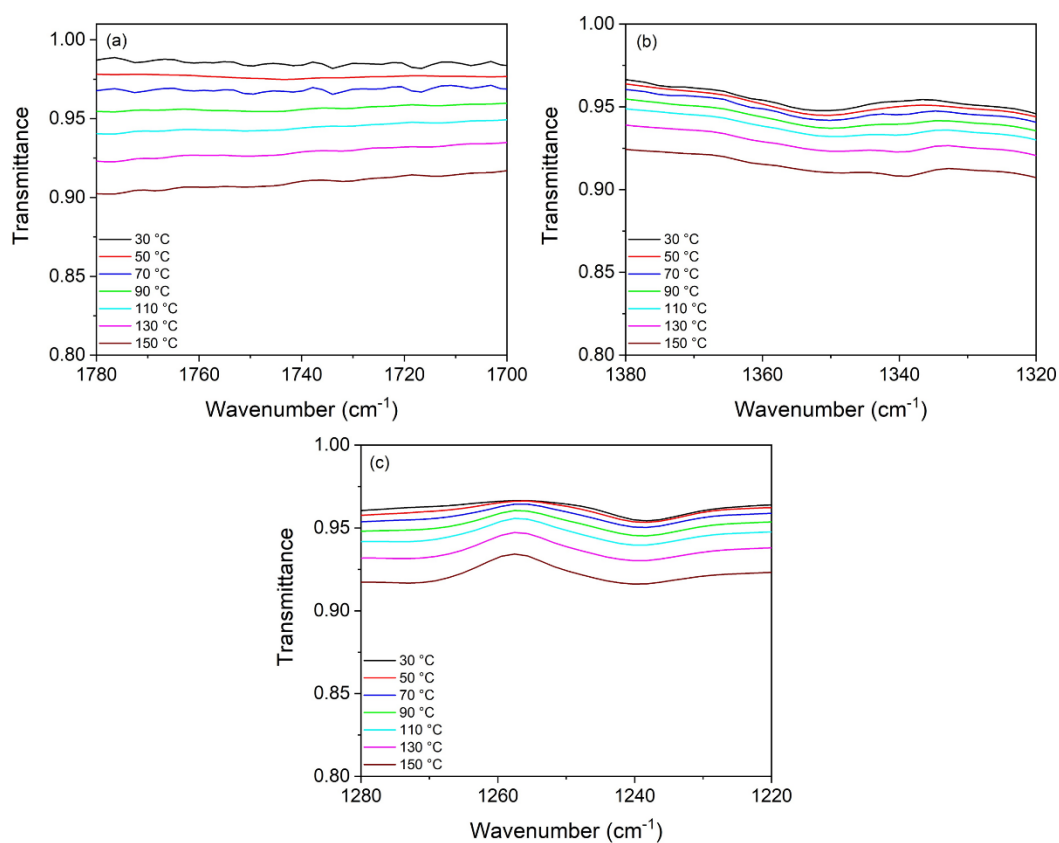
Appendix Figure 7 Comparison of electric field-polarisation loops under 10 MV m^{-1} electrical field for pristine MG-SBS, healed MG-SBS using a hypodermic needle to clear the pinhole site and healed MG-SBS using a needle probe to clear the pinhole site

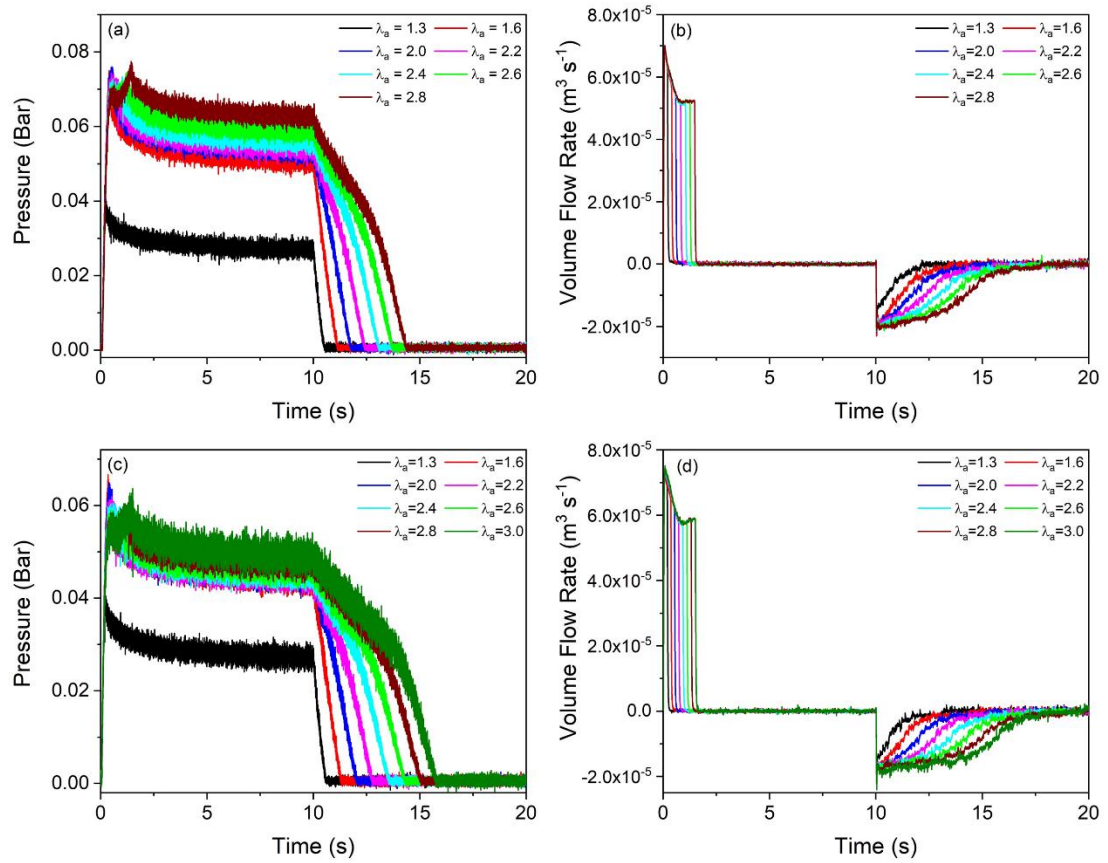


Appendix Figure 8 (a) Strain at break after self-healing for various times and (b) tensile strength after self-healing for various times for M3M-SBS

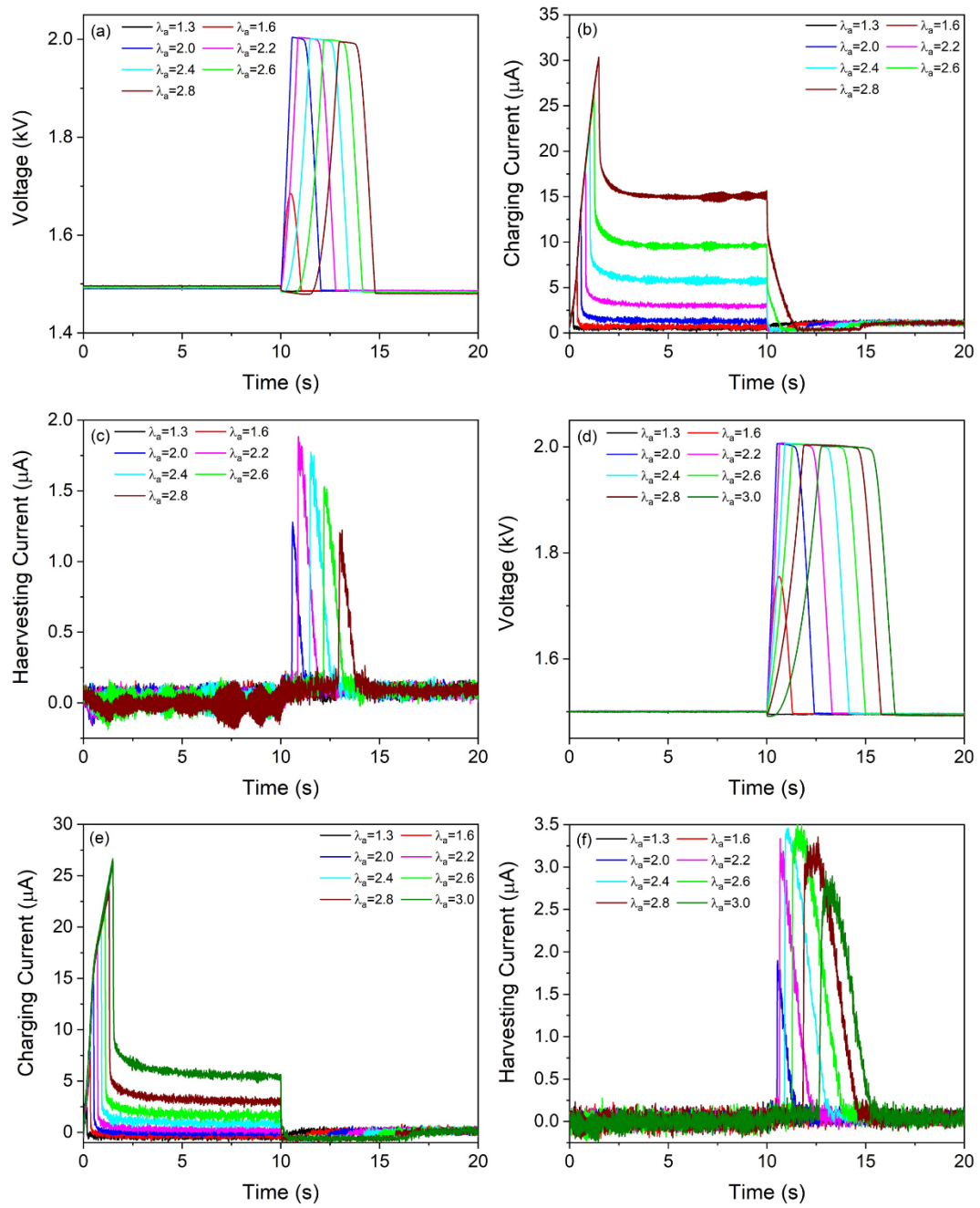


Appendix Figure 9 (a) Storage modulus and (b) loss modulus of M3M-SBS

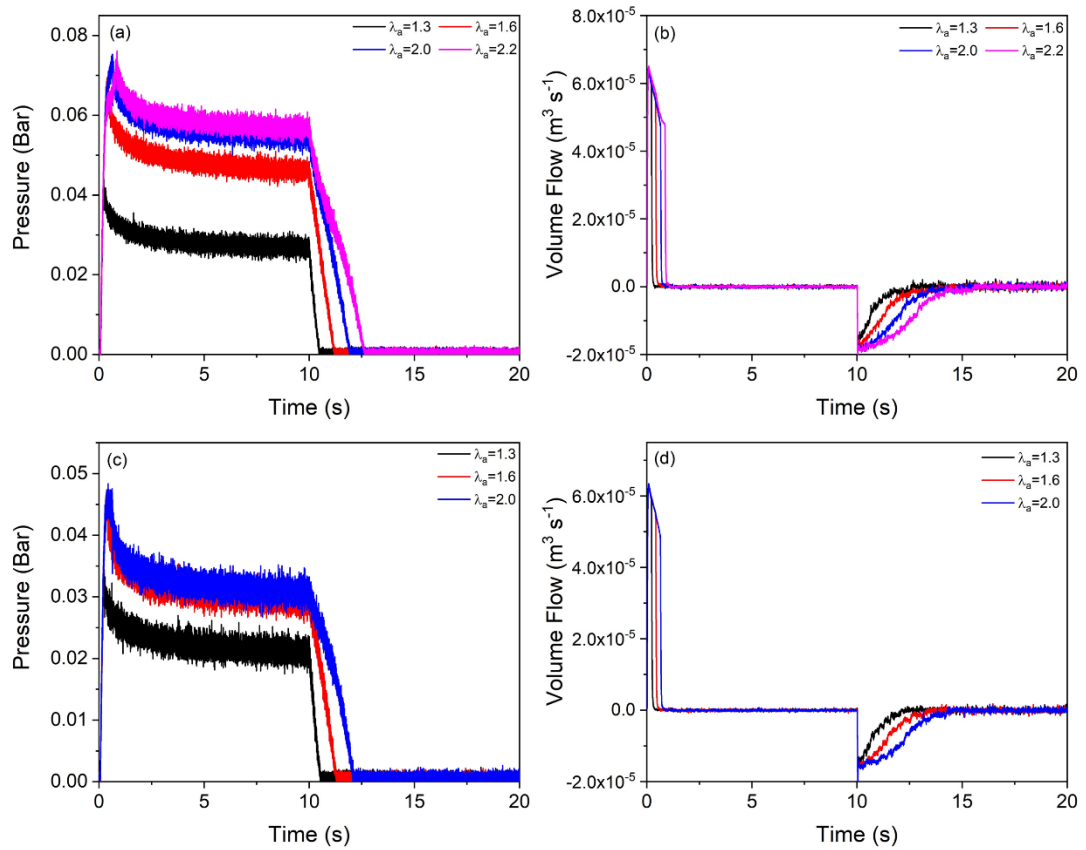
Appendix Figure 10 Temperature dependent FTIR for SBS between 30 °C and 150 °C for (a) 1730 cm^{-1} , (b) 1356 cm^{-1} and 1243 cm^{-1}



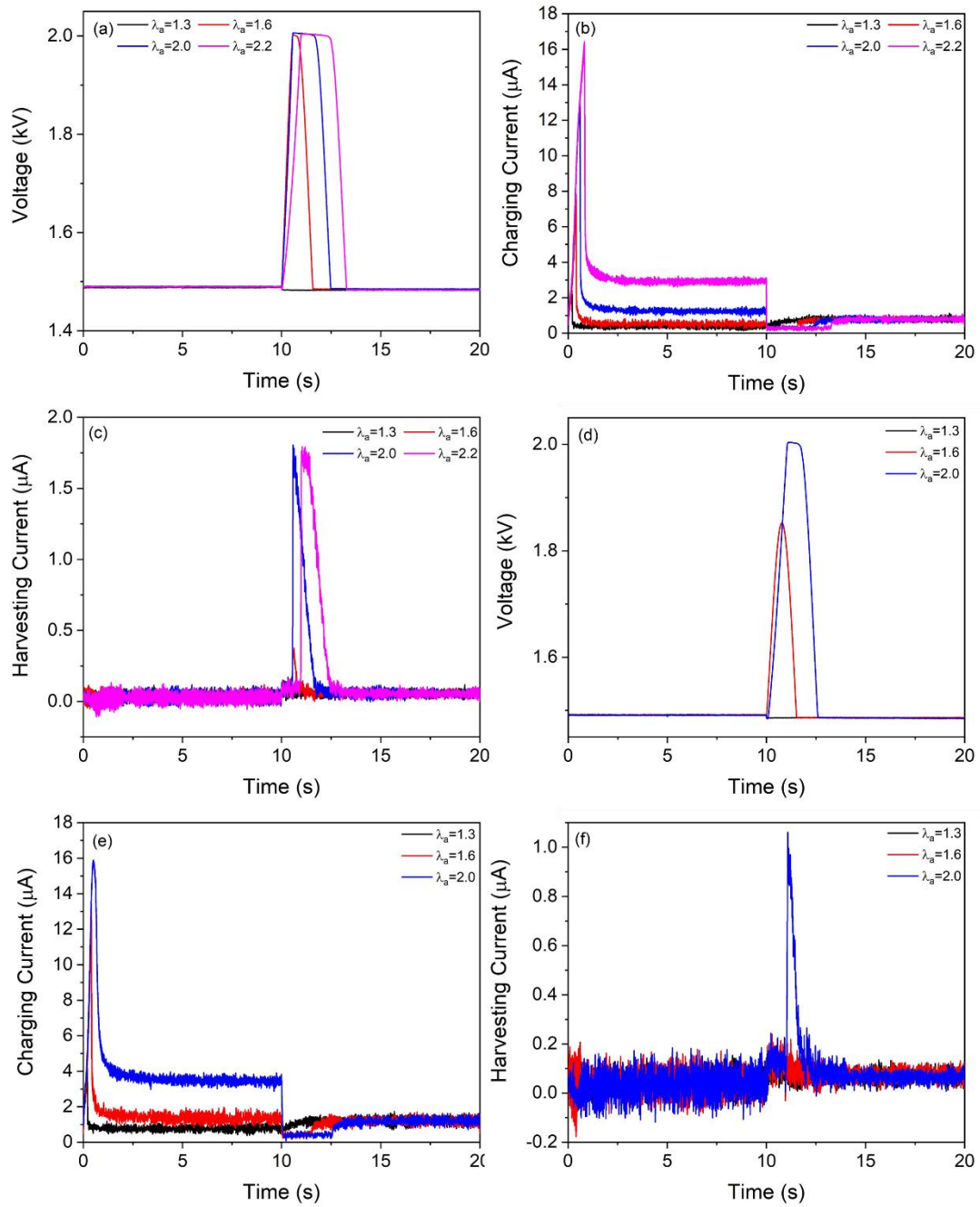
Appendix Figure 11 (a) Pressure and (b) air flow of MG-SBS energy harvesting cycles at different axial deformations. (c) Pressure and (d) air flow of M3M-SBS energy harvesting cycles at different axial deformations



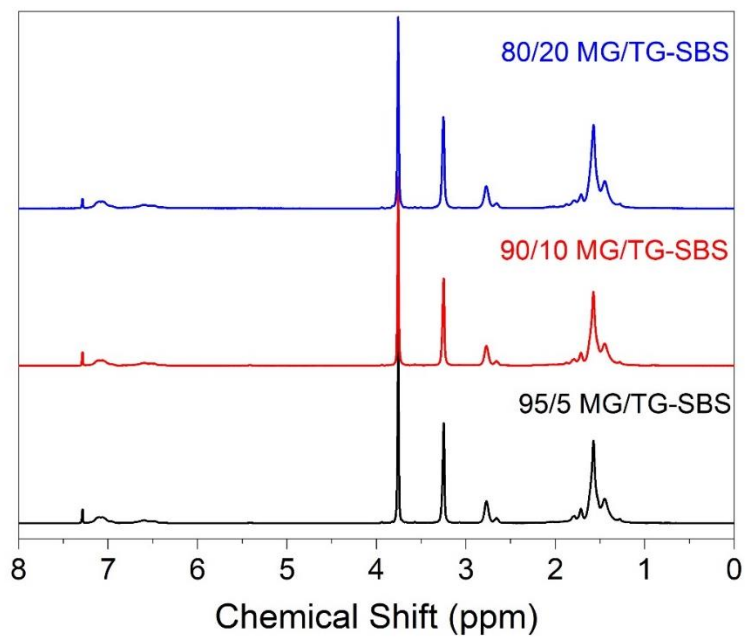
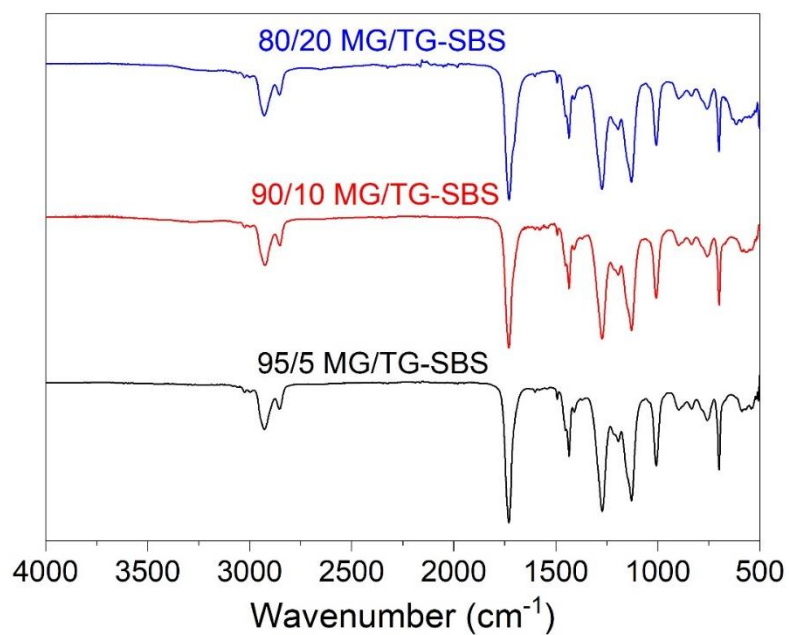
Appendix Figure 12 (a) Voltage, (b) charging current and (c) harvesting current of MG-SBS energy harvesting cycles at different axial deformations. (d) Voltage, (e) charging current and (f) harvesting current of M3M-SBS energy harvesting cycles at different axial deformations.



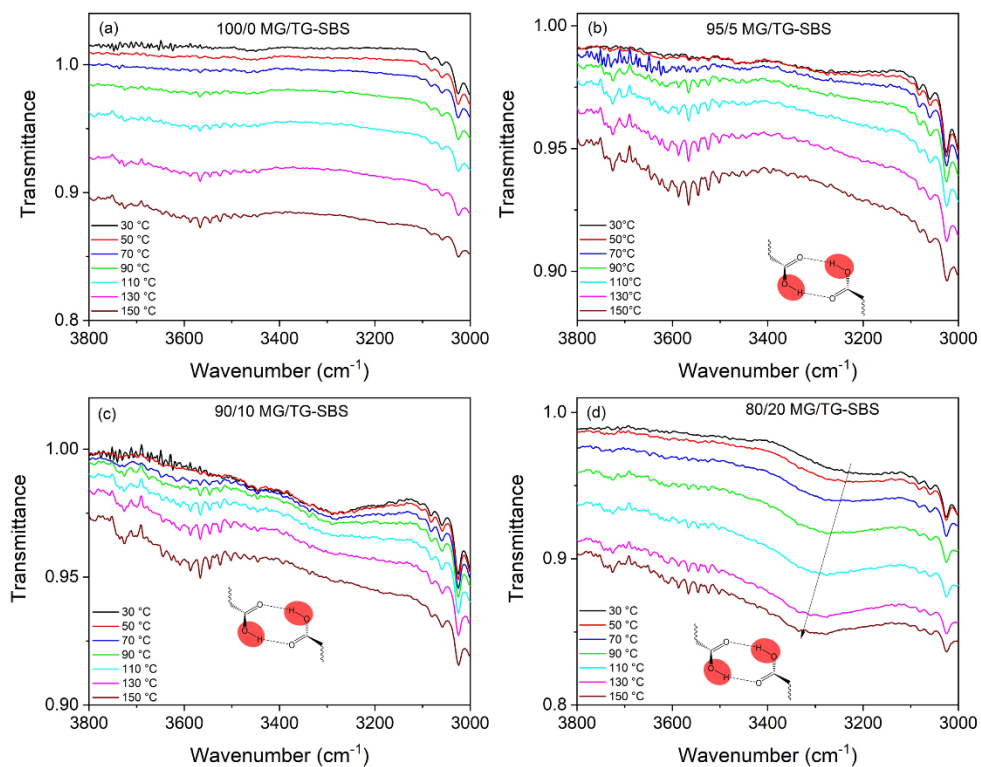
Appendix Figure 13 (a) Pressure and (b) air flow of healed MG-SBS energy harvesting cycles at different axial deformations. (c) Pressure and (d) air flow of healed M3M-SBS energy harvesting cycles at different axial deformations



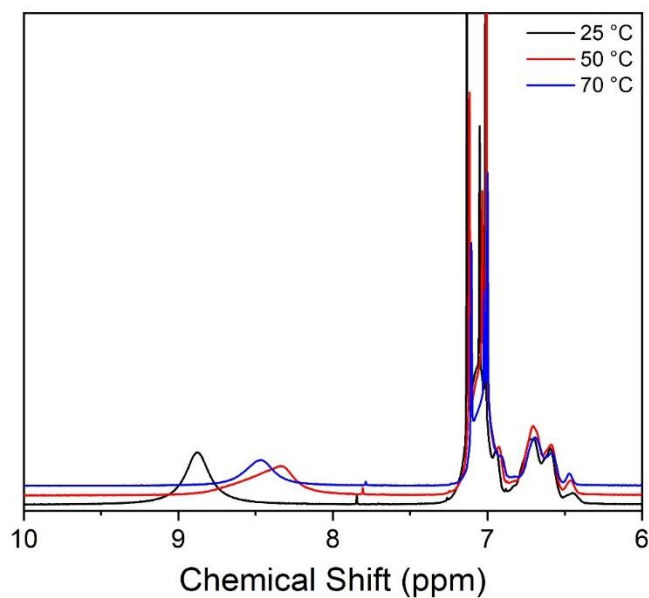
Appendix Figure 14 (a) Voltage, (b) charging current and (c) harvesting current of healed MG-SBS energy harvesting cycles at different axial deformations. (d) Voltage, (e) charging current and (f) harvesting current of healed M3M-SBS energy harvesting cycles at different axial deformations.

Appendix Figure 15 ^1H NMR spectroscopy of 95/5, 90/10 and 80/20 MG/TG-SBS

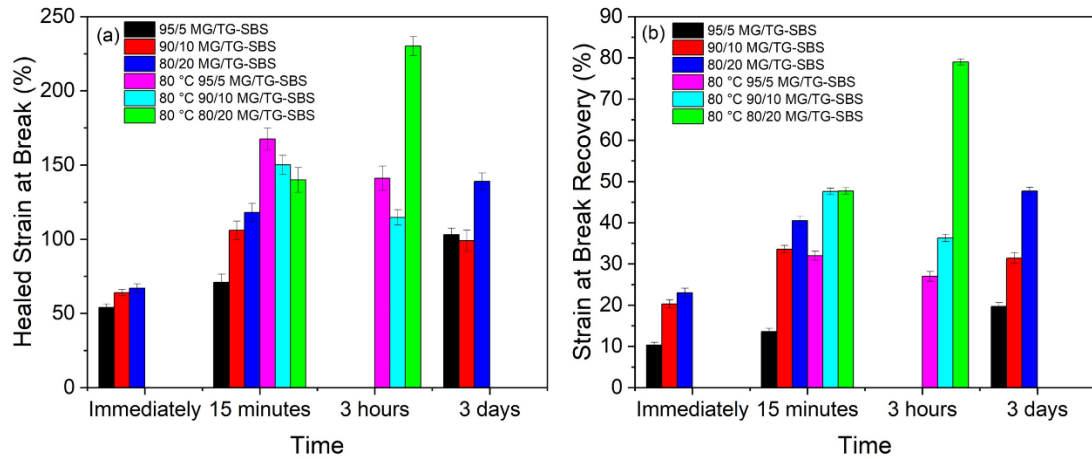
Appendix Figure 16 FTIR spectroscopy of 95/5, 90/10 and 80/20 MG/TG-SBS



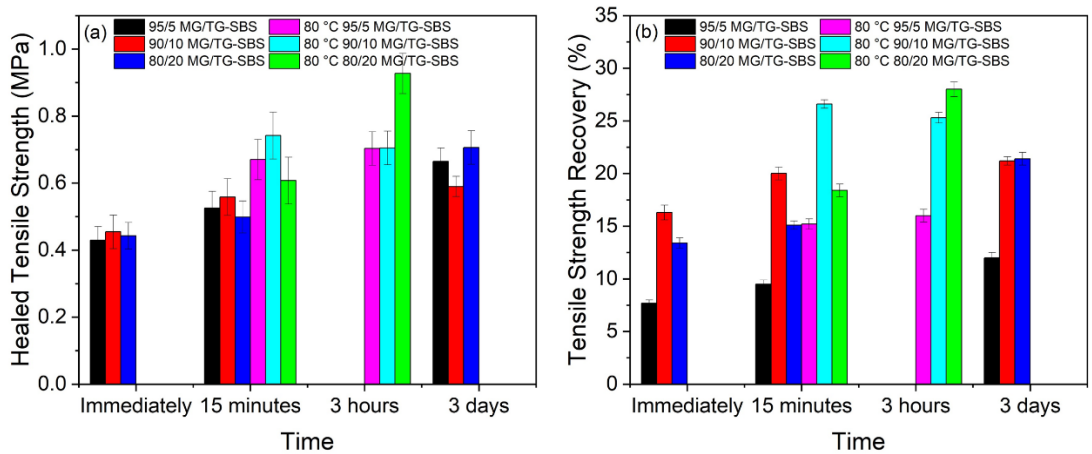
Appendix Figure 17 Temperature dependant FTIR for 100/0, 95/5, 90/10 and 80/20 MG/TG-SBS at 3320 cm^{-1} upon heating



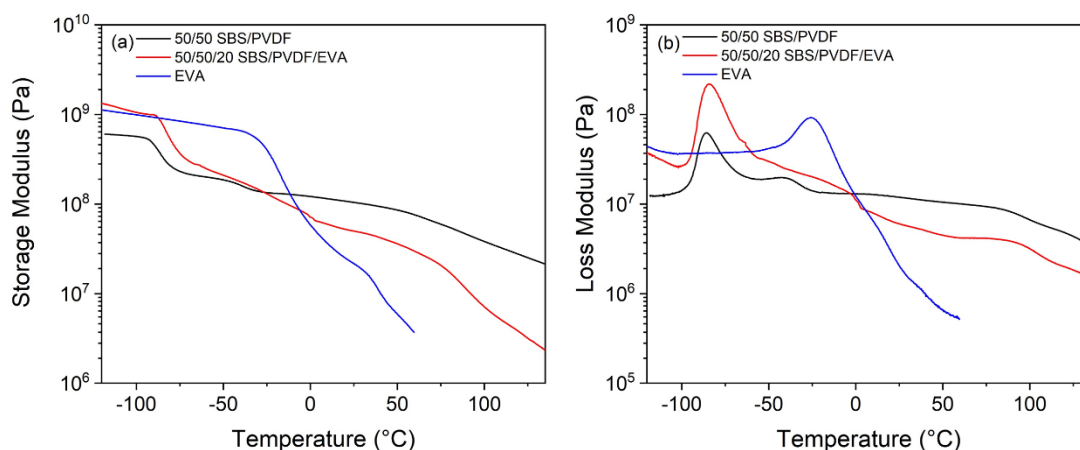
Appendix Figure 18 Variable temperature ^1H NMR spectra of 80/20 MG/TG-SBS at 25 °C, 50 °C and 70 °C



Appendix Figure 19 (a) Healed strain at break and (b) strain at break recovery for 95/5, 90/10 and 80/20 MG/TG-SBS at room temperature and at 80 °C after testing immediately, after 15 minutes, after 3 hours and after 3 days



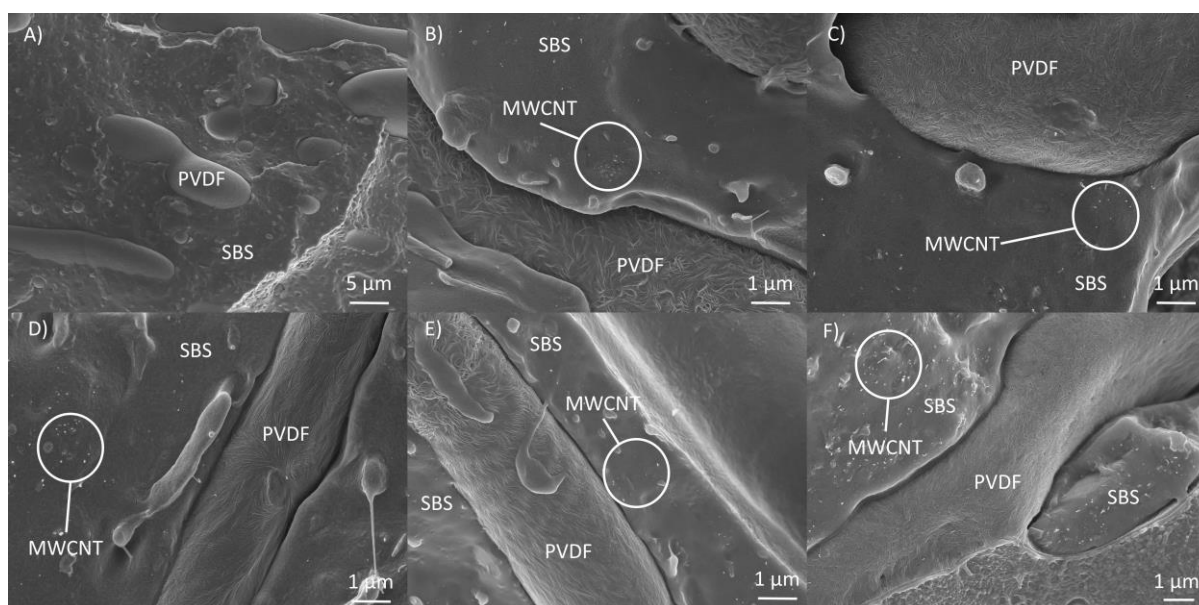
Appendix Figure 20 (a) Healed tensile strength and (b) tensile strength recovery for 95/5, 90/10 and 80/20 MG/TG-SBS at room temperature and at 80 °C after testing immediately, after 15 minutes, after 3 hours and after 3 days



Appendix Figure 21 (a) Storage modulus and (b) loss modulus of 50/50 SBS/PVDF, 50/50/20 SBS/PVDF/EVA and EVA

Appendix Table 1 β/α phase crystallinity ratios in PVDF and SBS/PVDF/EVA TPEs and the change with increasing MWCNT concentration

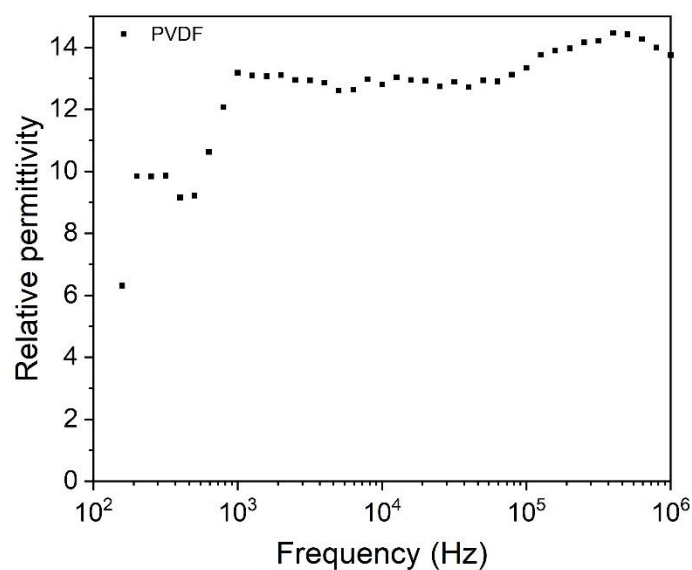
Material	763 cm ⁻¹ (α)	840 cm ⁻¹ (β)	β/α intensity ratio	615 cm ⁻¹ (α)	1275 cm ⁻¹ (β)	β/α intensity ratio
PVDF	0.742	0.532	0.717	0.782	0.760	0.972
SBS/PVDF/EVA (50/50/20)	0.740	0.834	1.127	0.778	0.930	1.195
SBS/PVDF/EVA/MWCNT (50/50/20/0.3)	0.844	0.951	1.108	0.876	0.979	1.118
SBS/PVDF/EVA/MWCNT (50/50/20/0.5)	0.814	0.916	1.125	0.834	0.955	1.145
SBS/PVDF/EVA/MWCNT (50/50/20/1)	0.646	0.811	1.255	0.696	0.899	1.292
SBS/PVDF/EVA/MWCNT (50/50/20/2)	0.616	0.733	1.190	0.642	0.857	1.335
SBS/PVDF/EVA/MWCNT (50/50/20/3)	0.395	0.663	1.678	0.502	0.845	1.683



Appendix Figure 22 SEM imaging of SBS/PVDF/EVA (50/50/20) containing (a) 0 wt% MWCNTs, (b) 0.3 wt% MWCNTs, (c) 0.5 wt% MWCNTs, (d) 1 wt% MWCNTs, (e) 2 wt% MWCNTs and (f) 3 wt% MWCNTs

Appendix Table 2 Normalised transmission intensity ratios for SBS/PVDF 50/50 and MG-SBS/PVDF 50/50 compared to SBS, PVDF and MG-SBS peaks

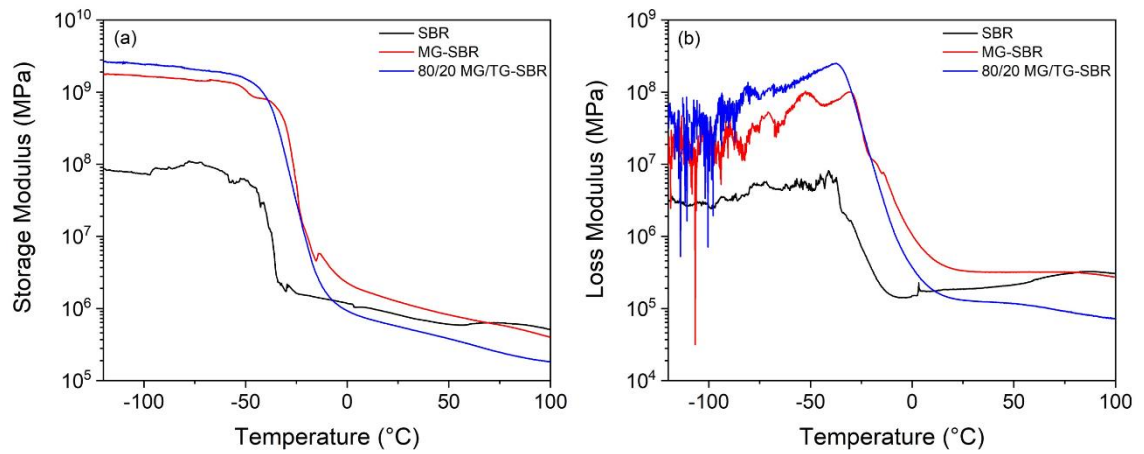
Material	Normalised transmission intensity for ester peaks				Normalised transmission intensity for C-F peaks	
	2917 cm ⁻¹	1732 cm ⁻¹	1272 cm ⁻¹	1130 cm ⁻¹	1400 cm ⁻¹	1177 cm ⁻¹
PVDF	-	-	-	-	1	0.81
SBS/PVDF 50/50	-	-	-	-	1	0.80
MGSBS	1	0.48	0.54	0.61	-	-
MGSBS/PVDF 50/50	1	0.61	0.61	0.61	1	0.72



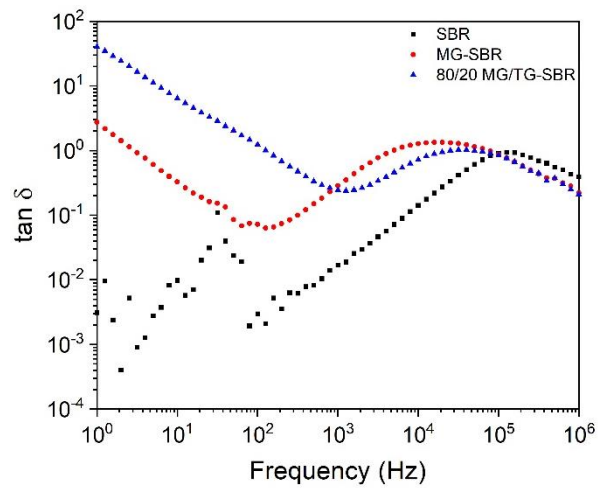
Appendix Figure 23 Relative permittivity of PVDF

Appendix Table 3 DSC crystallinity ($X_c(\%)$), crystallisation temperature (T_c) and melting temperature (T_m) for SBS/PVDF and MG-SBS/PVDF 50/50 and 70/30 blends and composites containing 1 wt% MWCNTs

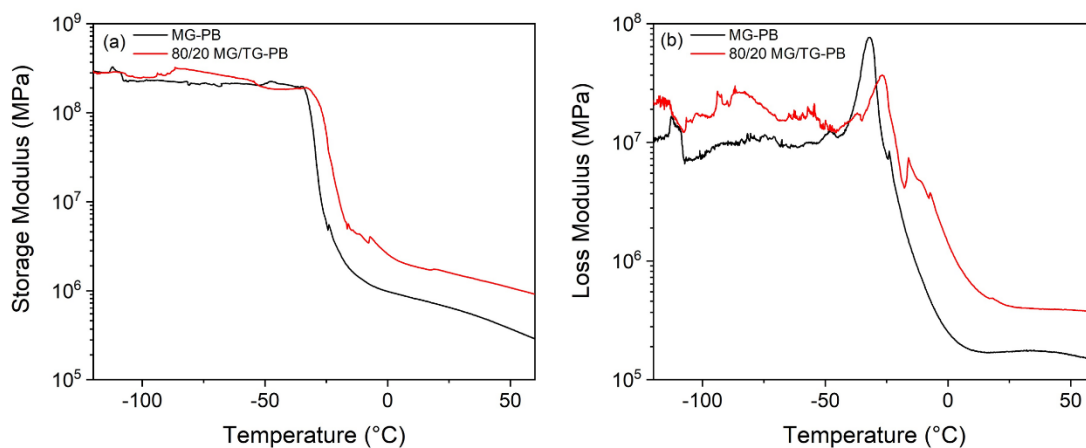
Material	$X_c(\%)$	T_c [°C]	T_m [°C]
PVDF	48.66	138.63	165.96
SBS:PVDF 70:30	72.68	136.60	165.61
SBS:PVDF 50:50	53.96	136.86	165.89
SBS:PVDF:MWCNT 69.5:29.5:1	38.98	137.01	165.38
SBS:PVDF:MWCNT 49.5:49.5:1	37.63	137.17	166.25
MGSBS:PVDF 70:30	48.26	137.27	167.10
MGSBS:PVDF 50:50	34.68	137.65	166.89
MGSBS:PVDF:MWCNT 69.5:29.5:1	43.71	135.76	166.75
MGSBS:PVDF:MWCNT 49.5:49.5:1	46.93	137.53	168.01



Appendix Figure 24 (a) Storage modulus and (b) loss modulus of SBR, MG-SBR and 80/20 MG/TG-SBR



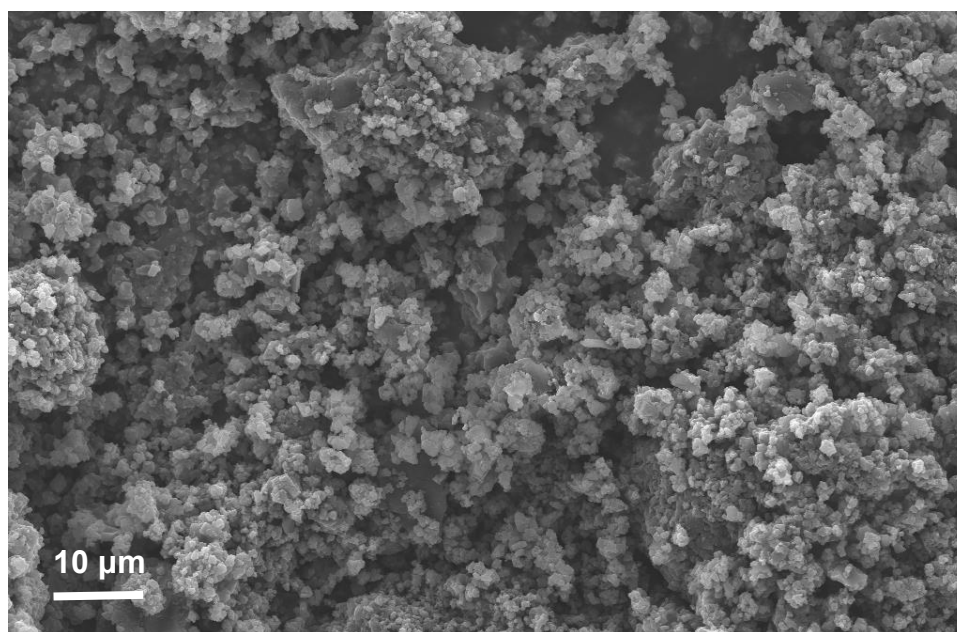
Appendix Figure 25 $\tan \delta$ graph from impedance spectroscopy of SBR, MG-SBR and 80/20 MG/TG-SBR with the $\tan \delta$ in \log_{10} form to highlight the atomic relaxation peaks



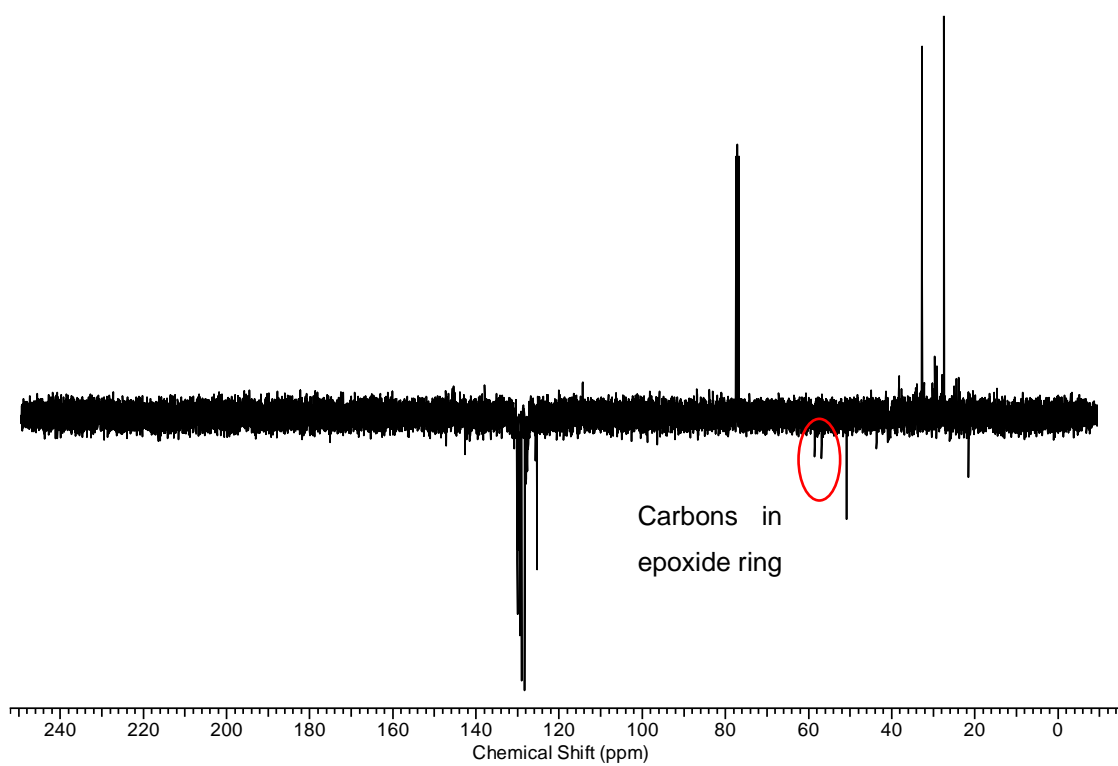
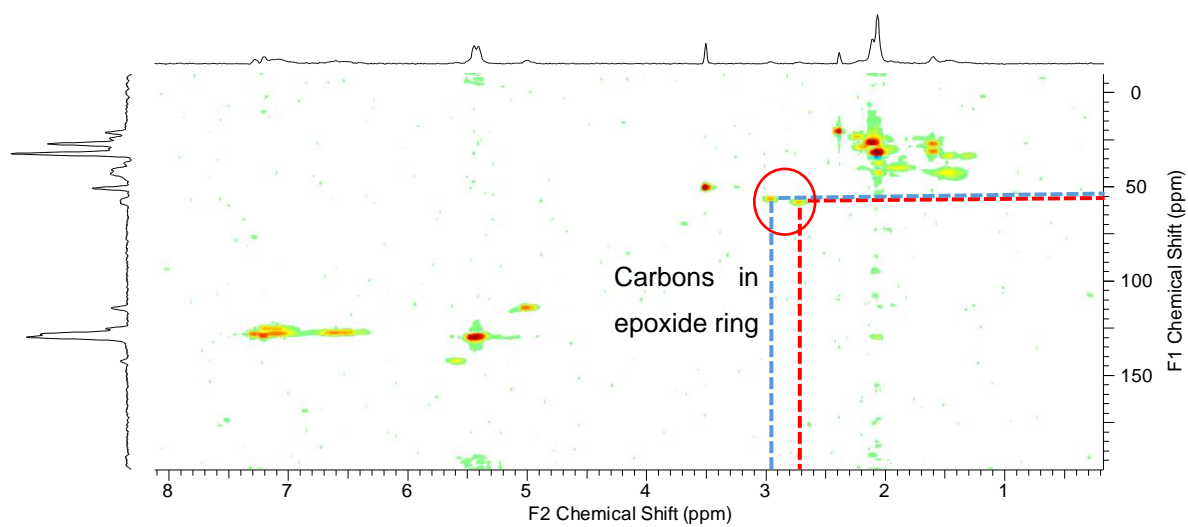
Appendix Figure 26 (a) Storage modulus and (b) loss modulus of MG-PB and 80/20 MG/TG-PB between -120 °C and 60 °C

Appendix Table 4 GPC containing M_n , M_w and \bar{D} for TANI synthesised with a two hour reaction time and a 90 minute reaction time

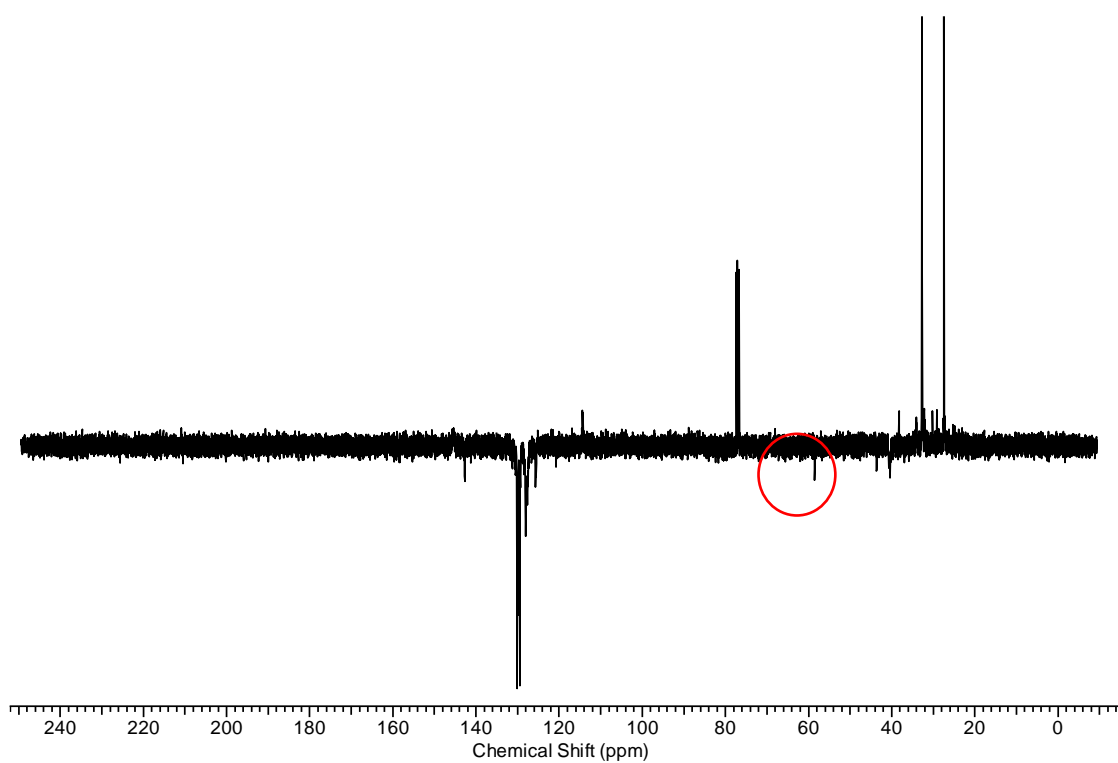
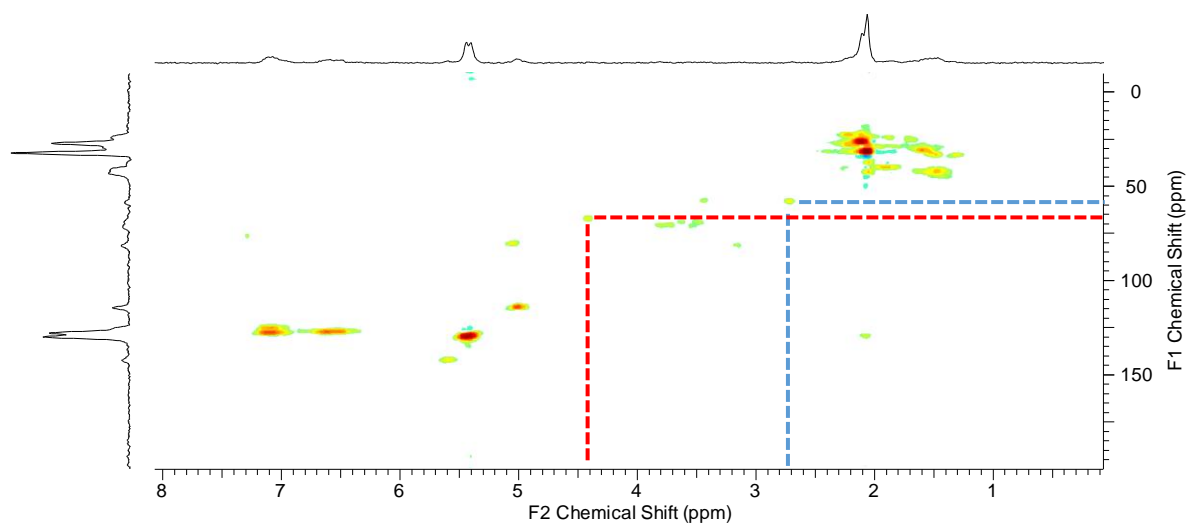
Product	M_n (g mol ⁻¹)	M_w (g mol ⁻¹)	\bar{D}
2 hr TANI	796	1629	2.05
1.5 hr TANI	648	1022	1.58



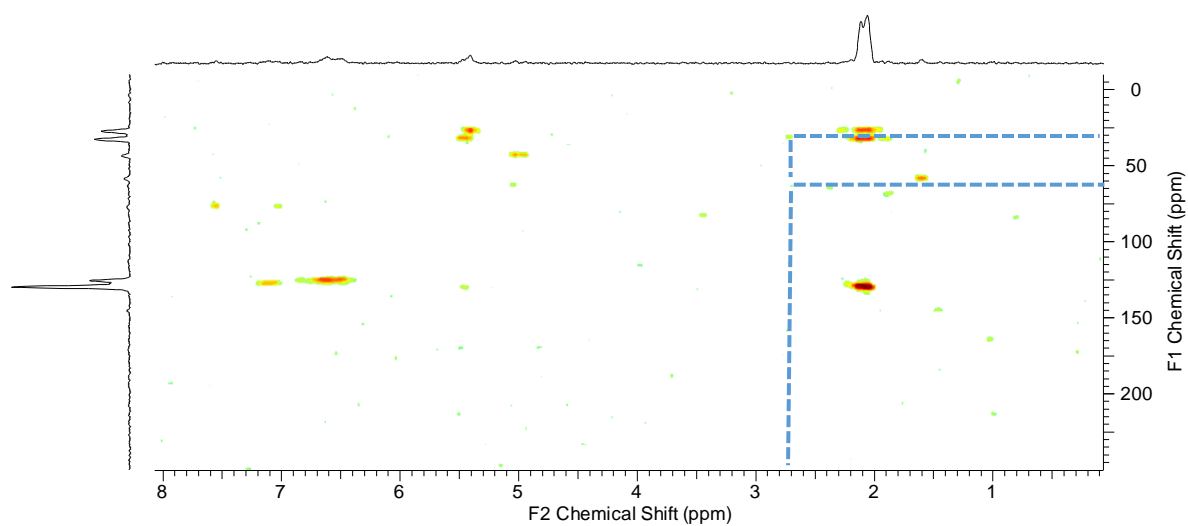
Appendix Figure 27 SEM image of emeraldine salt form TANI acidified using trifluoroacetic acid

Appendix Figure 28 ^{13}C NMR spectrum of E-SBS

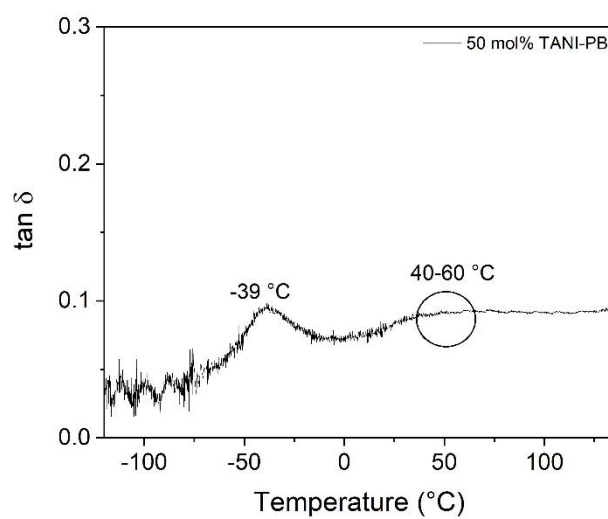
Appendix Figure 29 HSQC spectrum of E-SBS

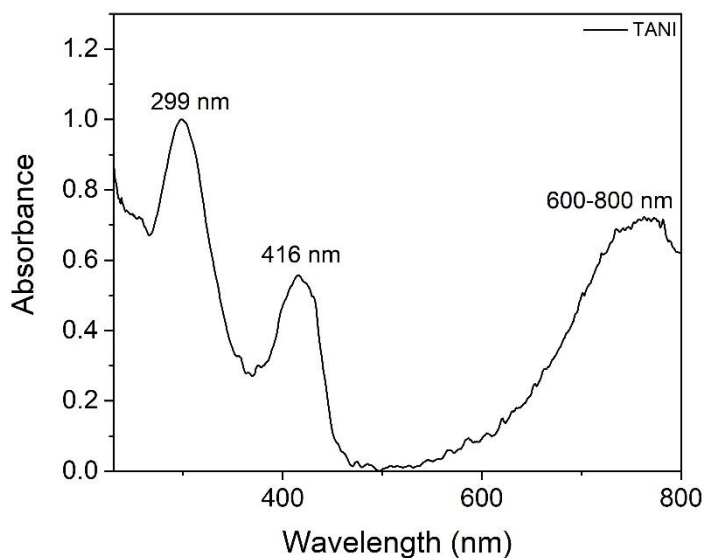
Appendix Figure 30 ^{13}C NMR spectrum of TANI-SBS

Appendix Figure 31 HSQC spectrum of TANI-SBS

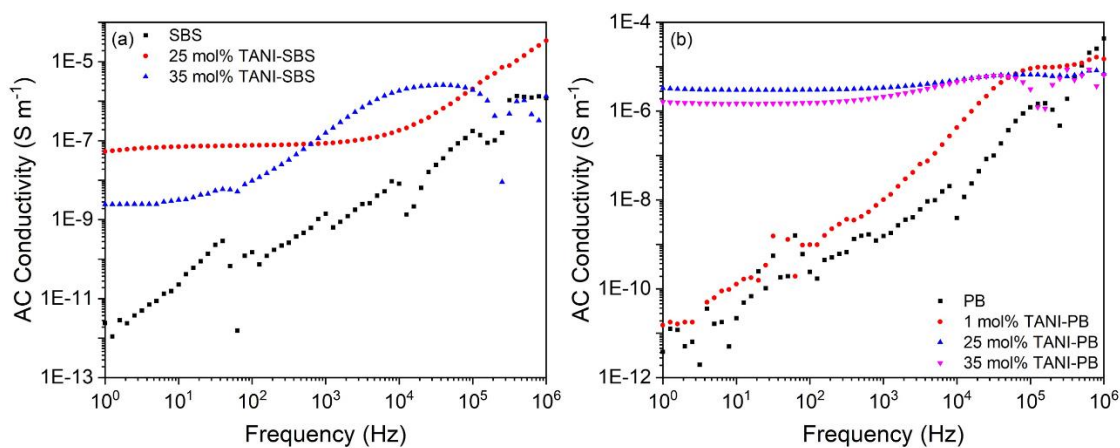


Appendix Figure 32 HMBC spectrum of TANI-SBS

Appendix Figure 33 DMTA $\tan \delta$ spectrum of 50 mol% TANI-PB



Appendix Figure 34 Solution state UV-Vis spectroscopy of TANI in emeraldine salt state



Appendix Figure 35 Impedance spectroscopy AC conductivity graphs for (a) SBS, 25 mol% TANI-SBS and 35 mol% TANI-SBS and (b) PB, 1 mol% TANI-PB, 25 mol% TANI-PB and 35 mol% TANI-PB

Journal Papers and Conference Presentations

Journal papers published and submitted

1. W. Wu, J. Ekeocha, **C. Ellingford**, S. N. Kurup and C. Wan*, Shape memory-assisted self-healing polymer systems, *Self-healing polymer-based systems*, 2020, 95-121
2. **C. Ellingford**, R. Zhang, A. M. Wemyss, Y. Zhang, O. Brown, H. Zhou, P. Keogh, C. Bowen and C. Wan*, Self-healing dielectric elastomers for damage-tolerant actuation and energy harvesting, *ACS Appl. Mater. Interfaces*, 2020, **12**, 6, 7595. Citations: 5
3. **C. Ellingford**, A. M. Wemyss, R. Zhang, I. Prokes, T. Pickford, C. Bowen, V. A. Coveney and C. Wan*, Understanding the enhancement and temperature-dependency of the self-healing and electromechanical properties of dielectric elastomers containing mixed pendant polar groups, *J. Mater. Chem. C*, 2020, **8**, 16, 5426. Citations: 2
4. Y. Huang, **C. Ellingford**, C. Bowen, T. McNally, D. Wu and C. Wan*, Tailoring the electrical and thermal conductivity of multi-component and multi-phase polymer composites, *Inter. Mater. Rev.*, 2020, **65**, 3, 129. Citations: 11
5. W. Wu, S. N. Kurup, **C. Ellingford**, J. Li and C. Wan*, Coupling dynamic covalent bonds and ionic crosslinking network to promote shape memory properties of ethylene-vinyl acetate copolymers, *Polymers*, 2020, **12**, 4, 983. Citations: 1
6. **C. Ellingford**, A. Pengchaicharoen, A. M. Wemyss and C. Wan*, Structure and dielectric properties of electroactive tetraaniline grafted non-polar elastomers, *J. Compos. Sci*, 2020, **4**, 1, 25
7. S. N. Kurup, **C. Ellingford** and C. Wan*, Shape memory properties of polyethylene/ethylene vinyl acetate/carbon nanotube composites, *Polym. Test.*, 2020, **81**, 106227. Citations: 3
8. H. Luo, X. Zhou, **C. Ellingford**, Y. Zhang, S. Chen, K. Zhou, D. Zhang, C. Bowen and C. Wan*, *Chem. Soc. Rev.*, 2019, **48**, 16, 4424. Citations: 131
9. Y. Zhang, **C. Ellingford**, R. Zhang, J. Roscow, M. Hopkins, P. Keogh, T. McNally, C. Bowen and C. Wan*, Electrical and mechanical self-healing in high performance dielectric elastomer actuator materials, *Adv. Funct. Mater.*, 2019, **29**, 15, 1808431. Citations: 24
10. **C. Ellingford**, H. Smith, X. Yan, C. Bowen, L. Figiel, T. McNally and C. Wan*, Electrical dual-percolation in MWCNTs/SBS/PVDF based

thermoplastic elastomer (TPE) composites and the effect of mechanical stretching, *Eur. Polym. J.*, 2019, **112**, 504. Citations: 7

11. E. Heeley, Y. El Aziz, **C. Ellingford**, A. Jetybayeva, C. Wan, E. Crabb, P. G. Taylor and A. Bassingdale, Self-assembly of fluoride-encapsulated polyhedral oligomeric silsesquioxane (POSS) nanocrystals, *CrystEngComm*, 2019, **21**, 4, 710. Citations: 2
12. E. Heely, Y. El Aziz, **C. Ellingford**, A. Jetybayeva, C. Wan, E. Crabb, P. G. Taylor and A. Bassingdale, Self-assembly of fluoride encapsulated POSS nanocrystals, *XMaS: The UK Materials Science Facility at the ESRF*, 2019, 11
13. **C. Ellingford**, R. Zhang, A. M. Wemyss, C. Bowen, T. McNally, L. Figiel and C. Wan*, Intrinsic tuning of poly(styrene-butadiene-styrene)-based self-healing dielectric elastomer actuators with enhanced electromechanical properties, *ACS Appl. Mater. Interfaces*, 2018, **10**, 44, 38438. Citations: 16
14. **C. Ellingford**, C. Bowen, T. McNally and C. Wan*, Intrinsically tuning the electromechanical properties of elastomer dielectrics: a chemistry perspective, *Macromol. Rapid Commun.*, 2018, **39**, 18, 1800340. Citations: 19
15. **C. Ellingford**, C. Wan*, L. Figiel and T. McNally, Mechanical and dielectric properties of MWCNT filled chemically modified SBS/PVDF blends, *Compos. Commun.*, 2018, **8**, 58. Citations: 7
16. **C. Ellingford**, C. Wan*, L. Figiel and T. McNally, Chemical modification of dielectric elastomers in *Modern Physical Chemistry: Engineering Models, Materials, and Methods with Applications*, eds. R. K. Haghi, E. Besalu, M. Jaroszewski, S. Thomas and K. M. Praveen, CRC Press, New York, 2018, pp. 59-94
17. A. Pitto-Barry, A. Lupan, **C. Ellingford**, A. A. A. Attia, N. P. E. Barry, New class of hybrid materials for detection, capture, and 'on-demand' release of carbon monoxide, *ACS Appl. Mater. Interfaces*, 2018, **10**, 16, 13693. Citations: 6

Conference Presentations

18. **C. Ellingford**, C. Wan, L. Figiel and T. McNally, Functional Elastomers for Energy Harvesting and Actuation. Poster presented at the Global Young Scientists Summit (GYSS) 2020, January 2020, One-North, Singapore.
19. **C. Ellingford**, C. Wan, L. Figiel and T. McNally, Self-healing Thermoplastic Elastomers for Actuation and Energy Harvesting. Oral presentation presented at the International Conference on Materials for Advanced Technologies (ICMAT) 2019, June 2019, Marina Bay, Singapore.

20. **C. Ellingford**, C. Wan, Ł. Figiel and T. McNally, Self-healing Elastomers for Energy Harvesting. Oral presentation presented at the Energy Forum 2019, May 2019, University of Warwick, UK.

21. **C. Ellingford**, C. Wan, Ł. Figiel and T. McNally, Intrinsically Tuning the Electromechanical Properties of Elastomeric Dielectrics. Oral presentation presented at the Thermoplastic Elastomers World Summit 2018, Nov 2018, Milan, Italy.

22. **C. Ellingford**, C. Wan, Ł. Figiel and T. McNally, Lightweight Elastomer Nanocomposites for Energy-storage Dielectric Capacitors. Poster presentation presented at the Jaguar Land Rover and WMG Catapult Energy Storage Technology Conference, Sept 2018, University of Warwick, UK.

23. **C. Ellingford**, C. Wan, Ł. Figiel and T. McNally, Advanced Light-weight Elastomeric Nanocomposites for Harvesting Mechanical Energy. Oral presentation presented at the International Conference on the Frontiers of Composite Materials, Nov 2017, Monash University, Melbourne, Australia.

24. **C. Ellingford**, C. Wan, Ł. Figiel and T. McNally, Light-weight Elastomeric Nanocomposites for Harvesting Mechanical Energy. Poster presentation presented at the WMG Doctoral Research and Innovation Conference, June 2017, University of Warwick, UK.